Preface

This master thesis is the final part of the study for Geodetic Engineer at the Delft University of Technology. In the period from May till December 2001 this thesis was written at the Alfred Wegener Institute for Polar and Marine Research in Bremerhaven, Germany. This master research was a combined project with my practical work that also was carried out at the Alfred Wegener Institute, during four months from mid December till mid April. During 7 weeks I worked on board the Research Vessel 'Polarstern'.

First I need to thank my supervisors, Hans Werner Schenke of the Alfred Wegener Institute, and Kees de Jong of the Delft University of Technology, and my professor P. J. G. Teunissen of the section Mathematical Geodesy and Positioning at Delft University of Technology for the opportunity to write my thesis at the Alfred Wegener Institute and to be a member of the scientific crew during the expedition to the Bellingshausen and Amundsen Sea in the Antarctic. For the time during the expedition I would like to thank Rainer Gersonde, as chief scientist on board RV 'Polarstern', my very helpful colleagues, also in Bremerhaven, Ralf Krocker and Steffen Gauger, and especially professor G. Udintsev of the Vernadsky Institute in Moscow.

During my stay in Bremerhaven, for answers on many difficult questions, for help during my research, and for a very pleasant time in Germany I must thank my colleagues of the group Bathymetry and Geodesy at the AWI, first Andreas Beyer for his help with the backscatter data, and of course Fred Niederjasper, Martin Klenke, Constanze Hohmann, Thomas Hartmann, Jörn Hatzky, Ottokarl Büchsenschutz-Nothdurft, Kathleen Lindner and Peter Kirchner. For help with ArcInfo and ArcGIS, for love and encouragement, and for refreshing week-ends I thank my girlfriend Sandra Barthel. For the wonderful six years in Delft, I want to thank all my friends inside and outside Geodesy. Finishing my study would not be possible without my parents Jan Jacops and Gerda Jacops and my brother Joris Jacops. I want to thank them for love, encouragement, believe, and everything else.

Bremerhaven, January 2002

Merijn Jacops

Contents

This master thesis includes some important overview maps on a scale of 1:500 000, these are presented at the end of the appendices.

Abstract

High resolution bathymetric data are widely used for interpretation of the morphology of the sea floor, for geological, and geophysical research, and for the creation of bathymetric maps. The Alfred Wegener Institute for Polar and Marine Research maintains a multibeam system, called Hydrosweep DS-2, for the surveying of the sea floor in the polar regions of the earth.
One of these research projects, in the last years, was the Eltanin Impact Area, situated in the Bellingshausen Sea, at the western entrance of the Drake passage, in the vicinity of the Antarctic waters, and some 700 nautical miles off the Chilean coast. This Eltanin Impact Area is yet the only known impact area affecting the deep ocean basins, and the evidence for this was found in the early 1980's [Kyte et al., 1981].
During two expeditions, in the year 1995 (ANTXII/4) and 2001 (ANTXVIII/5a), with the German Research Vessel 'Polarstern' this area was for the first time systematically surveyed, and bathymetric data was collected within a large area. However, during these two expeditions not only the bathymetric data were collected, but also pseudo side scan data, and backscatter data. These data formed the basis for the master research, presented in this thesis. The main tasks of this research project were first the derivation of a high resolution and accurate digital elevation model of the Eltanin Impact Area, better than 1% of the water depth, within the Geographic Information System (GIS) ArcInfo, and second the backscatter processing and analyses.

For the computation of a digital elevation model different steps were undertaken.
The most important step was the bathymetric data editing and cleaning, to remove the outliers, gross and systematic errors. This data editing and cleaning was performed using the software HIPS of the GIS program CARIS. The editing and cleaning procedure was split up in three parts. First the navigation editor was used to correct for navigational errors, followed by special filters within the swath editor to reject erroneous bathymetric data points. Finally a surface cleaning was performed to remove erroneous data points, based on statistical methods.
These edited and cleaned data were used within ArcInfo to compute a digital elevation model (DEM). Within ArcInfo different methods for the computation of a digital elevation model were analysed. These analyses were founded on the following assumption:

The modelled surface has to fit the original data in the best possible way, with the assumption that the noise does not influence the modelled surface. This means that an acceptable smooth surface has to be modelled within the measurement accuracy.

Within ArcInfo the inverse distance weighting interpolator was used to compute this DEM with the use of a search radius depending on the number of input points, but with a maximum size of 500 meters. The grid size of the DEM was chosen at 100 meters, based

on the average point density. Because of the noise that was present after the computation of the DEM, a slope depending filtering was performed to reduce these effects. For the filtering a binomial filter was used, with its size depending on the topography. In flat areas, because of the high signal-to-noise ratio, more filtering was performed than in steeper areas, where there is a lower signal-to-noise ratio. At the steepest areas no filtering was performed.
This DEM was used as input for the derivation of 20 meter contour lines, and for bathymetric mapping. The mapping was performed using ArcGIS. Four map sheets were produced on a scale of 1:100 000, and two overview map sheets on a scale of 1:200 000 and 1:500 000, covering the area from 56° 50' S to 58° 00' S, and from 90° 10' W to 92° 20' W. Further a basis for a GIS of the Eltanin Impact Area was created with information about bathymetry, geomorphology, and backscatter data.

After these analyses of the bathymetric data, it could be concluded that the software used to clean these data is an important and strong tool within the bathymetric data processing. Almost 10-15% of the bathymetric data had to be rejected because of outliers, gross, and systematic errors. These rejected data points were especially found within the less accurate outer beams. After the editing and cleaning, a digital elevation model, using ArcInfo, could be computed within the accuracy of the multibeam system, being in optimal conditions 0.5% of the water depth, and within the accuracy described in the tasks of the research project, being better than 1% of the water depth. Also the assumption made before, was realised. However, it should be analysed if the accuracy of the computed digital elevation would increase when using a special weighting function for the data points depending on the positions within the swath.

During the two expeditions the multibeam system Hydrosweep DS-2 not only collected the bathymetric data, but also backscatter strengths data. These data were analysed for an interpretation of the bottom roughness and bottom type within the Eltanin Impact Area. With the use of the computed digital elevation model the two important parameters for backscatter analyses, the backscatter strengths and the incidence angle, were computed. These data were combined for response curve analyses. This is a method to differentiate between different roughness of bottoms, and bottom types, depending on the incidence angle and the backscatter strength. Within ArcInfo a segmentation was performed using an unsupervised classification. Due to problems with the backscatter data of expedition ANTXII/4, only the backscatter data of expedition ANTXVIII/5a were used for this segmentation.

The use of an unsupervised classification for segmentation of the backscatter data, using the response curve analyses, proved to be successful. A global interpretation of the different roughness of bottoms, and bottom types, could be made, also in comparison with the digital elevation model of the Eltanin Impact Area. In flat basins probably thicker and finer sediments are found, whereas at steep flanks and in areas with a lot of relief, coarser bottom types with thin sediment layers are to be found. However for a full view and better analyses of the backscatter data, the analyses of ground truth data, grain size and bottom type of the upper sediment layer, is very crucial.

Samenvatting

Hoge resolutie bathymetrische data worden algemeen gebruikt als middel voor de interpretatie van de structuur van de zeebodem, voor geologisch en geofysisch onderzoek, en voor het vervaardigen van bathymetrische kaarten. Het Alfred Wegener Instituut voor Pool en Marien Onderzoek gebruikt in de onderzoeksprojecten voor het in kaart brengen van de zeebodem in de polare regionen van de aarde, het multibeam systeem Hydrosweep DS-2.
Een van de onderzoeksprojecten van de laatste jaren was het Eltanin Impact Gebied, gelegen in de Bellingshausen Zee, aan het begin van de Drake pasage, dichtbij de antarctische convergentie, en ongeveer 700 nautische mijlen verwijderd van de kust van Chili. Het Eltanin Impact Gebied is op dit moment het enige gebied in de diepzee waar een impact heeft plaatsgevonden. In de tachtiger jaren is hiervoor het eerste bewijs gevonden.
Tijdens twee expedities met het Duitse onderzoeksschip 'Polarstern', in het jaar 1995 (ANTXII/4), en 2001 (ANTXVIII/5a), is dit gebied voor het eerst systematisch in kaart gebracht, en zijn op uitgebreide schaal bathymetrische data ingewonnen. Het multibeam systeem verzameld echter niet alleen bathymetrische data, maar daarnaast ook nog sidescan and backscatter data. Deze datasets vormen de basis voor dit afstudeerproject, gepresenteerd in deze afstudeerscriptie. De belangrijkste thema's tijdens dit afstudeeronderzoek waren, de afleiding van een nauwkeurig hoogtemodel van het Eltanin Impact Gebied in het Geografisch Informatie Systeem (GIS) ArcInfo, met als doel een nauwkeurigheid beter dan 1% van de waterdiepte, en ten tweede het processeren van de backscatter data en de analyse hiervan.

Voor de berekening van het hoogtemodel werden verschillende stappen uitgevoerd.
De belangrijkste stap was het editeren en opschonen van de bathymetrische data om de grove fouten en de systematische fouten te verwijderen. Dit is uitgevoerd met de software HIPS van het uitgebreide GIS CARIS. Het proces bestond uit drie delen, namelijk het editeren van de navigatie data, het verwijderen van foute data in de 'swath editor' met behulp van speciale filtertechnieken, en tenslotte de 'surface cleaning' voor het opschonen van de data met behulp van statistische methoden.
Deze opgeschoonde data is vervolgens gebruikt in ArcInfo om een digitaal hoogtemodel te berekenen. Met ArcInfo zijn verschillende methoden voor het berekenen van een digitaal hoogtemodel geanalyseerd, gebaseerd op de volgende aanname:
Het gemodelleerde oppervlak moet het best bij de originele data passen, onder de aanname dat geen ruis het gemodellerde oppervlak beïnvloed. Dit betekent dat een glad oppervlak moet worden gemodelleerd binnen de meetnauwkeurigheid van het systeem.

In ArcInfo is de 'inverse distance weighting' interpolator gebruikt om dit digitale hoogtemodel te berekenen. Hiervoor is een instelling gebruikt met en zoekradius afhankelijk van het aantal punten, en zijnde maximaal 500 meter. De gridgrootte is 100

meter, gebaseerd op de gemiddelde puntdichtheid. Vanwege de ruis, die nog aanwezig was na berekening van het hoogtemodel, zijn nog filters gebruikt om deze ruis te verwijderen. Deze binomiaal filters zijn ingesteld afhankelijk van de helling. In vlakke gebieden is meer ruis aanwezig, vanwege de hogere signaal-ruis verhouding, dan in steilere gebieden. In de steilste gebieden is geen filtering gebruikt.
Het hoogtemodel was de basis voor het afleiden van de 20 meter isolijnen, en voor de kartografie. Deze kartografie is uitgevoerd met ArcGIS. Vier kaartbladen op een schaal van 1:100 000 en twee overzichtskaarten met een schaal van 1:200 000 en 1:500 000, zijn uitgegeven. Deze behelsen het gebied van 56° 50' Z tot 58° 00' Z, en van 90° 10' W tot 92° 20' W. Verder is er in ArcGIS een basis aangelegd voor een GIS systeem van het Eltanin Impact Gebied, met informatie over de bathymetrie, de geomorfologie en de backscatter data.

Na de analyse van de bathymetrische data kan worden geconcludeerd dat de software voor het editeren en opschonen van de data een sterk en belangrijk middel is in de bathymetrische postprocessing. Ongeveer 10-15% van de data moest worden verwijderd vanwege grove of systematische fouten. Deze verwijderde data waren vooral aanwezig in de buitenste, minder nauwkeurige, beams. Vervolgens kon een hoogtemodel worden berekend binnen de nauwkeurigheid van het multibeam systeem, in optimale omstandigheden 0,5% van de waterdiepte, en binnen de nauwkeurigheid van het van tevoren gestelde doel van 1% van de waterdiepte. Ook de gedane aanname kon worden gerealiseerd. Toch zou verder moeten worden onderzocht in hoeverre de kwaliteit van het hoogtemodel kan worden verhoogd door gebruik te maken van speciale gewichtsfuncties afhankelijk van de positie van de beam in de swath.

Tijdens de twee expedities zijn niet alleen bathymetrische data ingewonnen, maar ook backscatter data. Deze data zijn geanalyseerd voor een mogelijke interpretatie van de bodemstructuur en het type van de bodem binnen het Eltanin Impact Gebied. Met het gebruik van het berekende hoogtemodel konden de belangrijkste parameters voor de backscatter analyse worden berekend, namelijk de backscatter sterkte en de invalshoek. Deze data konden worden gebruikt voor de 'response curve analyses', een methode om onderscheid te kunnen maken in bodemstructuur of bodemtype afhankelijk van de invalshoek en de backscatter sterkte. In ArcInfo heeft een segmentatie plaatsgevonden met behulp van een 'unsupervised classification'. Vanwege problemen met de backscatter data van de expeditie ANTXII/4, zijn voor deze segmentatie alleen de data van de expeditie ANTXVIII/5a gebruikt.

Het gebruik van de 'unsupervised classification' voor de segmentatie van de backscatter data, uitgaande van de 'response curve analyse', blijkt succesvol. Een globale interpretatie van de bodemstructuur en bodemtype kan worden gemaakt, zeker in vergelijking met het hoogtemodel van het Eltanin Impact Gebied. In vlakke basins komen waarschijnlijk dikkere en fijnere sedimenten voor als op de hellingen in gebieden met veel reliëf. Hier komen waarschijnlijk grovere bodemstructuren en dunne sedimentlagen voor. Voor een volledige analyse en een volledige interpretatie van deze backscatter data, is het noodzakelijk dat de 'ground truth' geanalyseerd wordt. Het gaat hierbij om de korrelgrootte en de bodemtype van de bovenste sedimentlaag.

Zusammenfassung

Hochauflösende bathymetrische Daten werden heutzutage überall als Mittel zur Interpretation der Struktur des Meeresbodens benutzt, sowohl für geologische und geophysikalische Untersuchungen als auch für die Herstellung von bathymetrischen Karten. Das Alfred-Wegener-Institut für Polar- und Meeresforschung benutzt in Forschungsprojekten für die bathymetrische Vermessung in den polaren Gebieten der Erde das Fächerecholotsystem Hydrosweep DS-2.
Eines dieser Untersuchungsprojekte aus den vergangenen Jahren war das Eltanin Impact Gebiet, gelegen im Bellingshausen Meer, am Anfang der Drake Passage, in der Nähe der Antarktischen Konvergenz, ungefähr 700 nautische Meilen vor der Chilenischen Küste. Das Eltanin Impact Gebiet ist momentan das einzige bekannte Gebiet in der Tiefsee, in dem ein Impact statt gefunden hat. In den achziger Jahren ist der erste Beweis dafür gefunden worden.
Auf zwei Expeditionen mit dem Forschungsschiff ´Polarstern` im Jahr 1995 (ANTXII/4) und im Jahr 2001 (ANTXVIII/5a) ist dieses Gebiet das erste Mal systematisch vermessen worden. Ergiebige Mengen bathymetrischer Daten konnten gewonnen werden. Das Fächerecholotsystem liefert nicht nur bathymetrische Daten, sondern auch Pseudo Sidescan und backscatter (Rückstreuwerte) Daten. Diese Daten sind die Basis für diese Diplomarbeit. Die wichtigsten Themen dieser Diplomarbeit waren erstens die Ableitung eines genauen digitalen Höhengeländemodels des Eltanin Impact Gebietes mit dem Geografisches Informationssystem (GIS) ArcInfo mit einer Genauigkeit von besser als 1% der Wassertiefe, und zweitens das Prozessieren und Analysieren der backscatter Daten.

Die Berechnung des Höhengeländemodels erfolgte in verschiedenen Schritten.
Ein wichtiger Schritt war das Editieren und Bereinigen der bathymetrischen Daten, um grobe und systematische Fehler zu eliminieren. Dieser Bearbeitungsschritt wurde mit der Software HIPS, Teil der GIS-software CARIS, durchgeführt. Er bestand aus drei Teilen, erstens dem Editieren der Navigationsdaten, zweitens dem Editieren der bathymetrischen Daten anhand von speziellen Filtern im ‘swath editor’, und drittens dem ‘surface cleaning’ für das Bereinigen anhand von statistischen Methoden.
Diese bereinigten Daten sind in ArcInfo für die Berechnung eines digitalen Höhengeländemodels benutzt worden. Der Analyse von verschiedenen Berechnungsmethoden in ArcInfo lag folgende Annahme zu Grunde:
Die modellierte Geländefläche soll die originalen Daten am besten repräsentieren, unter der Annahme, dass das Messrauschen die Oberfläche nicht beeinflusst. Dies bedeutet, dass eine glatte Geländefläche innerhalb der Genauigkeit des Meßsystems berechnet werden muss.

In ArcInfo ist die ‘inverse distance weighting’ Interpolationsroutine zur Berechnung des Höhengeländemodels benutzt worden. Die Höhe des Gitterpunktes berechnet sich aus den umliegenden Messpunkten in einem Suchradius, abhängig von der Datenauflösung und einen Maximum von 500 Metern. Die Zellgrösse beträgt 100 Meter, basiert auf der

mittleren Datenauflösung. Wegen des Messrauschens, welches auch noch anwesend ist nach der Berechnung des Höhengeländemodels, wurden binomial Filter, in Abhängigkeit der Hangneigung, benutzt, um das Grid von diesem Rauschen zu befreien.
Das Höhengeländemodel diente als Grundlage zur Ableitung von Tiefenlinien im Interval von 20 Metern und für die kartografische Darstellung mit ArcGIS. Insgesamt vier Kartenblätter im Maßstab von 1:100 000 sind ausgegeben worden sowie zwei Übersichtskarten mit einem Maßstab von 1:200 000 und 1:500 000. Diese Karten umfassen das Gebiet von 56° 50' S bis 58° 00' S und von 90° 10' W bis 92° 20' W. Weiterhin wurde in ArcGIS noch die Basis für ein GIS des Eltanin Impact Gebietes gelegt, welches bathymetrische, geomorphologische und backscatter Daten beinhaltet.

Eine Schlussfolgerung aus der Datenanalyse ist, dass die Software zur Bereinigung der bathymetrischen Daten ein brauchbares und starkes Mittel im Postprocessing bathymetrischer Daten ist. Ungefähr 10-15% der Messwerte sind wegen grober und systematischer Fehler aus den Datensätzen eliminiert worden. Die Herkunft dieser Daten sind vor allem die äußeren, ungenaueren Beams. Im Ergebnis konnte ein Höhengeländemodel mit einer Genauigkeit gleich der des Messsystems, in optimalen Konditionen 0,5% der Wassertiefe berechnet werden, womit das Ziel, besser zu sein als 1% der Wassertiefe, erreicht wurde. Auch die zu Grunde gelegte Annahme konnte realisiert werden. Jedoch sollte weiterhin analysiert werden, ob die Genauigkeit des Höhengeländemodels sich verbessern würde, wenn spezielle Gewichte anhand der Positionen im Swath benutzt werden.

Während der zwei Expeditionen sind nicht nur die bathymetrischen Daten gesammelt worden, sondern auch die backscatter Daten. Diese Daten sind analysiert worden, um Aussage über die Bodenbeschaffenheit und den Bodentyp zu ermöglichen. Das Höhengeländemodel ist benutzt worden, um den wichtigsten Parameter für die backscatter Analyse, die backscatter Stärke und die Einfallswinkel, zu berechnen. Diese Daten sind anhand der 'response curve analyses' analysiert worden, eine Methode zur Unterteilung von verschiedenen Bodentypen und Strukturen mittels backscatter Stärke und Einfallswinkel. Eine Segmentierung hat in ArcInfo durch 'unsupervised classification' stattgefunden. Aufgrund von Problemen mit den backscatter Daten der Expedition ANTXII/4 sind nur die Daten der Expedition ANTXVIII/5a segmentiert und analysiert worden.

Die Benutzung der 'unsupervised classification' für die Segmentierung der backscatter Daten anhand der 'response curve analyses' ist sehr befriedigend. Eine globale Interpretation der Bodenbeschaffenheit und Bodentypen ist möglich, vor allem im Zusammenhang mit dem Höhengeländemodel des Eltanin Impact Gebietes. In ebenen Flächen gibt es sehr wahrscheinlich mächtigere und feinere Sedimente. In steileren Lagen an den Hängen gibt es eine grobe Struktur und eine dünne Sedimentschicht. Für ein gesamtes Bild und eine umfassende Analyse dieser backscatter Daten ist eine Analyse des 'ground truth' sehr wichtig. Dadurch können Informationen zu Korngröße und dem Bodentyp der obersten Sedimentschicht mit in die Auswertung einfliessen.

Introduction

Almost 2.15 million years ago an impact of a meteorite took place in the Bellingshausen Sea, at the western entrance of the Drake passage, in the vicinity of the Antarctic, and some 700 nautical miles off the coast of Chile. It is the only known example of an impact on the 60% of the Earth's surface covered by deep ocean basins. In 1981 evidence of this impact as an iridium anomaly, was found within a sediment core taken in 1964 by the USNS Eltanin, in the vicinity of the San Martin Seamount.
During two expeditions of the Alfred Wegener Institute on board the Research Vessel 'Polarstern', in 1995 (ANTXII/4) and in 2001 (ANTXVIII/5a), this area was systematically surveyed. The goal of these systematic surveys was to reconstruct and determine in more detail the age of the impact, the target area and the size of the impact body as well as its effect on the deep-sea sediment distribution and the environment.
The surveying of the sea floor was performed with the multibeam system Hydrosweep DS-2 to collect bathymetric, side scan, and backscatter data. These high resolution bathymetric data were the first systematic data within the Eltanin Impact Area, and provide a basis for the first accurate digital elevation model of the Eltanin Impact Area. The backscatter data will give information about the bottom roughness and bottom type, and can be combined with the ground truth. These data will help within the research and analyses of the geological, geomorphological, and geophysical structures.

The goal of this master research, presented within this master thesis, is to edit an clean the bathymetric data, collected during the expeditions ANTXII/4 and ANTXVIII/5a, and to create with these data an accurate elevation model of the Eltanin Impact Area. This digital elevation model will be used as a basis for the bathymetric mapping in a scale of 1:100 000, and for implementation within 3D-visualisation software. The processing and analyses of the backscatter data, collected also during both expeditions, forms the other part of this research project. This backscatter data can be used to be able to interpret the bottom roughness, and bottom type.

The structure of this master thesis is as follows. In chapter 1 an introduction will be given in the history of bathymetry and the development of the bathymetry at the Alfred Wegener Institute. Chapter 2 describes the theory of acoustics in water, and gives a short introduction in the technique of echo sounders, and multibeam systems. The multibeam system Hydrosweep DS-2, which is installed on Research Vessel 'Polarstern' of the Alfred Wegener Institute, is described in chapter 3. The errors and effects than influence the bathymetric measurements are discussed in chapter 4. Chapter 5 gives an introduction in the geological and geophysical background of the Eltanin Impact Area, and gives a description of the expeditions in that area. The first step to create a digital height model is the bathymetric data editing and cleaning, described in chapter 6. This is followed by chapter 7, with the analyses of the digital elevation modelling using ArcInfo. The bathymetric mapping of the Eltanin Impact Area, and the basis for a GIS of the Eltanin

Impact Area is presented in chapter 8. The analyses of the backscatter data for the interpretation of the bottom roughness and bottom type, will be discussed in chapter 9. The chapters 10 and 11, finally, will present the conclusions and the recommendations of this master research, respectively.

Some important maps are included within this master thesis, these can be found at the end of the thesis, as overview map sheets on a scale of 1:500 000.

1. The History of Bathymetry

Already in the 15th century the first example of a sonar was given, but only in the 20th century the technique of measuring depth's and surveying of the bottom of the sea developed. This chapter will give a short introduction in the history of underwater sound and in the use of multibeam systems at the Alfred Wegener Institute (AWI).

1.1 History of Underwater Sound

It was Leonardo da Vinci who wrote in 1490, that sound exists not only in the air but also beneath the surface of the water, or in his words: "If you cause your ship to stop, and place the head of a long tube in the water and place the outer extremity to your ear, you will hear ships at a great distance from you." This was the earliest example of a passive sonar (SOund NAvigation and Ranging) system [Caruthers, 1977].
Probably the first measurement in sound beneath the water surface was carried out in 1827 by the Swiss physicist, Daniel Colladon, and the French mathematician, Charles Sturm, in lake Geneva. They determined the sound velocity in water with a surprising degree of accuracy. In the second half of the 19th century, a lot of physicists were indirectly involved in underwater sound because of their interest in the conversion of electricity into sound and vice versa. In 1880 Jacques and Pierre Curie discovered the piezoelectricity; the ability of crystals, when stressed, to develop an electric charge across certain pairs of crystal faces. Another invention was the carbon-button microphone, the earliest and high sensitive microphone for underwater sound [Urick, 1983]. Although the first sound measurement was made and a lot of discoveries were made, the practical use of underwater sound had a start in the beginning of the 20th century.

In the years before World War I, the first systems were developed for detection of underwater objects. Just after the Titanic collided a patent was applied for the first echo ranging application, and in 1914 a transducer was built for submarine signalling and echo ranging. In 1912 the first patent for an echo sounder was applied by the German Alexander Behm.
During World War I a number of military applications of sonar systems were developed. In 1916 the Russian Constantin Chilowsky and the French Paul Langlevin, were able to obtain echoes from the bottom of the water and from a sheet of armor plate at a distance of 200 meters. In 1917 Langlevin used the piezoelectric effect and amplifiers for his experiments [Clay, 1977]. In that time also the British Investigations worked on secret experiments for detection of submarines, they used the word 'asdics', which stands for Anti Submarine Division –ics, according A.B. Wood [Urick, 1983].
The years between World War I and II saw a slow but steady advance in applying underwater sound. Depth sounding for ships, however, became commercially available in 1925. These systems for depth sounding were the so called fathometers. In the late

1930's fairly adequate systems were developed and a number of American ships were equipped with underwater listening and echo ranging devices. The most progress was made in the understanding of sound propagation in the sea. They found that the cause for the different quality of the echoes could be sought in the characteristics of the seawater. With the use of temperature-measuring devices it became evident that thermal gradients could refract the sound and could cause the target to lie in the 'shadow' zone. In 1937 A.F. Spilhaus built the first bathythermograph to indicate the temperature gradients in the upper layers of the sea. In these years also a good understanding in the absorption of sound in water was gained and accurate values of absorption coefficients at frequencies of 20 to 30 kHz were determined [Urick, 1983].

In World War II at both sides a lot of activity was found in the underwater sound research. Methods for quick calibration of projectors and hydrophones became in use, and understanding of the factors affecting sonar performance was gained. An innovation at the German side was the 'GruppenhörGerät', using flush-mounted arrays. They also produced a non-reflecting coating for submarines. Late in the war the word 'sonar' was used as counterpart of the word 'radar' (Radio Detection And Ranging) [Urick, 1983].
In the years after 1945 a lot of advances were made. The advances can be found in the development of the sonar devices and in the signal processing. New devices became available with sending frequencies of 70 Hz up to 12 KHz. These frequencies were chosen for a better propagation in the sea. Also the devices became larger and, compared to the time before, with more arrays. The research in sound propagation in the deep-sea also led to new discoveries and new developments [Tsoukalas, 1999]. In the 1960's the company General Instruments Corporation patented a technique for multiple narrow-beam depth sounding, the first multibeam systems, known under the name SASS (Sonar Array Sounding System). It used two separate sonar arrays oriented orthogonal to each other, one for sending and one for receiving [L-3, 2000]. This system was developed for the US Navy and became available for commercial use in 1976. The system SASS was first installed on the Australian Research Vessel 'Cook'. After this system became available for commercial use the name was changed in Seabeam Instruments. In 1979 this Seabeam system was installed on the French Research Vessel 'Jean Charcot'. Since this first installation multibeam systems form the basis for deep sea research and exploitation. Many companies nowadays produce multibeam systems for shallow, medium, and deep sea surveys. Examples of such systems are Hydrosweep, Seabeam, Simrad, and Reson.

1.2 History of Multibeam Systems at the AWI

In 1981 the first German research vessel 'Sonne' was equipped with the Seabeam system. In 1982 the German research vessel 'Polarstern', known as Polarforschungs- und Versorgungsschiff 'Polarstern', was built. During its construction, it was equipped with the Seabeam System. The reason was to be able to survey the seafloor in the unknown Polar regions of the world. This system had a frequency of 12.150 kHz and a fan aperture of almost 43°, resulting in a coverage of ~4.000 meters at a depth of 5.000 meters. This coverage was measured using 16 Pre-Formed-Beams (PFB). The system could reach depths up to 12.000 meters, because of the used frequency [Schenke, 1992].

Between 1984 and 1986 Krupp Atlas Elektronik in Bremen developed a new efficient bathymetric swath-mapping system. The name for this system 'Hydrosweep' was derived from: HYDROgraphic multibeam SWEEPing survey echosounder. The system was used in deep sea, therefore the system was called Hydrosweep-DS (Deep Sea), This system was first installed on the new German Research Vessel 'Meteor' in 1986. The technique used was the same 'crossed fan' technique as used by Seabeam. The Hydrosweep fan aperture of 90° realised a coverage of up to two times the water depth, using 59 PFB's instead of 16.
During extensive tests in the years between 1986 and 1989 with the Research Vessel's 'Meteor' and 'Polarstern' the two systems were analysed. Different kinds of sea bottom topography and structures were surveyed and analysed during these test cruises. In 1989 the new Hydrosweep system was also installed on the Research Vessel 'Polarstern', with the advantage of the ice protected acoustic elements [Schenke, 1989]. In 1993 and 1994 the system was technically improved. The fan aperture could be changed between 90°, for deep-sea, and 120°, for shallower waters. Also the capability for a pseudo Side Looking Sonar was installed. This Hydrosweep-DS system was in use until 1997, at that time a further developed system Hydrosweep DS-2 was installed, with an integrated Side Scan Sonar. A system description of Hydrosweep DS-2 will be given in Chapter 3, as it is the system used to collect the multibeam data, analysed within this thesis.

Figure 1.1: The German Research Vessel 'Polarstern'.

2. Acoustics in Water

A sound wave is a density disturbance that travels through the medium. Because of this density disturbance the particles, of which this medium consists, will start to move and the distance between these particles will therefore change from place to place. The speed of this disturbance, or the speed of the acoustical wave, depends on the characteristics of the medium. In an isotropic medium the speed of the acoustical wave will be constant in every direction and the distance is proportional to the travel time. However, in most of the cases the medium will be inhomogeneous and the speed of the sound wave will change when travelling.
This chapter will give an overview of the concepts of acoustic wave propagation. The chapter starts with the two principle theories, the wave theory and the ray tracing theory, followed by an introduction to the sonar equations in section 2. It continues in section 3 with a description of sound speed in the ocean and ends with section 4, describing the principle of echo sounding systems.

2.1 Wave Theory and Ray Tracing

Sound propagates in a way controlled by a linear, second-order partial differential equation. Actually there are two differential equations, both describing the same phenomenon. These differential equations (2.1), well known as the 'Wave Equations', are obtained from four basic equations [Caruthers, 1977], and are given as follows:

(2.1) $$\nabla^2 p_e - \frac{1}{c^2}\frac{\partial^2 p_e}{\partial t^2} = 0 \qquad \nabla^2 r_e - \frac{1}{c^2}\frac{\partial^2 r_e}{\partial t^2} = 0$$

In these equation p_e and r_e are the excess of 'acoustical' pressure and density, respectively. The time in seconds is given by t. Because the solutions of these equation are waves propagating with the speed c, this speed is called the sound speed.
The four equations, resulting in the wave equations, are, with the particle velocity u, the force per unit volume f and the bulk modulus k:

(2.2)
$$\text{Equation of continuity: } \frac{\partial p}{\partial t} + \nabla \cdot (ru) = 0$$

$$\text{Equation of motion: } f = \frac{\partial}{\partial t}(ru)$$

Force-Pressure Relation: $f = -\nabla p$

(2.2)

Equation of state: $p_e = \frac{k}{r_0} r_e \qquad p = p_0 + p_e, \quad r = r_0 + r_e$

The second-order differential equations (2.1) can be solved by two approaches: the wave theory and the ray tracing theory. In the wave theory functional solutions are sought within a set of boundary conditions. The ray tracing theory assumes a specific form of the solution which is inserted into the wave equation giving a new equation, the 'eikonal equation'.

2.1.1 The Wave Theory

The result when using the wave theory is a complicated mathematical function. This method is particularly suited for a description of sound propagation in shallow water [Urick, 1983]. Here a short introduction is given to this theory.
Therefore, let's consider the one-dimensional wave equation:

(2.3) $$\frac{\partial^2 p}{\partial x^2} - \frac{1}{c^2}\frac{\partial^2 p}{\partial t^2} = 0$$

The general solution for this equation is given by:

(2.4) $$p(x,t) = m(x - ct) + n(x + ct)$$

This solution can be verified by direct substitution into the wave equation (2.3). If m is zero, the solution represents a rigid wave propagating in negative direction along the x-axis. The wave propagates in positive direction along the x-axis if n is zero. Are both m and n zero, no specific direction can be assigned to the motion. When m and n are identical, then a standing wave exists [Caruthers, 1977].
A common used solution is the cosine wave form, given by (2.5), with a the wave amplitude and w the angular velocity. It is the plane wave equation.

(2.5) $$p(x,t) = a\cos\{w(t - x/c)\}$$

Now one can find with the equations (2.2), that the density variations r, particle velocity u and particle movement x are given by [Jong, 1988]:

$$r(x,t) = r_0 ka\cos\{w(t - x/c)\}$$

(2.6) $$u(x,t) = \frac{1}{r_0 c} a\cos\{w(t - x/c)\}$$

$$x(x,t) = \frac{1}{w r_0 c} a\cos\{w(t - x/c)\}$$

The quantity $r_0 c$, is the 'acoustical impedance'. The acoustical impedance is comparable with the electrical impedance and depends on the material or medium. It defines the possibility of a material or medium to resist the propagation of an acoustical wave. With this acoustic impedance also echoes can be explained. The wave propagates through the water, which has a low acoustic impedance. The water particles are moved by this propagating wave. When the wave interacts with the seafloor, the impedance increases and the movement of these rock particles is much smaller. Not all the wave energy can therefore be transmitted into the seafloor and because no energy may be lost, a part of this acoustic energy is reflected away. As a result, two things happen when a sound wave interacts with a new medium with a different impedance. One part of the wave is transmitted into the new medium, the other part is reflected away in the first medium [Tsoukalas, 1999].

The propagating wave carries mechanical energy with it. This energy is in the form of kinetic energy, the motion of the particles in the medium, and potential energy, the stresses set up in the elastic medium. Because the wave propagates, this means that a certain amount of energy per second will flow across a unit area oriented normal to the direction of propagation. This amount of energy per second is called the intensity of the wave, in the plane wave situation given by:

(2.7) $$I = \frac{a^2}{r_0 c}$$

When taking a closer look at (2.5) at a fixed time t_0, one can see that the plane wave has a period of $2p$ radians. Because of this periodicity the wavelength l can be defined. It follows with the wave number written as k.

(2.8) $$l = \frac{2pc}{w} = \frac{2p}{k}$$

Again with (2.5), but now at a fixed position x_0, one can see that there is a period between two equal amplitudes. Therefore the period T can now be defined. With f the frequency in Hertz it follows [Jong, 1988]:

(2.9) $$T = \frac{2p}{w} = \frac{1}{f}$$

2.1.2 Ray Tracing

The ray tracing theory is very useful for high frequencies. The essence of the ray tracing theory is the postulate of wavefronts, along which the phase or time function of the solution is constant, and the existence of rays that describe where in space the sound emanating from the source is being sent.

The ray tracing theory is based upon the 'eikonal equation'. The eikonal equation can be obtained from the wave equation (2.1) by substituting a solution of a particular form into this wave equation.

The solution is assumed to be:

$$p(x,t) = A\exp\left\{j\left(wt - {w}/{c_0}\right)W\right\} \tag{2.10}$$

In this solution (2.10), c_0 is a constant speed and place independent, whereas A and W are place dependent functions [Jong, 1988].

Substitution of equation (2.10) into the wave equation yields:

$$\nabla^2 A - \frac{w^2}{c_0^{\,2}} A\left|\nabla W\right|^2 + \frac{w^2}{c^2} A - 2j\frac{w}{c_0}\nabla A\cdot\nabla W - j\frac{w}{c_0}A\nabla^2 W = 0 \tag{2.11}$$

This equality (2.11) only is valid, when both the real and the imaginary parts are zero:

$$A\left(\left|\nabla W\right|^2 - \frac{c_0^{\,2}}{c^2}\right) = \nabla^2 A\frac{c_0^{\,2}}{w^2} = \nabla^2 A\frac{l_0^{\,2}}{4p^{\,2}A}$$

and (2.12)

$$A\nabla^2 W + 2\nabla A\cdot\nabla W = 0$$

Assuming A not to vary too much and assuming a frequency that is high enough, the equation (2.11) can be approximated by (2.13), the eikonal equation:

$$\left|\nabla W\right|^2 - n^2 = 0 \text{ with } \quad n = \frac{c_0}{c} \tag{2.13}$$

In this equation n is called the index of refraction and it may be dependent upon the position vector, W is called the eikonal. The eikonal W, as a function of the position vector, is a surface in three-dimensional space that can be associated with the wave fronts. This can be seen in the equation if the phase of (2.10) is set constant at a particular time t_0. With this it follows, with d a constant:

$$W(r) = \left(t_0 - \frac{d}{w}\right)c_0 \tag{2.14}$$

This equation shows a surface in space with a constant phase. The acoustical energy propagates along curved lines, the acoustical rays. These rays are everywhere perpendicular to the wave fronts and are also determined by (2.13) [Caruthers, 1977].

Snell's Law

The ray tracing theory can also be explained by Fermat's principle. This principle states that the path that a ray will take in going from point A to point B is such that the time will be an extremum; in most of the cases this extremum is a minimum.

This can be written as follows, with $c(s)$ the speed of sound as a function of the path s:

$$t = \int_A^B \frac{ds}{c(s)} \tag{2.15}$$

With this principle of Fermat (2.15) and the eikonal equation (2.13) Snell's law can be derived [Jong, 1988]. Snell's law states that in a medium consisting of constant velocity layers, the grazing angles q_1, q_2, K of a ray at the layer boundaries are related to the sound velocity c_1, c_2, K of the layers. This is expressed as follows:

$$\frac{\cos q_1}{c_1} = \frac{\cos q_2}{c_2} = \mathrm{K} \text{ = constant for a given ray} \tag{2.16}$$

At a given depth, when the speed of sound increases, there will be a point where the ray becomes horizontal. The grazing angle q becomes zero, which means that $\cos q$ becomes 1, and the constant will be the reciprocal of the sound velocity in this layer. This velocity c_v is called the 'vertex velocity'. A better understanding of Snell's law is given by Figure 2.1.

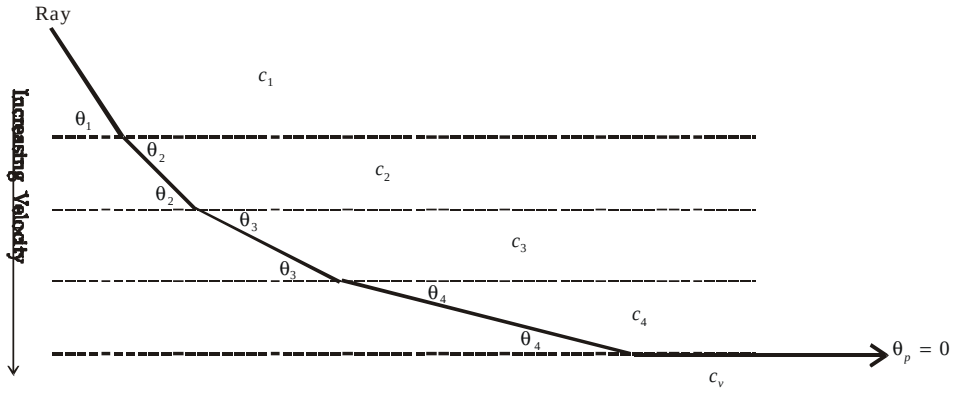

Figure 2.1: Snell's Law in a layered medium.

In a medium in which the sound velocity changes linearly, instead of increasing in layers as described above, the sound rays can be shown to be arcs of circles. The sound velocity will increase using $c = c_0 + gz$, with depth z and velocity gradient g. This can be shown as follows.

Consider two points P_1 and P_2 and the arc of a circle with a radius R connecting these two points. At these points the sound velocity is c_1 and c_2, respectively. The tangent to the circle is horizontal where the sound velocity is c_v. With Figure 2.2 it can be observed that:

$$\begin{aligned} d_2 - d_1 &= R\cos q_1 - R\cos q_2 \\ \mathrm{c}_1 &= c_v + gd_1 \\ \mathrm{c}_2 &= c_v + gd_2 \end{aligned} \tag{2.17}$$

It follows:

(2.18) $$d_2 - d_1 = \frac{c_2 - c_1}{g}$$

When Snell's law is satisfied the circle between points P_1 and P_2 will be a ray. This means that:

(2.19) $$c_v = \frac{c_1}{\cos q_1} = \frac{c_2}{\cos q_2}$$

Now one finds after elimination of $d_2 - d_1$, $\cos q_1$ and $\cos q_2$, with equation (2.17), (2.18) and (2.19) that the circle drawn between the points P_1 and P_2 will be a ray if, and only if:

(2.20) $$R = -\frac{c_v}{g}$$

Because the points P_1 and P_2 were arbitrarily selected, it follows that all rays in the medium will be arcs of circles [Urick, 1983].

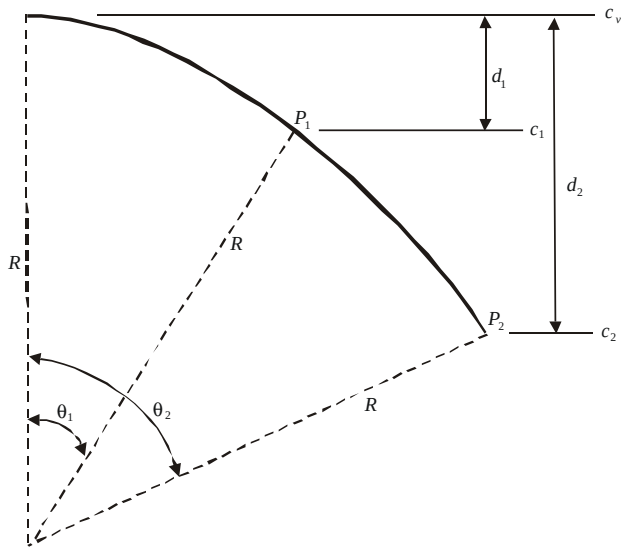

Figure 2.2: A ray shown as an arc of a circle in a medium with a constant sound velocity gradient.

In underwater sound usually the velocity gradient is chosen to be positive if the sound velocity increases with depth, and negative if the sound velocity decreases with depth. In the first case, a positive gradient, the ray will bend upwards. The curved ray will bend downwards in the second case when the gradient is negative.

2.2 Sonar Systems and Sonar Equations

Many phenomena and effects characteristic to sound underwater produce a variety of effects on the design and operation of sonar equipment. These diverse effects can be grouped together quantitatively in the so called 'sonar parameters'. These sonar parameters are related with each other in the 'sonar equations'. These equations combine the effects of the medium, the target and the equipment [Tsoukalas, 1999].

2.2.1 Active and Passive Sonar Systems

There are active and passive sonar systems. The active sonar systems send and receive the acoustic signal. The sound wave of a specific, controlled frequency is produced at the projector and propagates through the medium, water, to the seafloor. At the seafloor, a part of the sound wave and connected with this, the energy, is reflected and scattered back into the water. This echo travels through the water and is detected by the hydrophone of the sonar system. Passive sonar systems only receive the signal. In this case the source of the signal is not the sonar system itself but another object in the medium, water, sending out acoustic signals [L-3, 2000]. The multibeam system used for surveying the ocean floor is an active sonar system. Therefore only the active sonar equation will be discussed. For more literature about the passive sonar systems and the passive sonar equation [Urick, 1983] is recommended.

2.2.2 Sonar Equations

The sonar equations are based on an expression between the desired and the undesired portions of the received signal. At the receiver, the desired portion of the acoustical field is called 'signal'. The rest of the acoustical field, that is undesired, is called 'background' and consists of 'noise' and 'reverberation'. Noise is the portion not due to one's own echo-ranging, and reverberation is the slowly decaying portion of the background representing the return of one's own acoustic output by scatterers in the sea. The goal is to increase the signal-to-background ratio to be able to detect the received signal [Urick, 1983].

Parameters determined by the equipment	
Source Level	*SL*
Self-Noise Level	*NL*
Receiving Directivity Index	*DI*
Detection Threshold	*DT*

Parameters determined by the medium	
Transmission Loss	*TL*
Reverberation Level	*RL*
Ambient-Noise Level	*NL*

Parameters determined by the target	
Target Strength	*TS*
Target Source Level (passive systems)	*SL*

Table 2.1: The sonar parameters.

The sonar equation is written with the help of the sonar parameters determined by the equipment, the medium and the target. These parameters are levels in units of decibels (dB) relative to the standard reference intensity of a 1-μPa (microPascal) plane wave. The sonar parameters are listed in Table 2.1 [Urick, 1983].

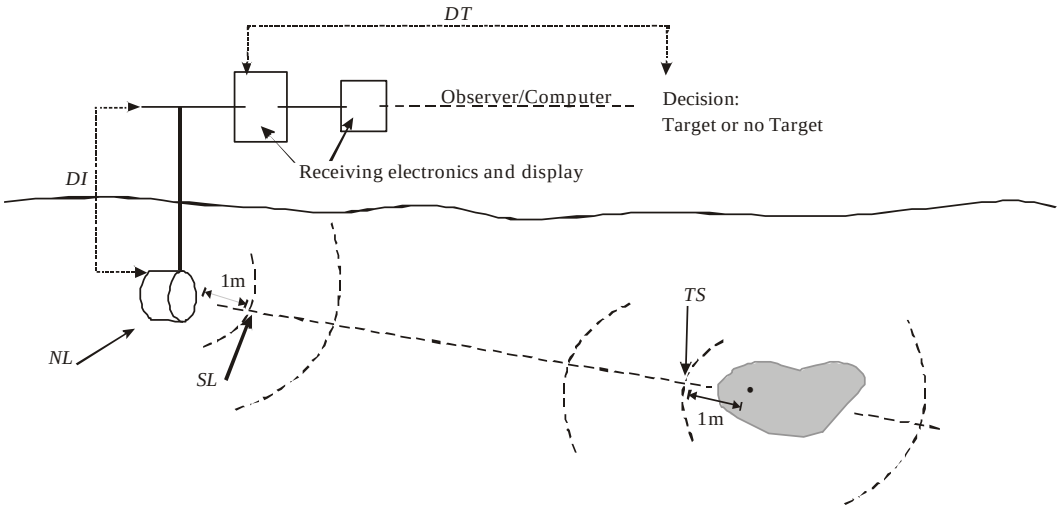

Figure 2.3: Simplified view of echo-ranging.

In Figure 2.3 [Urick, 1983] the meaning of these quantities is illustrated in a simplified way, and it will be used during the explanation of the sonar equation. The projector, also acting as a receiver, a so called transducer, produces a acoustic signal of *SL* dB. The signal reaches the target and its level will be reduced by the transmission loss, *TL*. The target with target strength *TS* reflects or scatters the signal. Therefore the reflected or backscattered level will be as follows, at a distance of 1 meter from the acoustic centre of the target in direction towards the projector:

(2.21) $$SL - TL + TS = \text{reflected/backscattered level}$$

Travelling back towards the source, or in this case the receiving hydrophone, this level is again attenuated by the transmission loss. The echo level at the transducer is now:

(2.22) $$SL - 2TL + TS = \text{reflected/backscattered level at transducer}$$

Let's now concentrate on the background being isotropic noise rather than reverberation. The background level is *NL* and is reduced by the directivity index *DI* of the transducer acting as a hydrophone. The relative echo power is unaffected by the transducer directivity, since the axis of the transducer is pointing in the direction from which the echo is coming. The echo-to-noise ratio at the transducer is therefore:

(2.23) $$SL - 2TL + TS - (NL - DI) = \text{echo-to-noise ratio at transducer}$$

The function of this sonar is to detect the seafloor. When the target is just being detected, the signal-to-noise ratio equals the detection threshold *DT*. The active sonar equation is then:

(2.24) $$SL - 2TL + TS - (NL - DI) = DT$$

This equation is often written in the form of (2.25) because the echo level is at one side of the equation and the noise-masking background level occurs on the other side.

echo level noise - masking level

(2.25) $$SL - 2TL + TS = DT + NL - DI$$

This active sonar equation is for the monostatic case. In this monostatic case the projector and the hydrophone are coincident and the acoustic return of the target is back toward the source. The multibeam system Hydrosweep DS2 is a monostatic sonar system and the hydrophones are at the same position as the projector. Some other systems are bistatic, and the projector and hydrophones are separated. The transmission losses in this case, to and from the target are , in general, not the same [Urick, 1983].
The sonar equation has to be modified in the case the background is reverberation instead of noise. Reverberation is not isotropic in comparison with the parameter *DI*, defined in terms of an isotropic background. The terms $(NL - DI)$ will be replaced by an equivalent plane wave reverberation level *RL*, observed at the hydrophones. The sonar equation with reverberation is then:

(2.26) $$SL - 2TL + TS = DT + RL$$

In Table 2.2 the terminology of the various combinations of the sonar parameters is shown. The 'figure of merit' is the most useful, it gives an immediate indication of the range at which a target can be detected by a sonar. When the background is reverberation, this figure of merit is not constant and therefore not useful as indicator for the sonar performance [Urick, 1983].

Name	Parameters	Remark
Echo Level	$SL - 2TL + TS$	The intensity of the echo as measured in the water at the hydrophone
Noise-masking Level	$NL - DI + DT$	Minimum detectable echo level
Reverberation-masking Level	$RL + DT$	Minimum detectable echo level
Echo Excess	$SL - 2TL + TS - (NL - DI + DT)$	Detection just occurs when the echo excess is zero
Performance Figure	$SL - (NL - DI)$	Difference between the source level and the noise level at the hydrophone
Figure of Merit	$SL - (NL - DI + DT)$	Equals the maximum allowable transmission loss

Table 2.2: Sonar parameter combinations.

Transmission Loss (TL)

Transmission loss may be considered to be the sum of a loss due to spreading and a loss due to attenuation. The weakening of the signal as it spreads outward from the source, is called spreading loss. Attenuation loss includes the effects of absorption and scattering. It is mostly defined as the loss in dB between a point at 1 meter of the source and a point at a distance of r meters from the source.

In the most simple propagation condition, where the medium is homogeneous, unbounded, and without any loss, the signal will propagate equally in all directions. The wave will spread spherically. The transmission loss will therefore be, with r distance in meters:

(2.27) $$TL = 20 \log r$$

In the case there is absorption loss, equation (2.27) will change. It involves a loss of acoustic energy to the medium due to the conversion of this energy into heat. The quantity expressing this loss, is the absorption coefficient a , in $^{dB}/_{m}$. This coefficient is a function of the frequency. The transmission loss is than:

(2.28) $$TL = 20 \log r + ar$$

At low frequencies the transmission losses will be mostly spreading losses, whereas for high frequencies the transmission losses are mostly absorption losses. Sending acoustic energy over greater distances with minimum transmission loss will ask for lower frequencies. This is shown in Figure 2.4 [Jong, 1988].

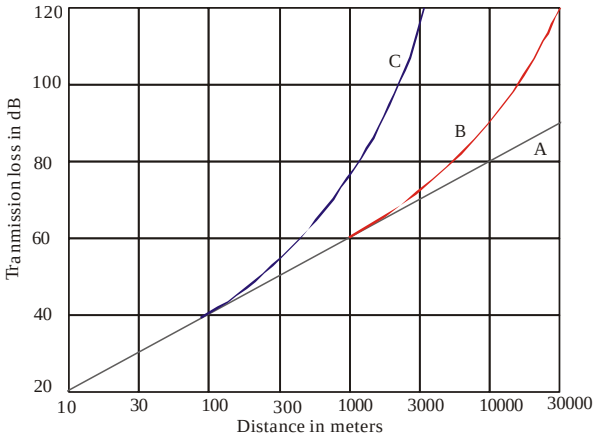

Figure 2.4: Transmission loss in seawater of 10° Celsius as a function of the distance. Curve A is at 1 kHz, curve B at 10 kHz and curve C at 50 kHz.

Directivity Index (DI)

When localising objects under water, not only the distance but also the direction is important. This can be realised by sending the signal through a narrow beam and receiving the signal in a narrow beam. The transducer is then only sensitive in one specific direction.

This is called directivity and is defined as follows:

$$d = \frac{\text{noise power of a nondirectional hydrophone}}{\text{noise power of the actual hydrophone}} \tag{2.29}$$

The directivity index *DI* finally:

$$DI = 10 \log d \tag{2.30}$$

Target Strength (TS)

When using an active sonar system, target strength refers to the echo returned by an underwater target. Mostly these targets are objects in the water, the sea bottom is actually not a target because of the indefinite size. The sea bottom returns the acoustic signal in the form of reverberation [Urick, 1983].
The target strength *TS* is defined as:

$$TS = 10 \log \frac{\text{echo intensity at 1 meter of target}}{\text{incident intensity}} \tag{2.31}$$

Reverberation Level (RL)

Underwater reverberation is caused by scattering of the acoustic signal because of inhomogeneities. These inhomogeneities form discontinuities in the physical properties of the medium, the water, and intercept and reradiate a portion of the acoustic signal. This is called scattering, and the total amount of scattering of all scatterers is reverberation.
The scatterers in the sea forming the basis for reverberation can be split up in two different classes. One type is the volume-reverberation, surface-reverberation is the other type. Examples of scatterers producing volume-reverberation are marine life and the inhomogeneous structure of the sea. Examples of surface-reverberation are scatterers located near the sea surface or near the sea bottom [Jong, 1988].
Reverberation is very complex. The sea bottom reverberation is the most interesting, because of the backscatter information that also can be collected by multibeam systems. For a detailed description of the other reverberation classes see [Urick, 1983], chapter 8.

Noise Level (NL)

There are different kinds of noise. First the noise of the sea itself, in Table 2.1 called ambient-noise level. It is that part of the total noise background observed with a nondirectional hydrophone which is not due to the hydrophone. The sources for this ambient-noise are various, and depend on the frequency. Tides and waves cause in the first place hydrostatic pressure changes of large amplitude at a low frequency, and therefore cause noise at also a low frequency. Because the earth is in a constant state of seismic activity, these activities also create noise of a low-frequency. In the higher frequencies ship traffic and surface waves produce ambient-noise. These are only examples producing ambient-noise, in fact there are more sources, each with different frequencies.

In the second place there is the self-noise caused while the hydrophone is located on board the noise-making vessel and also this hydrophone travels with this ship. Self-noise depends greatly upon the directivity of the hydrophone, its mounting, and its location on the ship. Most of the time the sonar transducer is placed as far forward on the vessel as possible, to reduce the possible noises from the propulsion machinery and the propeller. In Figure 2.5 the many different kinds of undesired sound are illustrated [Urick, 1983]

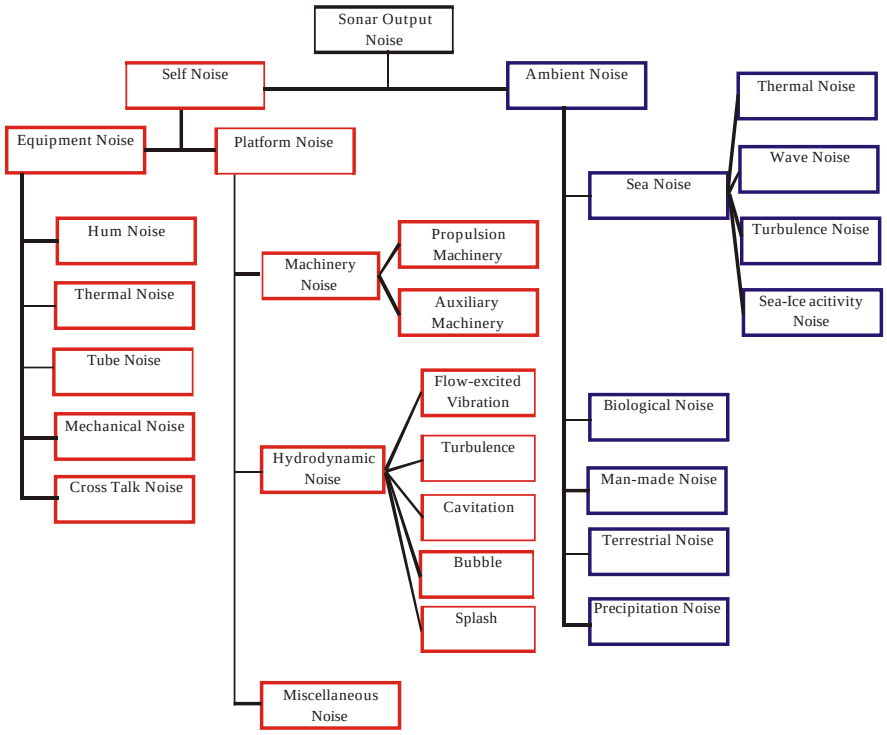

Figure 2.5: Sonar noise sources.

2.3 Sound Speed in the Ocean

For accurate measurements with sonar systems knowledge about the sound speed in the sea is very important. The sound propagation in the sea depends on many parameters, chemical and physical. These parameters change with time and depth and have influence on the sound speed and the path of the acoustic signal. The parameters that influence the sound speed can be measured with instruments. These are temperature, salinity and depth.

The speed of sound in water is approximately $1500\,{}^{m}/_{s}$, but the most accurate empirical formula for the sound speed is given by [Mackenzie, 1981]:

$$\begin{aligned} c = {} & 1448.96 + 4.591t - 5.304\times10^{-2}t^2 + 2.374\times10^{-4}t^3 \\ & + 1.340(S-35) + 1.630\times10^{-2}z + 1.675\times10^{-7}z^2 \\ & - 1.025\times10^{-2}t(S-35) - 7.139\times10^{-13}tz^3 \end{aligned} \tag{2.32}$$

with t temperature of the water in ° Celsius, S the salinity in parts per thousand, z the depth in meters.

2.3.1 Sound Speed in a Layered Medium

Let's consider a waterbody with n horizontally layered density layers. Such a model is called in geophysics 'vertically stratified'. The n density layers have each a constant gradient g_i.

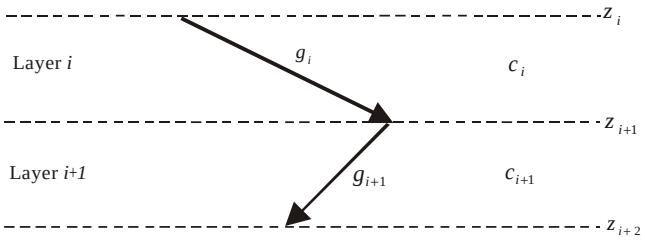

Figure 2.6: Horizontally layered water model.

With Figure 2.6 it can be shown that, with z the depth, the gradient is:

(2.33) $$g_i = \frac{c_{i+1} - c_i}{z_{i+1} - z_i}$$

The ray parameter p, and the radius of curvature of the layer R_i, are than defined as follows:

(2.34) $$p_i = \frac{\sin j_i}{c_i} \qquad R_i = \frac{-1}{pg_i}$$

In equation (2.33) the angle j is defined as $90 - q$, q can be found in equation (2.16). For the horizontal distance x_i one can than find:

(2.35) $$x_i = R_i(\cos j_{i+1} - \cos j_i) = \frac{\cos j_{i+1} - \cos j}{pg_i}$$

The travel time in the layer i is:

(2.36) $$t_i = \frac{R_i(j_i - j_{i+1})}{c_i}$$

This propagation model can be compared with Snell's law, see section 2.1.2. In other words, any density variation in the water column will give a change in ray direction and sound speed. Or mathematically, the equation (2.36) with s the path:

(2.37) $$s = c \cdot t$$

will transform into the integral [Tsoukalas, 1999]:

$$s = \int_0^s c \cdot tds \tag{2.38}$$

2.3.2 Velocity Structure of the Sea

The sound speed is not constant, as written before, and depends on temperature, depth, and salinity. With measurements of these parameters, so called 'velocity profiles' can be computed. These velocity profiles give a representation of the change of sound speed.
Figure 2.7 gives an example of a typical deep-sea velocity profile. A comparison can be made with Figure 2.8 where the temperature and the salinity as a function of the depth are given. These figures all give an impression of the characteristics of the sea [McCormick, 1976]. The velocity profile and its characterizations will be explained in short.

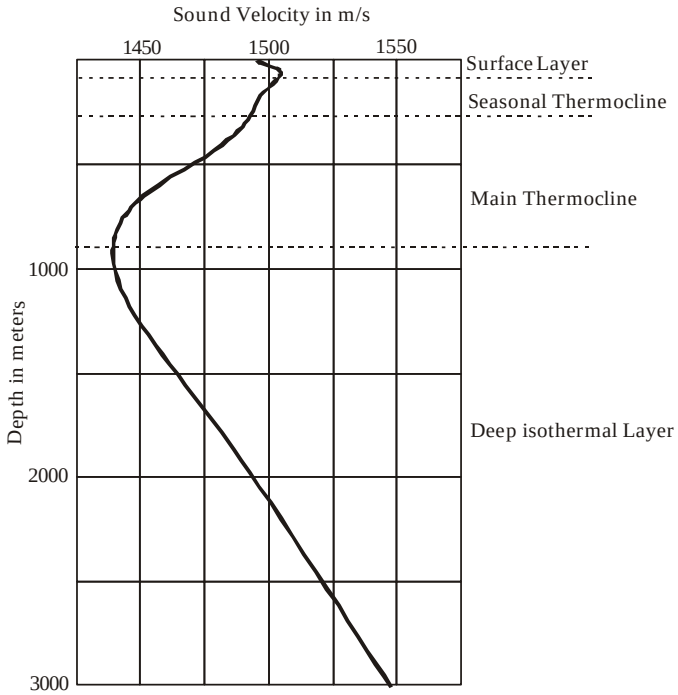

Figure 2.7: Example of a deep-sea sound velocity profile.

Just below the sea surface is the surface layer, in which the sound velocity changes due to daily and local changes of heating, cooling, and wind action. It is a mixed layer of isothermal water formed by the action of the wind. Below this surface layer lies the seasonal thermocline, a layer in which the temperature changes with depth. The layer is characterized by a negative velocity gradient, that varies with the seasons. The third important layer is the main thermocline. This layer is nearly not affected by seasonal changes. In this layer the changes in temperature are at their maximum. The changes in salinity are also found in this layer, most of the time the salinity is increasing. The deep isothermal layer reaches to the sea bottom. This layer has a nearly constant temperature

and salinity. In this layer the sound velocity increases because of the pressure effect [Urick, 1983]. Between the deep isothermal layer and the main thermocline is a velocity minimum, having effects on the sound propagation, because the path can be bent or refracted, a comparison with Snell's law in section 2.1.2 can be made.

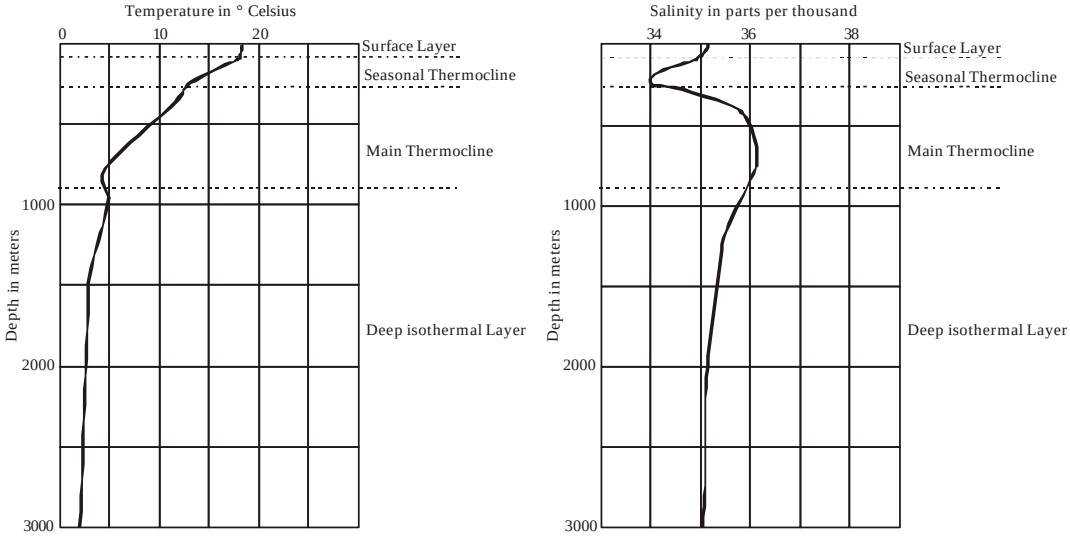

Figure 2.8: Typical temperature (left) and salinity (right) variations as a function of depth.

2.3.3 Measurements of Sound Velocity Profiles

Sound velocity profiles can be computed with the help of measuring the parameters that influence the sound speed in water. These parameters are, as described above: temperature, salinity and depth. With so called 'CTD-devices', which stands for Conductivity, Temperature, Density, these parameters can be measured. These devices measure not only the parameters conductivity, temperature, and density but also salinity, pressure and fluorescence. These devices are ejected from the vessel and sink at a constant rate. Afterwards the data can be read and interpreted.

2.4 Echo Sounding

The principle of echo sounding is to measure the time difference of a signal, travelling from the origin to the target and back to the receiver. The depth z, of the target can be computed, when the sound velocity is known, according the equation (2.38). In this equation the travel time is given by t, and c_{mean} is the mean sound speed within the water column [Jong, 1988].

(2.39) $$z = \tfrac{1}{2} c_{mean} t$$

The earliest, and still most used echo sounding devices are the single-beam depth sounders. These systems have many limitations for large scale bathymetric surveys. Therefore so called 'multibeam systems' have been developed. These systems act as a

single-beam echo sounder, but at several different locations on the ocean bottom, in a strip perpendicular to the track of the survey vessel [L-3, 2000]

2.4.1 Echo Sounder Concept

The echo sounder is a device which transmits a short burst of sound, and measures the time between transmitting and receiving the signal. After receiving a signal, a new pulse is transmitted and the cycle is repeated. Such a cycle is a called a 'ping', it is visualised in Figure 2.9 [L-3, 2000]. This ping is started at the transmitter, it generates an oscillating signal with a special frequency. The transducer converts this signal onto sound waves. The sound waves propagate through the water until they are scattered back at the sea bottom. The transducer, now working as a hydrophone, receives the reflected sound wave and converts it into an electric signal. The receiver system calculates the depth which is reported in a display.

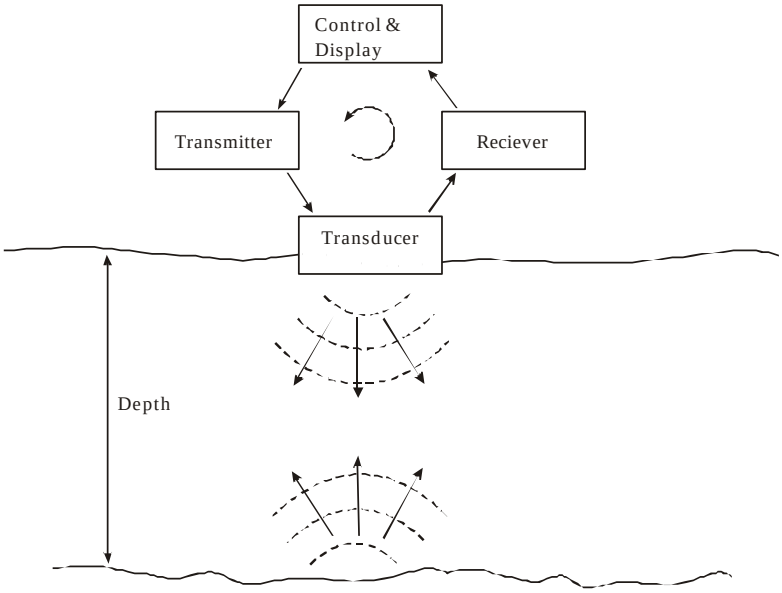

Figure 2.9: The echo sounder concept.

The sound wave transmitted at the transducer radiates equally in all directions, if it is transmitted from a point source. The pulse radiates spherically away from the source, with a thickness proportional to the pulse duration. The pulse will interact at the bottom of the ocean first as a simple disk, and when the spreading continues as a disk with a hole, that spreads wider and wider as the wave is spreading. This is shown in Figure 2.10. To be able to estimate a direction of the echo arrival at the receiver, a narrow beam has to be transmitted or received [Moustier et al., 2001].

2.4.2 The Multibeam Concept

Within multibeam systems there are more projectors within the transducer, and more hydrophones for receiving the signals. Both, projectors and hydrophones, can be used to produce narrow transmit beams or receive beams in a narrow sector. These transmitted beams can be within such a multibeam system targeted at specific angles. This process is

called beam steering. In this steering of a hydrophone array to be sensitive to a particular angle, only the interpretation of the recorded data is altered. This means that due to this data processing, the same array can be steered to observe any of a large range of angles. Otherwise, the hydrophone array can be used to examine the echoes of a ping at many different locations.

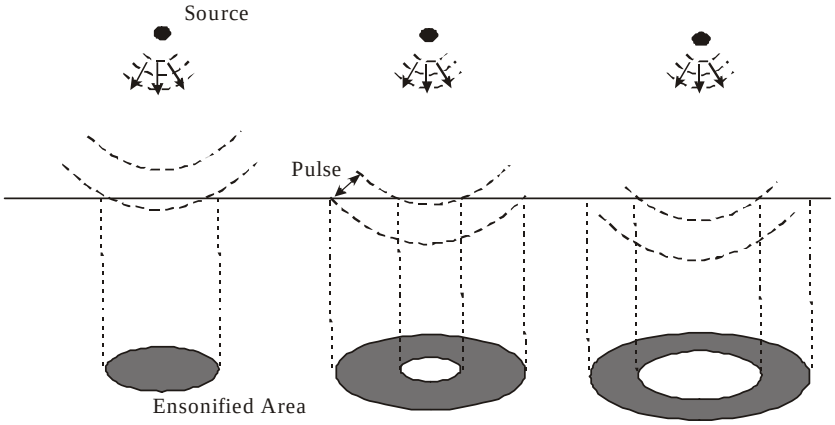

Figure 2.10: Ensonification pattern at the bottom.

The beam patterns are actually three dimensional, and to be able to locate accurately the echoes on the ocean floor it is not useful to transmit in an array, and receive in an array parallel to each other. Therefore the so called 'Mills Cross' is used. The projector and hydrophone array are placed perpendicular to each other. In this way the strip of the ocean floor ensonified by the projectors will intersect with the strip of the ocean floor observed by the hydrophones. This occurs only within a small area corresponding with the beam widths of the projector and hydrophone [L-3, 2000]. This is combined with the beam steering to receive the echoes from discrete locations all along the ensonified area, allowing the sonar to determine ranges to a strip of locations with each ping.

2.4.3 The Multibeam Geometry

Different angles and ranges are used within multibeam systems and the multibeam data analyses. In Figure 2.11 the different used angles are shown. These angles are all defined using the nadir as reference:

- Angle of incidence; q_i
- Grazing angle; q_g
- Angle of arrival; q_a
- Slope angle; q_s

The ranges used within multibeam are called 'slant ranges', as these distances are computed using the travel time and the speed of sound. These slant range defines the distance from the multibeam transducer to the location at the sea floor. The depth is the vertical distance between the transducer and the sea floor. The distance between the nadir location on the sea floor and the location of the beam on the sea floor is defined as

the horizontal range. The swath width of the multibeam system is twice the maximum horizontal range, and is defined by the swath angle or fan aperture a and the depth (see also section 5.4). These parameters are shown in Figure 2.12.

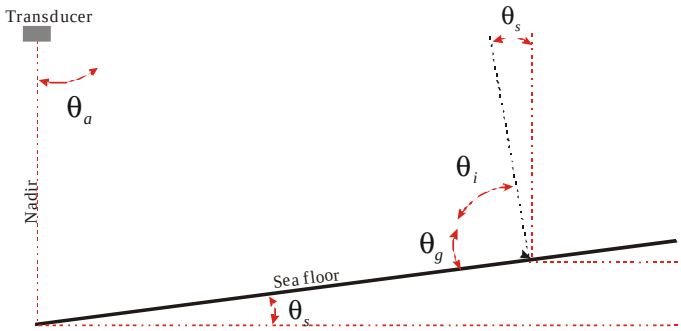

Figure 2.11: Multibeam geometry showing the used angles.

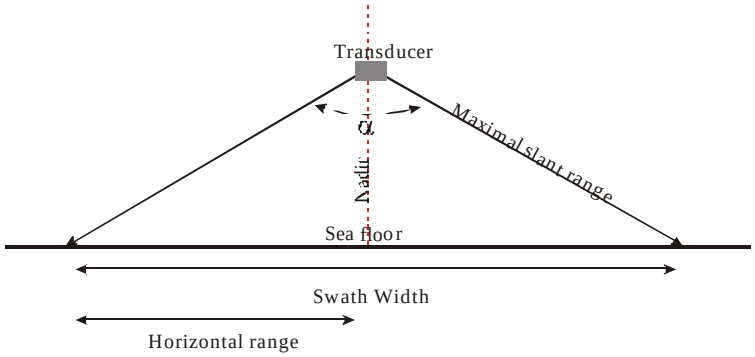

Figure 2.12: Multibeam geometry showing the used ranges.

3. Multibeam System Hydrosweep DS-2

A bathymetric multibeam system was developed in the years 1984-1986 by Krupp Atlas Elektronik. It carried the name Hydrosweep. This system was installed on RV 'Polarstern' in 1989 and is still in use. In the years between 1990 and 2000 some improvements were made, as can be read in Chapter 1. In this chapter a description will be given of the multibeam system Hydrosweep DS-2, followed in section 2 by the method of calibration. In section 3 the navigation will be discussed, and this chapter will end with a description of the software Hydromap Online.

3.1 Hydrosweep DS-2

Since 1989 RV 'Polarstern' is equipped with the multibeam system Hydrosweep. The hydroacoustic sensors of Hydrosweep DS-2 are located under the ship in the front, far away from the machinery and the propellers. These hydroacoustic sensors are shown in Figure 3.1 as the yellow elements. RV 'Polarstern' is not a normal survey vessel, but is also a double-hulled icebreaker. Therefore the location of the sensors is also chosen to be in the front under the ship. When icebreaking, the ice is pushed down under the ship, and this ice raises again in the middle and the end of the ship, having it's effect on the ship and the sensors, when they would be located at that position.

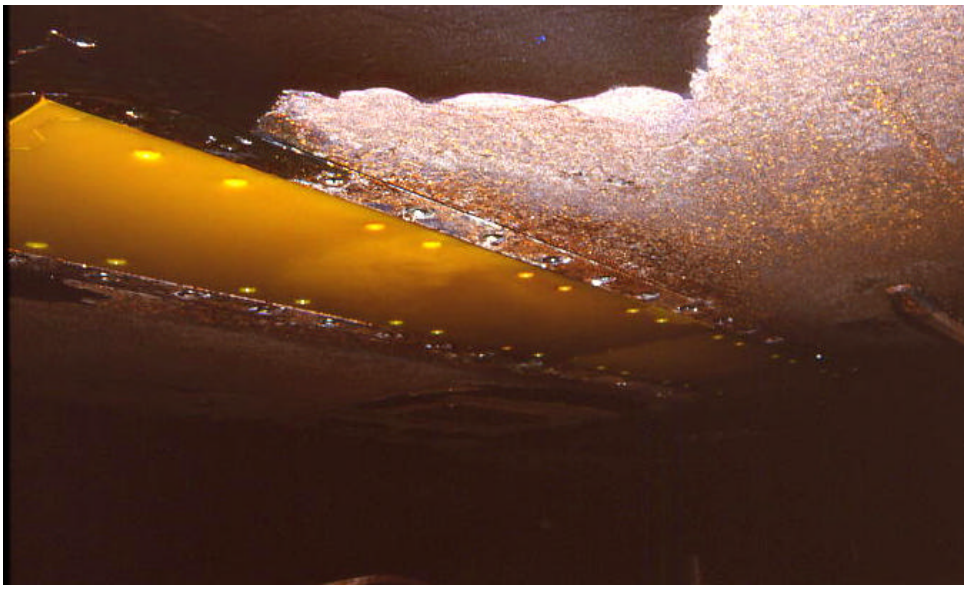

Figure 3.1: The hydroacoustic elements of Hydrosweep DS-2.

The specifications of the system are listed in Table 3.1, some of these specifications will be described. The survey principle is given in Figure 3.2.

Frequency	15.5 KHz
Bandwidth	1.5 KHz
Number of Beams	59
Fan aperture	90° or 120°
Beam spacing	2.3°
Pulse length	1-20 ms
Pulse repetition	1-22 s
Array dimension	3.0 m × 0.3 m
Stabilization	All axes
Depth range	10 – 11000 m
Swath Width	Min. 2 × water depth
Refraction Correction	Cross fan calibration
Accuracy	~0.5% of water depth
Maximum survey speed	15 Kt (knots)

Table 3.1: Hydrosweep DS-2 specifications.

The system operates at a frequency of 15.5 KHz with a bandwidth of 1.5 KHz, which was chosen to achieve two objectives. First is this frequency low enough to achieve the desired depth range, reaching the maximum ocean depths. In the second place this frequency is high enough to secure good vertical resolution, and the signal is reflected from the true bottom, rather than penetrating the sediment layers to the sub-bottom surfaces [Grant, 1990].

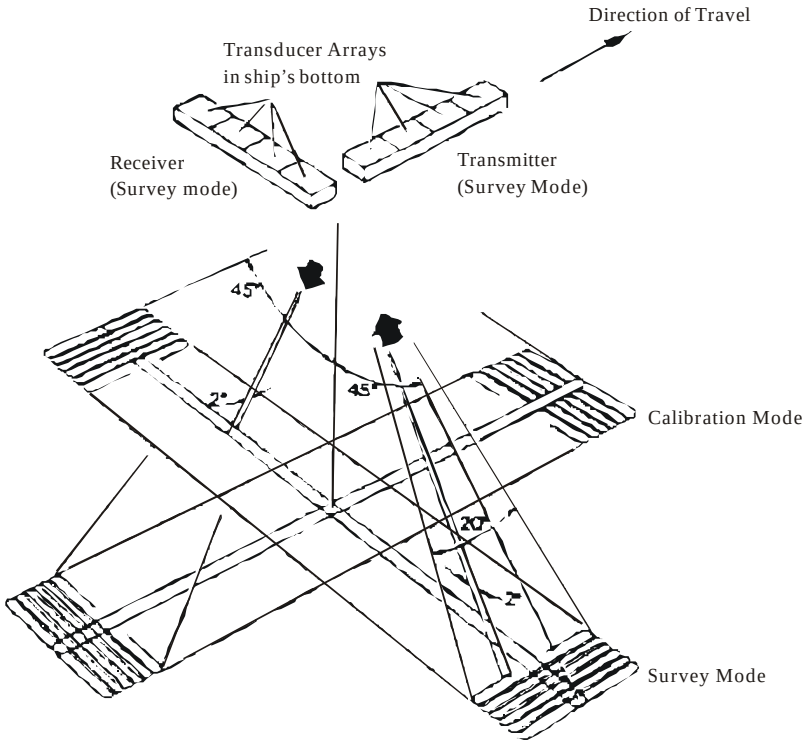

Figure 3.2: Survey principle of Hydrosweep DS-2.

The area is covered by a fan of 59 preformed beams (PFB), and has an aperture of 90°. This means that at equal depths the swath coverage is two times the water depth. However the fan aperture can be switched to 120°, having its effect on the swath coverage. The resolution of the system depends on speed and water depth. There are two reasons. The first is that in deeper water the 59 beams cover a wider line because of the swath coverage. The second reason, because the time between sending and arriving of the signal increases. At a depth of about 5000 meters and a speed of 10 knots the interval between two measurements is about 16 seconds. This means that the distance between two lines is about 80 meters. At a depth of about 3000 meters this distance reduces to ~55 meters.

Hydrosweep DS-2 offers two transmit modes, which are automatically selected by the system depending on the water depth, these are:

(1) ODT, Omnidirectional Transmission Modus for depths in the range of 10-1000 m. In this modus one beam is sent, and low energy emissions and short pulse lengths are used.

(2) RDT, Rotational Directional Tranmission Modus for depths > 1000 m. In this modus three beams are sent at –36°, 0°, and +36°, with a minimum of time separation. This way ensures that the system achieves uniform insonification of the swath. The pulse length will vary according to depth [Schenke, 1989].

The system has also two operation modes, automatically switched by the system:

(1) Shallow Water Modus for depths between 10 and 100 m. This mode has a *SL* (source level) of > 210 dB. The aperture of one PFB is 4.5°, and the *DI* (directivity index) is < 23 dB.

(2) Deep Water Modus for depths > 100 m. In this modus the two transmit modes can be used. When using RDT, the *SL* is > 237 dB, whereas the *SL* is > 220 dB in the ODT mode. The aperture of one PFB is in both transmit modes 2.3°, and the *DI* is < 27 dB.

The system also collects pseudo sidescan data and backscatter data. The sidescan collects every survey line 2048 amplitudes together with the needed parameters. Further more data and needed parameters are recorded for every PFB to be able to compute backscatter information. For backscatter see chapter 9.

3.2 Cross-Fan Calibration

There are two different measurements modes, the survey mode and the calibration mode. With the technique of quasi-real-time calibration the large swath coverage can be realized. The technique used is the Cross-fan calibration method.

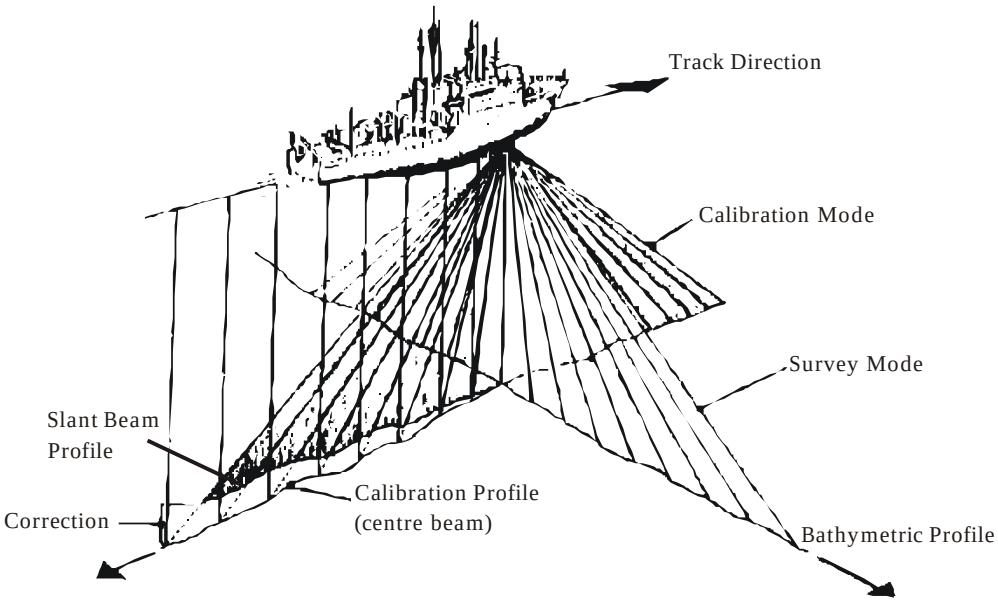

Figure 3.3: Principal of cross-fan calibration.

In the survey mode the sonar beam direction is perpendicular to the ship's long axis, and in the calibration mode the sonar fan beam lays directly in the ship's long axis. In Figure 3.3 this calibration principle is shown.

The principle of this calibration method is that the vertical centre beam measures the true shape of the depth profile along the ship's track. Various effects may deteriorate the measurements with the slant beams of the longitudinal fan of the same profile. With the calibration program the mean water sound velocity (C_m) will be determined with the following model as basis. If a seabed profile is surveyed with two independent and different hydro acoustic methods, both should provide identical results, if the mean water sound velocity that is applied, is correct. The Hydrosweep calibration program uses vertical and slant beam depth measurements. By measuring a depth profile with a vertical sound beam, variations of the mean water sound velocity result only in a proportional and linear depth variation of the complete profile without changing it's shape. For variations of the value of C_m by measuring the depth profile with slant sound beams, a nonproportional change of depth as well as the shape of the profile is the result. In both depth calculations, the C_m value must be used to determine the depth. During several iterations the C_m value is now changed for both calculations until a value is found that makes the slant beam profile fit best with the vertical beam profile. This is done with a least-squared residual comparison between the two profiles. This method for calibration is normally performed along the ship's track every kilometer [Schenke, 1989].

3.3 Navigation

Precise ship navigation is essential for mapping the sea bottom topography with multibeam systems. Because of the areas on high sea the lack of land-based reference points for determination of the ship position makes precise navigation very difficult. For precise positioning there are several GPS (Global Positioning System) antennas installed

on board. These antennas have different positions on the ship and the constellation is chosen in such a way that the movement of the ship can be measured in a good way. The primary set of GPS-antennas are three receivers of type Ashtech.
The differential GPS (DGPS) corrections are collected from the SkyFix system, und supplied via InMarSat (International Maritime Satellite) satellites. The DGPS corrections are not always available at the positions where the ship is travelling, because of the southern or northern tracks of the ship, and the coverage of the geostationary InMarSat satellites. The areas south of 79° S and north of 81° are not covered by the InMarSat satellites. During DGPS operation the positioning accuracy is between ± 5 and 10 meters, without corrections the accuracy drops to ± 10 to 50 meters. The ship is also equipped with an Integrated Navigation System (INS). These data are the input for the Hydrosweep system [Jacops, 2001].

3.4 Hydromap Online

The software used for acquisition, mapping and storage of the hydrographical data together with functions for navigation and planning is Atlas Hydromap Online. The tree of Hydromap Online is shown in Figure 3.4, in this figure the basic menus are listed. The most used and important menus are described in short.

The basis forms the menu ‘Survey’ and submenu ‘Presentation’; here the measured data is visualised real-time. One can choose between different options for visualizing the data. The best option for a good interpretation of the data is the colour-banded view. One can also open some additional windows for showing a waterfall structure of the topography, the ahead-profiles used for calibration, the depths-range and profiles over time, used for visualising important information about parameters changing with time such as roll, pitch, heave, speed and heading.

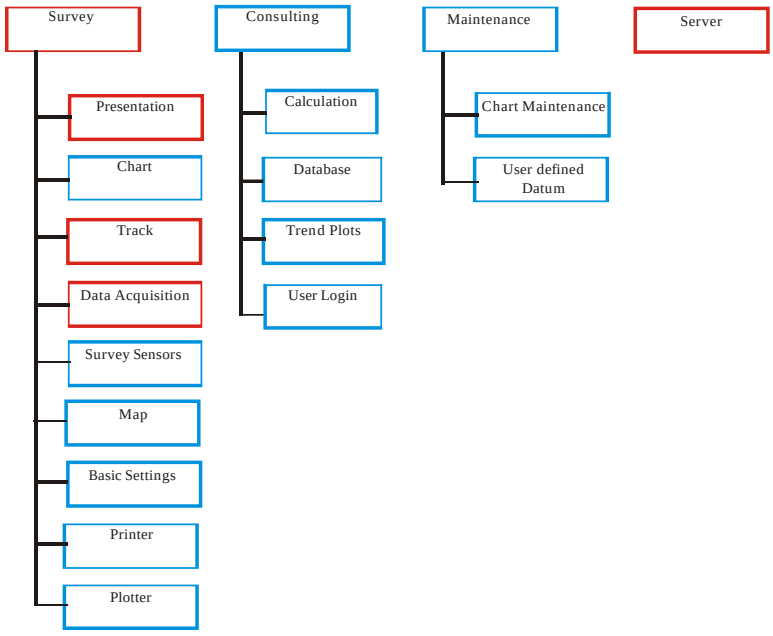

Figure 3.4: The tree of Atlas Hydromap Online.

For storage and raw data transformation the ‘Server’ menu can be activated. For raw data export first a profile has to be created. This profile contains several hours to be exported into the surf-format, an exchange format. The data is stored on DAT-tape and on hard disk. The data can also be saved on DLT-tapes.
The ‘Track’ menu is another important menu. In this menu there is the possibility to create waypoints, to create tracks and to plan routes. It can be used before sailing for planning bathymetric profiles, and during the bathymetric survey for controlling and navigation.
The last, often used, menu is that for the watchkeeping of the Hydrosweep data, the ‘Data Acquisition’ menu. In this menu the calibration, the Time Volume Gain (TVG), the swath width, the C-values for the sound velocity in water, and the Hydrosweep system itself, can be controlled. In the menu for controlling the C-values one can choose to use measured C-values, for example with a CTD, and not use the self-calibration of Hydrosweep, or to use the cross-fan calibration [Jacops, 2001].

4. Bathymetric Measurements and Errors

The accuracy of bathymetric measurements depends on many factors, for example the system performance, the sound velocity profile and the positioning of the ship. The inaccuracy of the measurements are caused by either coarse errors or systematic and accidental errors. In this chapter a short description of these errors and the different factors is given. The chapter will end with two specific bathymetric effects, the 'omega' effect and the 'tunnel' effect.

4.1 Bathymetric Errors

Two types of errors have influence on the accuracy of the bathymetric measurements, these are the coarse errors, and the systematic and random errors. Both these error types will be described in short.

4.1.1 Coarse Errors

The coarse errors are the clear mistakes not depending on the measurements, but depending on external effects. The reasons for these coarse errors, are for example the following factors [Tsoukalas,1999]:

- Ice reflection
- Operator decisions
- External noise from sea, ice, ship's propellers etc.
- Fish reflection
- Air bubbles

When breaking ice, the contact between the ship and the ice causes disturbing noise affecting the signals and giving coarse errors. The ice is also pushed down under the ship and reflect signals coming from the system. The ice also takes with it air bubbles also reflecting signals. This premature reflecting of the signals also occurs when fish swarms pass, and when, due to heavy sea, air bubbles appear or are pushed down under the ship. Signals reflecting with air bubbles, due to heavy sea, occur especially when the ship's heading is in the wind, and the bow comes, because of the swell, out of the water.

4.1.2 Systematic and Random Errors

Systematic errors occur at regular time intervals. Characteristic is that under the same conditions, they occur at the same proportion. It is possible to correct the data for such systematic errors, when they can be determined, for example by calibration. Random errors on the other hand take place irregularly and can not be predicted.

Some factors that can cause these systematic errors are [Schenke, 1992]:

- Roll and Pitch
- Heave
- Heading
- Ship's positioning
- Refraction of the rays
- Transducer orientation

Random errors can be caused by the following factors [Schenke, 1992]:

- Interference with ship's noise
- Interference with other acoustic survey systems
- Reverberation of the seafloor
- Omega-effect
- Tunnel-effect

In the time-interval between sending and receiving the signal at the transducer, the ship will never stay at the same position. Not only because the ship is sailing, but also because of movements of the ship due to external forces acting on the ship, for example swell, waves, ice, and wind. These motions of the ship, can be important error factors, and are called, heave, pitch, and roll. In most of the cases, good calibrated sensors are used to correct for these ship movements. If these corrections are false or fail, or if a good calibration fails, the result are cause errors. In Figure 4.1-4.3 these motions are shown, and the results are shown if a correction for these fails, or if the system is not good calibrated.

Heave

Heave is the vertical motion of the ship with as reference the idealised, flat sea surface. It is the movement along the z-axis. This heave motion will change the time-interval between sending and receiving.

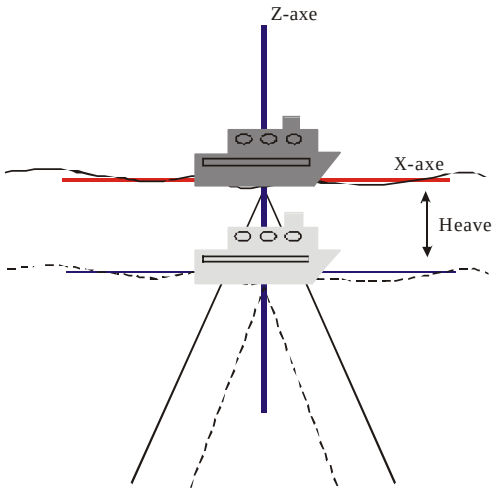

Figure 4.1: Heave effect.

Roll

The motion around the x-axis, the ship's along axis, parallel to the track, is called roll. This will result in a illumination of an unwanted location. The centre beam will not be, as expected, perpendicular to the idealised, flat sea surface.

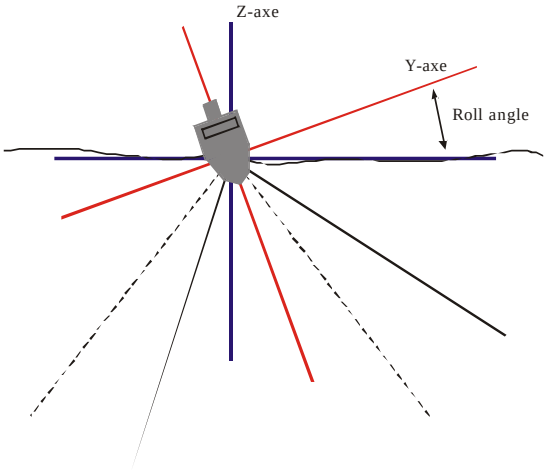

Figure 4.2: Roll effect.

Pitch

Pitch is called the motion around the y-axis, the ship's across axis, perpendicular to the track. In this case also an unwanted location will be illuminated, but at a position before or behind the expected survey line.

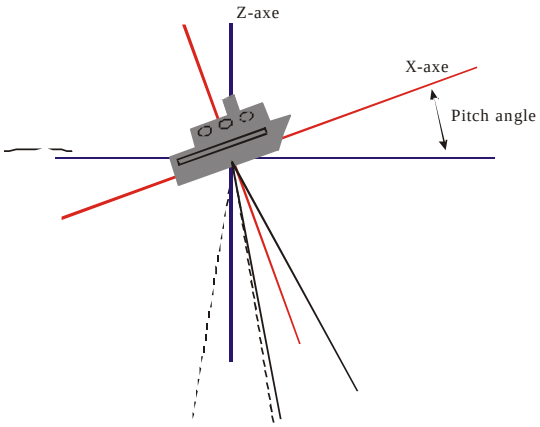

Figure 4.3: Pitch effect.

4.2 Omega and Tunnel Effect

As described above there are a lot of factors that influence the shape and amplitude of the acoustic signal. If the seabed morphology is extremely dynamic, other geometrical effects play an important role. Any transducer generate so called 'side lobes', pointing in

different directions than the main lobes. In such areas, the signal from a side lobe can be interpreted by the transducer as the main lobe, because the side lobe gives a short strong reflection, whereas the main lobe gives a weak long scatter. Such effects are known as 'omega' effect and 'tunnel' effect [Christen, 1999].

4.2.1 Omega Effect

The omega effect occurs at down slopes, when the side lobe echoes of the beams are received prior to the main echo. In Figure 4.4 this effect is visualised. Contour lines have in such a case a shape which represents the Greek letter Ω, these contour lines are bended to shallower depth under the vessel track [STN Atlas, 1997].

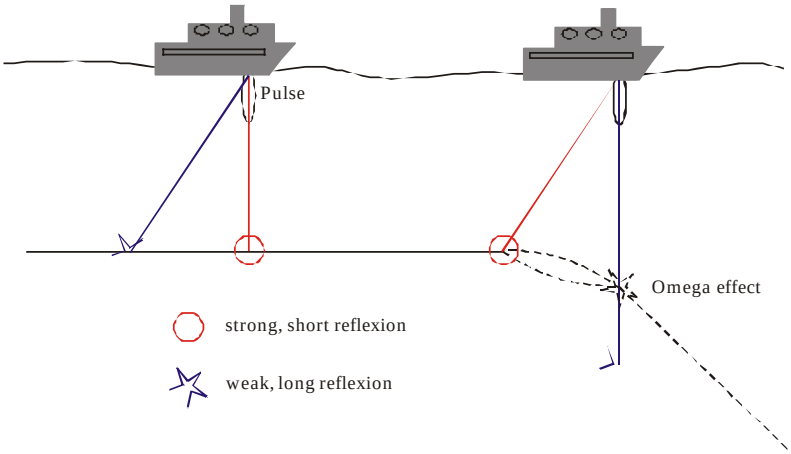

Figure 4.4: Omega effect.

4.2.2 Tunnel Effect

Th etunnel effect, on the other hand, occurs when the side lobes of slant beams, which point to the vertical and the echoes of which are therefore received earlier than the main echo, are processed instead of the main echo. On either side of the ship's track, the contour lines are showing shallower regions, and thus these contour lines form the shape of a tunnel [STN Atlas, 1997]. This effect is shown in Figure 4.5.

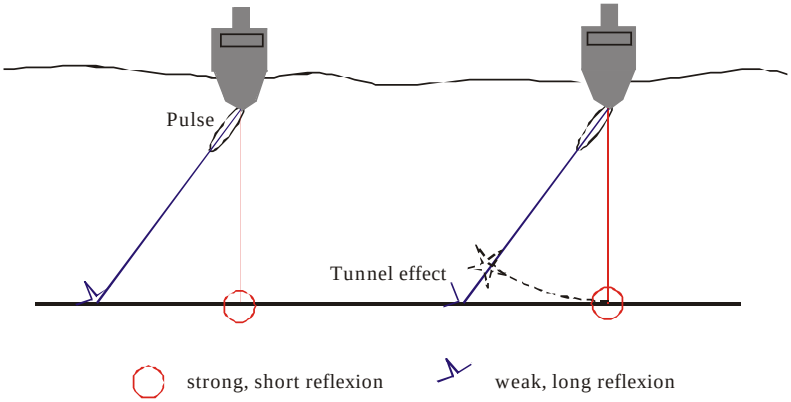

Figure 4.5: Tunnel effect.

5. Surveys in the Eltanin Area

The Eltanin Impact Area is until now the only known example of an asteroid impact in the deep ocean basins of the world. The Eltanin Area is situated in the Bellingshausen Sea at the western entrance of the Drake Passage, the passage between South America and Antarctica, and about 700 nautical miles[1] off the Chilean coast. This asteroid impact area was explored during two expeditions on board RV 'Polarstern'. The first expedition took place in 1995 from the end of March until the beginning of May, the second expedition started at the end February 2001 and ended almost two months later. During these expeditions a lot of data was collected, geological data, geophysical data, and of course bathymetric data. All these data collected during the two expeditions should provide better information for the reconstruction of the impact.
This chapter will start with a geological and geophysical description of the Eltanin Impact Area. It continues with a short review on the first expedition, ANTXII/4. In section 5.3 the work carried out during the second visit of the Impact Area during expedition ANTXVIII/5a, is described. The chapter will end with a description of bathymetric data collected within this area.

5.1 The Eltanin Impact Area

Of the ~140 terrestrial impacts, the impact of the Eltanin Asteroid is yet the only known impact event affecting the 60% of the earth's surface covered by deep ocean basins. Evidence of this impact was discovered in 1981 as an iridium anomaly in a sediment core collected by the USNS 'Eltanin' in 1964 [Kyte et al., 1981]. The meteorite ejecta are present in three USNS 'Eltanin' sediment cores, separated 500 kilometers. The highest concentrations of the impact debris were found in Eltanin core E13-4, at location 57°47.2' S, 90°47.6' W. After the first expedition in 1995, the first analyses and conclusions could be made. This section describes in short the results and analyses.

5.1.1 Geophysical description

The precise location and size of the Eltanin Impact Area are not yet known, but the possible area extends from 55°00 S, 88°00 W to 58°30 S, 95°00 W and covers almost 162.000 km². There is no evidence found for a crater caused by the impact and it is unlikely that the asteroid would have penetrated the ocean crust, although such an impact on land would have created a 15-40 kilometer diameter crater. The Impact Area is situated in an area with, in the south the San Martin Seamounts with a very irregular structure, and in the north a flat ocean basin. The San Martin Seamounts reach depths of about 2500 meters, whereas the abyssal basin has depths reaching 6000 meters.

[1] 1 Nautical mile ≈ 1.852 kilometer

In Figure 5.1 the location of the Impact Area is shown. In this schematic representation of the tectonic of the Bellingshausen Sea, the major fracture zones and subduction zones are shown. The San Martin Seamount group lies near a fracture zone in an area that was involved in a major plate reorganization episode about 50 Million years ago. In addition the Seamount group is bounded north and south by fracture zones. As can be seen in Figure 5.1 the Eltanin Area lies on the Pacific-Aluk portion of the Antarctic Plate and the magnetic lineations are shown on this portion of the plate [Cande et al., 1982].

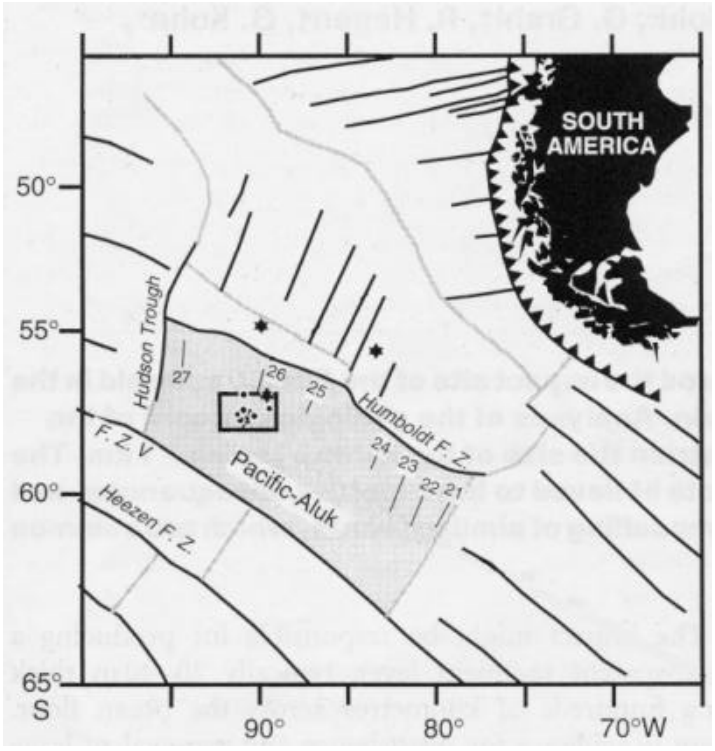

Figure 5.1: The Eltanin Area (box) shown in a geophysical background.

5.1.2 Geological Description

The impact, the related vapour explosion, and the subsequently generated tsunamis removed an Eocene, late Pliocene, sediment sequence and disturbed the sediments over a distance of several hundreds of kilometers. The created deposit consisting of stirred up sediments forms a seismically transparent layer. This layer has an average thickness of 20-40 meters, and is called the Eltanin Polarstern Transparent Zone (EPTZ). An example of the EPTZ can be seen in Figure 5.2. The EPTZ can be seen using the subbottom profiler Parasound. This echosounding system allows penetration of the upper 100-300 meters of sediment. In general the EPTZ was found as well in the basins as on elevated areas of the seamount group [Gersonde, Deutsch, 1999].

Sediment cores taken at different locations, showed sediment layers where impact deposits were found. The coring could only take place at locations where it could be observed that the seismically stratified sediments and the EPTZ were thinning. The thinning was especially observed towards the edges of topographic highs.

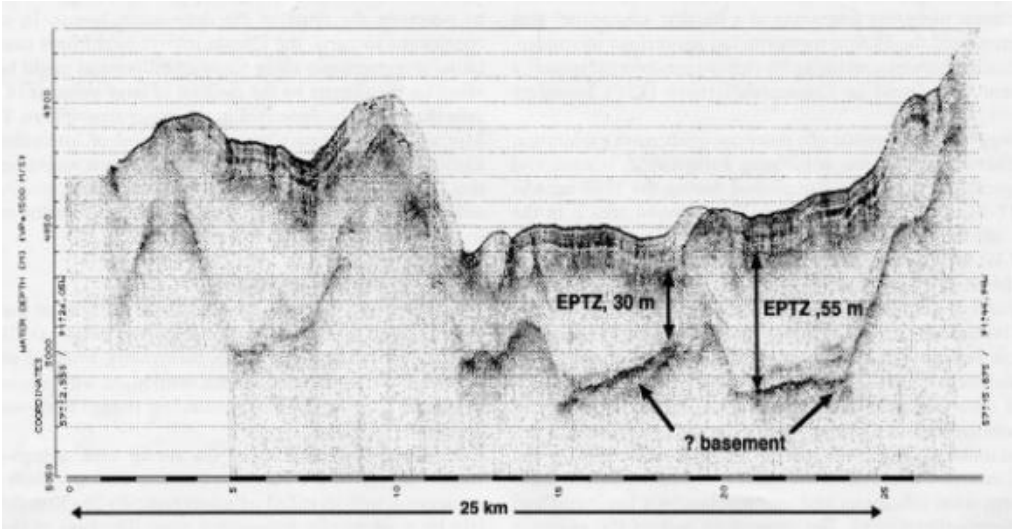

Figure 5.2: A profile of the Parasound subbottom profiler showing the EPTZ.

In the sediment cores five different sedimentary units (SU) can be recognised and distinguished. The lowermost SU V consists of autochthonous, undisturbed sediments. Deposit related with the impact begins with SU IV, an allochthonous, chaotic mixture of sedimentary clasts as large as 50 centimeters. SU III is laminated well-sorted and graded sand. In the uppermost part of this SU some meteorite ejecta can be found. In SU II this ejecta material can be found throughout the whole unit. The maximum concentrations occur in the lowermost part of the ejecta-bearing interval. The meteorite particles reveal an upward decrease in grain size overprinting the grain size distribution of the non-meteorite material. The meteorite material consists most of the time of vesicular impact melt, although a few percent are unmelted meteorite fragments. Further more, SU II consists mainly of fine-grained sediment. SU I, at the top of the impact deposits, is an undisturbed and bioturbated sequence of late Pliocene to Quaternary sediments. The sedimentary units and the meteorite ejecta can be seen in Figure 5.3 [Gersonde et al., 1997].

The sediment cores show the sequence of processes involving sediment mass erosion and redeposition, accompanied by the fallout of impact debris. Over a period of several hours after the impact event these processes occurred. The sediments on the San Martin Seamounts and in the surrounding basins were ripped up by the impact and redeposited. The laminated sediments of SU III were deposited from a turbid flow, it indicates a downslope gravitational sediment transport as well as rapid sedimentation of sorted particles from sediments stirred up into higher levels of the water column. A gradual transition to less turbulent conditions might be reflected by the transition from SU III to SU II. The deposition of SU II probably lasted for several hours to days after the impact. [Gersonde et al., 1997]

Biostratigraphic and paleomagnetic dating place the impact event in a time period in the lower Matuyama Chron, dated up to 2.15-2.14 million years ago. This is close to marine isotope stage 82, which represents one of the strongest cooling evens in that time period after the establishment of the Northern Hemisphere ice sheets [Gersonde, Deutsch, 1999].

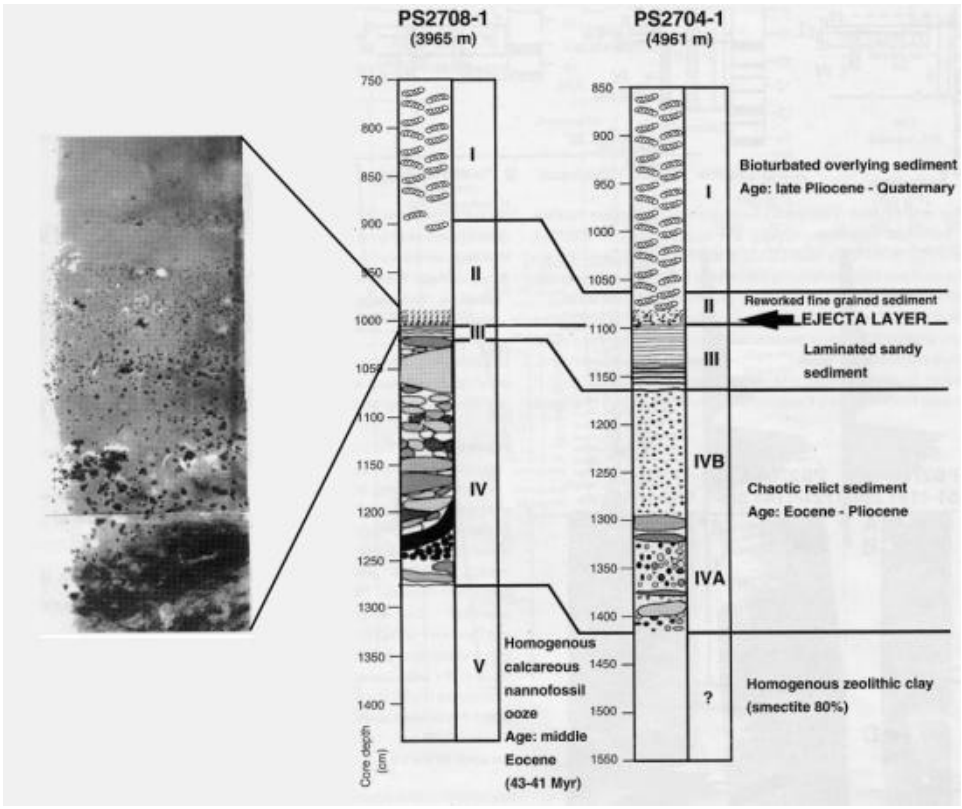

Figure 5.3: Sediment cores showing the different SU's. In the X-ray radiograph (left) the meteorite ejecta can be seen as coarse grains starting between SU III and SU II.

5.1.3 The Impact Event

The estimates of the size of the Eltanin Asteroid range from 1 to 4 kilometer in diameter. The 1 kilometer lower estimate was made considering the large area of disturbance and the probability that most of the asteroid ejecta were deposited far from the impact region. The upper limit of 4 kilometer was based on models indicating that the penetration of the asteroid should be in the order of the projectile diameter. Thus, based on the ocean depth, asteroids as large as 4 kilometer should avoid penetrating the ocean crust [Gersonde et al., 1997].

The explosive energies of asteroids in the size range of 1-4 km and with a velocity of ~ 20 $^{km}/_{s}$, typical for extraterrestrial projectiles, are in the range of 10^5-10^7 million tons TNT. Tsunamis will be generated in the order of 20-40 meters over deep water, and approaching the continental margins of South America and Antarctica these tsunamis have reached heights 10-25 times higher. Deep water waves with heights ranging from 5-10 meters would have extended into the North Pacific and around the Southern Ocean.
The impact would have been large enough for global distribution of ejecta, depending on impact models. Mainly the ejecta would consist of water, but also would include amounts of asteroidal material, salt and marine sediment. This deposition into the upper atmosphere have been hypothesized to have the potential to affect for several years insolation and possible even to deplete the ozone layer [Gersonde et al, 1997].

5.2 Expedition ANTXII/4

The first scientific visit to the Eltanin Impact Area, after the discovery of the meteorite ejecta in the USNS 'Eltanin' cores, was during expedition ANTXII/4. This expedition of the Alfred Wegener Institute on board RV 'Polarstern' started 22 March 1995 and ended 12 May 1995 in Punta Arenas (Chile).

The Eltanin Impact Area was visited twice. During the first stay, lasting for eight days from 29 March until 4 April, the first systematically planned bathymetric survey was made. This survey took place in the vicinity of the location of Eltanin core E13-4. A few cores were taken. The major bathymetric survey was made during the second visit. In about ten days from 30 April until 9 May, many additional profiles were collected, expanding the first survey to the northwest and the east. During this second stay many sediment cores were taken. A systematically bathymetric survey, called a mattress, is preferred for a homogeneous data distribution. Due to the geological stations and the weather conditions, this kind of surveying was not always possible. A list of the geological stations made in the Eltanin Impact Area during this expedition, can be found in Appendix B.
The profile planning was difficult to make due to the unknown sea topography. The profiles were often planned and surveyed without 100 % coverage of the seafloor. For bathymetric mapping the data distribution was too sparse, and many gaps remained.

5.3 Expedition ANTXVIII/5a

The expedition ANTXVIII/5a was the second scientific visit in the Eltanin Impact Area. This expedition left Punta Arenas on 24 February 2001 and ended there 12 April. During two weeks, from 26 March until 9 April, surveys and geological stations were made in the Eltanin Area. I was also a member of the scientific crew during this expedition, responsible for the multibeam system Hydrosweep DS-2, and especially for the planning of bathymetric profiles in the Eltanin Impact Area. In this section the planning and surveying, and the problems in relation with these will be discussed in short.

5.3.1 The Planning

The basis for creating a height model, is a homogeneous data distribution of the whole area. In case of bathymetry, this means that the profiles must be planned in such a way that a coverage of 100% is realised. The data distribution and the related profile coverage, depend however on the water depth. This implies for the profile planning an preliminary knowledge of the seafloor topography.
With the data of ANTXII/4 and the predicted topography of Sandwell & Smith [Sandwell, Smith, 1994], based on satellite altimetry and gravimetry, a profile planning was made to fill the gaps in the ANTXII/4 data, and to expand the survey area systematically. Time was an important factor during the expedition and therefore the profiles had to be planned in such a way that a 100% coverage was achieved, without overlap. In this case the most effective surveys could be made. The profiles were listed by priority. The most important profiles were planned in the vicinity of the Seamount group, to have at least

one well covered area for computing a Digital Elevation Model (DEM) afterwards. The profile list is shown in Appendix D. The profiles in this table are not listed by priority.

5.3.2 The Survey

The profile planning was used as a basis for the route planning of the ship. The basis of the route planning were the geological stations, where sediment coring was made. Between these geological stations there was the opportunity to survey along planned profiles. This means that no systematic survey was made, with the consequence that the data became more and more irregularly distributed over the area. A list of the geological stations in the Eltanin Impact Area during ANTXVIII/5a, can be found in Appendix C. Another aspect affecting the surveying of the planned profiles, was the weather. Almost the whole period of two weeks, storms and heavy seas, made bathymetric surveying, very difficult, also having its effect on data distribution, and data quality.
The first profiles were made in the western and southern part of the Seamount group, closing almost every data gap of ANTXII/4 in this area. After surveying the geological interesting northern part of the Eltanin Area, the ship returned to the vicinity of the Seamount group, were the last important gaps in the northern and north-eastern part were filled with bathymetric data. Due to time and the weather conditions, it was impossible to obtain a full sea floor coverage at the eastern side of the Seamount group. After the surveys the total area with almost full bathymetric data coverage stretches from 56°50 S, 90°10 W and 58°00 S, 92°20 W.
In Figure 5.4 the trackplot of the Eltanin Impact Area is given [Jacops, 2001]. The track lines of ANTXII/4 are in grey, in black are the track lines of ANTXVIII/5a. The red box defines the boundary of the selected mapping area, as can be read in chapter 7. The blue circle shows the location of the San Martin Seamount.

5.4 Bathymetric Data in the Eltanin Area

The total amount of bathymetric data in the Eltanin Impact Area given is very large. During approximately 31 days, 24 hours a day, bathymetric measurements were collected. This is shown in Figure 5.4, with the red box defining the boundary of the selected mapping area, describe in Chapter 8, and the blue circle representing the San Martin Seamount. As described above the data distribution varies from place to place, not only due to the geological stations. Geological stations were made at 22 locations during ANTXII/4 and almost the same amount of geological stations were made during expedition ANTXVIII/5a. Almost 75% of these stations lie in the selected mapping area (red box in Figure 5.4). The coring at geological stations took mostly between two and six hours and therefore locally very large amount of bathymetric data were collected.

The data is very irregularly distributed, due to geological stations, stormy weather conditions, and available time. The across track data distribution depend on the water depth, the fan aperture and the number of beams.

It can be defined using the following equations, with WD the water depth, a the fan aperture and B the number of beams:

$$\text{coverage}_{\text{across}} = 2 \cdot (WD \cdot \tan a) \tag{5.1}$$

$$\text{average resolution}_{\text{across}} = \frac{2 \cdot (WD \cdot \tan a)}{B}$$

In the case of Hydrosweep DS-2 the fan aperture a is mostly 90° (also during these two expeditions) and this system has a total of 59 beams.

The along track bathymetric data distribution depend not only on the water depth, but also on the ship's speed. Shallower water depths will result in sending and receiving the acoustic signal in a shorter time interval. The time interval between two sending beams and the ship's speed give an along track data resolution. It is not possible to compute the exact time interval, but only an estimate can be given. The estimated resolution is given by (5.2), where v is the ships speed in knots, and $t\{WD\}$ is the time interval as function of the water depth:

$$\text{average resolution}_{\text{along}} = v \cdot 1{,}852 \cdot t\{WD\} \tag{5.2}$$

Water Depth (meters)	Ship's Speed (Knots)	Average Time interval (seconds)	Coverage across (meters)	Average Resolution across (meters)	Average Resolution along (meters)	Accuracy (meters)
2000	8	9	4000	68	35	~10
2000	10	9	4000	68	46	~10
2000	11	9	4000	68	51	~10
2000	12	9	4000	68	56	~10
3000	8	11	6000	102	43	~15
3000	10	11	6000	102	57	~15
3000	11	11	6000	102	62	~15
3000	12	11	6000	102	68	~15
4000	8	14	8000	136	55	~20
4000	10	14	8000	136	72	~20
4000	11	14	8000	136	79	~20
4000	12	14	8000	136	86	~20
5000	8	16	10000	169	63	~25
5000	10	16	10000	169	82	~25
5000	11	16	10000	169	91	~25
5000	12	16	10000	169	99	~25
6000	8	19	12000	203	75	~30
6000	10	19	12000	203	97	~30
6000	11	19	12000	203	107	~30
6000	12	19	12000	203	117	~30

Table 5.1: Data resolution as function of the water depth and ship's speed.

In Table 5.1 the data resolution is given at different depths and different speeds, also is presented is the accuracy of the bathymetric measurements given by STN Atlas, and being ~0,5% of the water depth [Schenke, 1989], [Grant, 1990]. This accuracy is obtainable under ideal circumstances, and will decrease when surveying in extreme situations.
It can be concluded that the data resolution varies strongly with the ship's speed and the water depth. During both expeditions the time pressure and the weather conditions had their influence on the data resolution.

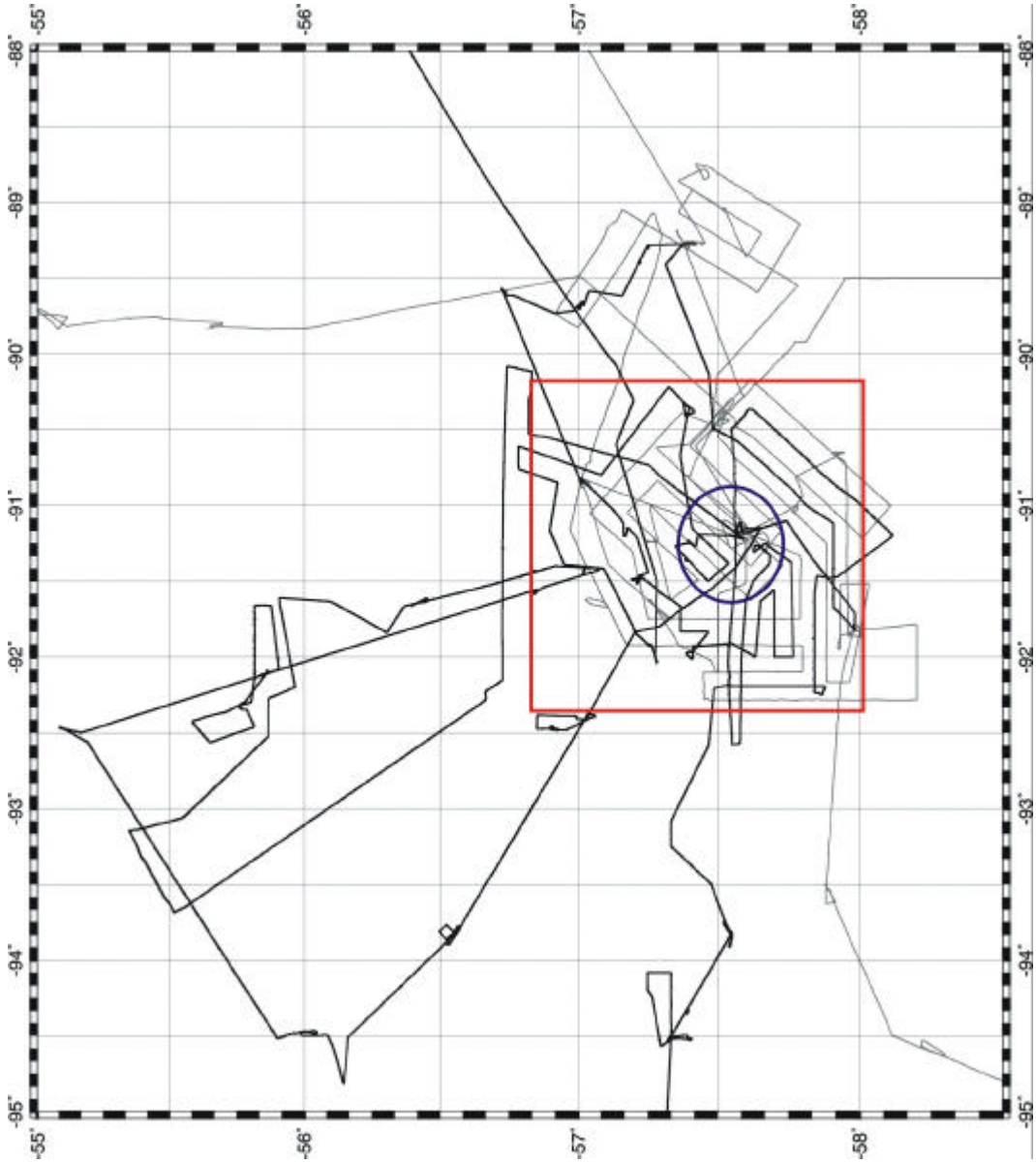

Figure 5.4: Track plot of the Eltanin Impact Area, ANTXII/4 in grey, ANTXVIII/5a in black.

6. Bathymetric Data Editing and Cleaning

The data editing and cleaning forms the first important step in the post-processing of bathymetric data. As described in Chapters 4 and 5, the quality of the data depends on many factors, and in this case especially the bad weather conditions had their influence on the data. Therefore the task is to remove outliers, and possible systematic errors in the bathymetric data, in order to achieve a homogeneous dataset.
This bathymetric data editing and cleaning is carried out at the AWI with the Hydrographic Information Processing System (HIPS), which is a part of CARIS (Computer Aided Resource Information System). This system is a GIS (Geographic Information System) especially for hydrographic data. It has to be remarked that only CARIS-HIPS is used for data editing and cleaning, and that the GIS CARIS is not used for post-processing but the GIS ArcInfo, described in Chapter 7.
This chapter will give first an overview of the program HIPS, followed by an explanation and description, in section 2, of the editing and cleaning of the bathymetric data in the Eltanin Impact Area and the problems that were encountered. Section 6.3, finally will describe the transformation from the cleaned bathymetric data into the files that were used for the computation of the Digital Elevation Model (DEM) in ArcInfo (see chapter 7).

6.1 Overview of the HIPS

The complex program HIPS was, at the AWI, for a long time used under the system UNIX as a part of the program HDCS (Hydrographic Data Cleaning System). This system was developed by the Canadian company Universal Systems Ltd. in Fredericton, New Brunswick, as a tool for editing and cleaning large hydrographic datasets [Christen, 1999]. This program HIPS was further developed under the system Microsoft Windows, and in this year also the bathymetric group at the AWI changed to this new version of HIPS. This HIPS version 5.1 was used as data editing and cleaning tool.

6.1.1 HIPS workflow

The HIPS workflow is visualised in Figure 6.1 [CARIS, 2001]. This workflow shows the different activities needed for the cleaning and editing of the data. The most important steps in this process are written in red. The basis of HIPS is the visualisation of the bathymetric data and the editing. HIPS is not only concentrated on the depth editing, but also offers position and ship's attitude data (roll, pitch, heave) editing, as well as the loading of tides and the possibility to apply sound velocity corrections.

The basis of the data cleaning and editing is made by the project setup. A project consists of: vessel, day, and lines, which are also hierarchically divided into the directory structure. The vessel has to be defined with a so called 'vessel configuration file', which

defines the constellation of the multibeam system on the ship. A vessel has one or more days with data, these days can have one or more survey lines. Because of this data structure it is possible to select either one or more lines, one or more days or a ship, of which the data has to be loaded for cleaning and editing.
The program offers conversion possibilities for almost every multibeam system, but because of the changes in the Hydrosweep system the old data of ANTXII/4 had to be converted using another program under UNIX (see section 6.2).

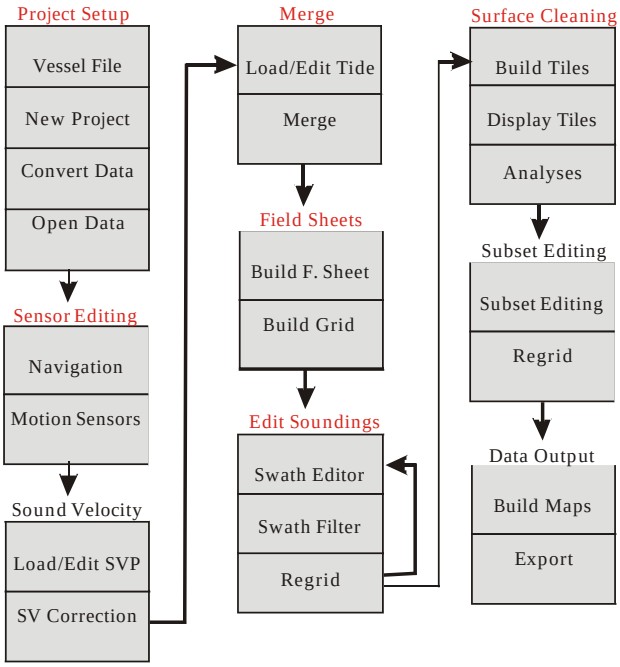

Figure 6.1: The HIPS workflow.

The first step in the editing process is the sensor editing. The sensors that can be edited in HIPS are:

- Roll
- Pitch
- Heave
- Gyro
- Navigation (see 6.1.2)

After the sensor errors are removed, specific sound velocity profiles can be loaded or edited to correct the data for wrong velocity profiles used during the surveys. In the case that tides play a role, a special tide file with the tide information can be baded. This is done before the lines are merged. In this step the sounding depth and position are calculated for every profile in the line.

Now the bathymetric data can be edited and cleaned. A very useful tool is first to create a weighted grid. This weighted grid is a good visualisation method for the bathymetric data, and shows places where data has to be cleaned. This weighted gridding can be

combined with the data editing and cleaning and the results are shown immediately. The swath editor is shortly described in section 6.1.3.

The next step in the bathymetric data editing and cleaning procedure, is the surface cleaning. This is a method to remove outliers based on a statistical testing procedure (see section 6.1.4). This surface cleaning is followed by the last step, the subset editor. In this editor different lines that overlap can be edited together. With this method the data can be combined and compared with each other to remove outliers in overlapping areas. An important condition is that the different datasets that overlap can be compared. The bathymetric data at the AWI is, after editing and cleaning, converted to so called soundings. To be able to combine different data sets, these soundings are, the bathymetric data referenced to a sound speed in water of 1500 m/s (see section 6.3).

6.1.2 Navigation Editor

In the navigation editor, the positions, at which multibeam data is collected, are checked and when needed rejected. It is an important tool in, for example, areas of bad GPS satellite constellation or in areas where no DGPS corrections are available. In such areas it is more likely that possible outliers can be found within the navigation.
The rejection of these erroneous positions can be performed either with or without interpolation. In the case of interpolation, the point is removed from the original position and interpolated from neighbouring values. This action results in a new position and the bathymetric data is combined with this interpolated position [CARIS, 2001]. No data will be lost.
When the point is rejected without interpolation, the value is not to be included and no interpolation is to be performed. All the bathymetric data between the previous and next accepted navigation point are to be rejected [CARIS, 2001]. In this case data will be lost. The three possible status flags that a navigation point can have are shown in Figure 6.2.

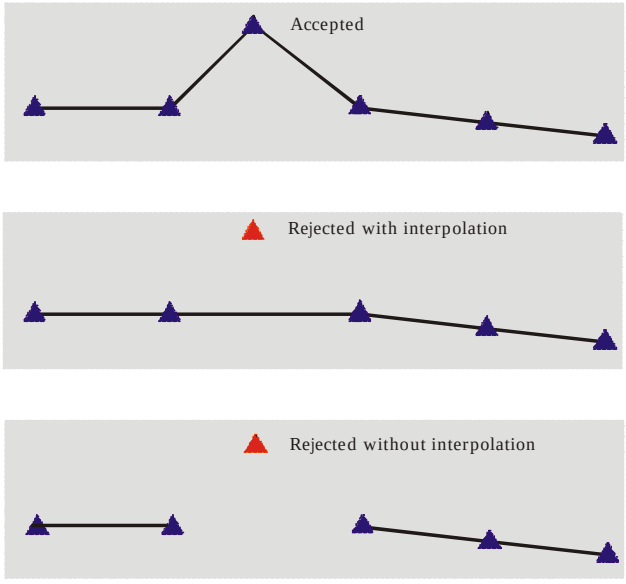

Figure 6.2: Navigation status flags.

The navigation editor also shows information about speed, distance and course. These windows can be used during the editing process. Within this navigation editor it is also possible to search for erroneous positions. This spike detection filter can search for these spikes using either speed jumps or time jumps within the data. These jumps can be defined, depending on the data characteristics.

6.1.3 Swath Editor

The swath editor is the main part of HIPS. In this editor the actual data cleaning is made by hand or with the help of filters. The observed swath data are represented in different views:

- Plan view; shows the different swath lines from above
- Rear view; shows the different swath lines within the plan view, and in along track direction
- Side view; shows the different swath lines within the plan view, and in across track direction
- Profile view; shows one selected swath line in the plan view as a profile
- Side Scan; visualises the side scan data

The depth data can be edited and cleaned first by hand. In the different views the data can be selected and either be accepted or rejected. A rejected data point can always be changed back into the accepted status. This interactive editing requires a good knowledge of the operator, in order to know whether it is an erroneous data point or not, and it also requires time.
To simplify and facilitate this interactive editing, different filters within the swath editor can be used. These filter parameters can be adjusted by the operator for every part of the survey line. This filtering can be analysed and when needed, the filter parameters can be changed. In Figure 6.3 the different filter parameters within the swath editor are shown [CARIS, 2001].

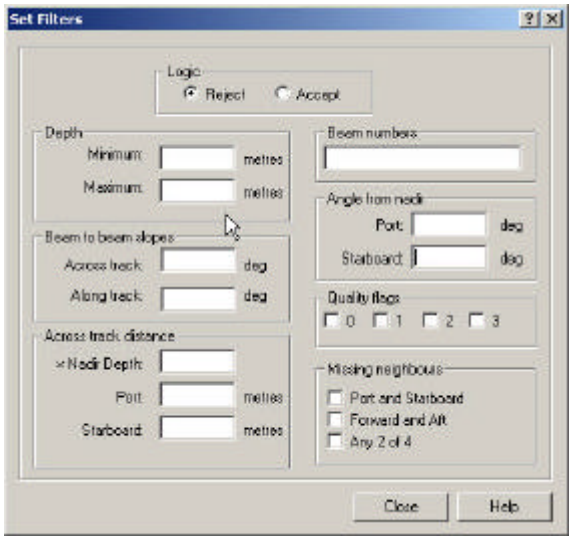

Figure 6.3: Filter parameters in swath editor.

The minimum and maximum depths define the upper and lower boundary of data points that should be rejected or accepted. This filter is used to find the coarse outliers in the data. In order to find isolated outliers within a swath line the beam to beam filter can be used. It calculates for each beam the slopes in degrees to the prior and post beams, and if both slopes exceed the defined value, the beam is rejected. This filter can be applied either in across track direction or along track direction. This is shown in Figure 6.4.

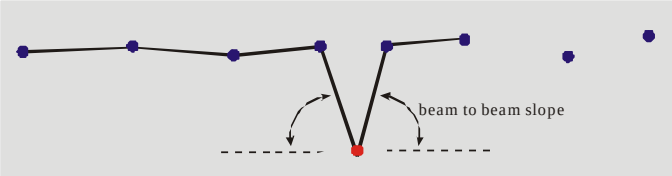

Figure 6.4: Beam to beam slope filter.

Depth data points with across track distances that exceed a user defined multiple of the average depth, will be rejected when the across track distance filter is used. Also specific distances at port or starboard can be defined.
With knowledge of the used multibeam system and the transducers, also specific beam numbers can be rejected. This filter plays a role when a beam number in every profile is erroneous. This might indicate that something was wrong at that transducer element.
The last important filter parameter is the angle from nadir. This filter eliminates the outer edges of swath widths. The reason to make use of this filter might be that the data points at the outer limits of the swath angle are not reliable, and do not show the required accuracy.

The filter parameters discussed above, are the most important filter parameters. These parameters were also used during the data cleaning and editing of the bathymetric data in the Eltanin Impact Area. This is discussed in section 6.2.

6.1.4 Surface Cleaning

In the data cleaning and editing in the swath editor, the relationship between swath lines are made by the operator. His knowledge about the morphology and the properties of the used multibeam system forms the basis for the decisions to reject or accept data. To realise a dataset that is more homogeneously edited and cleaned not only the filters within the swath editor are used, but also another cleaning tool. This tool is based on statistics and is called ‘surface cleaning’.

The idea of this cleaning procedure is that data points are rejected if these points do not fit within a surface, that is computed of data points in the neighbourhood. The surface cleaning tool works by iteratively building a polynomial surface to fit the data in a specific neighbourhood, the so called tile. Because the surface can not fit all the data in the tile exactly, there will be a difference between given point data and the generated polynomial surface. This difference is the residual value, and by defining and determining a specific residual cut-off, the outliers are defined [CARIS, 2001]. The surface cleaning tool has a lot of parameters shown in Figure 6.5. First a tiling is made, followed by the actual cleaning.

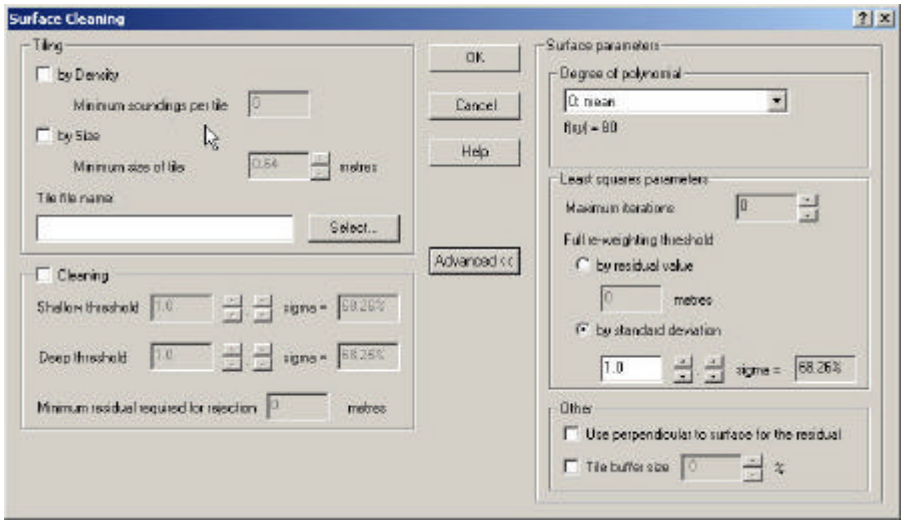

Figure 6.5: Surface cleaning parameters.

Tiling

First, a tile building procedure is started. This tiling is a process of aggregating several points together into a single tile, based on statistical criteria, as can be seen in Figure 6.5. It operates as an iterative procedure, from large to small. If the statistical criteria are not passed in a large area, this area is subdivided into four equal sized tiles. The data density and the tile size are the principal criteria. The tiling proceed to smaller tiles, until one of the sub-tiles would have fewer data points than the user-set minimum, or until the next iteration step would create tiles smaller than the minimum tile size, set by the operator [CARIS, 2001].

Cleaning

The cleaning tool works by iteratively building a polynomial surface to fit the data in each tile. There are five different surfaces, in order of complexity [CARIS, 2001], with $b_0 \ldots b_9$ constants:

- Mean;
  $f(x,y) = b_0$
- Tilted plane;
  $f(x,y) = b_0 + b_1 x + b_2 y$
- Curved tilted plane;
  $f(x,y) = b_0 + b_1 x + b_2 y + b_3 xy$
- Quadratic;
  $f(x,y) = b_0 + b_1 x + b_2 y + b_3 xy + b_4 x^2 + b_5 y^2$
- Cubic;
  $f(x,y) = b_0 + b_1 x + b_2 y + b_3 xy + b_4 x^2 + b_5 y^2 + b_6 x^2 y + b_7 y^2 x + b_8 x^3 + b_9 y^3$

The actual cleaning is performed with the cut-off limits defined by the operator. There are three values that are to be defined. The shallow and deep threshold define the upper

and lower limits, depending on the standard deviation of the differences. Also a absolute minimum cut-off can be defined. This is used to limit the use of the thresholds in very smooth surfaces. In such a case the deviation would be small, because the data points are close to the surface, and it is likely that good data points are rejected.

The results of this surface cleaning can be analysed and, when needed, the cleaning parameters can be adjusted. It is also possible to re-clean the already cleaned data with new parameters.

6.2 Eltanin Data Editing and Cleaning

This section describes the bathymetric data editing and cleaning of the expeditions ANTXII/4 and ANTXVIII/5a. The different steps, that will be explained, are the data conversion and the navigation editing. This is followed by the swath editor and the section will end with the surface cleaning.
The subset editing, often used to clean overlapping data, is for this data cleaning not used. The reason for this is the difference between the bathymetric data of ANTXII/4 and ANTXVIII/5a. As described earlier, the data has to be reduced to a sound velocity of $1500\,{}^{m}/_{s}$ to be able to combine and compare the bathymetric data of different expeditions at different times.

6.2.1 Data Conversion

Between the expedition ANTXII/4, in 1995, and the expedition ANTXVIII/5a, in 2001, the multibeam system, programs and data formats changed. The HIPS conversion tool offers only a data conversion of the new Hydrosweep data format, called ‘surf’. In this ‘surf’ data also sidescan information is present, which is also converted to help the operator with data editing. The bathymetric data of expedition ANTXVIII/5a could easily be converted. A problem formed the data of expedition ANTXII/4. At that time Hydrosweep-DS was installed on RV ‘Polarstern’ and the sidescan system was not integrated with the multibeam system. The data was available in the, so called, ‘dux’ format, a file format without sidescan information. This data could only be converted into HIPS on UNIX. Afterwards this data, together with the vessel configuration file, had to be transferred to HIPS under Windows.

6.2.2 Navigation Editor

First the data was checked in the navigation editor for erroneous points. In a few cases navigation points were rejected, two examples are given in Figure 6.6.
Not only the quality of the ship’s positioning has to be taken into account but also the ship’s speed and the ship’s motion. The accuracy of the positioning lies in the order of 5-10 meters. In heavy seas, with swell sometimes up to 15 meters, the pitching and rolling of the ship can, of course, cause changes in the position. It can be concluded that the navigational data in both datasets, was of good quality, although the data of ANTXII/4 showed a few more navigational errors. The percentage of navigational errors was in the order of a satisfying 0.1%.

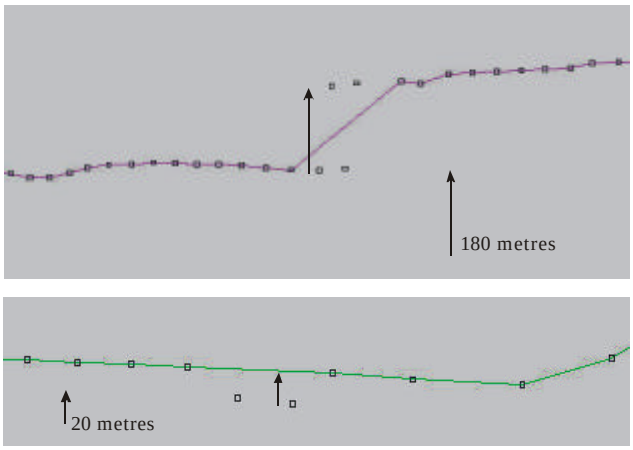

Figure 6.6: Example of navigation error.

6.2.3 Swath Editor

In the swath editor the bathymetric data was edited and cleaned. The data cleaning was split up in four different steps, see Figure 6.7. Because the survey lines consisted of 24 hours in the data of ANTXII/4, and of 8 hours in the ANTXVIII/5a data, the filtering steps were made for any part in the survey lines, that could be interpreted to have the similar characteristics.

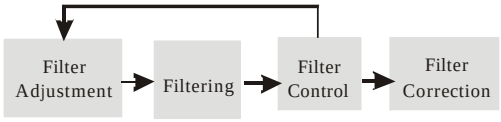

Figure 6.7: The four steps in the swath editor.

Bathymetric error visualisation

In Chapter 4 factors for errors in the bathymetric data were described. A few of these characteristic errors can be found during the editing procedure. The effect that occurred almost through all datasets, was the bad data due to heavy sea; an example is given in Figure 6.8. In the plan view the position of the single beams can be seen, in blue the beams at port side, in violet the starboard beams, and the rejected beams in red. The errors that occur in the outer beams can be seen, and are due to the whirls and the air bubbles in the seawater because of the rolling and pitching of the ship. During these situations, especially the quality of the outer beams was very bad and the amount of data was reduced with ~30%. This data reduction also has an important effect on the data resolution, in particular the resolution in the across track direction.
Another effect that occurred regularly was a wrong correction of the ship's rolling. This is shown in Figure 6.9, the red line in the rear view is tilted in reference with the other lines. Actually, this tilted line shows the same topography as the other lines. It can therefore be concluded that the error not occurs between the signal sending and receiving, but, because of the tilt in the across track direction, is due to a wrong roll correction. There is no possibility to correct for this error, and the swath lines have to be deleted.

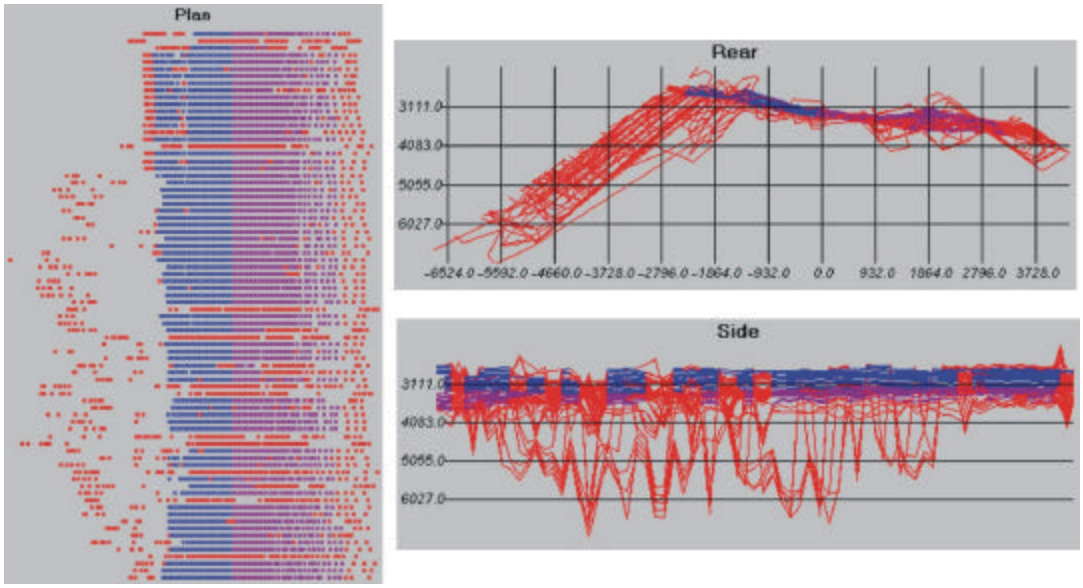

Figure 6.8: Effect of heavy sea.

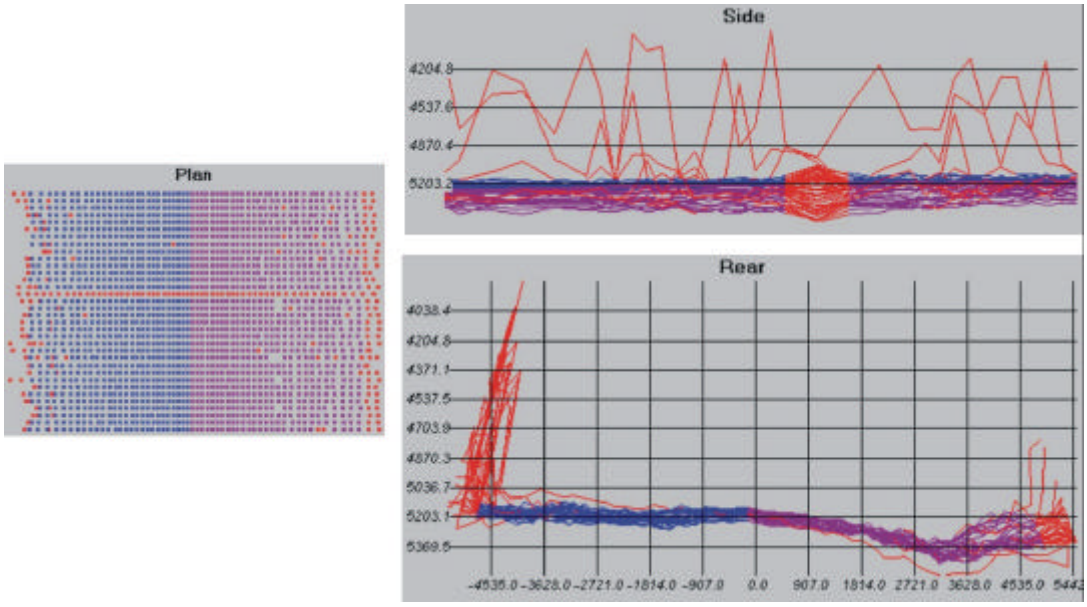

Figure 6.9: Effect of a wrong roll correction.

The last effect that will be discussed here, is a coarse error in Figure 6.10. This effect is probably due to false reflecting, because of air bubbles, fish, or noise. Compared with the roll error, in Figure 6.9, this single line does not represent the relative topography.
Figure 6.9 and 6.10 not only show a wrong roll correction or coarse errors, but also systematic errors at the outer beams. This effect occurred in many lines, and shows the inaccuracy of these outer beams. These beams are generally rejected in every line, depending on the quality. The number of rejected beams varied from two to sometimes six beams at each side, port and starboard.

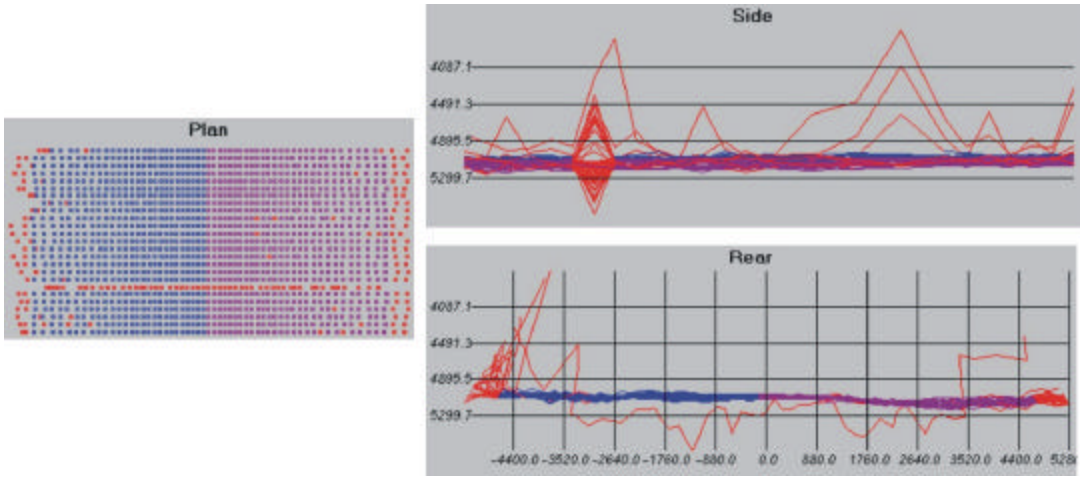

Figure 6.10: Coarse error, probably due to false reflection or noise.

Filtering

Each line was filtered with special filter parameters, depending on the data quality and the topography. The filtered data was checked, and still present single errors were rejected by the operator himself. This data rejecting of the operator is based on his knowledge (see 6.1.4).

The filter parameters are shown in Table 6.1. As can be seen the parameters vary with topography and point density. First of all the topography is divided into three different classes, depending on the slope. The classes are: flat terrain, in areas without obvious topography; smooth slopes, in areas with some small scale topography, and steep slopes, in heavily structured areas. The point density is divided into two classes. The first class contains the areas with low point density, along normally surveyed lines, with a customary survey speed of 7-12 Kt. The high point density is the second class, used at geological stations or during surveying at low speed, varying from 2-6 Kt.

Topography	Point density	Beam to beam slope (across)	Beam to beam slope (along)	× nadir depth	Angle from nadir (port & starboard)
Flat	Low	20°-25°	20°-25°	2	45°
Smooth	Low	25°-30°	25°-30°	2	45°
Steep	Low	30°-40°	30°-40°	2	45°
Flat	Dense	20°-25°	40°-50°	2	45°
Smooth	Dense	25°-30°	50°-60°	2	45°
Steep	Dense	30°-40°	60°-65°	2	45°

Table 6.1: Filter parameters depending on topography and point density.

The two filter parameters that depend fully on these classes, are the across and along beam to beam slope. Due to the distance between the data points (point density), and the effect of the topography, these across and along track slopes have to be changed. A slope of $\alpha°$ will result in various height differences between two points at short distance of each other or at a greater distance of each other, see Figure 6.11. The multibeam accuracy,

~0.5% of water depth (Table 3.1), has to be taken into account and the height difference has to be according to this accuracy.
The parameter nadir depth, rejecting the beams beyond the x-times this depth, is the same for every line. It is, in this case 2 times the nadir depth, because of the fan aperture of 90°. This fan aperture also defines the input for the angle from nadir. In both directions this is half of the aperture angle. Thus, every beam coming from an angle wider as this 45°, will be rejected.

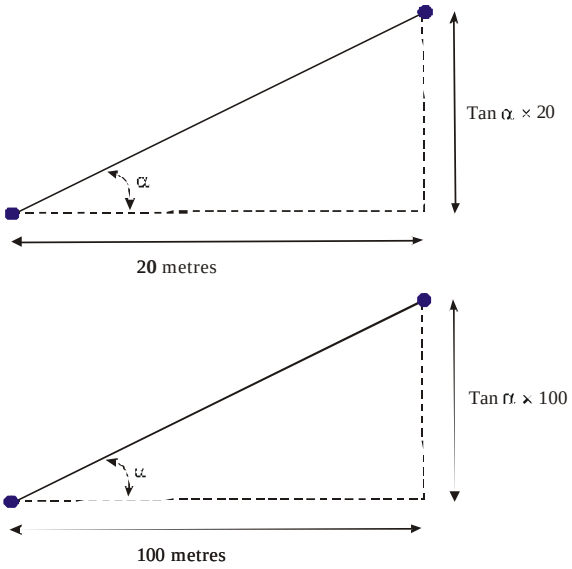

Figure 6.11: Point density and effect on the beam to beam slope.

The filter parameters minimum and maximum depth, are not shown in Table 6.1. These two parameters depend fully on the bathymetric data in the line and are defined by the upper and lower boundary of the topography. This is also the case with the parameter beam number. It defines the beam numbers that have to be rejected, due to the bad quality of the data at these beams. The two outermost beams were rejected in every swath line. These number of rejected beams could grow in the order of six beams at both sides.

Conclusions

The filtering in HIPS is a good method to help the manual cleaning of the bathymetric data. The datasets are cleaned homogeneously with this filtering. The filtering is an objective method, and the only subjectivities are during the checking of the data. Although the time for data cleaning and editing is reduced because of the use of these filters instead of the manual method, it still takes time to check the filtering. During the filtering, between 10-15% of the bathymetric data is rejected. In most of the cases because of the bad data quality, due to storms and heavy seas.
In areas of flat topography the noise exceeds the signal, or in other words, the signal of the small and high frequency topography in these flat areas disappears in the noise and cannot be detected. In such areas it is difficult to distinguish between noise and signal, or, so to say, between topography or no topography. This is in contrast with areas of varying

topography, here the signal of the topography exceeds the noise and the signal can easily be differentiated from the noise.

6.2.4 Surface Cleaning

The surface cleaning is the step, following the filtering in the swath editor. Each line is selected, and with the help of the statistical method (see section 6.1.4), data points are screened. The surface cleaning parameters that were used, can be seen in Figure 6.12.

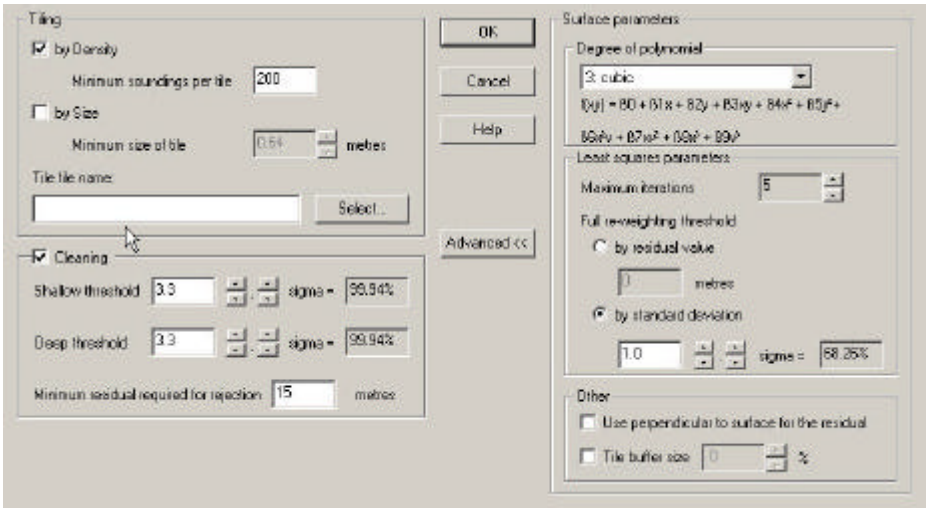

Figure 6.12: Used surface cleaning parameters.

The tiling is purely based on the point density, and the minimum is 200 data points, chosen in order to be able to use the statistical method on the data points. The cleaning parameters are set to 3.3σ (99.94%) as shallow threshold as well as deep threshold. Using these thresholds, only the real outliers are rejected. The minimum residual threshold required for rejecting is 15 meters by consideration of the depth accuracy. The surface which has to be fit through the data in the tile, is a cubic polynomial. In this way the surface also can be fit in areas of strong varying topography.

The lines were first cleaned separate, to reject the remaining outliers. The lines from one expedition, ANTXII/4 or ANTXVIII/5a, were after this line cleaning, put together in one surface cleaning. In this way the overlapping data could be checked and cleaned. The data of the two expeditions could not be cleaned together in one step, because of the difference in reference level. Therefore these data first have to be referenced to the same level. This is done in the conversion step to the hyd-format (see section 6.3).

Tiles analyses

An example of this surface cleaning is given in Figure 6.13. In this figure the tiling is represented in an area of high point density. The point density has, as can be seen, influence on the size of the tiles. The colours represent the amount of rejected data, light blue defines the minimum and dark blue the maximum. The yellow line is the survey line that is selected for this surface cleaning, and the yellow tile is the selected tile. The

histogram of this tile is also shown. The red lines in this histogram define the thresholds at 3.3σ, which in this tile are equal to 19.90 meters. This tile lies at a depth of almost 5000 meters, and given Table 3.1, the accuracy of the multibeam data is, for this depth, 25 meters. The histogram shows that this accuracy is achieved. Within small tiles the accuracy of the measurements can be improved, because the variation in topography is very small in such an area, and the amount of data points is very large. All these data points define and describe the same surface, that is fitted through this data, and thus give some redundancy.

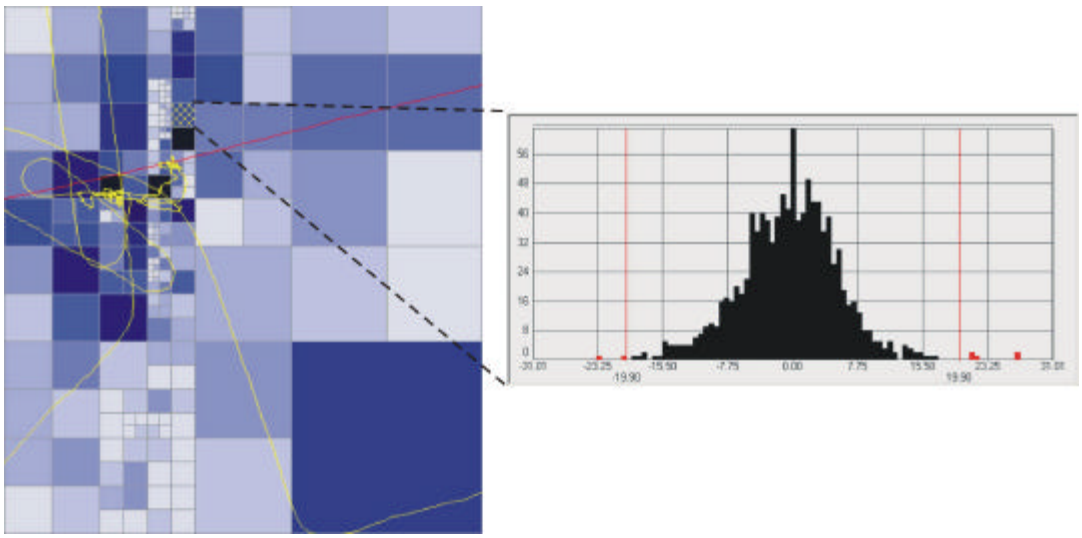

Figure 6.13: Tiling results in an area with high point density.

These histograms have been analysed and the results of the surface cleaning were checked. In some of the tiles, the deep and shallow thresholds were changed a little, because the thresholds had to be defined a little stronger or weaker.

Conclusions

Only 0.5-2% of the left bathymetric data was rejected. This shows the good results of the data filtering and cleaning in the swath editor. Most of the rejected data was found in areas of high point density, and the overlapping regions.
An advantage of the surface cleaning tool is the ability to interpret the surrounding topography and the surrounding data points. Therefore the surface cleaning is an important tool to clean bathymetric data of different lines when combining these lines. The data is cleaned homogeneously and changes per tile can be made by giving these tiles different thresholds. This tiling is especially useful in areas with a higher point density. In areas with a lower point density the tiles become very large which makes the surface cleaning more difficult. Another disadvantage of the surface cleaning is that different datasets can not be combined because of the different reference level.

6.3 Data conversion from HIPS to ArcInfo

The cleaned HIPS-data had to be transferred into xyz-format data, to be able to use the data in ArcInfo. The steps for the total conversion process are as follows:

- Transferring datasets from Windows to UNIX
- Convert surf-format to dux-format for non-cleaned ANTXVIII/5a data
- Convert HIPS-data to new dux-format data
- Convert new 'dux' data to hyd-format data
- Convert hyd-format data to a xyz-format
- Splitting xyz-format into xy-file and z-file

First the cleaned bathymetric data was converted under UNIX, because the HIPS under Windows was not able to convert the data back into the original dux-format or surf-format. Under UNIX it was possible to convert the data in the original dux-format, but not in the surf-format, used with the data from ANTXVIII/5a. Therefore the non-cleaned ANTXVIII/5a data, in surf-format, was converted to a dux-format. These dux-format files had to be combined with the HIPS-data, to be able to convert the cleaned data back into a new dux-format.
The new dux-format files, created from the cleaned HIPS datasets, are referenced to the same level during the conversion step to the hyd-format. In this binary file format, a backup format for bathymetric data at the AWI, the data is reduced to a speed of sound of $1500\,{}^{m}\!/_{s}$, see section 6.3.1. This hyd-file consists only of depths and positions. The other information, for example sidescan and signal amplitude are removed.
These hyd-files are converted to xyz-data files, with four columns. In the first column the line number, longitude and latitude in the second and third column, and in the last column the depth, with a minus sign. These files are only readable in ArcInfo when split up into two different files. The first file with the line number and the position, the second file with the line number and the depth. In ArcInfo these files are combined, given the unique line number. The used commands in ArcInfo are given in Appendix E.

6.3.1 Bathymetric Data Referencing

Because the mean sound velocity changes and is different at every location at any time, this parameter has to be known accurately to estimate the depth of the ocean floor. Due to wrong calibration, or too little knowledge about the changing within the sound velocity structure, because of a small amount of CTD measurements, differences are possible between different datasets. To be able to combine different bathymetric datasets with each other, these are referenced to the same sound speed, assuming $1500\,{}^{m}\!/_{s}$. The depths are then called 'soundings'. This procedure is visualised in Figure 6.14.
The original data are given an offset in depth direction, but the beam position stays unchanged. The following model is used to calculate these soundings out of the real depths:

(6.1) $$\text{sounding} = {}^{(1500\times\text{depth})}\!/_{C_{mean}}$$

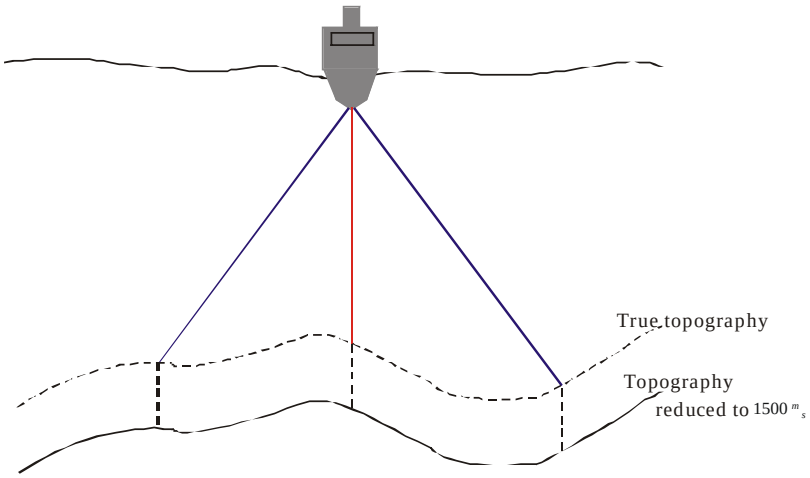

Figure 6.14: Referencing of bathymetric data.

7. Digital Elevation Modelling

Bathymetric data can be represented in the best way by the use of a Digital Elevation Model (DEM). A digital elevation model, or digital terrain model (DTM), is a digital representation of a portion of the earth's surface. DEM is used in this thesis, as it is used in the literature for digital models representing the topography. A DTM is a fuller model of the earth's surface, representing not only topographic elevations but also other terrain features [Worboys, 1997], for example houses, or morphological structure lines.
A DEM is a simplification of the earth's topography. The x,y-coordinate pairs have, to represent the topography, a third z-coordinate, defining the elevation of that coordinate pair. It is assumed that this spatial field function is single-valued, so overhangs are not represented. In this sense a DEM is moreover a '2.5 D' rather than a '3-D' model [Weibel, Heller, 1991]. The way the DEM represents the true surface topography depends on interpolation method, and the data density and quality.
These elevation models are a major constituent in processing geographical information, helping to model, analyse, and display phenomena related to the topography. Geo-scientists often use these models as a basis for their research. Further these bathymetric elevation models are used within oceanography and biology. For these purposes many operations are possible on DEM's. Not only the, in bathymetry important, derivation of contour lines, but also complex mathematical operations. These can be for example [Worboys, 1997]:

- Volume analyses
- Visibility analyses (not often used within bathymetric models)
- Slope, aspect, or higher derivatives computation
- Route planning
- Profiling

This chapter describes the process of the elevation modelling of the bathymetric data in the Eltanin Impact Area. First possible mathematical methods will be discussed for surface modelling, followed in section 2 by a discussion of the methods utilized at the AWI, and in ArcInfo for surface modelling. In this section the analyses of these different methods within three test areas are described. Section 3 discusses the surface modelling in ArcInfo with the Inverse Distance Weighting (IDW) method. This method gave the best results, and these are described and analysed separately. The chapter continues with section 4 discussing the contour line smoothing and noise removal depending on the slopes. In section 5 conclusions are given, based on the analyses in the test areas. The final surface modelling of the Eltanin Impact Area will be described in section 6.

7.1 Data Structures and Interpolation Methods

To convert observed point data to a continuous surface, interpolation is required. Interpolation is the procedure of predicting the value of attributes at unsampled sites from measurements made at point locations within the same area or region [Burrough, 1986]. The opposite of interpolation is extrapolation, which predicts values of an attribute at sides outside the by observations covered area. There are many different methods for interpolation of point data, classified by their characteristics. A popular classification of interpolation techniques can be made by the range of influence of the data points [Weibel, Heller, 1991]:

- Global methods; all sample points are used within the interpolation
- Local methods; only nearby data points are considered for interpolation

Another often used classification is, the grouping of interpolation into exact and approximate methods. Exact interpolation methods preserve the measured values at the data points, whereas the approximate methods smooth the data. The statistics of the differences between the predicted values and the measured data points are often used as an indicator of the quality of the interpolator [Burrough, 1986] and can also be used as an indicator of the quality of the data.
In this section a few of the most common and, for bathymetric data, useful interpolation methods are discussed. First the data structures for representing continuous surfaces are briefly described.

7.1.1 Continuous Surface Data Structures

The surfaces obtained from interpolation techniques can be represented by different data models. The most common classification of these data models is made by the data distribution. The data distribution is either regular or irregular. The used data models for these different classes, see also Figure 7.1, are [Weibel, Heller, 1991]:

- Rectangular grid; regular
- Triangulated Irregular Network (TIN); irregular

A grid presents a matrix structure that records topological relations between data points implicitly, a so-called ‘elevation matrix’. The handling of these matrices is simple and grid-based algorithms are relatively easy. Disadvantages of regular grids is that the point density cannot be adapted to the relief complexity, and rectangular grids cannot describe special topographic features [Weibel, Heller, 1991]. These regular grids are common used within geological and geophysical research because of their simplicity and the analyses that can be carried out easily on such regular grids.
Triangulated irregular networks, are based on triangular elements, with the vertices at the data points. Topographic features can be incorporated into the structure, and a TIN reflect the variable data density and the terrain roughness. TIN’s however, are more complex and also difficult to handle [Weibel, Heller, 1991]. The TIN building is based upon different mathematical methods to build, when possible, equilateral triangles with minimum side length (see section 7.1.3).

Neither a grid nor a TIN data structure is superior to the other. It depends on the tasks of the digital elevation modelling, data quality and data distribution. The advantages and disadvantages of these different data structures are not discussed within this thesis, but are described in literature, for example [Peucker, 1978].

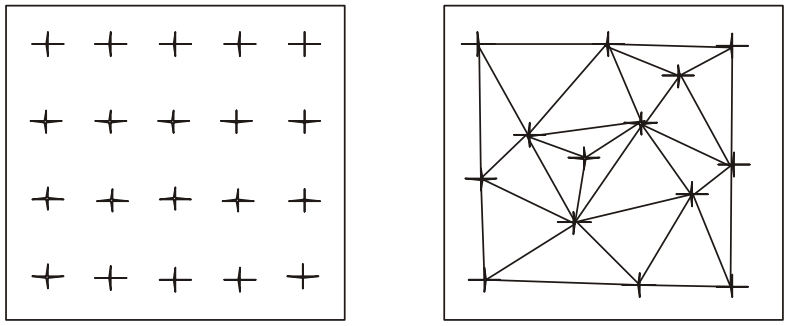

Figure 7.1: Two DEM data structures; regular grid (left), TIN (right).

7.1.2 Trend Surface Interpolation

The basis of the trend surface interpolation is to explore a possible functional relation between measured attributes and attributes to be predicted. The measured attributes would be in this case the multibeam data points, and the topography the attribute to be predicted. In the case of trend surface interpolation this is only based on the geographical coordinates.

The idea is to fit a polynomial surface, by least squares, through the data points $z(x_i)$ thereby minimizing the sum of squares for $\hat{z}(x_i) - z(x_i)$. In this case the dependent variable z is the attribute of interest and it is assumed to be normally distributed. It is also assumed that the regression errors are location independent. This last assumption however is not often realistic [Burrough, 1986]. The polynomial surfaces of order p, that are derived by regression, are of the form:

$$f(x,y) = \sum_{r+s \le p} (b_{rs} x^r y^s) \qquad (7.1)$$

In (7.1) b_{rs} are the polynomial coefficients. During the surface cleaning this method for data interpolation was used.

With trend surface interpolation, broad features of the data can be modelled by low-order polynomials, but it is becoming difficult to ascribe a physical meaning to higher order and complex polynomials. A common negative effect of trend surfaces is the waving of the edges to fit the data in the centre of the area, resulting that surfaces may reach ridiculously large or small values outside the data area. Other disadvantages are the susceptibility of surfaces for outliers, and the method dos not handle well large data sets. An advantage of this method is that it provides an analytical solution of the surface. Because of these advantages and disadvantages this method is often used to remove broad features out of the data prior to the use of a local interpolator [Burrough, 1986].

7.1.3 Thiessen Polygons and Delaunay Triangulation

A 'Delaunay Triangulation' is used to create a TIN as equilateral as possible. The dual of this triangulation are the 'Thiessen Polygons'. These polygons are built with as basis the nearest neighbourhood. This means that predictions for attributes at unsampled locations are provided by the nearest single data point. Thiessen polygons divide a region in a way that is determined totally by the configuration of the data points [Burrough, 1986]. This means that if the data lie on a regular grid, then the Thiessen polygons are equal to the grid spacing. If, however, the data are irregularly spaced, then the result is an irregular lattice of polygons.
The Delaunay triangulation is now formed with the use of these Thiessen polygons, where the data points from the polygons form the nodes of the triangles. This results in a unique triangulation with the following properties [Worboys, 1997]:

- The outer edges of the triangulation form the convex hull of the pointset.
- The circumcircles of the triangles contain in their interior no other points of the pointset.
- The Delaunay triangles are the best-possible equilateral triangles.

A visualisation of this triangulation is given in Figure 7.2. First Thiessen polygons are built around every data point. A polygon defines an area of the nearest neighbourhood of the point within this polygon. The triangulation is the dual of these Thiessen polygons. The triangles are built with the data points as nodes. In Figure 7.3 the circumcircles of the triangles are shown. These circumcircles only contain the nodes of the triangles, and no other data points are within the interior of these circles.

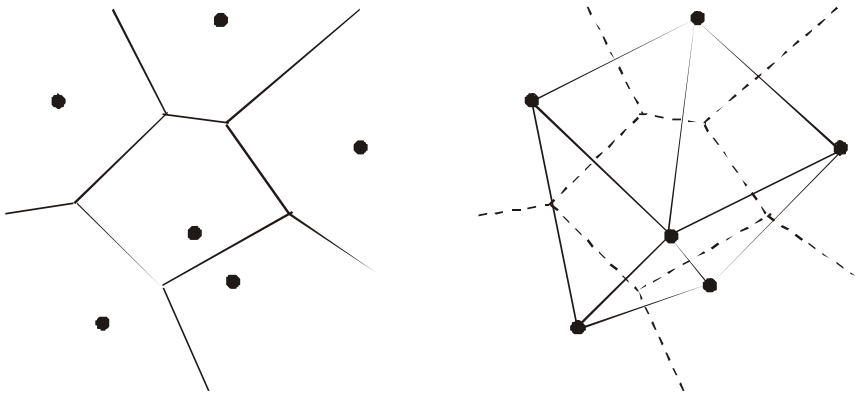

Figure 7.2: Thiesen polygons (left) and the Delaunay triangulation (right).

TIN's are widely used within GIS. Some advantages of a TIN structure are:

- Data points are fitted exactly [Burrough, 1986].
- In areas of complex topography extra information can be gathered without gathering also hugh amounts of redundant data in areas with simple relief [Burrough, 1986].
- Handle discontinuities in the topography.

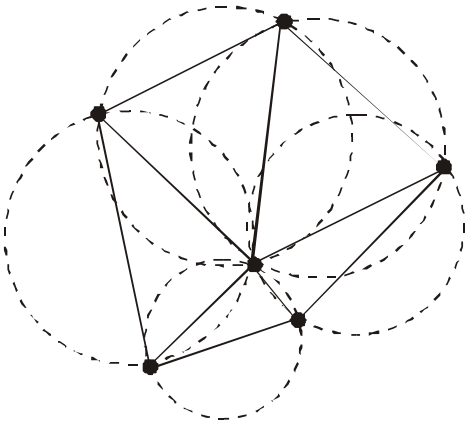

Figure 7.3: The circumcircles of the triangles.

A TIN has also disadvantages:

- TIN generation is slow and complex.
- Computation of surface depending attributes, as contour lines, hill shades, slope, is difficult and complex [Burrough, 1986].
- To update a TIN, the generation has to be repeated.
- TIN's are difficult to compare with each other.

7.1.4 Inverse Distance Weighting

The inverse distance weighting (IDW) method for interpolation combines the ideas of proximity of the Thiessen polygons with the gradual change of the trend surface. It is commonly used in GIS to create regular grids from point data. The assumption is that a distance-weighted average of the data, within a neighbourhood of the data point to be computed, gives the value for that data point [Burrough, 1986]. The irregular spaced data is, in most of the cases, interpolated on a regular grid.
These averaging methods compute, with W_i weights and $z(x_i)$ the original attribute of the data points:

$$\hat{z}(x_0) = \sum_{i=1}^{n} W_i z(x_i) \qquad \sum_{i=1}^{n} W_i = 1 \tag{7.2}$$

The weights W_i are given by a special function $\Phi(d(x, x_i))$. The most common function of $\Phi(d)$ is an inverse distance weighting. The weights depend on the distance between the point to be computed and the neighbouring data point, and on the weighting factor r. This inverse distance weighting predictor is as follows, with d_{ij} the distance between the grid points and the data points [Isaaks, Srivastava, 1989] :

$$\hat{z}(x_0) = \sum_{i=1}^{n} z(x_i) d_{ij}^{-r} \Big/ \sum_{i=1}^{n} d_{ij}^{-r} \tag{7.3}$$

The linear interpolator is the simplest form of this predictor. The weights are then computed from a linear function of distance between data points and the grid point. The distance *D* defining the neighbourhood in which data points are weighted, corresponds to a radius of circle for data that are relatively uniformly distributed.

The advantages of this inverse distance weighting are:

- Computational simplicity.
- Updating of the grid is easy.

Disadvantages:

- The weighting function cannot be changed within the data set, the choice for the parameters is important.
- Outliers have influence and have to be filtered out.

7.2 Surface Modelling: The Test Areas

The Eltanin Area was split up in three small test areas to test the different interpolation methods. In these areas interpolation methods were tested and analysed to be able to model the whole Eltanin Area in the best possible way.

The analysis of the methods is founded on the following assumption:
The modelled surface has to fit the original data in the best possible way, with the assumption that the noise does not influence the modelled surface. This means that an acceptable smooth surface has to be modelled within the measurement accuracy.

This is an important assumption because the bathymetric data of the Eltanin Area are the first accurate measurements of the seafloor topography. Therefore it is not possible to make any comparisons between different datasets. The only method for quality analyses is possible only with the original data itself. The possible creation of a control dataset would result in a less accurate height model, because of the loss of data, therefore this is not realised. This means that every data point within the Eltanin Area is used during the surface modelling.

7.2.1 The Test Areas

The three locations of the test areas were based on the contour maps of the Eltanin Area and the grid made during the cleaning and editing. The contour maps gave a first impression of the bathymetric data and were made with the program ‘contour’ used at the AWI. This program creates contour lines closest to the original data to be able to interpret the original data. It uses the Delaunay triangulation method. It is often used during the expeditions to make real time maps of the surveyed areas.

The test areas are located at three different topographic regions with also different data resolution. In Figure 7.4 these three areas are presented. The blue lines in the figure

represent the data of expedition ANTXII/4, and the yellow lines the ANTXVIII/5a expedition data.

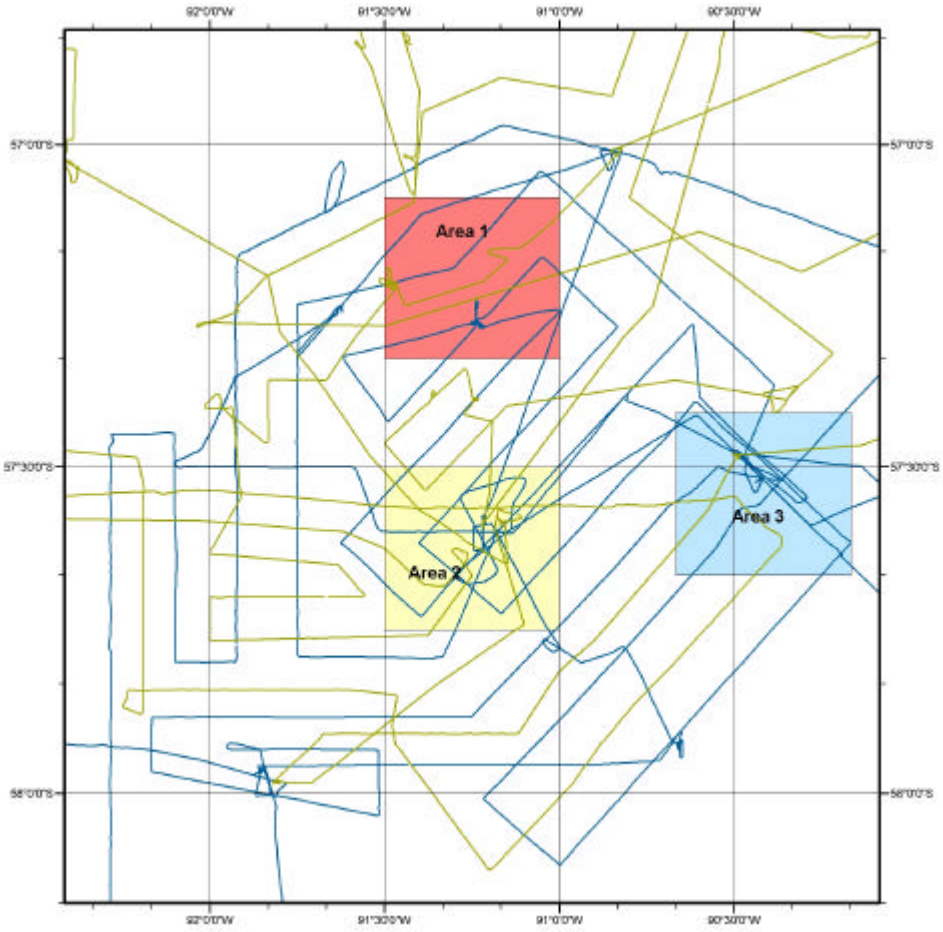

Figure 7.4: The test areas within the Eltanin Impact Area.

These areas will be shortly described:

- **Area 1:** This area has its centre in a valley with at one side a steep slope up to the seamount, at the other side there are some small scale mountains, most of them have a cone form. The data density is high within the flat valley at the geological station, at the steeper slopes the data density decreases very quick. The boundaries of this area are the parallels at 57° 05' S, and 57° 20' S, and the meridians at 91° 00' W, and 91° 30' W. This area is chosen because of the smaller scale mounts, and to test the influence of the varying data resolution at the locations where the flat terrain changes into steep slopes.

- **Area 2:** The top of the San Martin Seamount lies within this area. The depth of the top is about 2300 meters. At all sides the flanks of the mountains are very steep with some ridges. The top of the seamount has a high data density, whereas the neighbourhood has a much lower data resolution. The surface

modelling at steep slopes is tested within this area and the influence of the higher accuracy of the multibeam system in areas of shallower depth. The area is situated between 57° 30' S, 91° 00' W and 57° 45' W, 91° 30' S.

- **Area 3:** Test area 3 is situated in a flat small basin at depths around 5000 meters. The location is between 57° 25' S, 90° 10' W and 57° 40' S, 90° 40' W. The centre has a high data resolution around the geological stations, most of the area however is covered with a lower data density. There are no specific topographic features within this area. Not only the influence of the point density in flat areas was tested, but also the accuracy of the multibeam system at deeper places of the ocean bottom.

In the Figures 7.5, 7.6, and 7.7 the data density in these three areas is presented. In these figures the blue dots represent a high point density, and the orange dots a low point density. Almost every data point is visualised, and therefore the track lines and the locations of the calibration of the system can be well distinguished. These calibration locations (described in Chapter 3) are the small interruptions within a track. This calibration is performed every kilometre, or after every 10^{th} - 15^{th} swath, depending on waterdepth and speed (see section 5.4). The geological stations give of course a higher point density, but as can be seen, always only in one direction. At these stations the ship was positioned in the wave direction and only moved within one ship length

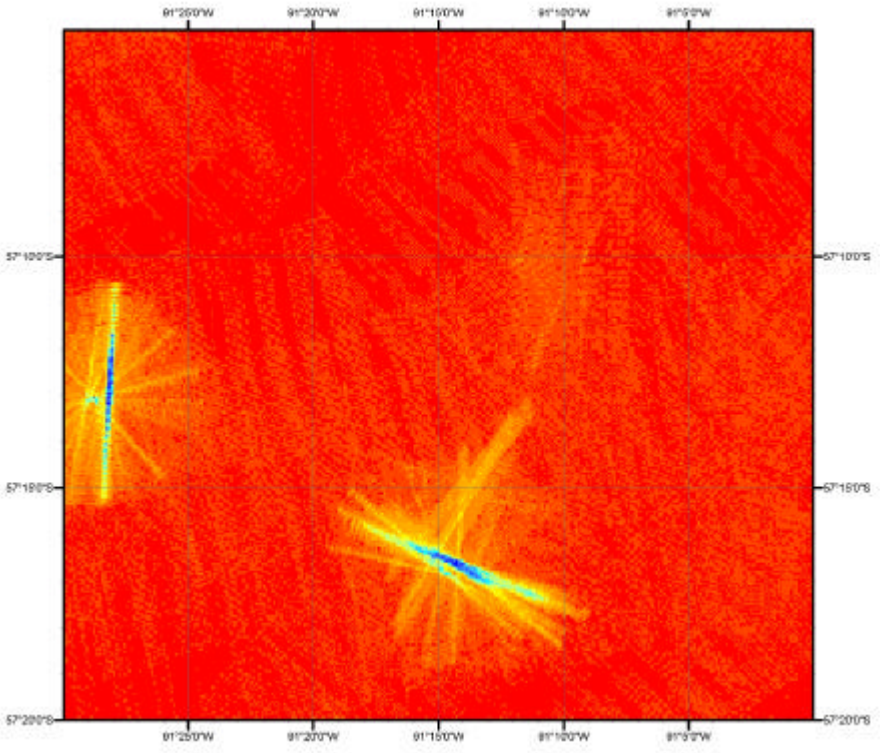

Figure 7.5: The data density in test area 1.

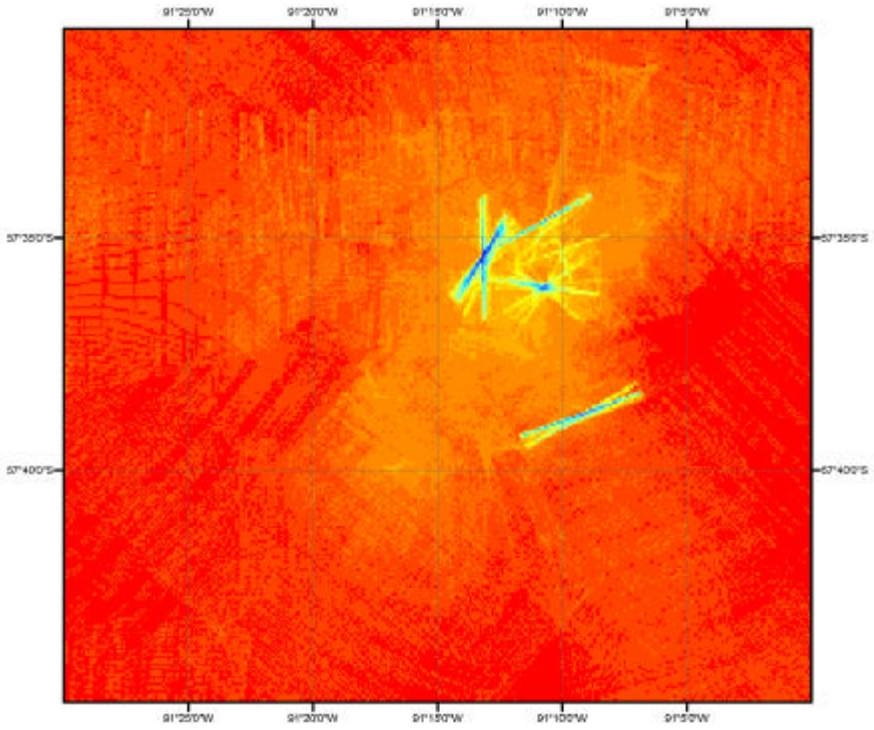

Figure 7.6: The data density in test area 2.

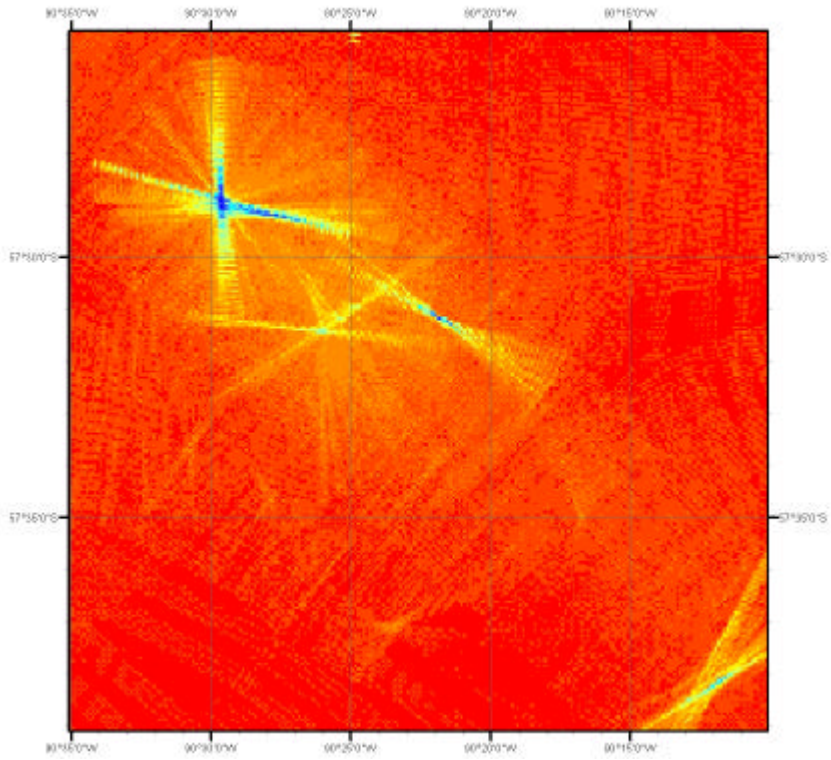

Figure 7.7: The data density in test area 3.

7.2.2 Surface Modelling using the program DTM-fn

The program DTM-fn (Digital Terrain Modelling Fred Niederjasper) is developed at the AWI, originally as a program to automatically remove outliers form bathymetric data. The program has not really improved to a surface modelling tool, but can be used to create DEM's easy and fast. DTM-fn is in an early stage of development, but will not be developed further.
The advantage of this program is not only the use of a distance weighting but also the weighting depending on the beam position. In other words the centre beams will have a higher weighting than the outer beams [Beyer, 2001]. The disadvantages are the untransparency of the program, the possibility to change only a few parameters and the difficult conversion to ArcInfo.

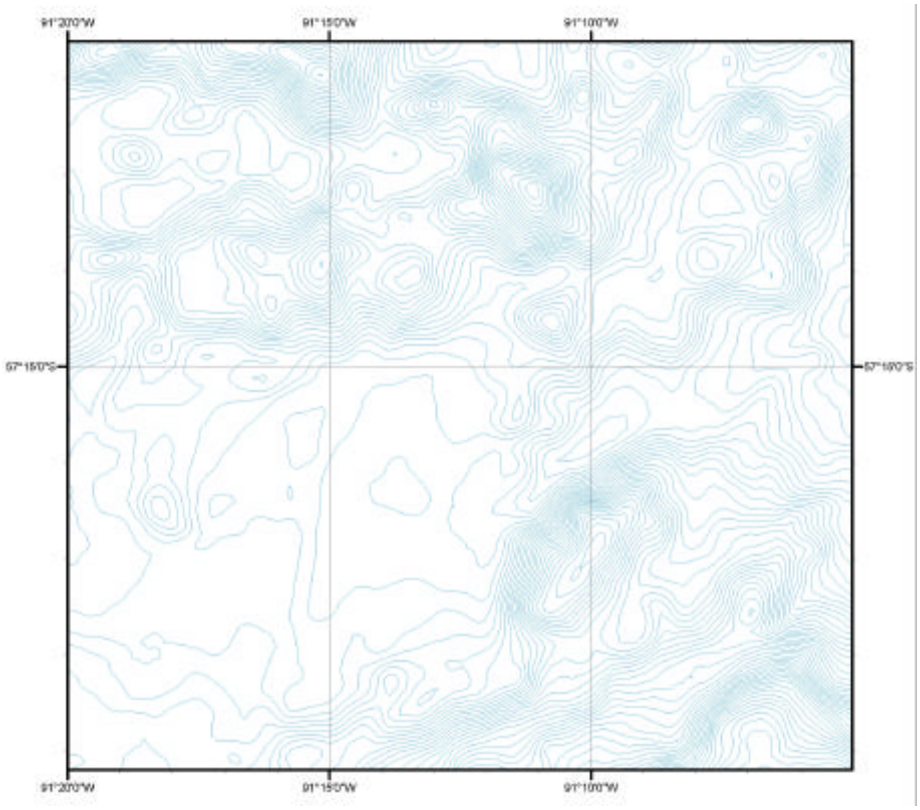

Figure 7.8: Contour lines (20 m.) after surface modelling with DTM-fn.

The task of this research was to use the methods within ArcInfo for DEM generation, therefore DTM-fn was only used to compare the ArcInfo results with this surface modelling program. The choice to use DTM-fn instead of other programs, for example GMT, was based on the advantages of this program to weight the beams depending on their position within the swath.
In Figure 7.8 the contour lines of the DEM computed with DTM-fn are shown. The area lies within test area 1. The resulting contour lines are smooth and the effect of noise is reduced.

7.2.2 Surface Modelling using Triangulation

Triangulation of point data to model the topographic surface has proven to be accurate and useful. Within a triangulation the point density can be managed depending on the topographic variation and so a minimum number of points can be used. However to create a DEM of the Eltanin Impact Area, this method is not very useful.
Every data point within the data set will be used during the triangulation. This results in a triangulation with the following disadvantages:

- A varying point density not depending on the topography.
- Influence of the measurement noise and data accuracy.
- No data areas are extrapolated.

The data density in the original data is varying from place to place depending on ship's speed, water depth, track overlapping and geological stations. This has an effect on the triangulation because most of the data points lie in flat areas whereas the steep topography parts are covered with little data points. According to the triangulation a higher point density is needed within areas of steep topography. This data distribution is not possible with the bathymetric data sets of the Eltanin Impact Area.
Because every data point is used within the triangulation the noise and varying accuracy of the data (see Table 5.1) has strong influence on the TIN. This can be clarified with the following example. In areas with a data accuracy more than several meters (assume > 20 meters), every data point is visible in the DEM, and the DEM shows topography not depending on the real seafloor topography but on the data accuracy. This DEM is therefore, as an interpretation of the seafloor topography, not useful. The resulting DEM is a very inhomogeneous TIN, purely fitting the original data exactly.
Also in areas with a very low point density a triangulation is made, resulting in data extrapolation. Extrapolation of the data is not desired, because the created surface model within the no data area is based on data outside that area; no connection can be made with the real topography.

The triangulation and contour generation is carried out with ArcInfo, with the Thiessen polygons as basis. With the TIN command in ArcInfo it is also possible to use multiple input sources, for example break lines describing topographic structures. Because no further information about the topography was available, only the point data was used to create the TIN. A result of a triangulation can be seen in Figure 7.9. The shown contour map is a part of test area 1. As can be seen the noise is present in the contours. This is due to the data accuracy as described above. It can be concluded that this surface modelling method does not result in the desired surface, as described by the assumption which was made before.

7.2.4 Surface Modelling using Inverse Distance Weighting

The IDW, inverse distance weighting (section 7.1.4), is a commonly used surface modelling method. It creates a regular grid surface. Many programs used at the AWI use this method for DEM generation, such as GMT and DTM-fn. The inverse distance weighting method in ArcInfo has different parameters to control the interpolation. These parameters were tested during this research project and the results are discussed in the

next section, section 7.3. This method is also used, based on the results in the test areas, in the final surface modelling of the Eltanin Area, described in section 7.6.

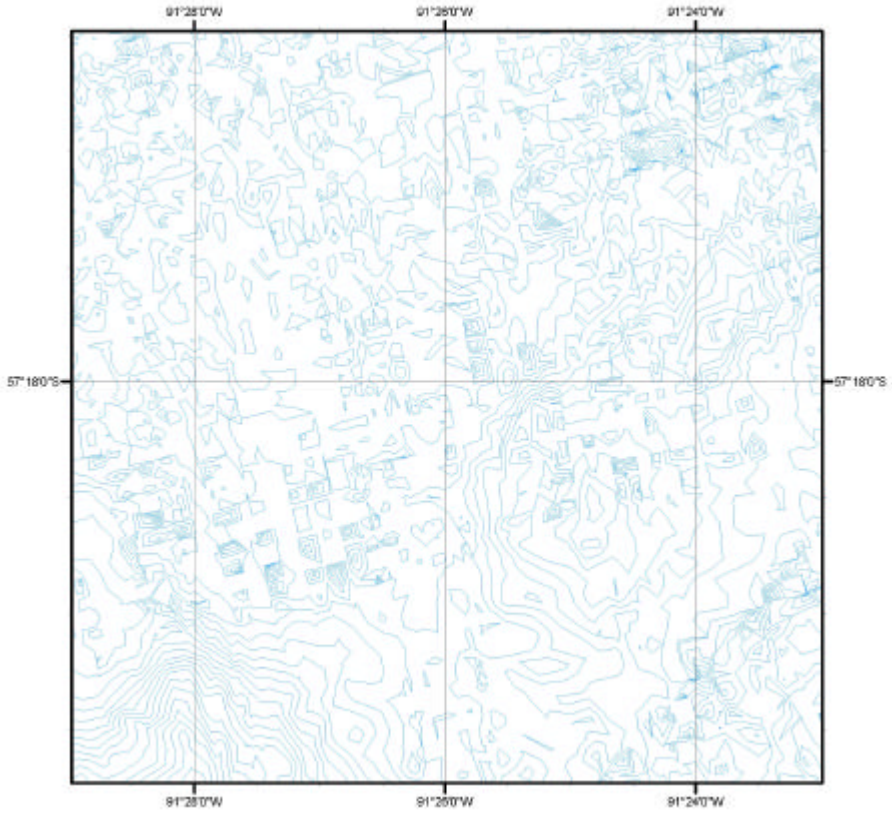

Figure 7.9: Contour lines (20 m.) after a TIN generation.

7.3 Inverse Distance Weighting in ArcInfo

This section discusses the IDW in ArcInfo to create a DEM. This method has different parameters, which were tested and analysed. The inverse distance weighting in ArcInfo makes use of the following commands [ESRI, 1999]:

- IDW(<point_cover|point_file>,{spot_item},{barriers},{power},{SAMPLE, {num_points},{max_radius}},{cellsize},{xmin,ymin,xmax,ymax})

- IDW(<point_cover|point_file>,{spot_item},{barriers},{power},{RADIUS, {radius},{min_points}},{cellsize},{xmin,ymin,xmax,ymax})

The subcommands or parameters with description are listed in Table 7.1. Some of these subcommands have an effect on the surface modelling, these subcommands are discussed in the following subsections.

{point_cover}	The data source containing z-values to be interpolated to a grid.
{spot_item}	Defines the item in the point coverage that is to be used as the z-value for the interpolation.
{barriers}	Coverage containing arcs to be used as boundary in searching for input sample points.
{power}	Exponent of the distance. Controls the significance of surrounding points upon the interpolated value.
{SAMPLE}	A method for searching input points.
{num_points}	Number of nearest input sample points to be used.
{max_radius}	Maximum distance to limit search for the nearest sample points.
{RADIUS}	A method for searching input points.
{radius}	Distance specifying that all input sample points within this radius will be used
{min_points}	Minimum number of points to be used for interpolation
{cell_size}	The cell height or width
{xmin,ymin,xmax,ymax}	The boundary of the interpolation area

Table 7.1: Subcommands within the ArcInfo command IDW.

7.3.1 Cell Size

The most important parameter is the cell size, it has to be chosen first before generating the DEM. The cell size defines the resolution of the grid, and has influence on the presence of structures in the topography. A wider cell size will give a smoother (only low frequency), representation of the seafloor topography, whereas a smaller cell size also shows smaller structures (higher frequencies) in the topography. Aliasing effects, occurring when the cell size is too small, need to be reduced. These artificial structures occur because of wrong interpolation and extrapolation in no data areas [Christen, 1999]. Based on the data resolution, described in section 5.4, the cell size is chosen to be 100 meters. This cell size is small enough to represent smaller topographic features in the Eltanin Area with respect to the data quality.

7.3.2 Power of the Distance Weighting

In equation 7.2 and 7.3 the inverse distance weighting was presented. It can be concluded that the weighting factor r has strong influence on the representation of the modelled surface. The weighting factor controls the influence of the neighbouring points. A higher weighting factor (>2) will give the nearby data more influence and the data further away a lower weighting. It will make the surface less smooth. A smaller weighting factor (<2) will smooth the data because the data points further away will have more influence on the interpolated grid point [ESRI, 1999]. This is visualised in Figure 7.10 for a distance D of 500 meters, it shows the weights against the point distance. In this figure the violet line represents a weighting factor of 0.5, the blue line a weighting factor 1, and the yellow and pink line a weighting factor of 1.5 and 2, respectively.

These weights can be computed, with d_i the distance between the grid point and a data point and r the weighting factor, according the following equation:

(7.4) $$W_i = \left(1 - \left(d_i / D\right)\right)^r$$

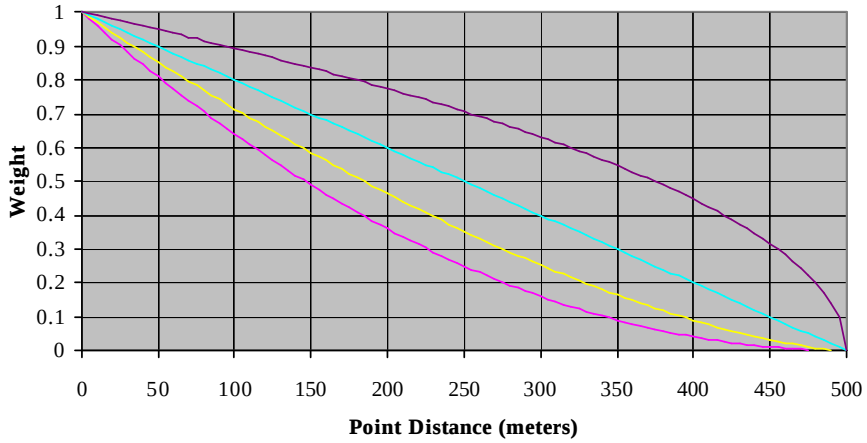

Figure 7.10: The weight depending on the point distance.

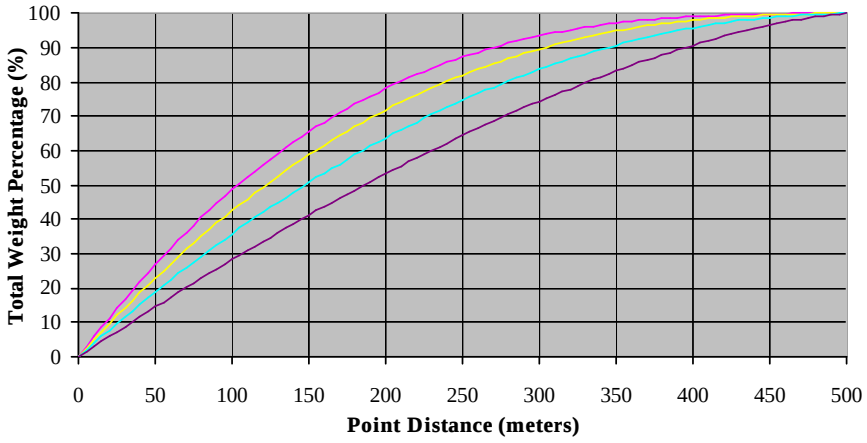

Figure 7.11: The total weight in percents depending on the point distance.

Figure 7.11 visualises the percentage of the total weight against the point distance. The colours in this figure correspond with the colours in Figure 7.10. As can be seen a higher weighting factor puts more emphasis on the neighbouring data points. For example 78% of the total weight is assigned to a distance less than 200 meters when a weighting factor of 2 is used, but this reduces to only 53 % with a weighting factor of 0.5.

This parameter effects the surface modelling of the Eltanin Area. To model the surface smoothly enough, in order to reduce the effects of the noise of the data, the weighting

factor had to be chosen smaller. The disadvantage that ridges and small topographic features will be smoothed or removed is more or less neglected because of the low data density, the data quality and the cell size of 100 meters. This is shown in Figure 7.12. The red lines show the 20 meter contour lines of the grid with a weighting factor of 0.5, the blue lines the contour lines generated of the grid with a weighting factor of 1.5.

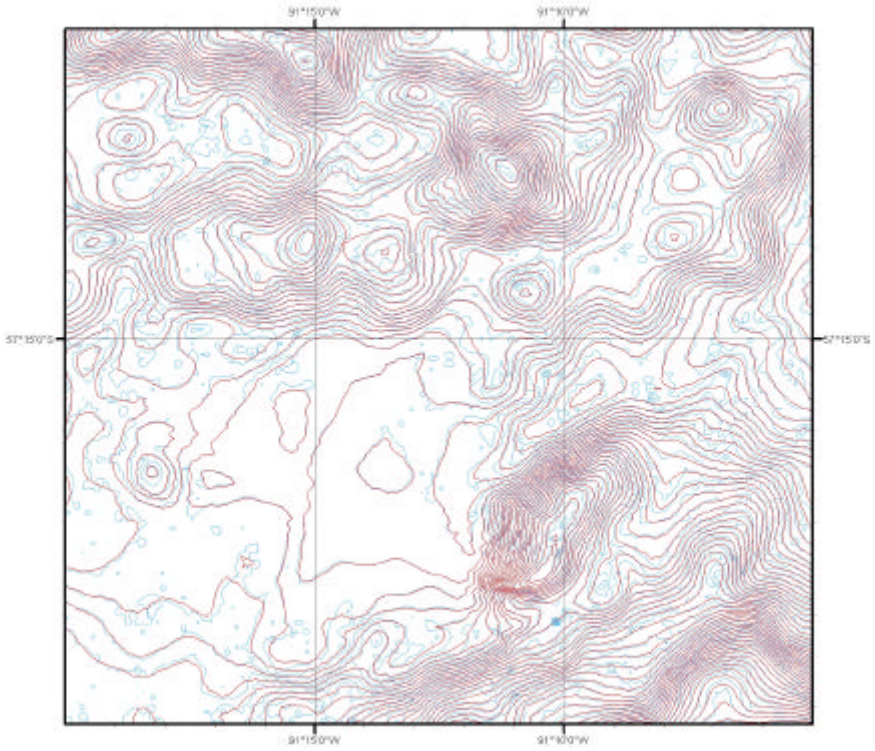

Figure 7.12: Contour lines (20 m.) of two grids with different weighting factor.

It can be concluded that the contour lines of the grid with factor 0.5 are smoother, but are located almost at the same location as the contour lines of the grid with weighting factor 1.5. This grid shows a lot of small contour lines, and they eventually show small topographic features. This however cannot be proved, because of the low data resolution and the data quality. Therefore these are classified as noise. Therefore a weighting factor of 0.5 will be used within the further analyses.

7.3.3 Method for Input Point Search

The IDW in ArcInfo has two different methods to search for input points. These are called the ‘sample’ and ‘radius’ method.

The ‘radius’ method uses as first parameter a specified search radius, and as second parameter a minimum number of points. The search radius is set to the specified radius, but will increase when the minimum number of input points is not available. In other words this minimum number of input points defines the actual search radius, but this radius will not be smaller than the user defined radius. This means that in areas of a very

low point density, this method will search for input points in a very large area. In areas without any data points the result will be an extrapolation.
The 'sample' method has as first parameter a number of input points, and as second parameter a specified search radius. The number of points is used as parameter to define the actual search radius. The actual search radius is, however, set to a user defined maximum radius. This means that the radius will never exceed the defined maximum, but will always be equal or smaller, depending on the number of input points. The advantage is that no extrapolation will be performed, and that the search radius depends on the point density.

A comparison of these two methods is visualised in Figure 7.13. The red lines in this figure represent the 20 meter contour lines generated out of the 'sample' grid, the blue lines are the contour lines of the 'radius' grid. In this figure the different methods show different results, especially in areas with a higher point density, as is expected. A comparison can be made with Figure 7.5 showing the point density.

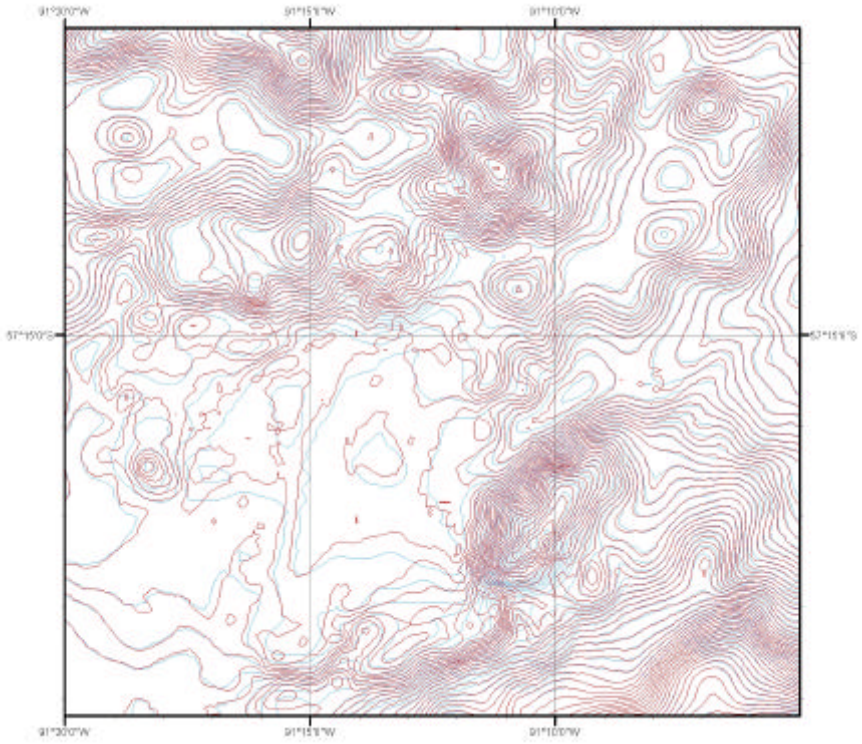

Figure 7.13: Contour lines (20 m.) of different methods for searching input points.

The difference between these two grids is visualised in Figure 7.14. The deep red and deep blue colours show large differences, more than 50 meters, between the two grids. Comparing the three Figures 7.5, 7.13 and 7.14, it can be concluded that the main differences occur at locations with a quickly changing point density and steeper slopes. This effect is shown in Figures 7.15, the contour lines represent the 'radius' grid (in Figure 7.13 shown in blue), and 7.16, the contour lines are generated by the 'sample' grid (shown in red in Figure 7.13). An explanation can now be given. At locations where steep slopes

rise out of the flat planes the point density plays an important role. When using the 'radius' method it can happen that, with a quick varying point density, a lot of points, within the minimal search radius, are weighted and effect the interpolation in a negative way. This is reduced when the search radius is chosen according to a specified number of input points.

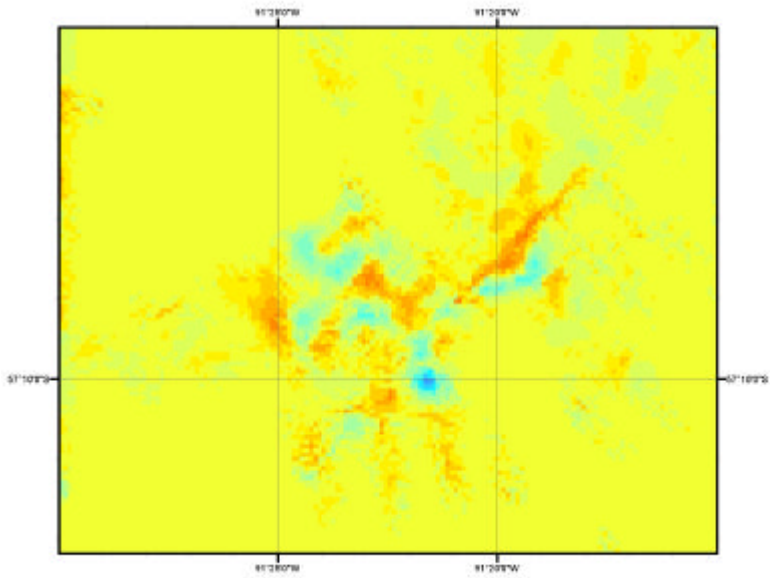

Figure 7.14: Difference between two methods for searching input points.

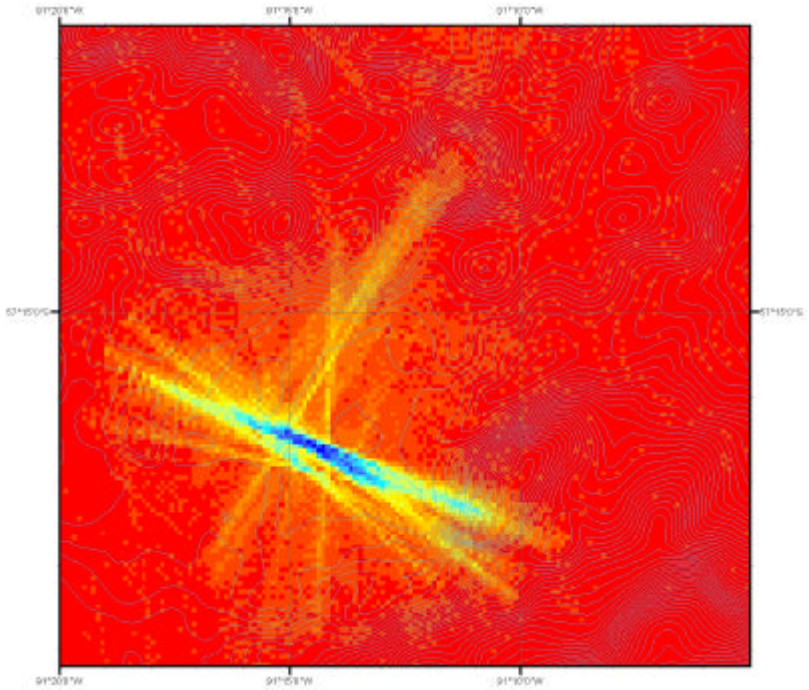

Figure 7.15: Contour lines (20 m.) from the 'radius' grid and the point density.

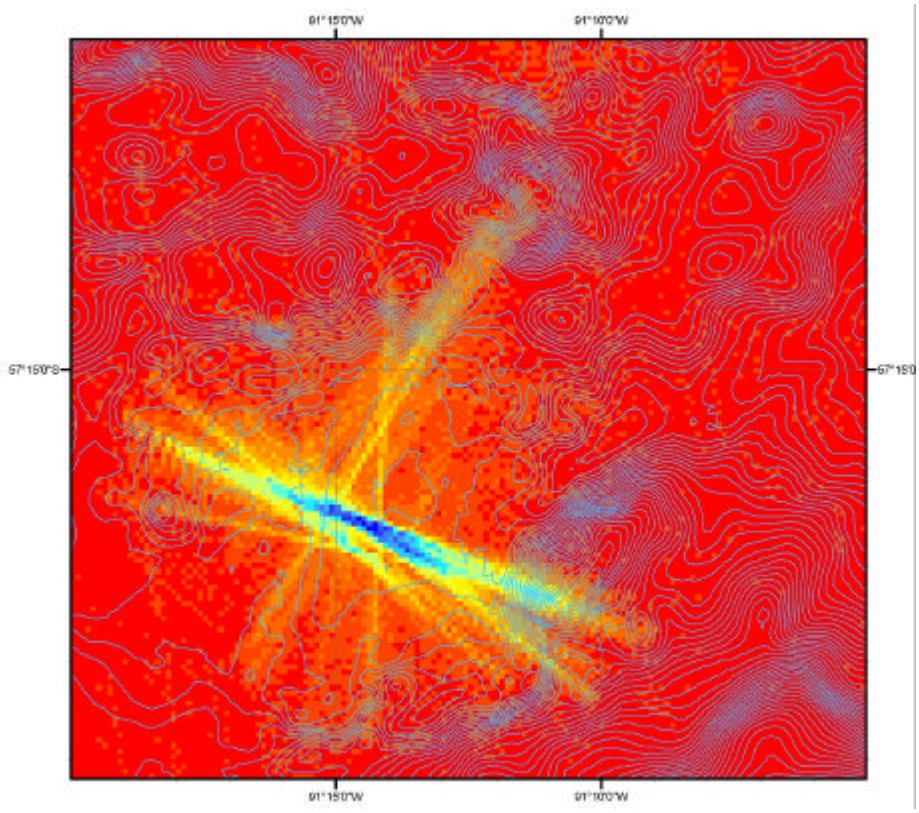

Figure 7.16: Contour lines (20 m.) from the 'sample' grid and the point density.

These two grids, based on the same dataset, are both a representation of the seafloor surface. However one of these modelled surfaces gives a wrong interpretation of the data. To test which grid represents the data in the best way, several methods can be used. It is, however, not possible to use other datasets with the same resolution and quality, so a method needs to be used that compares the original data with the modelled surface. A first approach to qualify the accuracy of the grids, is a comparison with the grid generated by DTM-fn which is discussed in the following subsections, correlation, scattergram, and contour lines. The second approach is to compare the grid with the original bathymetric data, this analyses is described in the subsection empirical standard deviation.

Correlation

To compare different grids with each other a correlation coefficient can be computed. The correlation coefficient can be computed with the following equation [Wackernagel, 1995]:

$$r_{zq} = \frac{\frac{1}{n}\sum_{i=1}^{n}(z_i - m_z)(q_i - m_q)}{s_z s_q} \qquad (7.5)$$

In this equation z and q are the data values for the different grids, m the mean, and s the standard deviations. The correlation coefficient lies between the values –1 and 1. If the

two data grids are identical the correlation coefficient will be 1, if this coefficient is –1 the grids are each other's opposite [Hengstum, 1995]. The correlation coefficients are given in Table 7.2. On the basis of these coefficients it can be concluded that the 'radius' grid differs only a little more from the grid generated by DTM-fn and the 'sample' grid gives the best correlation. The differences are however small, and it is difficult to make conclusions out of these results.

Grid 1	Grid 2	Correlation Coefficient
DTM-fn	'Radius' grid	0.99759
DTM-fn	'Sample' grid	0.99845

Table 7.2: The correlation coefficients between different grids.

Scattergram

A scattergram is the display of bivariate data or two data sets in a graph, on which the x-coordinates correspond to the values of one variable and the y-coordinates correspond to the value of the other variable [Isaaks, Srivastava, 1989]. It shows the correlation of the different data or data sets. If the data correlates which each other, the scattergram would create a line along $x = y$. If there is a discontinuity between the data sets a small point cloud is visible.
In Figure 7.17 the scatterplot of the two grids is visualised. The data follows the $x = y$ line but shows a strong discontinuity between –4400 and –4900 meters. This is at those locations were the largest differences are found in Figure 7.14. This confirms the conclusions that only one of these grids can fit the original bathymetric data in the best way. To know whether the 'radius' or the 'sample' grid is closest to the data, scattergrams are made showing these grids against the DTM-fn grid. These are shown in Figure 7.18 and 7.19. With these figures the conclusion can be made that the 'sample' grid has the most resemblance with the DTM-fn grid. The 'radius' grid shows the same discontinuity with the grid DTM-fn as with the 'sample' grid. The results presented by the correlation are therefore confirmed. Based on these scattergrams, and the assumption that the grid generated with DTM-fn fit the original bathymetric data and has a better accuracy, it can be concluded the 'radius' grid interpolates the bathymetric data at some locations erroneous.

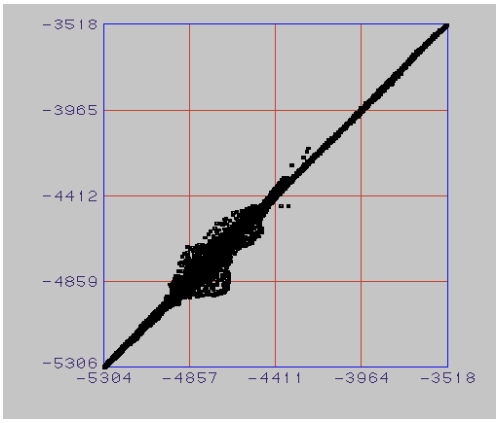

Figure 7.17: Scattergram of 'radius' grid (x-axis) against 'sample' grid (y-axis) (test area 1).

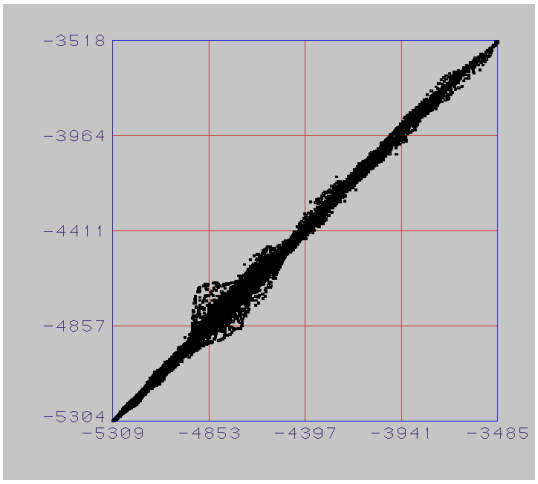

Figure 7.18: Scattergram of DTM-fn grid (x-axis) against 'radius' grid (y-axis) (test area 1).

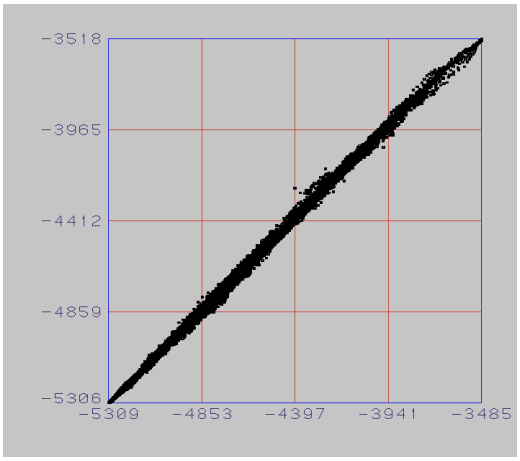

Figure 7.19: Scattergram of DTM-fn grid (x-axis) against 'sample' grid (y-axis) (test area 1).

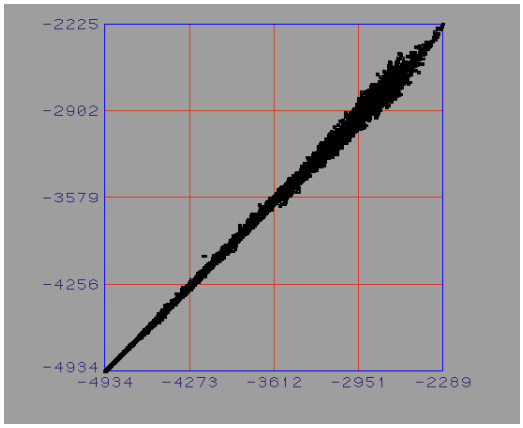

Figure 7.20: Scattergram of 'radius' grid (x-axis) against 'sample' grid (y-axis) (test area 2).

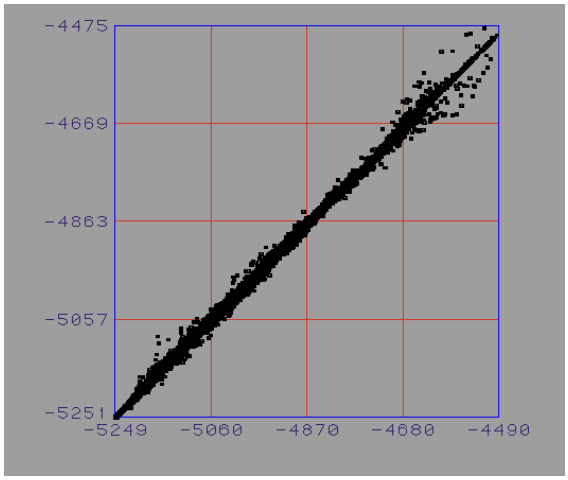

Figure 7.21: Scattergram of 'radius' grid (x-axis) against 'sample' grid (y-axis) (test area 3).

The scattergrams, shown in Figure 7.20 and 7.21, were made in the test area 2 and 3. The same effects are visible in these scattergrams, and the conclusion that these different methods for surface modelling give different results is confirmed. The surface modelling results are only compared with each other. In both figures the x-axis represents the 'radius' grid, and the y-axis the 'sample' grid.

Contour lines

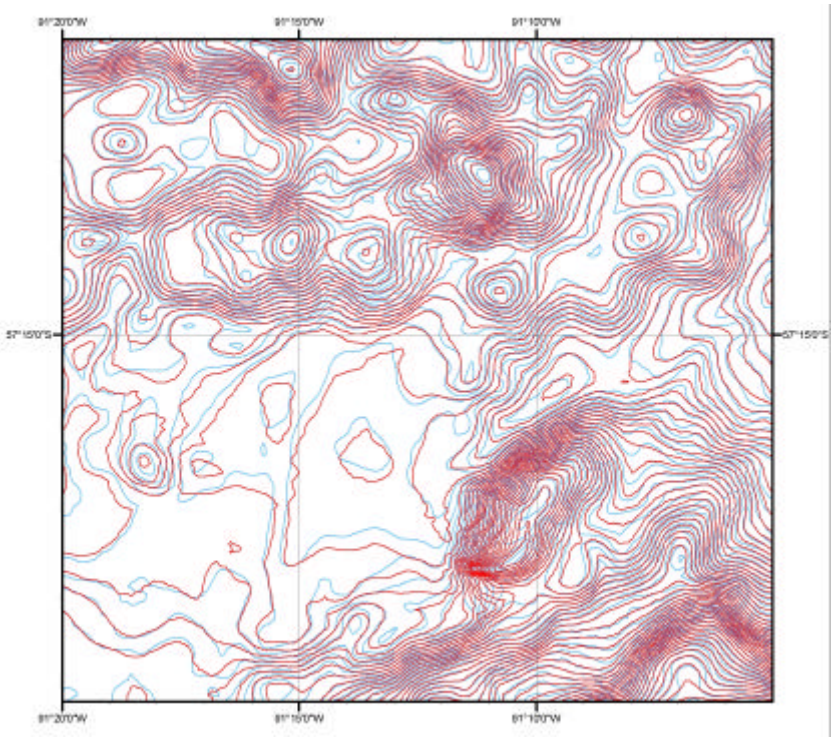

Figure 7.22: Contour lines (20 m.) from the DTM-fn grid (blue) and the 'radius' grid (red).

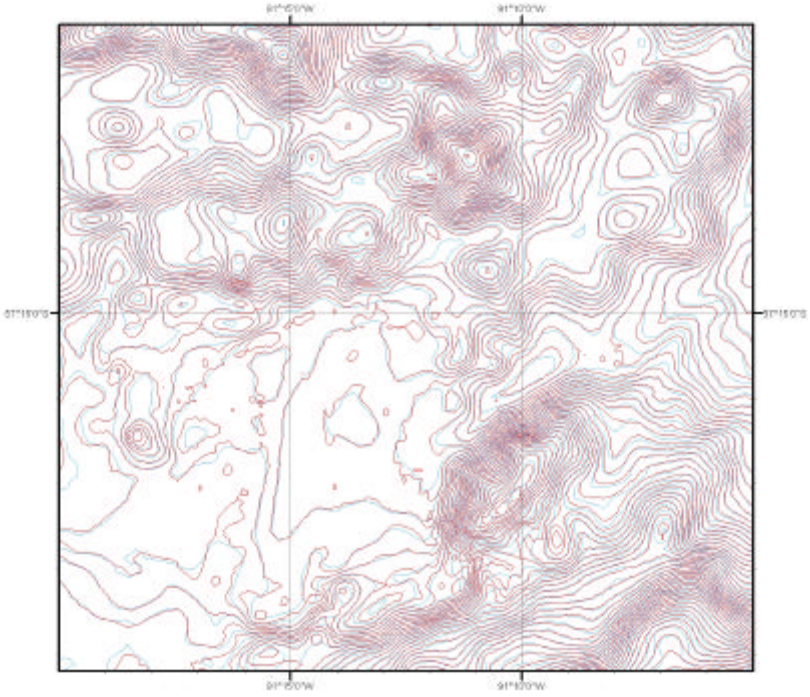

Figure 7.23: Contour lines (20 m.) from the DTM-fn grid (blue) and the 'sample' grid (red).

The contour lines generated out of the grids give a good visualisation of the surface, and can be compared with each other. With the conclusions made before, it can be expected that the contour lines generated from the DTM-fn grid differ strongly with the 'radius' grid, but are close to equal with the contour lines of the 'sample' grid. This expectation is confirmed with the Figures 7.22 and 7.23. In these figures the blue contour lines represent the DTM-fn grid, and the red contour lines represent the 'radius' grid and the 'sample' grid, respectively. Because the results of the 'sample' grid and the DTM-fn grid are almost equal, this 'sample' method for the IDW surface modelling will be further tested and discussed.

Empirical Standard Deviation

The modelled surface should represent the original bathymetric data. For a quality description of this modelled surface, these original data and the surface can be compared with each other. This is performed with the empirical standard deviation, given by [Hengstum, 1995]:

$$s_{emp} = \sqrt{\frac{1}{n-1}\sum_{i=1}^{n}\left(z_i - m\right)^2} \qquad (7.6)$$

For every grid cell this standard deviation is computed. The data points within one cell were used to calculate the mean, and the number of points (see Appendix E). The empirical standard deviation can be used as a method to compute the measurement accuracy, but will here also be used to analyse the different surface modelling methods. A

higher standard deviation indicates that the modelled surface does not fit well with the original bathymetric data, this can be both an effect of the original bathymetric data accuracy, and an erroneous interpolation. It can be expected that the mean of this empirical standard deviation will be around the bathymetric data accuracy, given in Table 3.1, and being, in optimal conditions, 0.5% of the water depth.
Because this data accuracy depends on the water depth it is useful to represent the empirical standard deviation as function of the water depth with the following equation:

$$s_{emp} = \frac{1}{d_{mean}} \left(\sqrt{\frac{1}{n-1} \sum_{i=1}^{n} (z_i - m)^2} \right) \times 100\% \qquad (7.7)$$

The mean depth at the grid point is given by d_{mean}, and is calculated out of the original data points, which should be more or less equal to the depth given by the surface modelling. The results of this empirical standard deviation are given in Figure 7.24 and 7.25. These histograms show the number of grid points that fall within a specified empirical standard deviation given as percentage of the water depth. It can be seen that the histogram in Figure 7.24 has a higher mean, and the basis of the histogram is wide. On the other hand, in Figure 7.25 the mean is lower and the basis of the histogram is smaller. These histograms also confirm the conclusion that the surface, modelled with the 'sample' method of the IDW, match the data points better than the surface of the 'radius' grid.

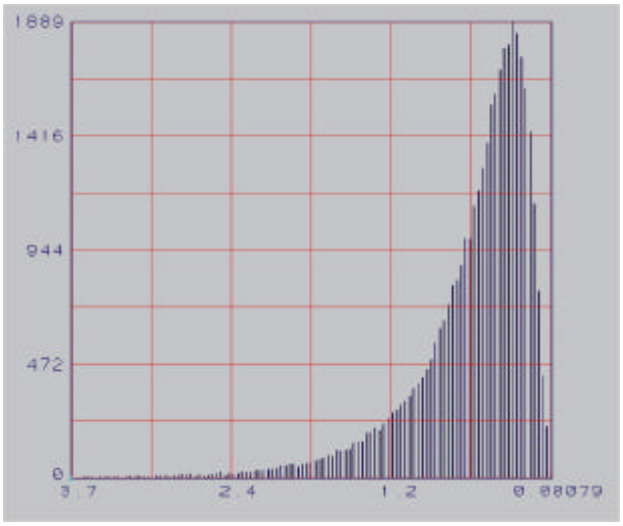

Figure 7.24: Histogram of empirical standard deviation for the'radius' grid.

These results are also listed in Table 7.3, where the mean and standard deviation of the histograms are given. The results for the grids within test areas 2 and 3 are listed in Table 7.4. Here only the 'radius' grid and the 'sample' grid are compared with each other. The mean of the 'sample' grid and the DTM-fn grid are almost equal to the expected data accuracy, in contrast to the mean of the 'radius' grid.

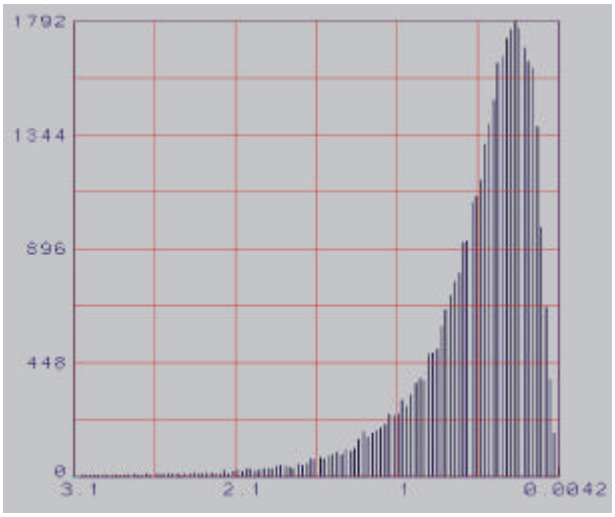

Figure 7.25: Histogram of empirical standard deviation for the 'sample' grid.

Grid	Mean	Standard Deviation
DTM-fn	-0.513	0.390
'Radius' grid	-0.610	0.483
'Sample' grid	-0.516	0.383

Table 7.3: The histogram coefficients of the different grids (test area 1).

Grid	Mean	Standard Deviation
'Radius' grid test area 2	-1,302	1,098
'Radius' grid test area 3	-0.409	0.277
'Sample' grid test area 2	-0.693	0.507
'Sample' grid test area 3	-0.378	0.253

Table 7.4: The histogram coefficients of the different grids (test area 2 and 3).

7.3.4 Number of Input Points

It was proven in the previous subsection, that the sample method for searching input points gave better results, according to the assumption that was made before, than the radius method for searching these points. Therefore the following tests for the surface modelling with IDW, are all based on this sample method.
The sample method has two parameters, listed in Table 7.1, that influence the surface modelling. These are the number of maximum input points and the search radius. Both will be shortly discussed and analysed.

Search Radius

The search radius will have an effect on the interpolation in smoothing the surface, as can be concluded from Figure 7.10 and 7.11. The search radius of 500 meters has proved to give the desired results, as given in the assumption which was made before. As can be seen in Figure 7.26 a larger search radius gives a more smoothing effect on the surface, especially in areas with a low point density. In this figure the blue lines represent the grid

with a search radius of 500 meters and the red lines the grid with a search radius of 750 meters. The search radius and the weighting factor are linked together. A smaller search radius will have almost the same effects on the contour lines as a higher weighting factor of the IDW. It is not possible to find the optimal combination of these two parameters. Only with the help of a visual interpretation of the grids and contour lines, a preference can be given. This preference is given to the combination of a search radius of 500 meters and a weighting factor of 0.5.

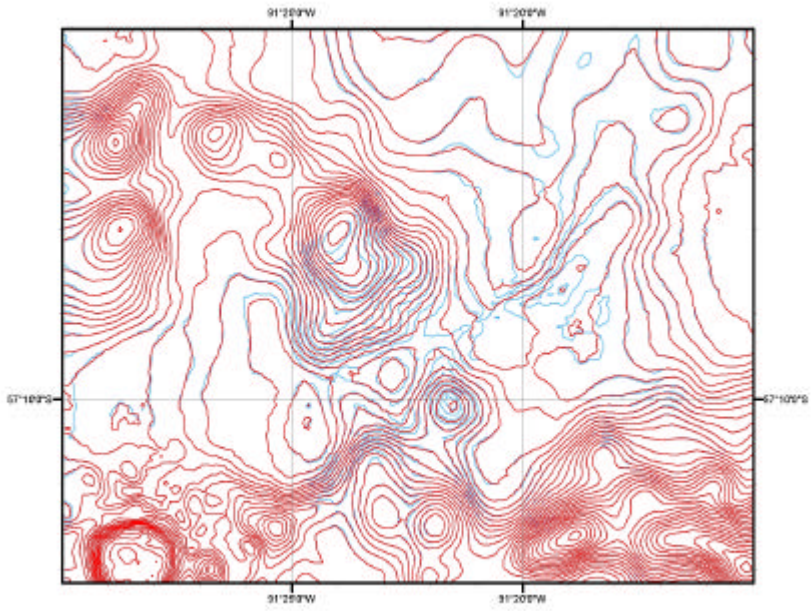

Figure 7.26: Contour lines (20 m.) representing two grids with different search radius.

Number of Points

The number of points that is used as a maximum for the surface modelling is chosen to be 100 points. This is based on a visual test and on the empirical standard deviation. The different contour lines in the different test areas are presented in Figure 7.27, 7.28 and 7.29. The blue lines represent the contour lines generated from the grid with a number of 75 input points, and the red lines from the grid with a number of 100 input points.
The effect of the number of points on steeper slopes is almost negligible, also because the point density in these areas is much lower. In areas with a higher point density the effect of the number of input points is visible, especially in flat areas. In these areas the noise, represented by the small contour lines, is more or less removed. Of course this has a negative effect on the empirical standard deviation. Because of a higher number of input points, noise has been reduced and the modelled surface will smooth the original data points more, decreasing the value of the empirical standard deviation. These effects are however very small in comparison with the effects of the method for searching input points. The results of the empirical standard deviation are listed in Table 7.5. As given in the assumption for the surface modelling, the noise has to be removed within the data quality, and therefore the choice was made to use a number of input points of 100.

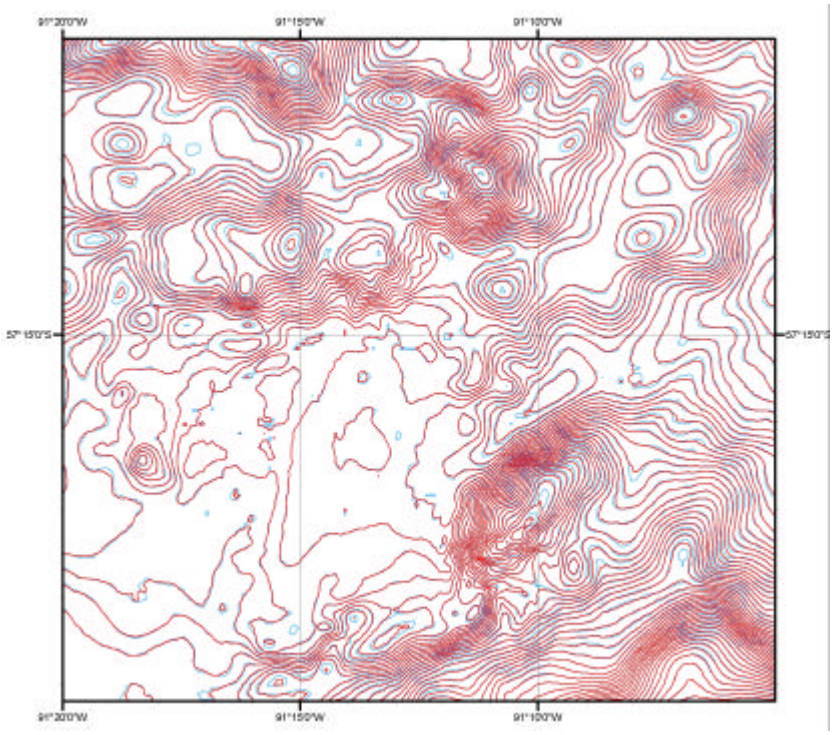

Figure 7.27: Contour lines (20 m.) representing different number of input points (test area 1).

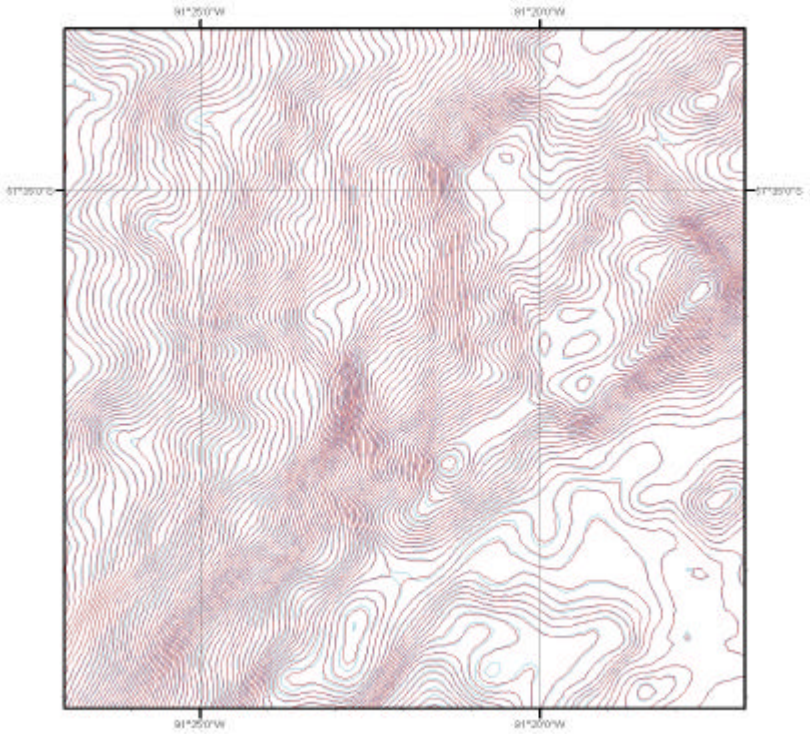

Figure 7.28: Contour lines (20 m.) representing different number of input points (test area 2).

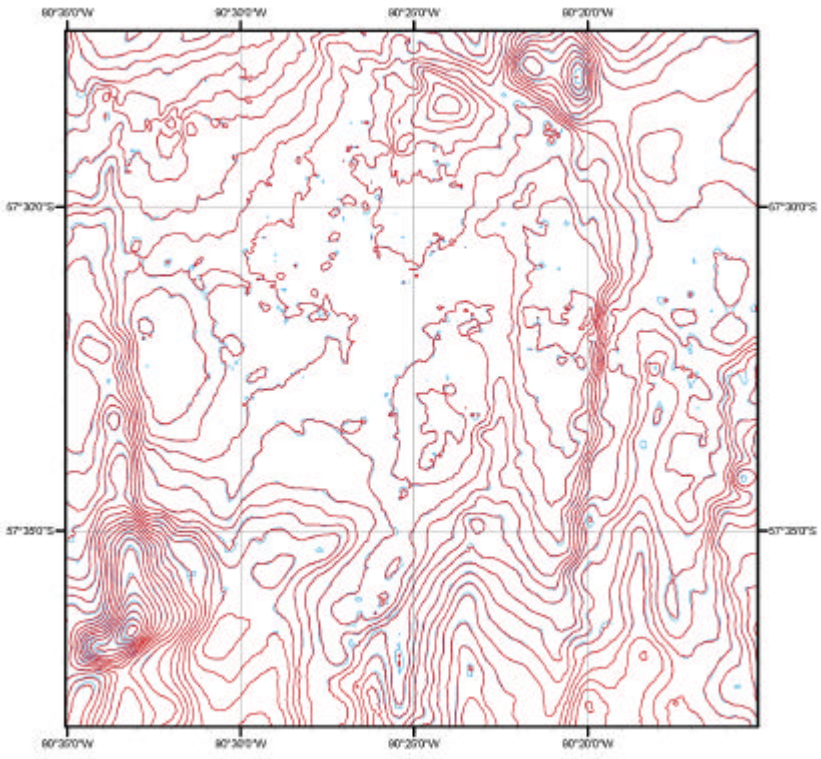

Figure 7.29: Contour lines (20 m.) representing different number of input points (test area 3).

From the scattergrams of these grids with different number of input points, visualised in Figures 7.30, 7.31 and 7.32, it may be concluded that no systematic effects occur. There are no discontinuities found, and the line $x = y$ is represented by all data combinations. Based on these figures, it can be concluded that an increasing number of input points only results in a surface smoothing. This has also some negative effect on the empirical standard deviation, see Table 7.5, but these differences are only small, and are pure a result of the surface smoothing.

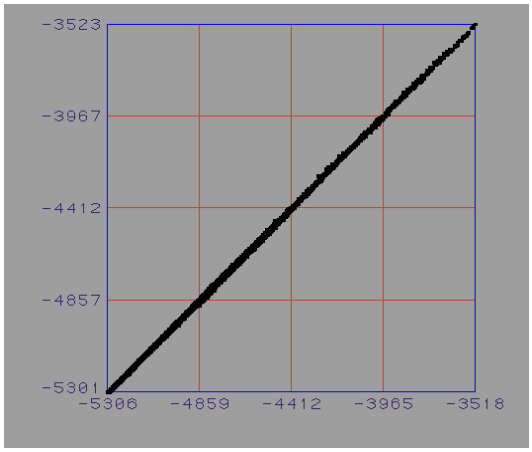

Figure 7.30: Scattergram of '75 point' grid (x-axis) against '100 point' grid (y-axis) (test area 1).

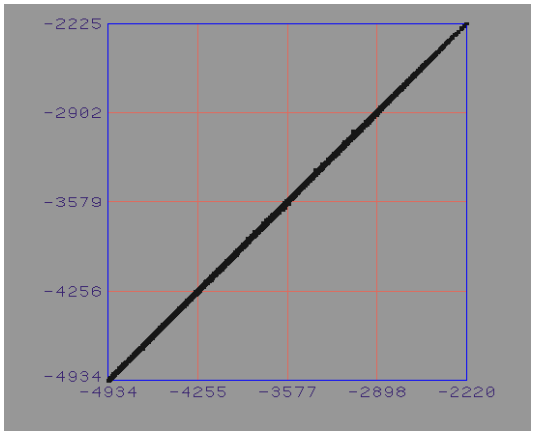

Figure 7.31: Scattergram of '75 point' grid (x-axis) against '100 point' grid (y-axis) (test area 2).

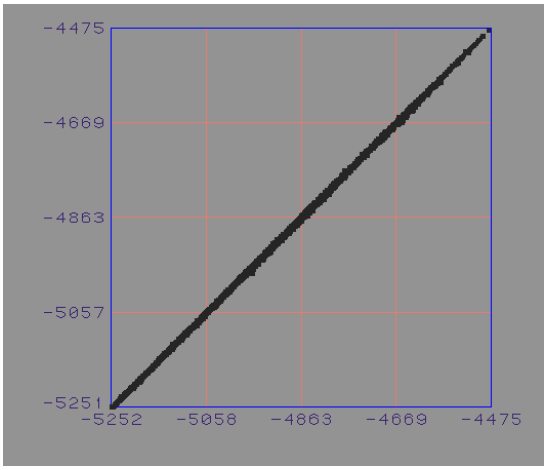

Figure 7.32: Scattergram of '75 point' grid (x-axis) against '100 point' grid (y-axis) (test area 3).

Grid	Mean	Standard Deviation
'75 point' grid test area 1	-0.516	0.383
'100 point' grid test area 1	-0.536	0.403
'75 point' grid test area 2	-0.693	0.507
'100 point' grid test area 2	-0.718	0.524
'75 point' grid test area 3	-0.378	0.253
'100 point' grid test area 3	-0.384	0.259

Table 7.5: The empirical standard deviation of grids with different number of input points.

7.4 Contour Line Smoothing and Noise Reduction

In the previous section the surface modelling using the IDW method in ArcInfo was discussed. This method gave, with adapted parameters, promising and good results. However the resulting grid still contained some small scale noise. This noise was especially present in flat regions and in regions with a higher point density. In regions with steeper slopes and larger scale topography this noise was not present or at least

could not be detected. This noise is found within the contour lines as small scale random patterns, or as solitary and small contour lines. In Figure 7.33 a region, within test area 2, is shown with a changing topography. The contour lines are all smooth and the noise can not be detected. The opposite is shown in Figure 7.34, here a flat region within test area 3 is shown. There are some small solitary contour lines, and the larger contour lines show random effects with some strange outliers.

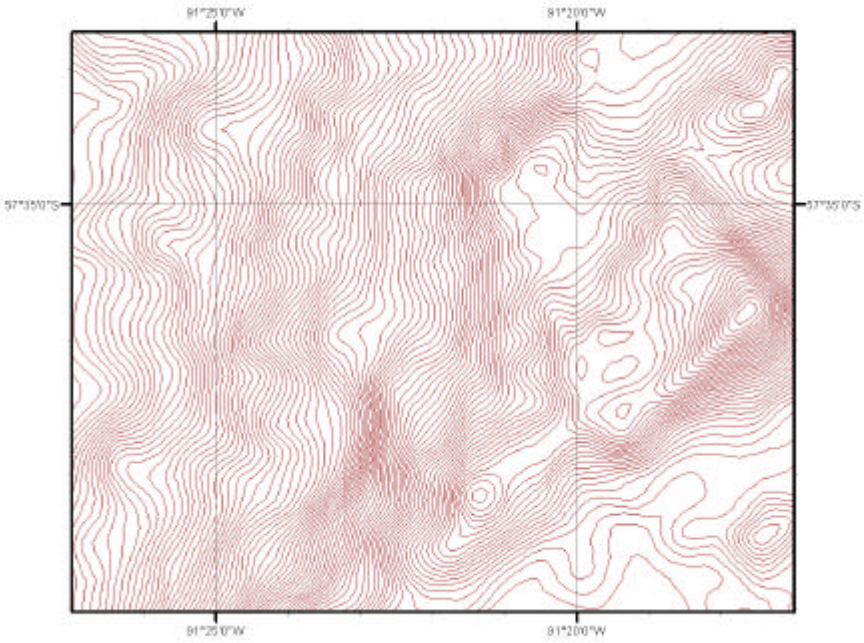

Figure 7.33: Contour lines (20 m.) in an area with topography within test area 2.

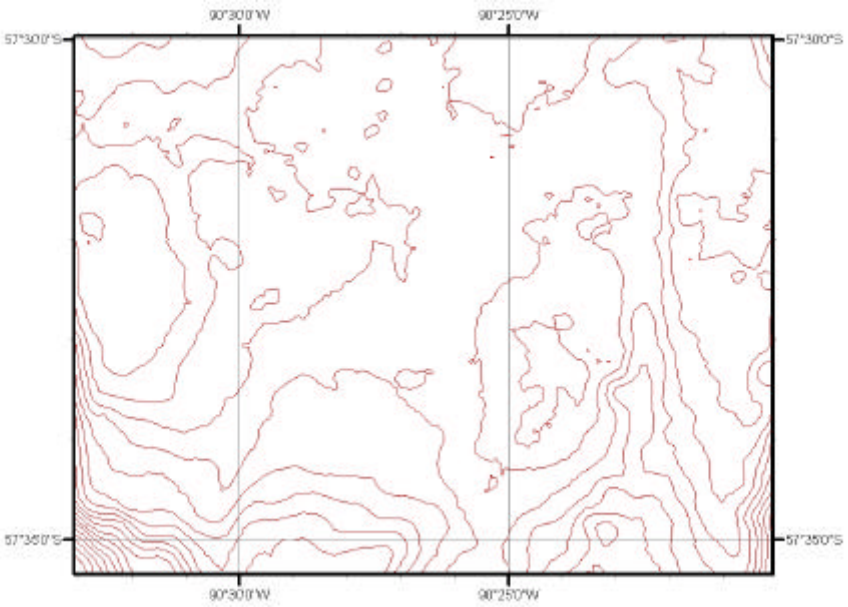

Figure 7.34: Contour lines (20 m.) in a flat area within test area 3.

These noise effects have to be reduced, to create smoother contour lines and a smoother grid. The method that is used is a slope-dependent filtering of the DEM, described in [Beyer et al., 2001], and has proven to give good results. This method is adapted to the situation in the Eltanin Impact Area with respect to the bathymetric data, and topography.

7.4.1 Slope-dependent Filtering

The assumption is made that the signal to noise ratio within flat areas is different from the signal to noise ratio within inclining areas. Therefore the DEM is split up in different slope classes and these slope classes are used to filter the DEM. The contour lines that are generated out of this filtered DEM will therefore be smoother and the noise will be removed.

Within the Eltanin Impact Area the slopes were classified in four classes. These classes, and their filters, are listed in Table 7.6. The filter size decreases depending on the slope to reduce the smoothing effect of the filters in areas of steeper slopes, as describe above. In areas with a very steep slope no filtering will be performed.

Class	Slope (%)	Slope (°)	Filter
1	< 5	< ~ 3	7×7 binomial
2	< 15	< ~ 9	5×5 binomial
3	< 30	< ~ 22	3×3 binomial
4	> 30	> ~ 22	None

Table 7.6: The slope classes with the used filter.

The binomial filter is chosen to decrease the influence of grid cells further away, but also to smooth effectively the DEM. This filter is widely used to reduce noise, and the basis is an averaging method with specific weights, depending on the position within the filter. The two dimensional binomial filter is computed according to the following equation [Jähne, 1989]:

$$(7.8) \qquad {}^{n}B_{kl} = \frac{1}{2^{2n}} \frac{n!}{(n/2-k)!(n/2+k)!} \cdot \frac{n!}{(n/2-l)!(n/2+l)!} \qquad k,l = -n/2,\mathrm{K}\ ,n/2$$

In this equation the binomial coefficient n is even, resulting in a filter dimension of $(n+1)\times(n+1)$. The used 3×3, and 5×5 binomial filter are given in the matrices 7.9 and 7.10.

$$(7.9) \qquad \begin{bmatrix} 0.5625 & 1.1250 & 0.5625 \\ 1.1250 & 2.2500 & 1.1250 \\ 0.5625 & 1.1250 & 0.5625 \end{bmatrix}$$

(7.10)
$$\begin{bmatrix} 0.09765625 & 0.39062500 & 0.58593750 & 0.39062500 & 0.09765625 \\ 0.39062500 & 1.56250000 & 2.34375000 & 1.56250000 & 0.39062500 \\ 0.58593750 & 2.34375000 & 3.51562500 & 2.34375000 & 0.58593750 \\ 0.39062500 & 1.56250000 & 2.34375000 & 1.56250000 & 0.39062500 \\ 0.09765625 & 0.39062500 & 0.58593750 & 0.39062500 & 0.09765625 \end{bmatrix}$$

A problem with this filtering procedure is found at locations where the topography changes within a short distance. This is found at flat mountain tops and at locations were a steep mount raises out of a flat plane. These extremes have to be separated, to prevent a strong smoothing at these locations, and to cut off mountain tops, or flatten slopes. Therefore every location in a specified neighbourhood is given the maximum value within that neighbourhood (maximum neighbourhood filter). That neighbourhood is chosen equal to the maximum size of the slope-dependent filter, 7×7 grid cells.
In the Figures 7.35 - 7.40 the original slope classes and the slope classes after the maximum slope is computed within the neighbourhood, are visualised for test area 1, test area 2, and test area 3, respectively. The grey tones correspond with the classes given in Table 7.6, with light grey class 1, and black class 4. It can be seen that the extreme regions are now classified by other slope classes to prevent them from smoothing.

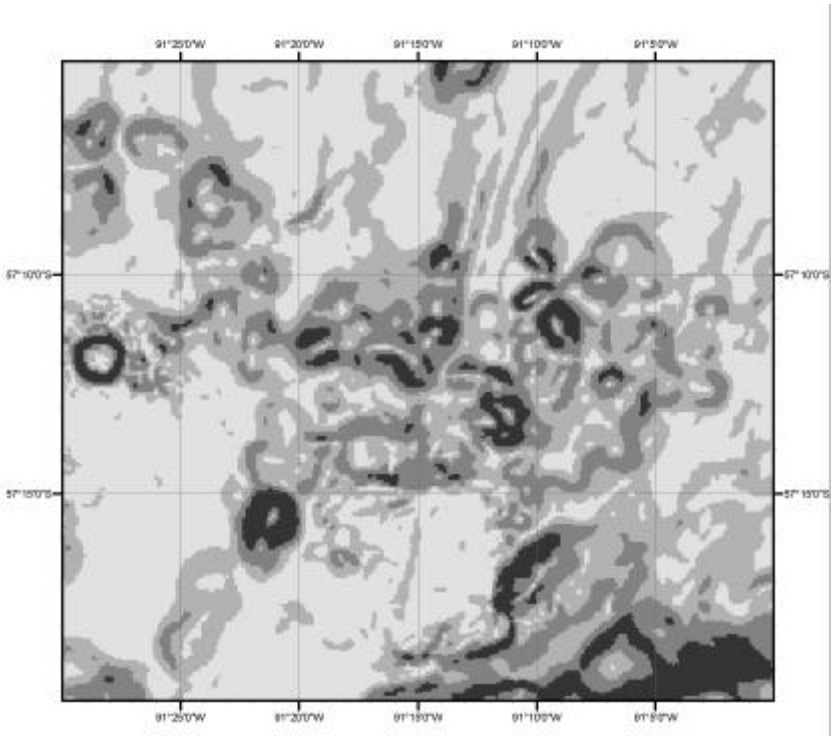

Figure 7.35: Slope classes within test area 1.

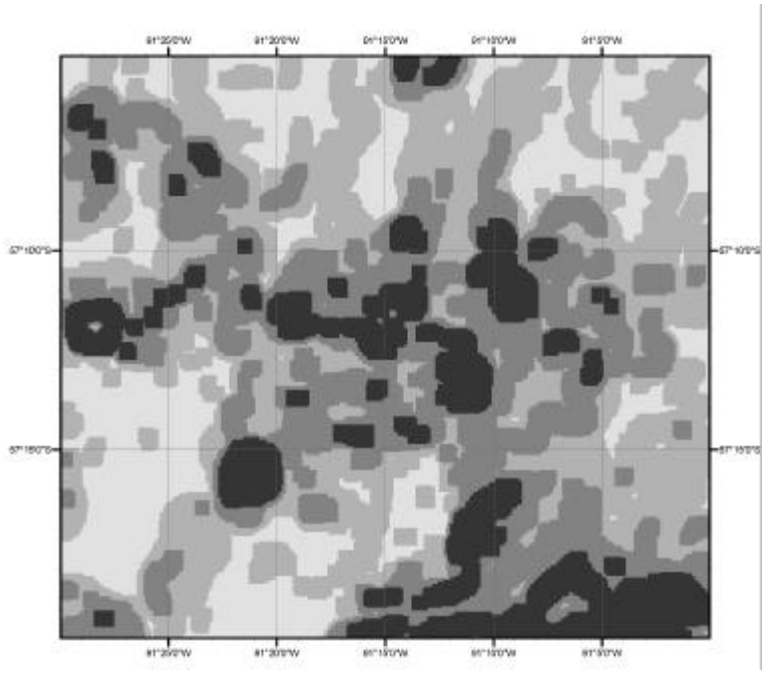

Figure 7.36: Slope classes after maximum neighbourhood filter within test area 1.

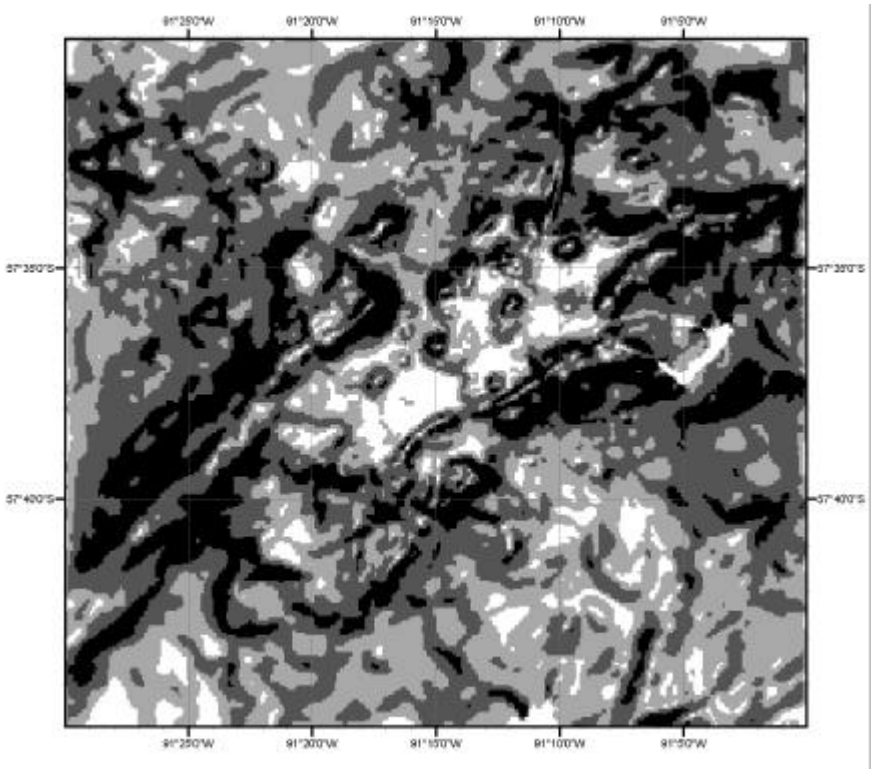

Figure 7.37: Slope classes within test area 2.

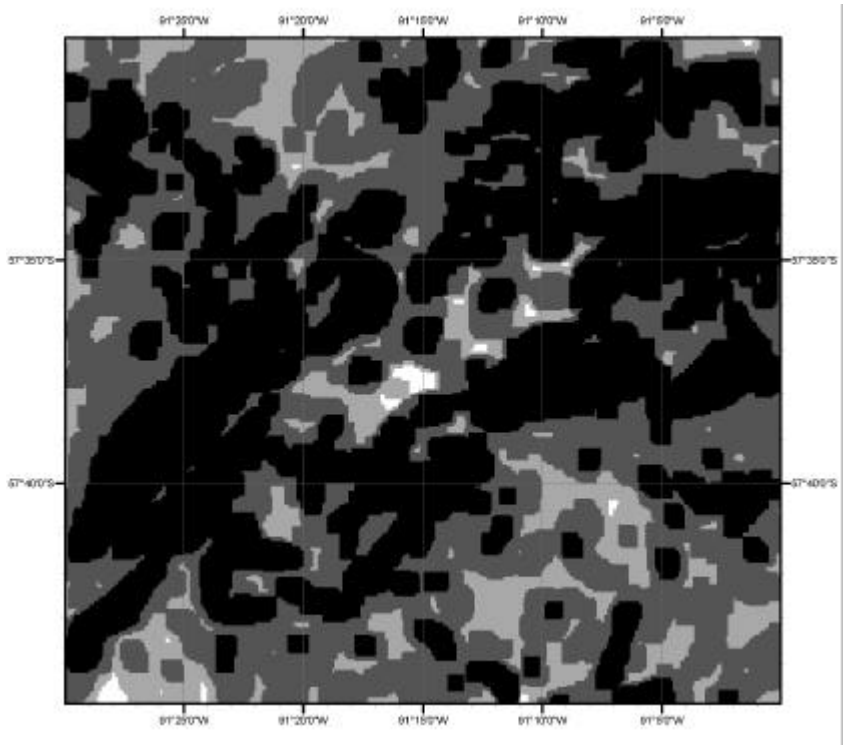

Figure 7.38: Slope classes after maximum neighbourhood filter within test area 2.

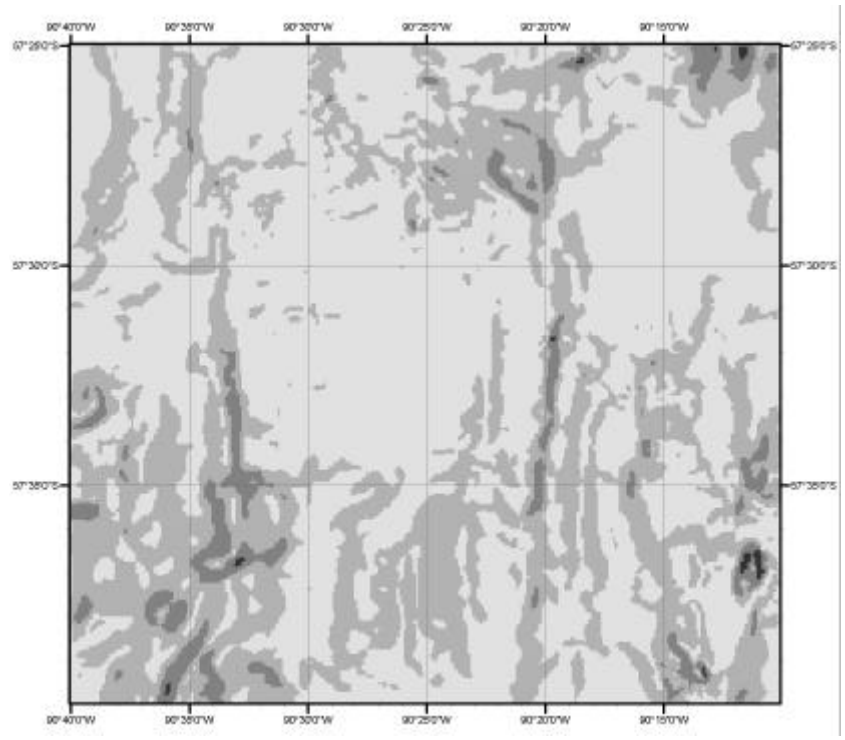

Figure 7.39: Slope classes within test area 3.

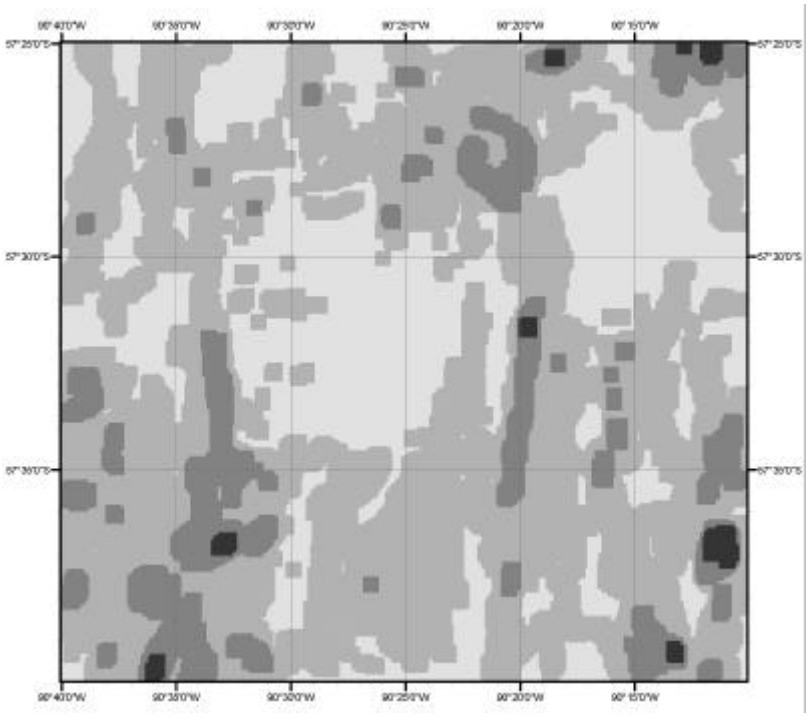

Figure 7.40: Slope classes after maximum neighbourhood filter within test area 3.

7.4.2 Results on Contour Line Smoothing and Noise Reduction

The slope depending filtering of the DEM gave very good results. These are visualised in Figure 7.41, 7.42 and 7.43. The red lines correspond with the contour lines generated using the filtered DEM, the blue lines are the original contour lines.

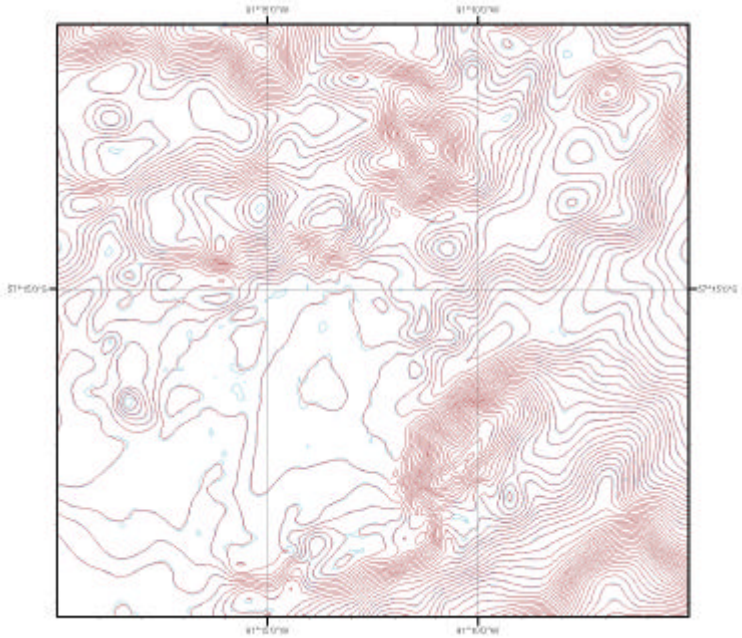

Figure 7.41: Contour lines (20 m.) from the filtered and original DEM (test area 1).

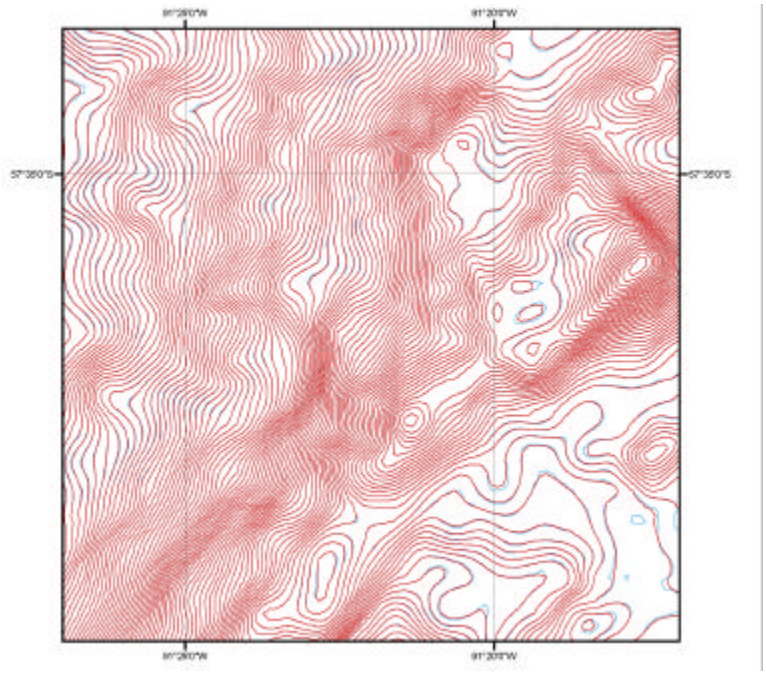

Figure 7.42: Contour lines (20 m.) from the filtered and original DEM (test area 2).

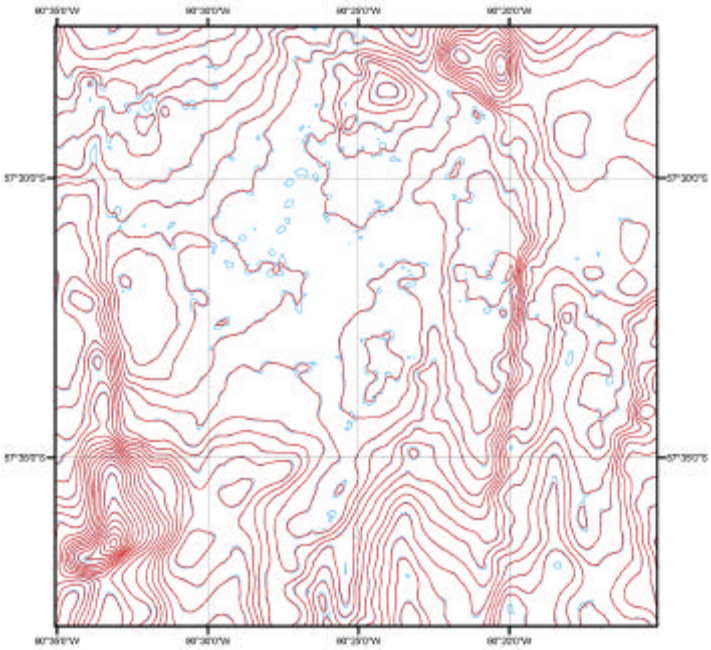

Figure 7.43: Contour lines (20 m.) from the filtered and original DEM (test area 3).

Almost all the noise was reduced, and the contour lines were smoothed very accurately. The contour lines are located almost at the same position as in the original DEM, but the random patterns, that are visible in Figure 7.34, are removed. The mountain tops, or steep slopes are not flattened, because of the maximum neighbourhood filtering.

7.5 Conclusions after Testing

The assumption made in section 7.2 for the surface modelling was:
The modelled surface has to fit the original data in the best possible way, with the assumption that the noise does not influence the modelled surface. This means that an acceptable smooth surface has to be modelled within the measurement accuracy.

The surface modelling in ArcInfo with the IDW method has proved to be very useful to create such a DEM. Different parameters could be used to change the results of this method. The best results were found with the following ArcInfo command, compare with Table 7.1:

<grid name> = idw(<coverage>, <item>, <boundary coverage>, 0.5, sample,
100, 500, 100, <xmin>, <ymin>, <xmax>, <ymax>)

The analyses of the results of the surface modelling were based on three different methods. The first method was a comparison with another surface modelling program used at the AWI, the second method used the empirical standard deviation to compare the original bathymetric data with the modelled surface. The visual analyses of the contour lines and the scattergrams formed the third method, and in this case, without the possibility to compare the DEM with other data, was a very important method.
The modelled surface was afterwards filtered depending on the slope, to remove the remaining noise and to smooth the contour lines. For this filtering different sizes of binomial filters were used. Before the filtering, to prevent flat mountain tops and steep slopes from being flattened, a maximum neighbourhood filter was used to classify those regions in another class. This method proved to be very successful and effective.

The data resolution and data quality in the Eltanin Impact Area is very inhomogeneous, affecting very strongly the surface modelling. In for example more structured area the quality of the modelled surface, according to the empirical standard deviation, decreases. This is of course a result of the low point density in these areas. As expected the outer beams give a higher empirical standard deviation, due to the lower data quality of these points. This is visualised in Figures 7.44, 7.45, and 7.46 for the test areas 1, 2, and 3, respectively. In these figures standard deviations of more than 1% of the water depth are visualised. A higher standard deviation results in a darker shade of grey. In these figures possible systematic effects would be visible between the different data sets. However, no systematic effects of special kind could be found, but only the effect of the location of the points within the swath. At locations with a dense distribution of points with a high standard deviation, also a high amount of data points were found.
No systematic effects between the different data sets of ANTXII/4 and ANTXVIII/5a was found, but at some locations there might be a small difference between these datasets. An explanation of this is that during the data editing and cleaning the different datasets were not combined with each other and were not compared to remove errors between them.
An example can be found in test area 2, in Figure 7.45, were a small point cloud can be found at one location. These effects are however not systematic, and therefor the decision was made to remove all the points with a standard deviation of more than 2 % of the

water depth during the surface modelling of the Eltanin Impact Area, described in the next section.

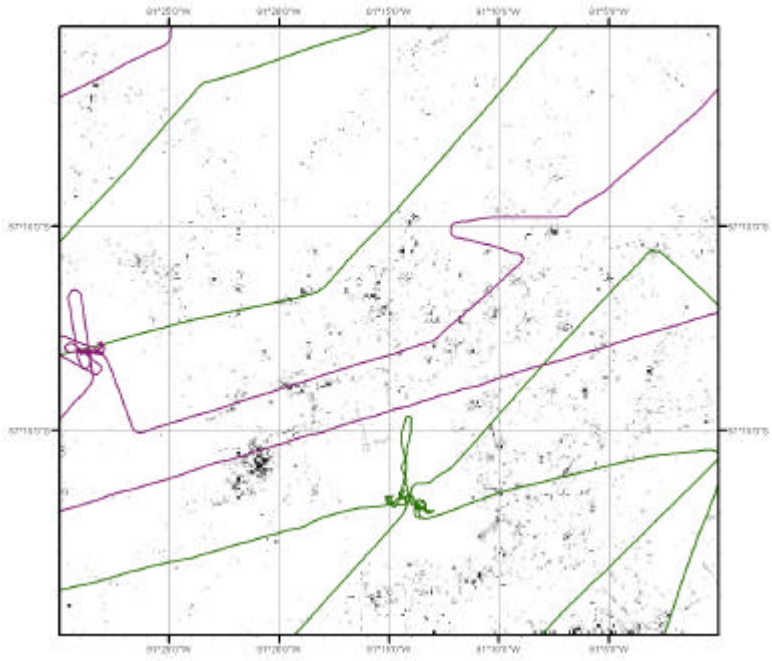

Figure 7.44: Locations with a higher empirical standard deviation (test area 1).

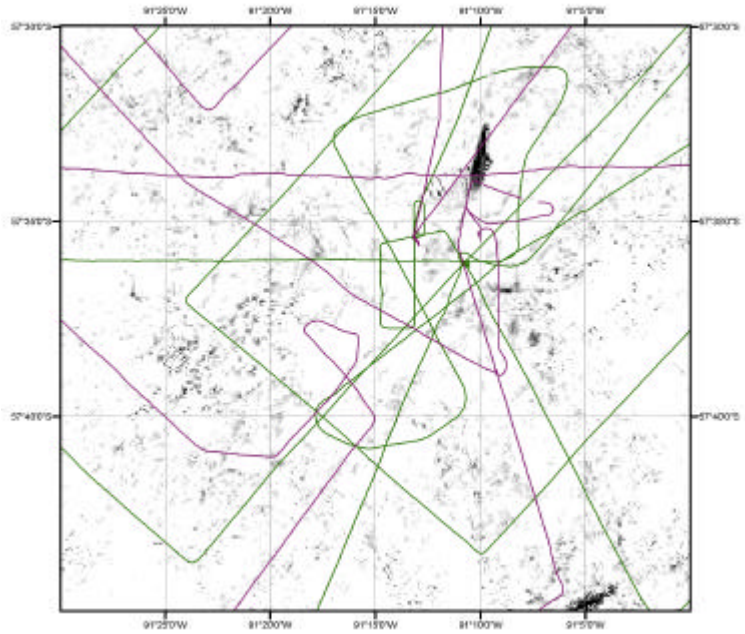

Figure 7.45: Locations with a higher empirical standard deviation (test area 2).

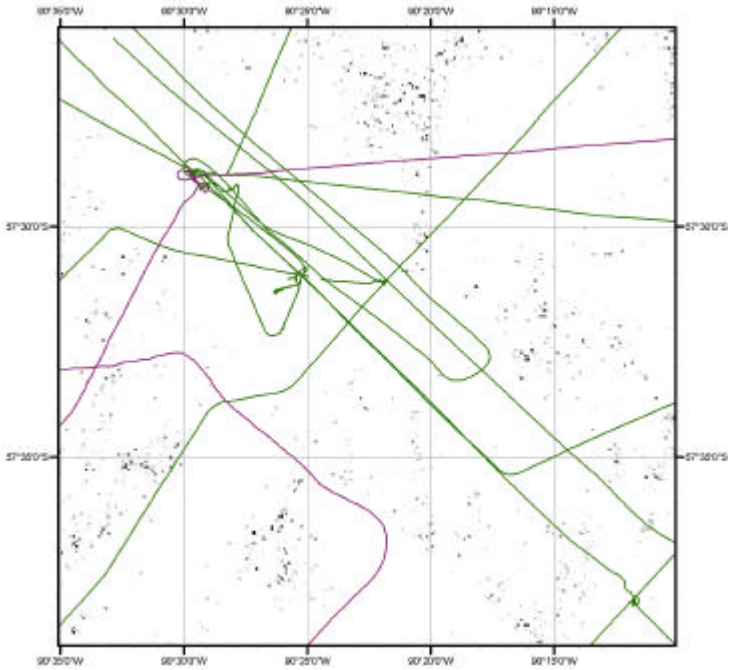

Figure 7.46: Locations with a higher empirical standard deviation (test area 2).

7.6 Surface Modelling: The Eltanin Impact Area

The results of the surface modelling test within the three test areas were used to determine the best method for generating a DEM of the whole Eltanin Impact Area. In this section the different steps from the point data to the final grid are described:

- Defining the area and map projection
- Surface modelling with the IDW method in ArcInfo
- Slope-dependent filtering
- Removing extrapolated data

7.6.1 Mapping Area and Map Projection

The selected mapping area for the Eltanin Impact Area was bounded in the north, south, east and west by 56° 50 S, 58° 00 S, 90° 10 W, and 92° 20 W, respectively. This area was chosen because of the almost 100% data coverage within the centre, at the San Martin Seamount, and because the geologically most interesting area is located at the northern flanks of the Seamount and in the northern abyssal plane. For the DEM this area was extended in each direction with 10 minutes of arc to prevent possible systematic errors at the boundaries.

For this area the conformal Mercator projection was used. The parameters for this projection are listed in Table 7.7. The standard meridian and parallel were chosen in the centre of the area to realise almost the same scaling effect in all directions. The coordinates for the boundaries are listed in Table 7.8.

Units	Meters
Z Units	Meters
Datum	WGS84
Standard meridian	91° 15’ 00 W
Standard parallel	57° 25’ 00 S
False scaling	0.0000

Table 7.7: The parameters for the used Mercator projection.

Geographic	Mercator (meters)
56° 50’ 00 S	-65098.9958
58° 00’ 00 S	65098.9958
90° 10’ 00 W	-4151318.6526
92° 20’ 00 W	-4281260.4588

Table 7.8: The coordinates of the Eltanin Area boundaries.

7.6.2 Inverse Distance Weighting

The IDW method that was used to model the Eltanin Area was based on the results given in section 7.4. The different parameters with their value are listed in Table 7.9.

Parameter	Value
{power}	0.5
Input point search	SAMPLE
{num_points}	100
{max radius}	500
{cell size}	100
{xmin, ymin} {xmax, ymax}	-75100, -4300100 75100, -4133000 (meters)

Table 7.9: The IDW parameters for the Eltanin Area.

After a first surface modelling the empirical standard deviation was computed. As written in section 7.5, the data points with a standard deviation of more than 2% of the water depth were removed to improve the DEM of the Eltanin Area. The total amount of original bathymetric data points within the extended Eltanin Area was 4.231.736, and after removing the erroneous data points still 4.209.745 data points were left, a decrease of only 0.5%. These cleaned data were used for a new surface modelling with the IDW method.

7.6.3 Slope-dependent filtering

The surface modelled with the IDW was used to create slope classes. As described in section 7.4 first a maximum neighbourhood filtering was used to prevent mountains and steep slopes from being flattened. The slopes were classified as listed in Table 7.6.

7.6.4 Removing Extrapolated Data

At the locations where no bathymetric data was available, the IDW method extrapolated within the maximum search radius. At these locations the data of the DEM had to be removed, because extrapolation results in an erroneous surface modelling. Therefore another grid was computed with a maximum search radius of 200 meters. Only the cells within a no-data value were replaced in the DEM.

7.6.5 Quality of the DEM

The steps described before resulted in the final DEM. For a quality description of this DEM the assumption that was made before has to be kept in mind.

This assumption can be proved with the empirical standard deviation, described in section 7.4. The result of the histogram of the empirical standard deviation is shown in Figure 7.47. This histogram shows the quality of the DEM of the Eltanin Impact Area with respect to the original bathymetric data.
The mean of this histogram is at 0.511 % of the water depth, according to the system accuracy, see Table 7.10. This means that it was possible to create a DEM within the quality of the original bathymetric data. After analysing the results of this empirical standard deviation, the conclusion can be made that the outer beams have a higher standard deviation and have an accuracy that is worse than the centre beams. An obvious explanation for this quality loss, is the changing path of the signal through the water layer. The path of the signal at the outer beams is almost 40% more than the path of the signal at the centre beams.

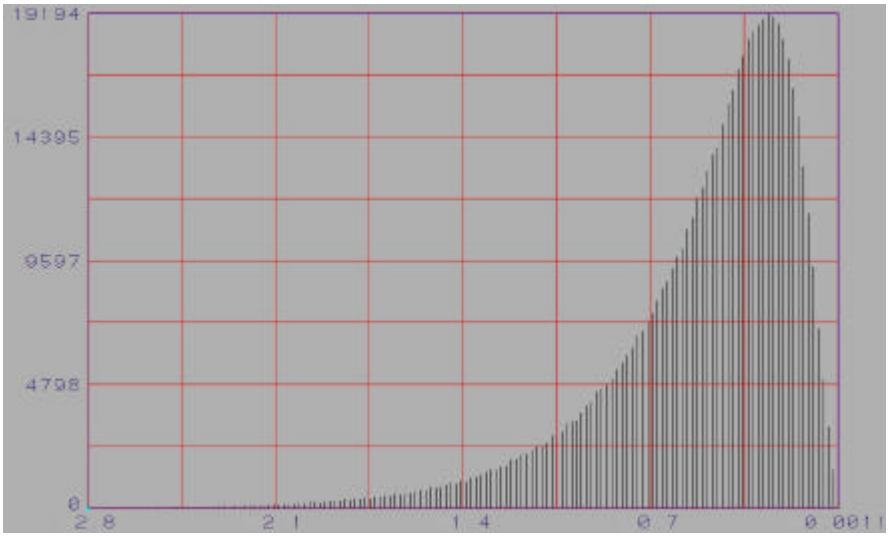

Figure 7.47: Histogram of empirical standard deviation of the Eltanin Impact Area.

Eltanin Impact Area	0.511
System Accuracy	0.5

Table 7.10: Empirical standard deviation of the Eltanin Impact Area and the system accuracy in % of the waterdepth.

8. Mapping the Eltanin Impact Area

The DEM of the Eltanin Impact Area can be used as basis for modelling, analysing and displaying the topography related phenomena. Some of the, widely used, operations on DEM's are already listed in Chapter 7, for example slope and aspect. These can be used for example within oceanography, biology, geophysics, and geology.
In this chapter different operations and products will be discussed. In section 1 the, for bathymetry important, derivation of contour lines are discussed. The final bathymetric mapping will be described in section 2. This mapping is performed with ArcMAP, a subprogram of the extensive Geographical Information System ArcGIS, developed by ESRI. The data of the Eltanin Impact Area, used within this master research, can be used as basis for a GIS, this is shortly described in section 3. A very useful program for displaying the DEM, Fledermaus, is described in section 4.

It is within this written thesis not possible to present the computer based results, but the data can be found on the CD-rom that is attached to this thesis (see also Appendix F).

8.1 Contour line generation and editing

For the contour line generation in ArcInfo the following command, within grid was used:

<contour coverage name> = contour(<output grid name>, interval, 20, 0)

The interval of the contour lines was chosen to be 20 metres. This interval could be used because of the grid smoothing, described in section 7.4. A smaller interval would result in contour lines that not represent the quality of the DEM and the accuracy of the bathymetric data. It would result in a too optimistic and a too detailed representation of the seafloor. A larger contour interval would result in a loss of topographic information.

These contour lines had to be verified, and at some places contour lines were removed or added for a better cartographic product. The removed contour lines were found at locations without redundant information within the DEM. An example is given in Figure 8.1. The red and blue lines represent the original contour lines, but the red lines are the removed contour lines.
At some special locations contour lines were added. At these locations a visual extrapolation was used to connect contour lines. This is shown in Figure 8.2. The red lines represent the original contour lines, the blue lines the extrapolated contour lines.

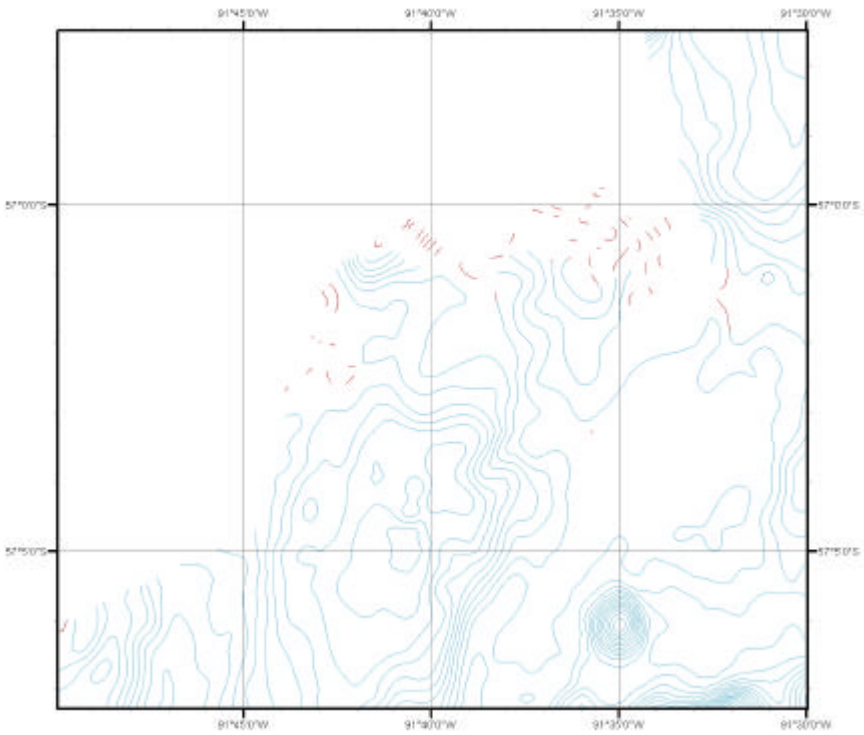

Figure 8.1: Contour line editing, original and removed (red) contour lines.

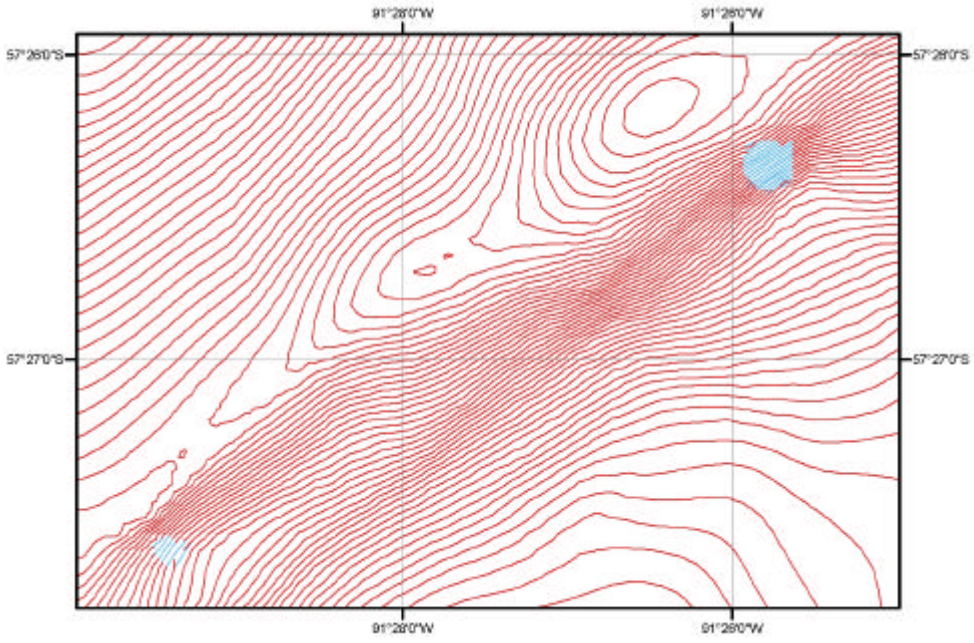

Figure 8.2: Contour line editing, original (red) and extrapolated (blue) contour lines.

8.2 Mapping using ArcMAP

These contour lines were used to create three different coverages for the bathymetric mapping. These coverage are listed in Table 8.1.

Coverage Name	Content
Contour 20	20 meter contour lines
Contour 100	100 meter contour lines
Contour polygon	1000 meter polygons

Table 8.1: Coverages derived from the contour lines.

Each contour line representing a depth of $X \times 100$ meters is extracted into the arc coverage 'contour 100'. The arc coverage 'contour 20' contains the four contour lines between each 100 meter contour line. The polygon coverage 'contour polygon' contains the polygons built from the contour lines representing every 1000 meter. The polygons that are created within the Eltanin Area are listed in Table 8.2, with the colour code.

Polygon Name	Depth Interval (meters)	Colour (CMYK)
2030	-2000 … -3000	20 7 0 0
3040	-3000 … -4000	25 9 0 0
4050	-4000 … -5000	30 11 0 0
5060	-5000 … -6000	35 13 0 0

Table 8.2: The polygons within the polygon coverage.

The maps of the Eltanin Impact Area were created on a scale of 1:100 000, in four map sheets with a contour interval of 20 meters. The extensions of these map sheets are shown in Figure 8.3. The yellow polygons with grey boundary define each map sheet, numbered form 1 to 4.
Overview maps were created on a scale of 1:200 000 and 1:500 000, with contour intervals of 100 meters. These map products of the Eltanin Impact Area are listed in Table 8.3.

Eltanin Map Name	Scale	Page Size
Map Sheet 1	1:100 000	A0
Map Sheet 2	1:100 000	A0
Map Sheet 3	1:100 000	A0
Map Sheet 4	1:100 000	A0
Overview	1:200 000	A0
Overview	1:500 000	A3

Table 8.3: The bathymetric map products.

The lay out of the maps is according to other bathymetric maps published at the AWI. The 1:100 000 maps show on the left hand side, first the title and legend, followed by some notes about data sources and references. Two small scale maps finally show information about the ship tracks, the geological stations and the overview of the map

sheets. The overview map shows the same legend and notes, but only one small scale map with the track information.
The text of the notes about data sources and references are formulated as follows:

Data sources:
Hydrosweep Multibeam data collected during RV 'Polarstern' cruises ANTXII/4 1995, and ANTXVIII/5a, 2001.

Multibeam surveys:
R. Hagen, V. Kodagali, M. Ulrich (ANTXII/4); S. Gauger, M. Jacops, R. Krocker (ANTXVIII/5a).

Data cleaning and editing:
M. Jacops, using CARIS/HIPS 5.1 developed by Universal Systems Ltd.

DEM modelling and contour generation:
M. Jacops, using ArcInfo developed by ESRI.
Gridding is performed with a grid spacing of 100 meters.
Contouring, based on the DEM, is performed with an interval of 20 meters.

Cartography:
M. Jacops, using ArcGIS, developed by ESRI.

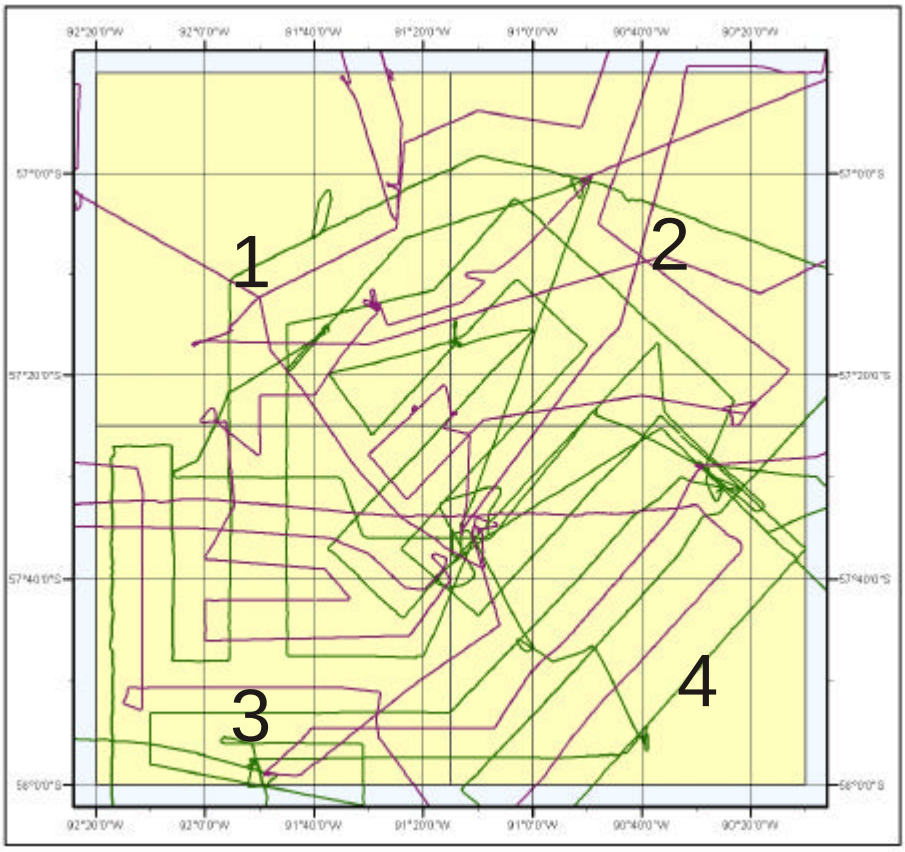

Figure 8.3:The extensions of the map sheets of the Eltanin Impact Area.

8.3 A GIS-basis of the Eltanin Impact Area

ArcGIS, and especially ArcMap, can be used for mapping. But the GIS functionality for analysing geographic data, can also be used. Therefore a basis was created in ArcGIS.
Different products and useful geographic information about the Eltanin Impact Area, used within this master research, were combined together within this program, these are:

- Geological stations of ANTXVIII/5a
- Geological stations of ANTXII/4
- Track lines of ANTXVIII/5a
- Track lines of ANTXII/4
- Contour lines 20 meter
- Contour lines 100 meter
- Contour polygons 1000 meter
- DEM grid
- Backscatter segmentation grid
- Backscatter information ANTXVIII/5a
- Incidence angle ANTXVIII/5a
- Backscatter information ANTXII/4
- Incidence angle ANTXII/4
- Data density grid
- Data quality grid
- Slope grid
- Aspect grid

These different datasets, is transformed into these using ArcInfo. These coverages were converted into layers using ArcToolbox and ArcCatalog within ArcGIS. These created layers can be used within different tools of ArcGIS. First in ArcMap for editing, mapping, and visualisation. Second within ArcScene for 3D-analyses with the functionality 3D-analyst. And last of course again within ArcInfo.

8.4 DEM Visualization in Fledermaus

The 3D-visualization program 'Fledermaus', developed by Interactive Visualization Systems Inc., provides a set of tools to prepare data for, and to perform interactive 3D visualisation. It allows one to assemble and explore a virtual 3D world containing many possible object models, such as surfaces, volumes, density fields and cross-sections. The software is very useful for the display of geographic data [Interactive Visualizaion Systems Inc, 1999].
The DEM of the Eltanin Impact Area is converted to a grid in 'Fledermaus' to be able to fly through the Eltanin Impact Area. Results can be found on CD-rom and in Figure 8.4 and 8.5, showing the San Martin Seamount seen from the south and from the north, respectively.

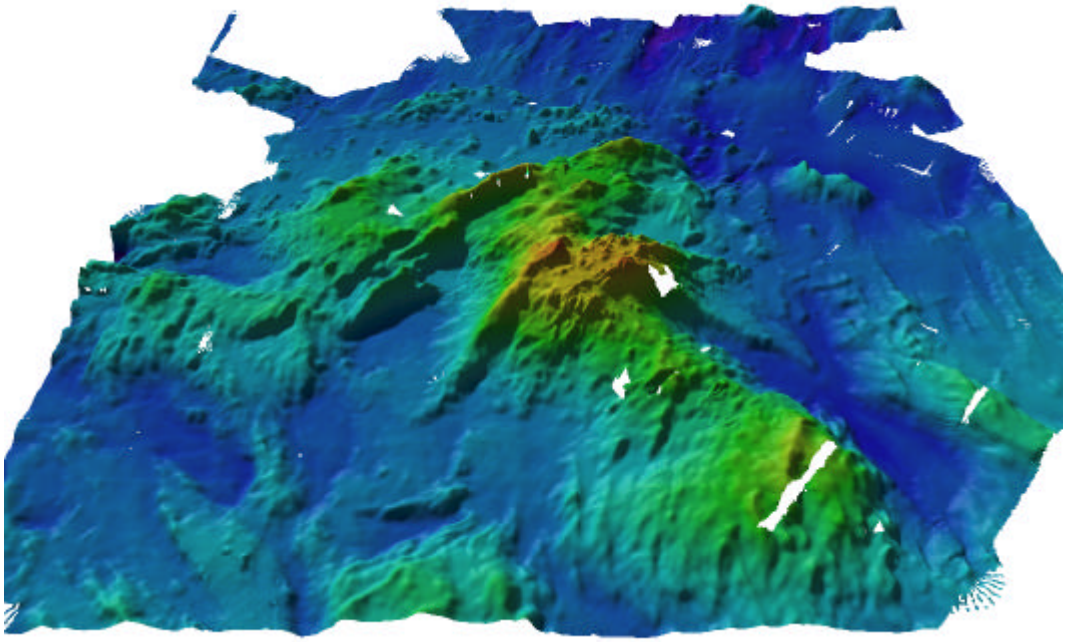

Figure 8.4: The Eltanin Impact Area seen from the south.

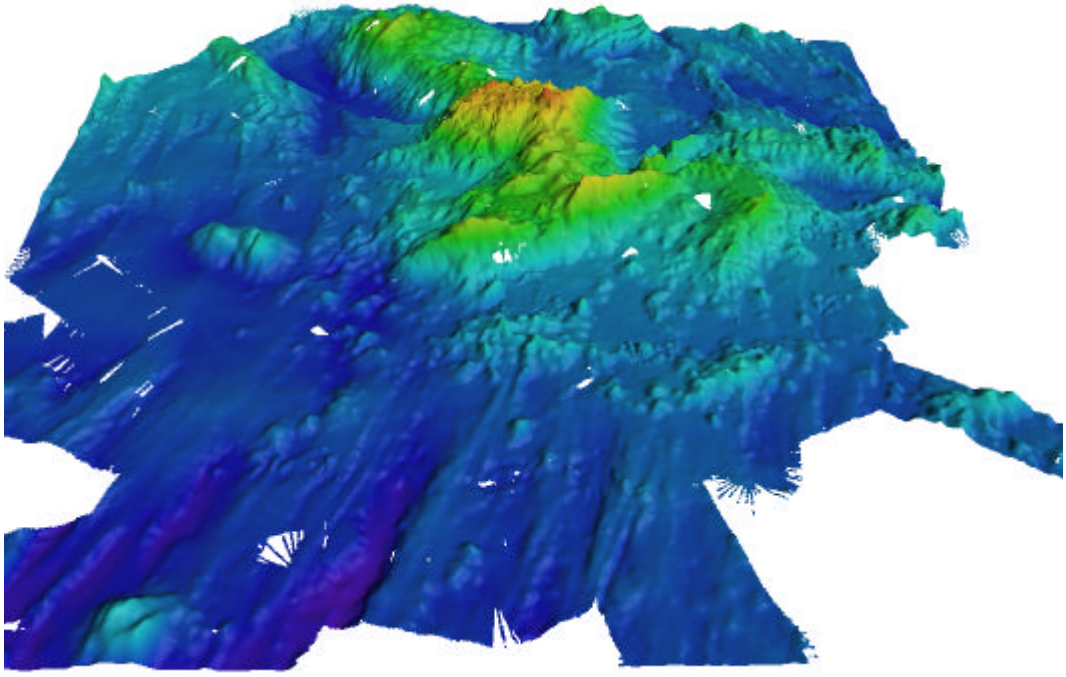

Figure 8.5: The Eltanin Impact Area seen from the north.

9. Backscatter Analyses

Multibeam systems were originally designed for measuring the depth of the ocean floor for bathymetric charts. Especially the ocean geo-scientists preferred also to collect other information that could be extracted out of the multibeam measurements, for example about the physical properties of the seafloor. This information can be extracted from the amplitudes of the returned signal, being backscatter and pseudo sidescan data. The upgrade of the Hydrosweep system on RV 'Polarstern' in 1994 consisted not only of an increasing of the swath width from 90° to 120° but also made it possible to collect sidescan sonar data and to measure backscatter strengths.
Analyses of these backscatter strengths is presented in this chapter. First, in section 1, a short introduction on backscatter is given, followed by section 2 with a description of the backscatter measurement of the Hydrosweep system and the computation of the backscatter strengths afterwards. Section 3 discusses the available backscatter data of the expeditions ANTXII/4 and ANTXVIII/5a. The analyses of the backscatter data of expedition ANTXVIII/5a and the segmentation of this data is described in section 4. Finally in section 9.5 a comparison will be made between the bathymetry, the backscatter data, and the segmentation results.

9.1 Backscatter at the Ocean Floor

In this section a short introduction is given in the backscattering at the ocean floor. A detailed description of the physical theory falls beyond the scope of this thesis and will not be discussed. For further reading [Urick, 1983], [Clay, Medwin, 1977], [Moustier, 1986] and [Moustier, Alexandrou, 1991] are advised.

9.1.1 Backscattering at the Sea Floor

For a plane wave interacting with a flat water/sediment interface, with different acoustic impedances (see section 2.1), the normal incidence reflection R_0 is given by (9.1), with c is the speed of sound and r the density of the mediums [Moustier, 2001].

$$R_0 = \frac{r_s c_s - r_w c_w}{r_s c_s + r_w c_w} \tag{9.1}$$

With (9.1) the conclusion can be drawn that the amount of acoustic energy that is transmitted into the sea floor depends on the impedance contrast. This means a low impedance contrast gives higher penetration, and a higher impedance contrast gives a lower penetration.
The ocean floor surface is however not flat but has some roughness. This roughness, or small scale topography, giving small elevation differences, causes phase shifts on the

reflected wave, also influencing the reflection of the signal. This phase difference Δj , due to an elevation difference Δz , relative to a mean plane, is given by [Moustier, 2001]:

(9.2) $$\Delta j = 2k(\Delta z \cos q)$$

In this equation k is the wave number, see also equation (2.8), and q is the incidence angle. This phase shift is also visualised in Figure 9.1 [Urick, 1983].

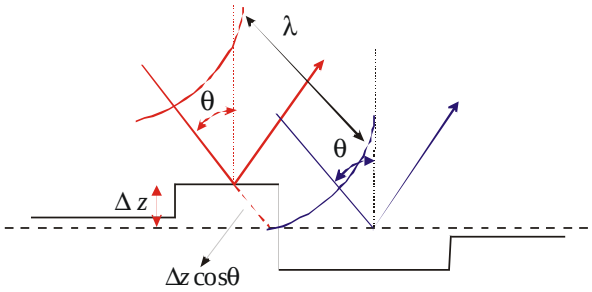

Figure 9.1: Surface roughness effect.

The roughness of the surface can be described with the Rayleigh parameter, with s the root-mean-square displacement of the rough surface, defined as [Brekhovskikh, Lysanov, 1990]:

(9.3) $$P = 2ks\cos q$$

This parameter shows the scattering of a signal due to the roughness of the surface. A Rayleigh parameter much smaller than 1, scatters sound slightly and most of the sound energy propagates into the specular direction. Roughness causing considerable sound scattering in a relatively wide angular interval, correspond with a Rayleigh parameter greater than 1. However this scattering depends on the wavelength and it can be concluded that a surface that appears rough to short wavelengths, will appear smooth to long acoustic waves.

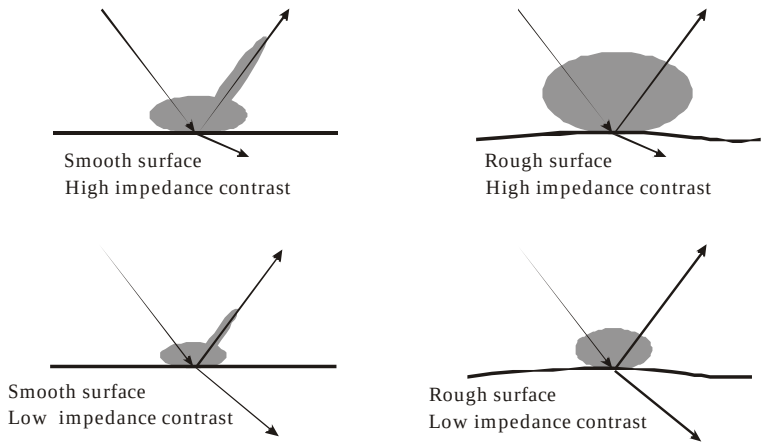

Figure 9.2: Echo patterns for different conditions of surface roughness and impedance contrast.

It can be concluded that the scattering at a rough surface is a combination of the contributions due to the impedance contrast at the interface and to the scale of the roughness of the interface relative to the acoustic wavelength. This is visualised in Figure 9.2. In this figure different echo responses are shown for different conditions of surface roughness and impedance contrast [Urick, 1983].

However for a full model one should also consider scattering from within the volume of the sediment. This is not discussed anymore within this thesis, also because the dominant determining characteristic is, in most of the cases, the surface roughness.

9.1.2 Backscattering Strength

A sound pulse with an acoustic intensity *I* transmitted at a range *R* above a sea floor area, and incidence angle q will result in an intensity of the backscattered signal, at a reference distance from the surface, by [Jackson et al, 1986]:

$$I_s = I\frac{As(q)}{R^2} \tag{9.4}$$

In this equation A is a patch of seafloor reached by the pulse, $s(q)$ is the backscatter coefficient, which is a dimensionless quantity which accounts for the acoustic backscatter per unit area per unit solid angle.
The surface scattering strength in decibel units is than given by [Caruthers, 1977]:

$$\text{Backscatte r strength} = 10\log(s(q)) \tag{9.5}$$

The equation (9.4) is a simplified expression of the backscattered signal. More precisely the backscatter strength has to be specified taking into account other aspects, as there are the transducer characteristics, and range dependent effects, for example transmission loss due to absorption, The backscatter strength is then in a specific direction expressed as [Moustier, Alexandrou, 1991]:

$$S(q) = 10\log\left\{I^{-1}\int_{Á}\frac{I_s(j)R^4 10^{2a_w R/10}}{b(q,j)b'(q,j)}dA\right\} \tag{9.6}$$

The beam pattern of the source is given by $b(q,j)$, and the beam pattern of the receiver is given by $b'(q,j)$. The seawater absorption coefficient for a particular angle is a_w, and in this equation I_s is the scattered intensity integrated over the element area dA.

9.1.3 Variation with Incidence Angle and Bottom Type

With the previous equations in mind, it can be easily concluded that the scattering strength from a particular sea surface depends on the incidence angle of the acoustic wave. Actually all bottom types have their own particular response curves for a given frequency. It is therefore possible to classify backscatter strengths with respect to their

roughness. For different bottom types and different frequencies, models are used to compute the backscatter strength. For more details see [Jackson et al., 1986].
Functions showing the backscatter strength as function of the incidence angle are shown in Figure 9.3. The curve A shows a specific function of a rough surface bottom, curve B for a smooth bottom [Jackson et al, 1986].

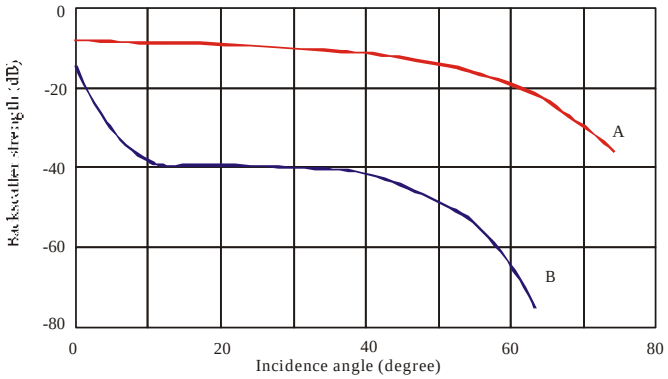

Figure 9.3: Curves showing angular response of different bottom types.

This method for classifying different bottom types is used in this master research. With the use of this method the assumption is made that the bottom types are not changing too much within a specific area. In this case this area is defined by the swath width. This will be further discussed in section 9.4.

9.2 Backscatter Measurements with Hydrosweep

For backscattering strength calculation three basic groups of parameters are required, first the equipment related constants, second the variables which are related to the equipment operating conditions, and finally the echo data measured by the system. The system Hydrosweep records all these parameters and uses them in the computation of the backscatter. These parameters supplied by the system are [STN Atlas, 1993]:

- Sound transmission parameters: transmission level, transmission pulse, transmission beam pattern
- Parameters to calculate transmission loss including spherical spreading loss and sound absorption
- Receiving voltage response of the receiving transducer array
- Correction coefficient due to the beam pattern of individual transducer elements
- Signal processor characteristics
- Echo root-mean-square voltage and signal duration

The signal processing algorithm, first developed only for depth measurements, now computes also the energy contained in the returning signal. The received electrical envelopes are sampled and converted to root-mean-square voltages within a –6 dB window around the peak amplitude. The derivation of the seafloor acoustic backscatter strength from the raw root-mean-square echo energy value for each individual beam is

carried out using an algorithm developed at the Marine Physical Laboratory, Scripps Institution of Oceanography. In addition two essential corrections for backscatter strength computation are performed, these are [Hagen et al., 1994]:

- Geometric correction
- Area of ensonification

The geometric correction is computed with the DEM of the Eltanin Impact Area, described in chapter 7, as input data. The slope data out of this DEM is used to correct the angles of arrival and to obtain angles of incidence (see also Figure 2.11).
The ensonified area of a beam is less than the projected area for the same beam because it depends on the length of the pulse. It is used to compute a correction coefficient by integrating the footprint of the transmitted pulse over the ensonified area. For more details see [Moustier, Alexandrou, 1991].

9.3 Backscatter Data in the Eltanin Impact Area

The backscatter data in the Eltanin Impact Area were collected during both expeditions, ANTXII/4 and ANTXVIII/5a. In order to be able to analyse these backscatter data, first the computation of these backscatter strengths had to be analysed. This will be discussed in this section.

9.3.1 Transmission Level and Pulse Length

Two important parameters for the backscatter strength calculation are the transmission level, and the pulse length of the acoustic signals. These parameters are recorded and used to compute the backscatter data. It is verified if these parameters are taken into account in the right way within the program, which calculates these backscatter data. The transmission level is described as, 'the nominal value of the transmission sound level specified by the system', and the pulse length as, 'the duration of the transmission beam'. The different record items within the 'dux'-format (see section 6.3), defining these parameters, are listed in Table 9.1 [STN Atlas, 1993]. The transmission level is given in deciBel (dB), and the pulse length in milliseconds (ms).

Bytes	Name	Format
3	Transmission level starboard, outer	ddd
3	Transmission level starboard	ddd
3	Transmission level vertical	ddd
3	Transmission level port	ddd
3	Transmission level port, outer	ddd
2	Pulse length starboard, outer	ss
2	Pulse length starboard	ss
2	Pulse length vertical	ss
2	Pulse length port	ss
2	Pulse length port, outer	ss

Table 9.1: Record items within the dux-format.

Day	Transmission level (dB)	Pulse length (ms)
950331	000239236239000	0023112300
	000239236239000	0011051100
950401	000239236239000	0023112300
	000239236239000	0011051100
950402	000239236239000	0023112300
	000239236239000	0011051100
950403	000239236239000	0023112300
950430	000239236239000	0023112300
	000239236239000	0011051100
950501	000239236239000	0023112300
	000239236239000	0011051100
	239239236239239	0023112300
	239239236239239	0011051100
950502	000239236239000	0023112300
950503	000239236239000	0023112300
950504	000239236239000	0023112300
950505	000239236239000	0023112300
950506	000239236239000	0023112300
	000239236239000	0011051100
950507	000239236239000	0023112300
	000239236239000	0011051100
950508	000239236239000	0023112300
	000239236239000	0011051100

Table 9.2: Transmission level and pulse length for ANTXII/4.

Day	Transmission level (dB)	Pulse length (ms)
010327	000239236239000	0023112300
010328	000239236239000	0023112300
	000239236239000	0011051100
010329	000239236239000	0023112300
010330	000239236239000	0023112300
010331	000239236239000	0023112300
	000239236239000	0011051100
010401	000239236239000	0023112300
	000239236239000	0011051100
010402	000239236239000	0023112300
010404	000239236239000	0023112300
010405	000239236239000	0023112300
010406	000239236239000	0023112300
010407	000239236239000	0023112300
	000239236239000	0011051100
010408	000239236239000	0023112300
010409	000239236239000	0023112300

Table 9.3: Transmission level and pulse length for ANTXVIII/5a.

The values of these parameters for the data in the Eltanin Impact Area is given for ANTXII/4 and ANTXVIII/5a in Table 9.2, and Table 9.3, respectively. These are the values

that are found within the dux-format for every survey day. The tables have to be read in combination with Table 9.1. In this table the record items are explained. For example the transmission level at day 950403 (3 April 1995) was 0 dB at both outer beams, 239 dB at starboard and port, and 236 dB at the centre beams. The pulse length for the same day is than 0 milliseconds at the outer beams, 23 milliseconds at starboard and port, and 11 milliseconds in the centre beam area. For a better understanding of these values it has to be noticed that the operation mode during both expeditions was 'Deep Sea' (see section 3.1), and that in both expeditions a 90° coverage was used. One exception has been found in the data of expedition ANTXII/4. Within a very short period the 90° coverage was changed to 120°, which can be seen in Table 9.2. The reason for the change of the swath width is not known.

The Figures 9.4, and 9.5 show the backscatter strength at those locations were the pulse length is changing. In these figures, the blue colours show a small backscatter strength, and the red colours a strong backscatter strength. At these locations neither systematic effects, nor changes in the backscatter strengths, due to the changing of the pulse length, are visible. Such changes would be visible as an offset in the backscatter strength, resulting as an overall changing colour in these figures.

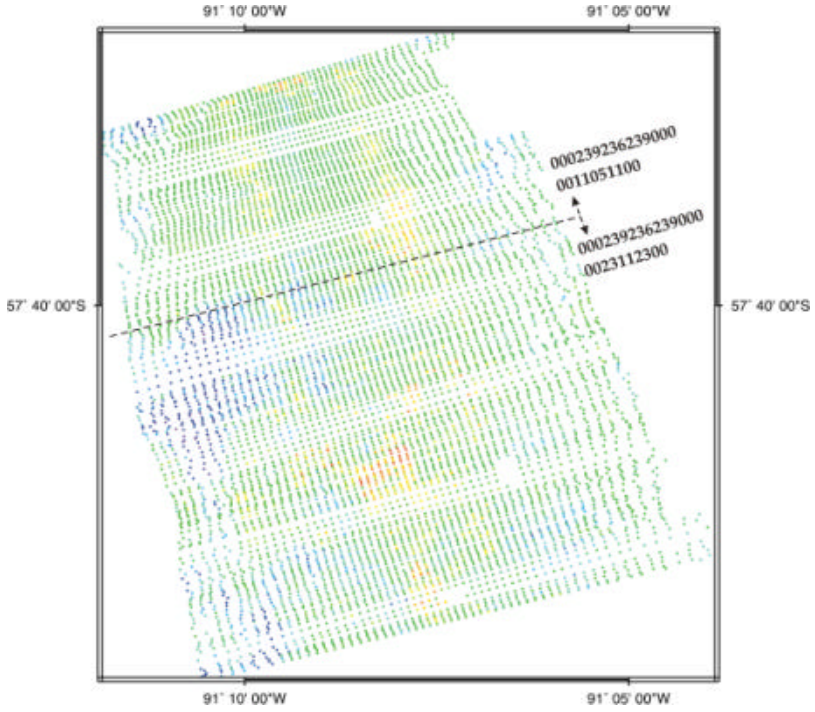

Figure 9.4: Backscatter strength at location of changing pulse length (010331).

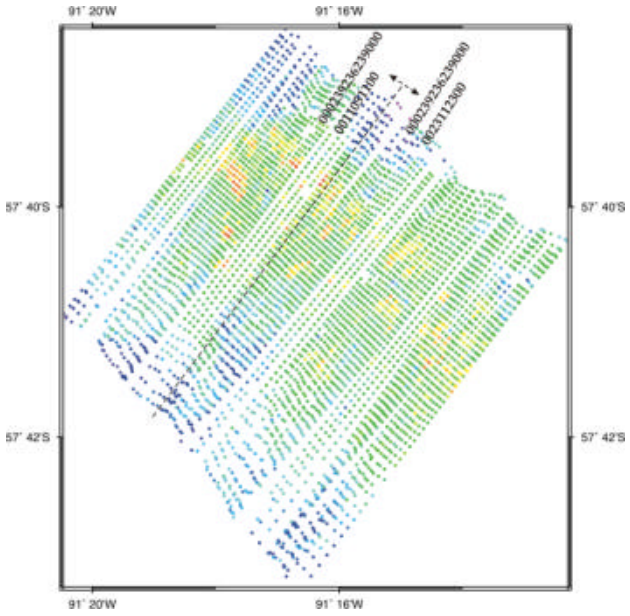

Figure 9.5: Backscatter strength at location of changing pulse length (950501).

9.3.2 Geometric Correction

The geometric correction is performed to get the angle of incidence of the acoustic signal at the ocean floor (see Figure 2.11). In this correction the slope of the DEM of the Eltanin Impact Area is used. This slope was calculated in the original software only within the direction of the swath, but the software was changed by AWI (contact, Andreas Beyer) to correct for a slope in three dimensions. This geometric correction is visualised in Figures 9.6, 9.7, and 9.8.

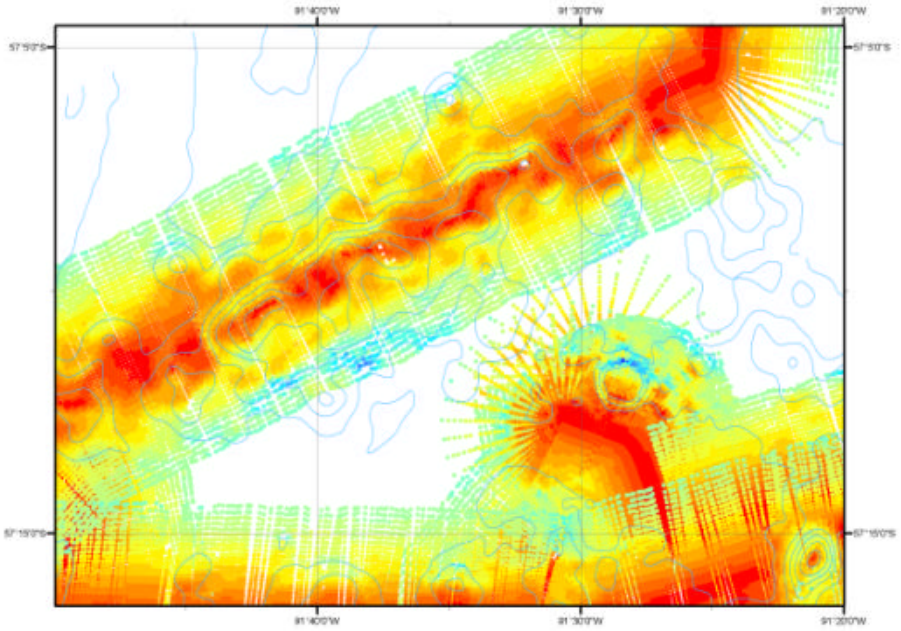

Figure 9.6: Example 1 of incidence angle and 100 meter contour lines.

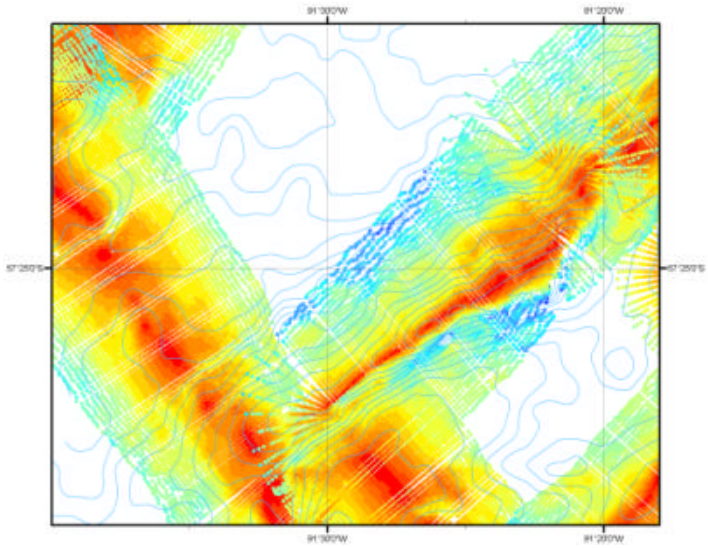

Figure 9.7: Example 2 of incidence angle and 100 meter contour lines.

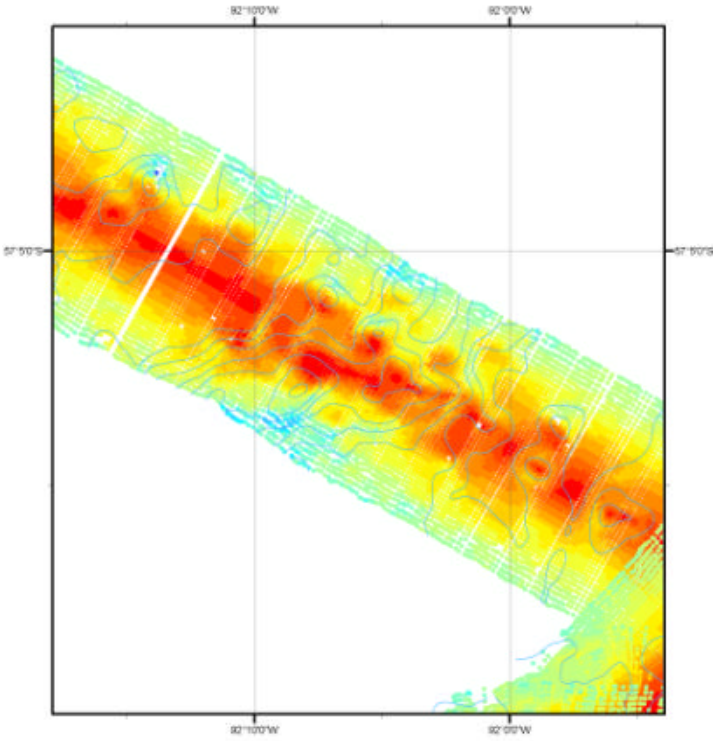

Figure 9.8: Example 3 of incidence angle and 100 meter contour lines.

In these figures the computed incidence angle is shown in different colours, the blue colours represent a high incidence angle and the darkest red colour an incident angle of almost 0°, which represents an incidence angle perpendicular to the topography. The 100

meter contour lines show the topography within each region. In these figures it is clearly visible that the incidence angle is computed according to the changes in the topography.

9.3.3 Comparison between Data of ANTXII/4 and ANTXVIII/5a

For a detailed analyses of the backscatter data within the Eltanin Impact Area, a combined analyses of the backscatter data of the two expeditions is needed. However, although the backscatter strength data of the two expeditions are calculated in the same way, there are some differences between these datasets.

The overall data quality of the data of expedition ANTXVIII/5a is better than the data of expedition ANTXII/4. In this last dataset a lot of erroneous data within the swath lines are found; this is visualised in Figure 9.9. The biggest problem however is formed by a systematic effect which concentrates on the centre beams, and is visible through the whole dataset of ANTXII/4. The areas within the centre beams show systematically a stronger backscatter strength, which can be seen in Figure 9.10. The reason for this is not found, and could not be solved within this master research, but it might be that the parameters which are used by the system, and the parameters that are recorded by the system are not the same.

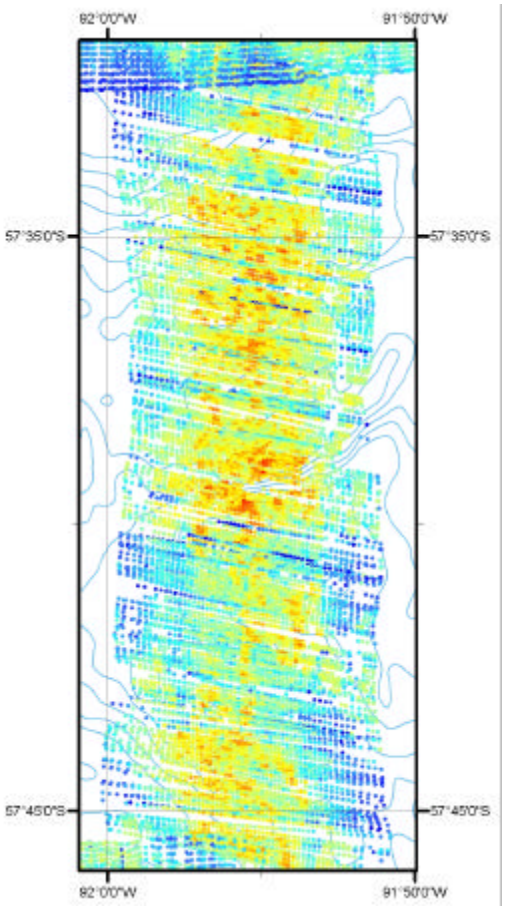

Figure 9.9: Erroneous backscatter data points of ANTXII/4 .

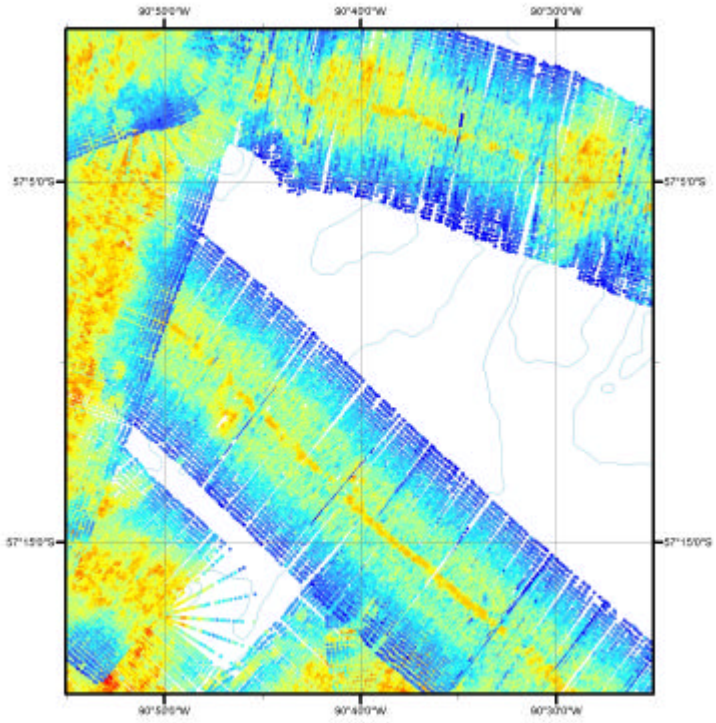

Figure 9.10: Systematic backscatter data errors in the centre beams of ANTXII/4.

At some locations almost the same profiles were surveyed and at those locations a comparison of the backscatter datasets could be made. The result was a difference between the datasets of ANTXII/4 and ANTXVIII/5a in the form of a varying offset in the backscatter strength. This offset, depending on location, prevents a comparison of these backscatter data. At two locations the backscatter strength was plotted against the incidence angle. These histograms can be seen in Figure 9.11 and 9.12. The red dots represent a large percentage of data points, and the violet dots a small percentage of data points.

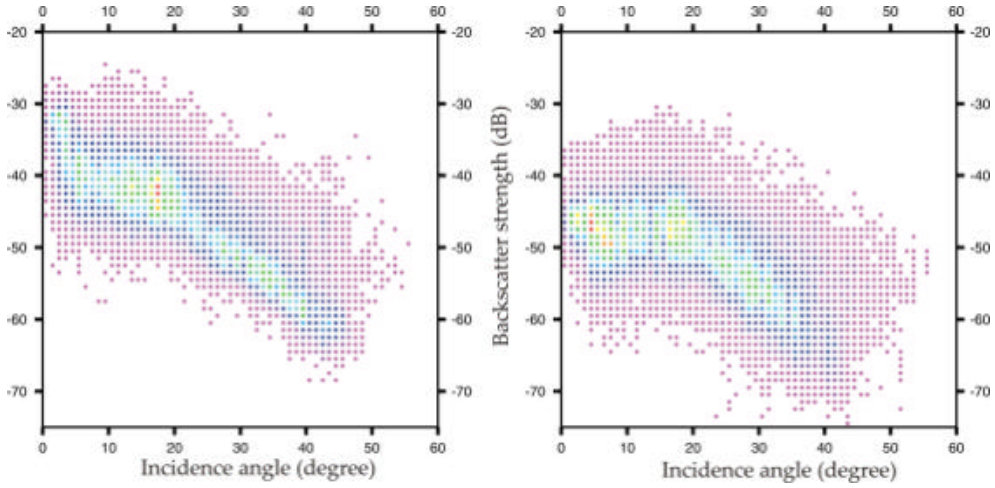

Figure 9.13: Histograms showing backscatter strength against incidence angle of ANTXII/4 (left) and ANTXVIII/5a (right) at location 1.

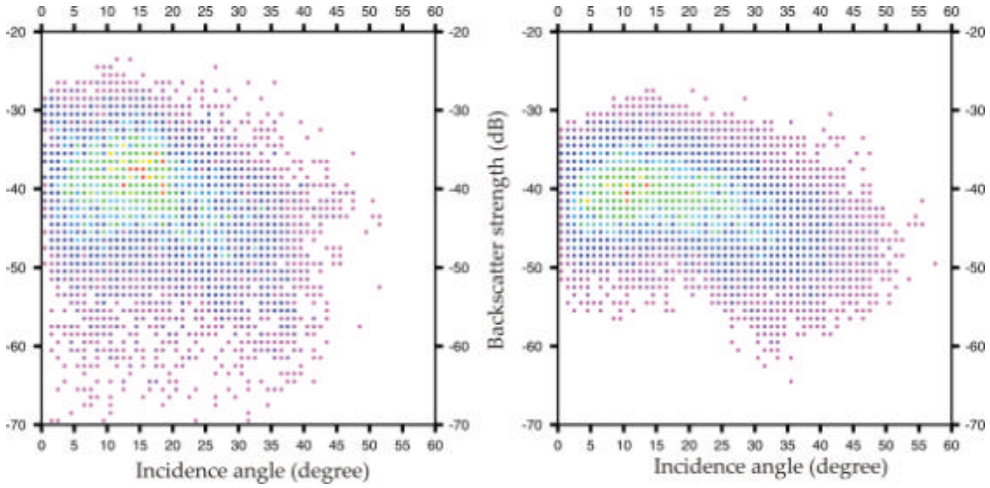

Figure 9.14: Histograms showing backscatter strength against incidence angle of ANTXII/4 (left) and ANTXVIII/5a (right) at location 2.

The offset at location 1 is larger than at location 2. An estimate of the offset, based on a visual interpretation, was found to be about 7 dB at location 1, and at about 3 dB at location 2. In these histograms also the difference in data quality can be seen, especially within area 2. The effect of a higher backscatter strength within the centre beams is also visible within the histogram of area 1. Because of the differences discussed here, only the backscatter data of ANTXVIII/5a were further analysed. This will be discussed in the following section.

9.4 Backscatter Data Segmentation of ANTXVIII/5a

The backscatter data of expedition ANTXVIII/5a were used to perform a classification of bottom type. The backscatter analysis that was used is the response curve analysis, described in 9.1.3. To differentiate between different response curves a classification was used. The goal of this classification method is to make it possible to interpret the results of this classification for a global bottom type model. This method for classification is within this master research tested and analysed for the Eltanin Impact Area. It has to be noted that this method is in an early stage of development and should be developed further to draw true conclusions. However, as will be seen, this method gives already promising results.

An unsupervised classification had to be used because nothing about sediments and structures of the ocean floor was known in the Eltanin Impact Area. This classification and the analyses of this classification are discussed within this section. But first a short introduction in unsupervised classification and clustering is given. This unsupervised approach classifies data by aggregating them into natural spectral clusters. The last step of the classification is to combine these results with ground truth. This ground truthing is not used within this classification process, because no ground truth about grain size and type of the sediments were yet available. Therefore in this research not the word classification will be used but segmentation.

9.4.1 Unsupervised Classification

The unsupervised classification does not use training data as basis, but uses algorithms that examine the unknown pixels and aggregate them into a number of classes based on the clusters that are present. The identity of these classes is not known, but has to be collected out of reference data [Lillesand, Kiefer, 1994]. After this clustering an algorithm can be used to classify every data point to a cluster. The result is a segmentation of the data in the number of clusters that was defined by the analyst.

Clustering

There are a lot of clustering algorithms that can be used. The method that is used within ArcInfo, and also in this master research, is the K-means approach. It accepts from the analyst a number of clusters that have to be located, and the algorithm then locates that number of cluster centers.
It starts in a multidimensional space by dividing a specified line (in two dimensions this line makes an angle of 45° with the axis) into the number of classes defined by the user. With the shortest distance algorithm the pixels are classified to a class. This is done for every sample point and then the procedure starts again and will iterate. Before anext iteration step, a new mean center is calculated based on the data points within that cluster. This is visualised in two dimensions in Figure 9.15. Within ArcInfo this iteration process is repeated until the maximum number of iterations is reached or until less than 2 percent of the cells change from one cluster to another [ESRI, 1999].

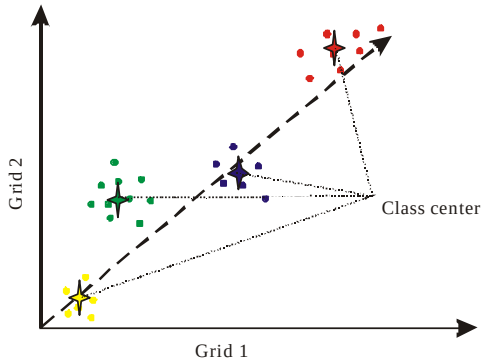

Figure 9.15: Clustering in two dimensions used in ArcInfo.

For the shortest distance within this clustering procedure, the Euclidian distance is used, as defined as [Richards, Jia, 1999]:

$$d(x_1, x_2) = \left\{ \sum_{i=1}^{N} \left(x_{1_i} - x_{2_i} \right)^2 \right\}^{1/2} \tag{9.7}$$

In this equation N is the number of spectral components, or layers, and x_1 and x_2 define two pixels the similarity of which has to be checked.

Maximum Likelihood Classifier

To assign every cell to a cluster a classifier algorithm has to be used. Within ArcInfo the used classifier is the maximum likelihood classifier. This qualifier quantitatively evaluates both the variance and covariance of the clusters when classifying a pixel. The assumption is made that the distribution of the cloud points forming the clusters is normally distributed. For each pixel a probability is computed for each cluster, the pixel is then classified to the most likely cluster, or in other words, to that class which has the highest probability value [Lillesand, Kiefer, 1994].
In Figure 9.16 the maximum likelihood classifier is shown in a simplified way. In this case the pixel to be classified would have the highest probability in cluster B and the smallest probability in cluster A. Therefore it would be classified in cluster B.

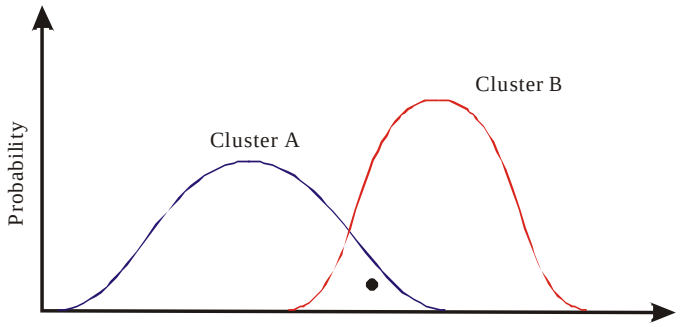

Figure 9.16: Maximum likelihood classifier.

9.4.2 Segmentation of the Backscatter Data

For the backscatter data segmentation the data were partitioned in data at port side, and data at starboard side. The reason is that at both sides, because of the geometry of the multibeam system, almost the same incidence angles are present, and separate analyses of both sides of the swath, instead of the swath as a whole for the segmentation, will improve the quality of this segmentation, based on the following assumption:
The bottom type on the seafloor, which interacts with the acoustic signals, is the same at one side of the swath.

In ArcInfo different grids, combined within a stack, are needed to perform a segmentation. To be able to segment the data within a stack, all the grids have to have a value at a specific location. Therefore the backscatter data at each side of a swath were given a specified location. So within a swath there are now two locations with, together, the information about incidence angle and backscatter strength of 59 beams. This is visualised in Figure 9.17, with the blue arrow showing the track line, and the red dots representing the original backscatter data points within the swath. The combination of the data to the same location within each side of the swath, is represented by the green dots.

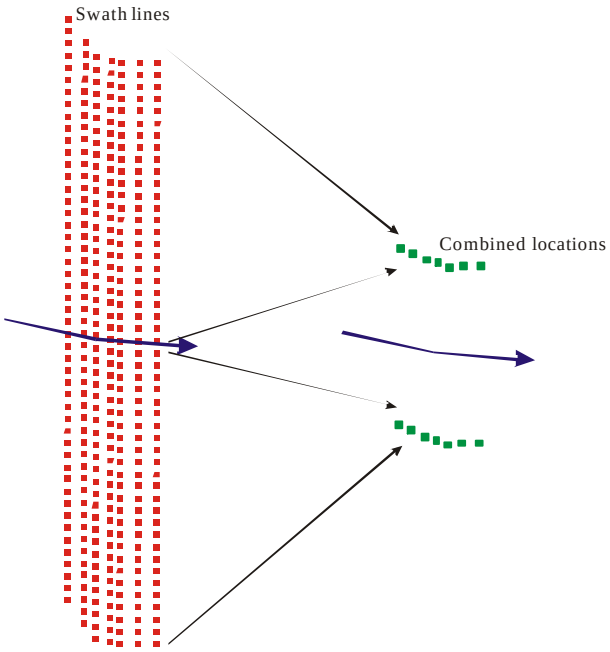

Figure 9.17: The combination of the backscatter data to the swath sides.

These combined locations form the input for the segmentation within ArcInfo. However to fill every grid point, which can be interpreted by the green dots in Figure 9.17, with a value, channels of incidence angles are created. With these channels of incidence angle it is possible to fill the grids with data. Each channel represents within the classification process a grid, and with that forms a part of the stack. This grid is computed out of the data at the combined locations with a grid size of 50 meters. The incidence angle channels that are created are listed in Table 9.4, with the number of grid cells that are filled within this grid. The grids with an incidence angle between 0° - 5°, 40° - 45°, and 45° - 50° are less filled, and a lot of grid cells have a value of zero. This reduces the grid cells that can be segmented. Therefore only the grids are used within the stack that fall between 5° and 40°. This means that 7 grids are combined together in the stack for segmentation. The used ArcInfo commands can be found in Appendix E.

Grid name	Incidence angle	Filled grid cells
bsct05grd	0° - 5°	26495
bsct10grd	5° - 10°	34824
bsct15grd	10° - 15°	37217
bsct20grd	15° - 20°	37619
bsct25grd	20° - 25°	37465
bsct30grd	25° - 30°	37028
bsct35grd	30° - 35°	36125
bsct40grd	35° - 40°	33906
bsct45grd	40° - 45°	25746
bsct50grd	45° - 50°	9063

Table 9.4: Grids for the segmentation within ArcInfo.

A number of 4 clusters were used for the segmentation. This was based upon the histogram of all backscatter data, shown in Figure 9.18. In this histogram it is clearly visible that at least different response curves can be found, shown within the red box, with a higher backscatter strength at all incidence angles, and the green box, with a lower backscatter strength especially at locations with a higher incidence angle. For a global interpretation of the backscatter data a segmentation of 4 clusters was preferred. A segmentation in less clusters would result in a segmentation almost impossible to interpret, in more classes would result in a noisy segmentation for which interpretation is also impossible.

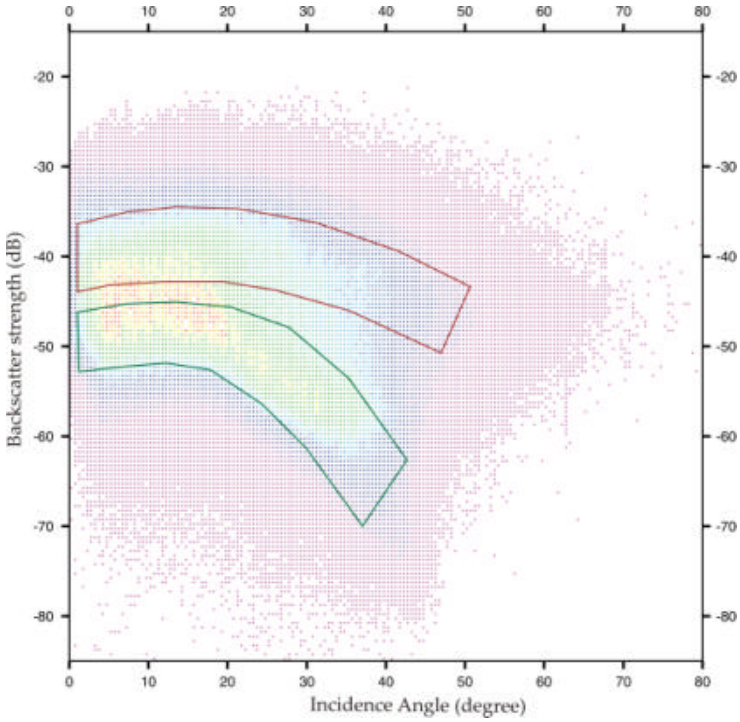

Figure 9.18: The response curve of the ANTXVIII/5a backscatter data.

The results of the segmentation are listed in Table 9.5. In this table the reject fraction is given, which is defined as the lowest possibility of correct assignment, and the number of segmented cells, which is also given as percentage of the total cells. Based on these results the segmentation is used with a reject fraction of 0.5. This means that the chance that the pixel is segmented in the correct cluster is 50%.

The segmentation in different clusters is difficult because, as can be seen in Figure 9.18, the different response curves lie very close together and a separation is not easy. The segmentation splits this total response curve into 4 parts. The result of the segmentation in the 4 clusters is given in Table 9.6. In this table the number of cells are listed that are segmented within each cluster. The results of the response curves for the different clusters and the interpretation of this segmentation, are discussed in the following section, section 9.4.3.

Reject Fraction	Number of segmented cells	Percentage of segmented cells (%)
0	24527	100
0.25	18734	76
0.5	14109	58
0.75	8425	34
0.9	3973	16
0.99	257	1

Table 9.5: The reject fraction and the segmented cells.

Cluster	Number of cells
I	3576
II	3654
III	3722
IV	3157

Table 9.6: The number of segmented cells within each cluster.

9.4.3 Analyses of the Backscatter Data Segmentation

The result of the backscatter segmentation into 4 clusters with a reject fraction of 0.5, is shown in Figure 7.19. In this figure the colours define the different clusters in which the backscatter data are segmented. These colours have the following sequence: yellow, violet, green, red. The contour lines in this figure, have an interval of 100 meters, and the track of RV 'Polarstern' is shown as a purple line. This figure, showing the result of the segmentation, has to be interpreted in general way. A detailed interpretation is, because of the assumptions made, very difficult to make and almost impossible. As can be seen, the partitioning in a port and starboard side is very useful for a better interpretation of the segmentation results, because in a lot of areas these port and starboard side data are segmented in different clusters.

The result of the segmentation gives a global view of the changing of the backscatter strength due to small scale roughness of the sea floor. It is possible to make, on basis of this segmentation, a general interpretation of the change of the sea floor roughness. This means that, as can be seen in Figure 9.19, changing colours result in a change of the sea floor roughness. It is not possible to make an absolute differentiation between the different clusters, and the locations of changes between different clusters are not exact boundaries. At these boundaries it can only be concluded that something within the sea floor roughness is changing.

Figure 9.19: The segmentation result showing the different clusters in different colours.

Response Curves

For a better interpretation of the segmentation in the four clusters, 3 test areas for each cluster were chosen at locations with a clear segmentation. These polygons are shown in Figure 9.20. Each polygon within a cluster is numbered from 1 to 3. The used backscatter data points within each polygon for each cluster are listed in Table 9.7. These backscatter data were used for plotting a backscatter response curve and for fitting a polynomial function through these data. It is expected that for each cluster these response curves are more or less the same, and that a difference is visible between the curves of different clusters. With these curves, the segmentation, and the bathymetry, a better interpretation can be made about the small scale roughness of the sea floor, described in section 9.5.

Figure 9.20: The polygons for each of the four clusters.

Polygon	Backscatter data points
Red 1	8976
Red 2	16780
Red 3	4952
Green 1	7086
Green 2	3708
Green 3	2788
Violet 1	4450
Violet 2	29542
Violet 3	6930
Yellow 1	13570
Yellow 2	21540
Yellow 3	8094

Table 9.7: The number of segmented cells within each cluster.

The response curves are shown in Figures 9.21 – 9.24 for the red, green, violet and yellow clusters, respectively. In these curves the red colours represent a high amount of data points, the violet colours a small amount. The fitted functions are given by the black lines.

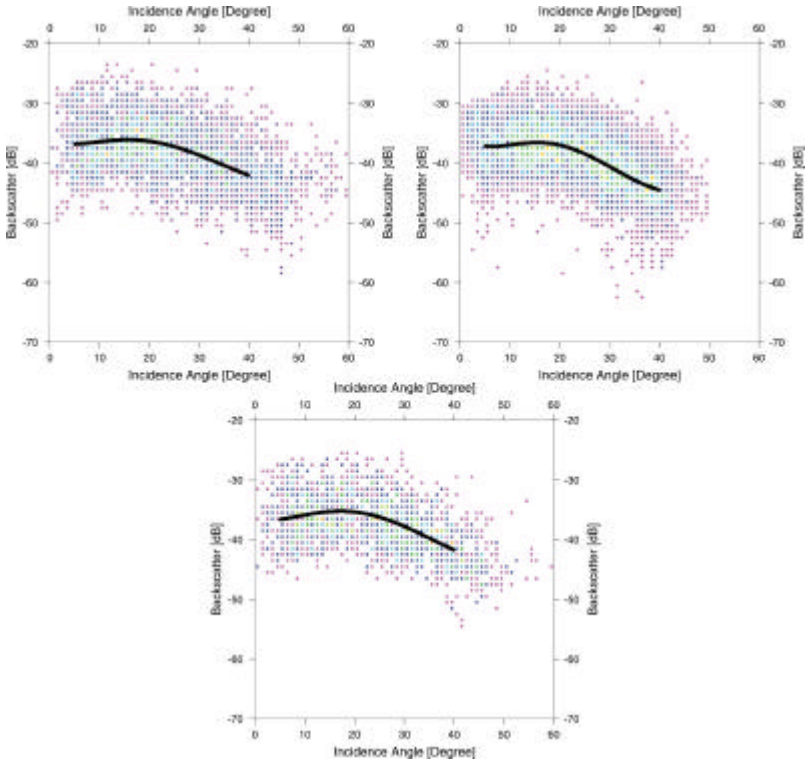

Figure 9.21: Response curves of the red cluster, 1 (upper left), 2 (upper right), 3 (lower middle).

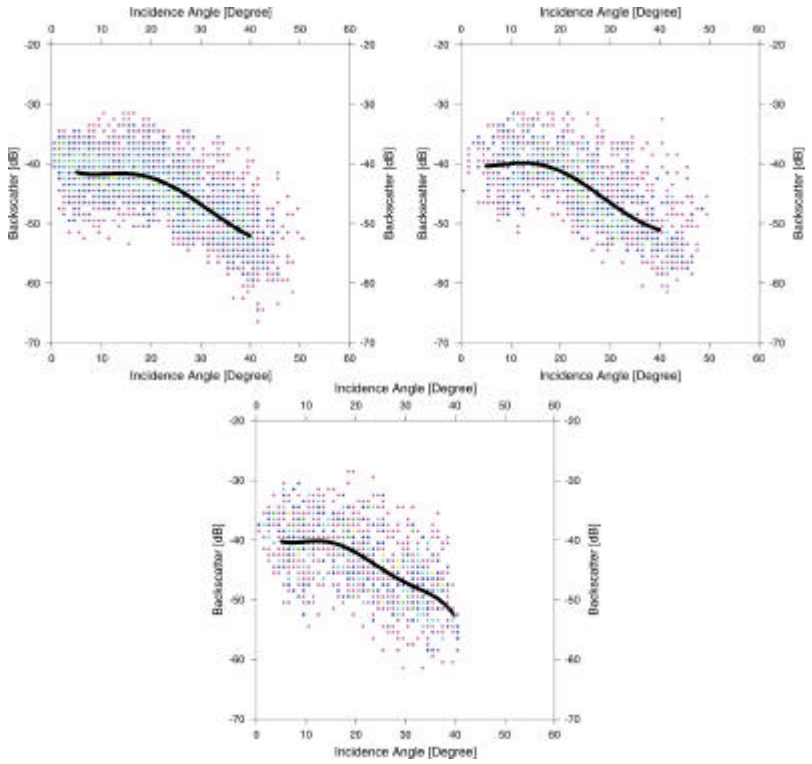

Figure 9.22: Response curves of the green cluster, 1 (upper left), 2 (upper right), 3 (lower middle).

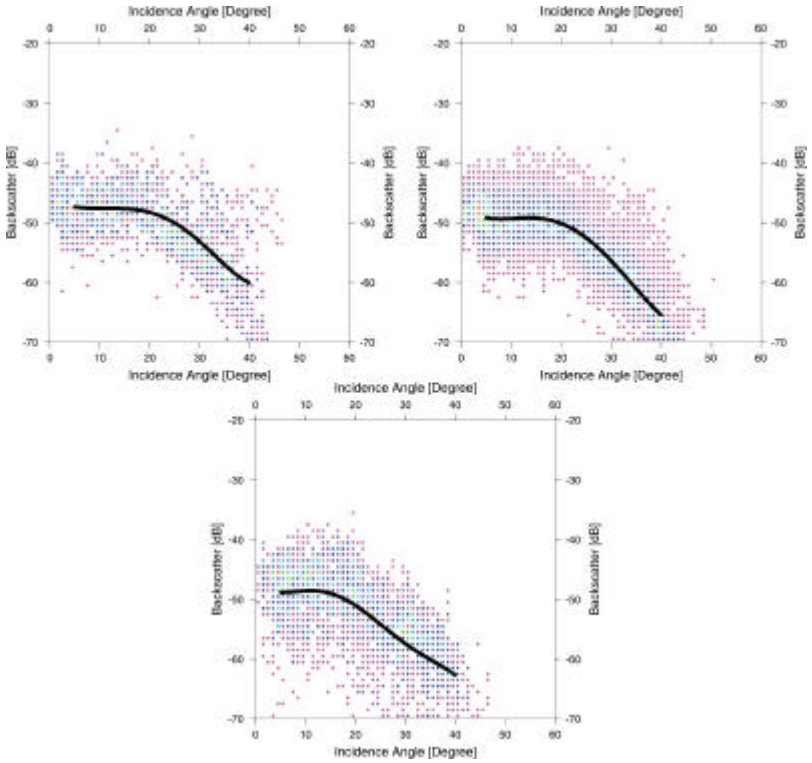

Figure 9.23: Response curves of the violet cluster, 1 (upper left), 2 (upper right), 3 (lower middle).

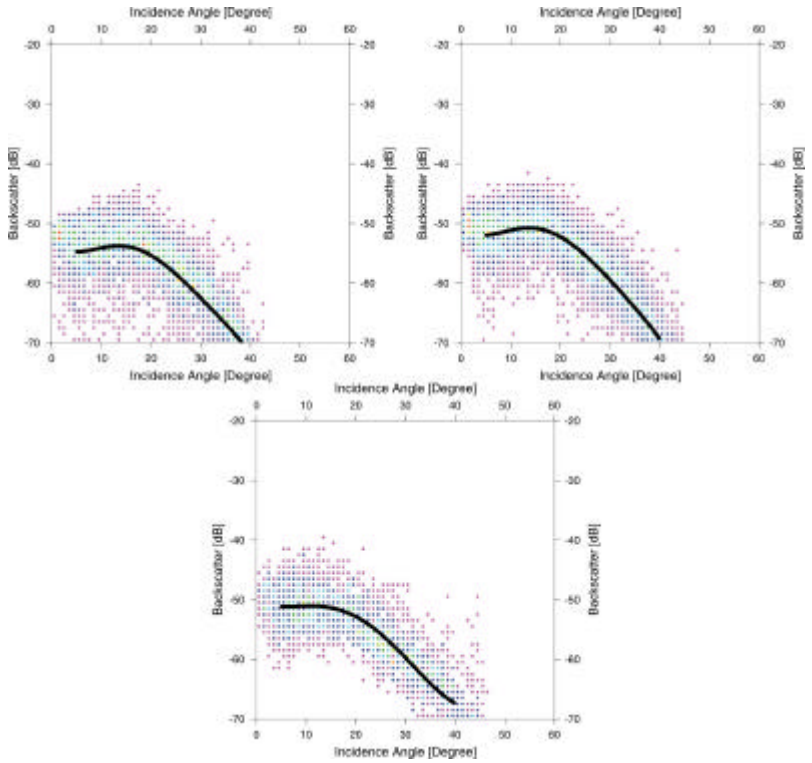

Figure 9.24: Response curves of the yellow cluster, 1 (upper left), 2 (upper right), 3 (lower middle).

The curves within each cluster show the expected similarity. The response curves of the red cluster show a very high backscatter strength, almost at all incidence angles. The backscatter strength decreases only slightly at higher incidence angles. The green cluster shows almost the same response curves as the red cluster, but with a more decreasing backscatter strength at higher incidence angles. Lower backscatter strengths are visible in the response curves of the violet cluster. The backscatter strength also decreases more at higher incidence angles than in the green cluster. The lowest backscatter strengths with the steepest descent for increasing incidence angles, are found in the yellow cluster.
With the theory, as described above, this would result in the conclusion that in areas where the red and green cluster are present, there is a lot of small scale topography, and so to say, the bottom type is rough. This in contrast to the areas of segmentation in the yellow and violet cluster, here there is almost no small scale topography, and the bottom type is more flat. At locations were the clusters are changing, also the bottom type is changing. This, however, is only a very general interpretation. Details are not visible within this segmentation.

Ground Truth for classifying the Bottom Roughness

The bottom roughness within the Eltanin Impact Area changes, as concluded. This results of the segmentation however could not be classified and compared with ground truth data, because at this time no information is available of the grain size of the different sediments. At different locations sediment cores of both expeditions will give this information to make it possible to fully understand the backscatter segmentation. The analyses of the grain size and bottom type fall beyond the scope of this master thesis, and will not be discussed any further. When this information is available, a comparison has to be made with the segmentation that is presented here and also more analyses of the backscatter data are then needed.
It is now only possible to compare the results with the bathymetry of the Eltanin Impact Area. This will be discussed within the next section, section 9.5.

9.5 Comparison of Bathymetry and Backscatter Data

In this section a comparison will be made between the bathymetry, the backscatter data, and the segmentation results. It will give an overall interpretation of the geomorphology in the Eltanin Impact Area, and the changing bottom roughness. Figure 9.19 should be used for the interpretations that are given within this section. For a better interpretation of the bathymetry also the Figures 8.4 and 8.5 can be used.

9.5.1 Geomorphology based on the Digital Elevation Model

The Eltanin Impact Area lies on the Pacific-Aluk plate, as shown in Figure 5.1, near fracture and subduction zones. In the centre of the Eltanin Impact Area the influence of the plate reorganisations is visible in the form of the San Martin Seamount. The San Martin Seamount and the area around this mount, are of volcanic origin. The area has a very irregular shape and structure, visible in the grid and the bathymetric maps by the steep ridges, flat top, the small cones in the north and the east, and the overall orientation of the slopes in the direction south-west to north-east. The highest point of the San Martin

Seamount lies at about 2240 meters at the position of approximately 57° 35' 40" S and 91° 17' 30" W. In the north the San Martin Seamount shows an abrupt boundary, formed by a steep ridge in south-west to north-east direction. From this ridge to the north a flatter basin is found with many small mounts which have a cone shape. These small mounts follow lines also oriented form south-west to north-east. The east side of the seamount ends in a flat basin with depths around 5200 meters with at location 57° 21' S, 90° 38' W a high isolated seamount.
In the south-east a small and narrow, maximal 10 kilometers wide, deep basin is found. This basin is in the north splitted into two parts by a long ridge of the seamount, which gives it a Y-form. In the east and west this basin is bounded by steeper flanks of higher topography. The western side of the seamount shows the steepest flanks, from the highest point of the sea mount into a little basin with depths of 5000 meters. This basin is in the south and west bounded by some smaller scale irregular topography. In the south-west corner another flat basin is formed bounded in the north by irregular topography.

9.5.2 Backscatter Data and Bathymetry

The backscatter data and the segmentation results show a high correlation with the bathymetry. This can be expected because of the geomorphology of the area. The yellow and some violet clusters are only found within the flat basins. In these areas the basins are probably filled with thick fine sediment, due to the isolated location of these basins. In the areas were the clusters change from yellow and violet to green and red, the topography also changes dramatically. At these locations the probably thick fine sediments change to thinner and more rougher sediments and bottom types. At locations were the red clusters are present it is likely that no fine sediments are found and only the rough and eroded volcanic bottom type is present. This can also be concluded from the bathymetry where irregular topography and steep flanks can be found. It is not likely that sedimentation processes have taken place at these locations. For such processes flat and more isolated locations are needed.
The backscatter data that is presented here gives only a global view of the possible changes in bottom type roughness. For a detailed overview more research, especially combined with Parasound data, and geological ground truth data, is needed.

10. Conclusions

In this chapter the conclusions of the master research, presented in this thesis, are given. This master research was split up in three important parts. First the bathymetric data editing and cleaning, second the digital elevation modelling within ArcInfo based on the edited and cleaned bathymetric data, and third the backscatter strength analyses. The conclusions are also structured using these three parts of the master research. In section 10.1 the conclusions are given about the data editing and cleaning, section 10.2 gives the conclusions of the digital elevation modelling, and finally in section 10.3 the conclusions of the backscatter data analyses are presented.

10.1 Conclusions: bathymetric data editing and cleaning

Two different data sets were used, of expedition ANTXVII/4 and ANTXVIII/5a, during the bathymetric data editing and cleaning. Both these data sets are of the same data quality, and of these data 10 – 15 % were removed. Especially during bad weather conditions and the heavy seas caused by these weather conditions, a lot of data had to be removed. These removed bathymetric data were located especially at the outer beams.

The filters that are presented in the software HIPS, a part of the GIS CARIS, proved to give good and homogeneous results. The most important filters that could be used were a maximum and minimum depth filter, a beam to beam slope filter, and a filter to reject specific beam numbers. The parameters of the beam to beam slope filter were set depending on the point density and on the type of topography, described as flat, smooth or steep topography.

The surface cleaning within the software HIPS, is a good and reliable technique to clean the bathymetric data based on statistic methods. An assumption is that these data have to have a Gaussian distribution. Before this method can be used, the data has to be cleaned of gross errors and outliers. The result using these objective cleaning technique are homogeneous data sets less influenced by subjectivity of the operator.

The bathymetric data sets are cleaned to create homogeneous data sets. The subjectivity of the operator is reduced to a minimum, and only used to verify and check the results of the filtering and the surface cleaning.

There are differences between the bathymetric data sets due to the use of different, and not correct mean sound velocities. These bathymetric data sets could not be combined for cleaning and editing within the CARIS software, because the data is not referenced to the same sound velocity.

A lot of very different data formats make the data handling very difficult.

10.2 Conclusions: digital elevation modelling

The best method for digital elevation modelling within ArcInfo, with the bathymetric data of the Eltanin Impact Area, is the inverse distance weighted interpolation. This inverse distance weighting gives the best results using the 'sample' method for searching for the input points. The other important parameters for the inverse distance weighting interpolation are listed in Table 10.1.

Power	0.5
Number of sample points	100
Cell size	100
Maximum search radius	500

Table 10.1: The parameters for the inverse distance weighted interpolation in ArcInfo.

For a smoothing of the digital elevation model and the removal of the noise, filters are used depending on the slope. Within flat areas, where the signal-to-noise ration is higher, a larger binomial filter was used, then in area with steeper slopes. At the steepest slopes, with a small signal-to-noise ratio, no filtering was used.

The quality of the digital elevation model and the bathymetric data is described with the use of the empirical standard deviation. It compares the original data points with the DEM. The mean of this empirical standard deviation lies at ~0,5 % of the water depth. The digital elevation model is therefore created within the accuracy of the multibeam system Hydrosweep DS-2, which has in optimal conditions, an accuracy of 0.5 % of the water depth, and within the task of the research project to achieve an accuracy of better than 1% of the water depth.

For the bathymetric mapping of the Eltanin Impact Area on a scale of 1:100 000, 20 meter contour intervals were derived from the digital elevation model. The area with the best data coverage was chosen for the bathymetric mapping within four map sheets. The boundaries of the total area are the parallels 56° 50 S, 58° 00 S, and the meridians 90° 10 W, 92° 20 W. Furthermore, 2 overview map sheets are produced on a scale of 1:200 000 and 1:500 000.

A basis for a GIS of the Eltanin Impact Area was created within ArcMap. The data related to the bathymetric data, and the backscatter data, are available and can be used for further geologic and geomorphologic research.

A lot of very different data formats make the data handling very difficult.

10.3 Conclusions: backscatter strength analyses

The backscatter data of expedition ANTXII/4 had poor quality, in comparison with the backscatter data of expedition ANTXVIII/5a. The data set shows not only gross errors but also systematic errors at the centre beam locations. These data are not used for further analyses and interpretation.

The method for segmentation of the backscatter data within different classes with the use of an unsupervised classification within ArcInfo, has proved to be successful. For the segmentation the response curve analysis was used, which combines the incidence angle and the backscatter strength. It can be used for an interpretation of the bottom roughness and bottom type.

The segmentation of the backscatter data can only be used for a global interpretation of the change of the bottom roughness and bottom type. Without the use of ground truth data, a classification, and full analyses of the backscatter data and segmentation results, are not possible.

The segmentation results are successful combined with the digital elevation model. These two data sets are, as expected, correlated with each other. Out of these comparisons the conclusions can be made that the flat basins possibly have thicker and fine sediments, and that the steep flanks have a rougher surface with probably coarse sediments.

11. Recommendations

In this chapter the recommendations of the master research, presented in this thesis, are given. These recommendations can be used for further analyses and further research within the Eltanin Impact Area. As within the previous chapter, these recommendations are also presented using the three different parts of the master research. First in section 11.1 the recommendations of the bathymetric data editing and cleaning are given, the recommendations of the digital elevation modelling within ArcInfo based on these edited and cleaned bathymetric data, are given in section 11.2. Finally in section 11.3 the recommendations are given of the backscatter strength analyses.

11.1 Recommendations: bathymetric data editing and cleaning

For combining different bathymetric data sets within the bathymetric data editing and cleaning, the data should be referenced first to a sound velocity of $1500\,{}^{m}/_{s}$. It is, after this referencing, possible to clean the data sets at overlapping areas.

Within the data editing and cleaning it should be possible to correct bathymetric data, and not only to reject the data.

A definition of only one bathymetric data format should make the data handling and organisation easier.

11.2 Recommendations: digital elevation modelling

Within the methods of ArcInfo for computing a digital elevation model out of bathymetric data, a weighting of the different input data points depending on the position in the swath, should give better results. The outer beams need another weight than the centre beams, depending on the quality of the data.

Better results of the digital elevation modelling within the methods of ArcInfo, should be possible with the use of different interpolation parameters at different locations, depending on the point density.

A definition of only one bathymetric data format should make the data handling and organisation easier.

A GIS of the Eltanin Impact Area with the geological and geophysical data, is needed for further research and analyses of the geological, geomorphological and geophysical

structure of the Eltanin Impact Area. The data within this developed GIS, will form the basis for analyses of the impact event.

For a better interpretation of the bathymetrical, geological, geomorphological, and geophysical structure within the Eltanin Impact Area, more detailed bathymetric profiles are needed within the northern and eastern part of this area.

11.3 Recommendations: backscatter strength analyses

Analyses of the grain size, and bottom type at different locations have to be made to collect ground truth for the backscatter segmentation.

The differences between the backscatter data sets of the expedition ANTXI/4 and ANTXVIII/5a need to be analysed, and solved.

The method for using classification methods for segmentation of the backscatter data should be further analysed.

The results of the backscatter segmentation should be combined with other possible methods for backscatter analyses.

Methods for local interpretation of the backscatter data need to be analysed.

For a better interpretation of the bathymetrical, geological, geomorphological, and geophysical structure within the Eltanin Impact Area, more detailed bathymetric profiles, with the collection of backscatter data, are needed within the northern and eastern part of this area.

List of Symbols

Chapter 2:

p	pressure
r	density
c	sound speed
c_{mean}	mean sound speed
t	time (in seconds) temperature (in Celcius)
u	particle velocity
x	particle movement
f	force per unit volume, frequency of a wave
k	bulk modulus
a	wave amplitude
w	angular frequency
I	intensity of a wave
l	wavelength
k	wave number
T	period of a wave
W	eikonal
n	index of refraction
s	path
q	grazing angle
j	angle, $90 - q$
c_v	vertex velocity
g	velocity gradient
R	radius of a circle
r	distance
a	absorption coefficient, fan aperture or swath angle
d	directivity
SL	source level
NL	noise level
DI	directivity index
DT	detection treshold
TL	tranmission level
RL	reverberation level
TS	target strength
S	salinity

z	depth

Chapter 5:

B	number of beams
a	fan aperture
WD	water depth
v	ships speed in knots
$t\{WD\}$	time interval as function of water depth (in seconds)

Chapter 6:

a	beam to beam angle
$b_0 ... b_9$	polynomial constants

Chapter 7:

p	polynomial order
b_{rs}	polynomial coefficients
W_i	weights
$\Phi(d)$	weight function
r	weighting factor
d_{ij}	distance between grid point and data point
r_{ij}	correlation coefficient
s	standard deviation
d_{mean}	mean waterdepth
s_{emp}	empirical standard deviation

Chapter 9:

c	sound speed
R_0	normal incidence reflection
r	density
Δj	phase difference
Δz	elevation difference
l	wavelength
k	wave number
q	incidence angle
P	Rayleigh parameter
s	root-mean-square of displacement
I	intensity
R	range
A	area
$s(q)$	backscatter coefficient
$S(q)$	backscatter strength
$b(q, j)$	beam pattern source

$b'(q, j)$	beam pattern receiver
a_w	water absorption coefficient

List of Abbreviations

ANTXII/4	Twelfth RV 'Polarstern' Antarctica Expedition, leg four, 1995
ANTXVIII/5a	Eighteenth RV 'Polarstern' Antarctica Expedition, leg five A, 2001
ASDISC	Anti Submarine Division –ics
AWI	Alfred Wegener Institute
CARIS	Computer Aided Resource Information System
C_m	Mean Water Sound Velocity
CTD	Conductivity, Temperature, Density
dB	Decibel
DGPS	Differential Global Positioning System
DEM	Digital Elevation Model
DTM	Digital Terrain Model
DTM-fn	Digital Terrain Modelling Fred Niederjasper
FRISP	Filchner-Ronne Ice Shelf Programme
GIS	Geographic Information System
GPS	Global Positioning System
HDCS	Hydrographic Data Cleaning System
HIPS	Hydrographic Information Processing System
HYDROSWEEP-DS	HYDROgraphic multibeam SWEEPing survey echosounder Deep Sea
IDW	Inverse Distance Weighting
IERS	International Earth Reference System
IGS	International GPS Service
INS	Integrated Navigation System
InMarSat	International Maritime Satellite
ITRF	International Terrestrial Reference Frame
KHz	KiloHerz
Kt	Knotes
µPa	MicroPascal
M	Meter
ODT	Omni Directional Transmission modus
PFB	Pre-Formed-Beams

RADAR	RAdio Detection And Ranging
RDT	Rotational Directional Transmission modus
RV	Research Vessel
S	Second
SASS	Sonar Array Sounding System
SONAR	SOund Navigation and Ranging
TIN	Triangulated Irregular Network
TU	Technische Universiteit
TVG	Time Volume Gain
WMO	World Meteorological Organisation

List of Figures

List of Tables

References

- *Atlas Hydrosweep DS, Data for backscattering analysis*; GE6017F101SB, STN Atlas Elektronik, Bremen, 1993
- *Atlas Hydrosweep DS, Magnetic Tape Recording (DUX-format)*; GE6017F102SB, STN Atlas Elektronik, Bremen, 1993
- *Atlas Hydrosweep DS-2, Service Manual*; Volume 1, ED1029G042, STN Atlas Elektronik, Bremen, 1997
- ESRI; *Software Help ArcInfo 8.0*; ESRI, 1999
- Beyer, A.; 'Hochauflösende Bathymetrie am europäischen Kontinentalhang'; *Dokumentation Hydrographentag 2001*; DhyG, 2001
- Beyer, A., H.W. Schenke, M. Klenke, F. Niederjasper; 'High Resolution Bathymetry of the Eastern Slope of the Porcupine Seabight'; *Marine Geology*, in press
- Brekhovskikh, L.M., Yu.P. Lysanov; *Fundamentals of Ocean Acoustics*; second edition; Springer Verlag Heidelberg, 1990
- Burrough, P.A.; *Principles of Geographical Information Systems for Land Resources Assessment*; Clarendon Press, Oxford, 1986
- Cande, S.C., E.M. Herron, B.R. Hall; 'The early Cenozoic tectonic history of the southeast Pacific'; *Earth and Planetary Science Letters*, vol. 57 (1982), p. 63-74
- Caruthers, J.W.; *Fundamentals of Marine Acoustics*; second impression; Elsevier, Amsterdam, 1979
- Christen, S., *Diplomarbeit, Aufbereitung, Visualiserung und Interpretation einer bathymetrischen Vermessung im Süd Sandwich Tiefseegraben*, Fachhochschule Hamburg, Fachbereich Vermessungswesen, 1999
- Clay, C., H. Medwin; *Acoustical Oceanography*; John Wiley & Sons, New-York, 1977
- Gersonde, R., A. Deutsch; 'Oceanic Impacts: Mechanisms and Environmental Perturbations'; *Berichte zur Polarforschung (AWI)*, vol. 343 (1999)
- Gersonde, R. et al.; 'Geological record and reconstruction of the late Pliocene impact of the Eltanin asteroid in the Southern Ocean'; *Nature*, vol. 390 (1997), p. 357-363

- Grant, J.A., R. Schreiber; 'Modern Swathe Soundings and Sub-Bottom Profiling Technology for Research Applications: The Atlas Hydrosweep and Parasound Systems'; *Marine Geophysical Researches*, volume 12 (1990), p. 9-19

- Hagen, R.A., B. Chakraborty, H.W. Schenke; 'Preliminary backscatter results from the hydrosweep multibeam system'; *Summary report of the research work accomplished on international scientific cooperation initiatives – Marie Curie Fellowship*; appendix 2, 1994

- Hengstum, M. van; *'Stageverslag: Een onderzoek naar de kwaliteit van de terreinbeschrijving van terrestrische metingen en vliegtuig-laserscanning'*; Geodan Geodesie BV, 1995

- *HIPS/SIPS on Windows NT Training Notes*; CARIS, Universal Systems Ltd.; January 2001

- *Fledermaus User's Guide, Version 4.2*; Interactive Visualization Systems Inc., Fredericton, 1999

- Isaaks, E.H., R.M. Srivastava; *An introduction to Applied Geostatistics*; Oxford University Press, New York, 1989

- Jackson, D.R., D.P. Winebrenner, A. Ishimaru; 'Application of the composite roughness model to high-frequency bottom backscattering'; *Journal of Acoustical Society of America*, volume 79 (1986), p. 1410-1422

- Jacops, M.; *Practical Work Report, a grid of the Weddel Sea & Bathymetrie in the Antarctic*; Alfred Wegener Institute for Polar and Marine Research; Bremerhaven, 2001

- Jähne, B.; *Digitale Bildverarbeitung*; Springer-Verlag, Berlin, 1989

- Jong, G. de, J.C. de Munck; *Onderwater akoestiek*; Technische Universiteit Delft, faculteit der geodesie; 1988

- Kyte, F.T. et al.; 'High noble metal concentrations in a late Pliocene sediment'; *Nature*, vol. 292 (1981), p. 417-420

- Lillesand, T.M., R.W. Kiefer; *Remote sensing and image interpretation*; John Wiley & Sons, New York, 1994

- Mackenzie. K.V.; 'Nine-term Equation for Sound Speed in the oceans'; *Journal of Acoustical Society of America*, volume 70 (1981), p.807

- McCormick, J.M., J.V. Thiruvathukal; *Elements of Oceanography*; W.B. Saunders Company USA, 1976

- Moustier, C. de; 'Beyond Bathymetry: Mapping acoustic backscattering from the deep seafloor with Sea Beam'; *Journal of Acoustical Society of America*, volume 79 (1986), p. 316-331

- Moustier, C. de, D. Alexandrou; 'Angular dependence of 12-kHz seafloor acoustic backscatter'; *Journal of Acoustical Society of America*, volume 90 (1991), p. 522-531

- Moustier, C. de et al.; 'Lecture 2, Fundamentals of echo sounding'; *Ocean Mapping Group Multibeam Sonar Training Course*, Amsterdam, 15-20 October 2001

- Moustier, C. de et al.; 'Lecture 18, Acoustic Seabed Interaction Theory'; *Ocean Mapping Group Multibeam Sonar Training Course*, Amsterdam, 15-20 October 2001

- *Multibeam Sonar Theory of Operation*; L-3 Communications SeaBeam Instruments; 2000

- Peucker, T.K.; 'Data structures for digital terrain models:discussion and comparison'; *Harvard Papers on Geographic Information Systems, no. 5*, 1978; Harvard University Press

- Richards, J.A., X. Jia; *Remote sensing digital image analysis: in introduction*; Springer, Berlin Heidelberg, 1999

- Smith, W.H.F., D.T. Sandwell; 'Bathymetric prediction from dense satellite altimetry and sparse shipboard bathymetry'; *Journal of Geophysical Research*, vol. 99 (1994), p. 21803-21824

- Schenke, H.W.; 'GPS und Fächersonarmessungen mit Hydrosweep auf FS Polarstern'; *ZIV 8/9*, 1992, p. 599-616

- Schenke, H.W., M. Gutberlet; 'Hydrosweep, A new era in high precision bathymetric surveying in deep and shallow water'; *Marine geodesy*, vol. 13 (1989), p. 1-23

- Tsoukalas, N.; *Studienarbeit, Vorbereitung und durchführung bathymetrischer Vermessungen mit dem eisbrechenden FS Polarstern im Rahmen eines geophysikalischen Untersuchungsprogramms im zentralen arktischen Becken*; Universität Stuttgart, Institut für Photogrammetrie, 1999

- Urick, R.J.; *Principles of Underwater Sound*; third edition; McGraw-Hill, New York, 1983

- Wackernagel, H; *Multivariate Geostatistics*; Springer Verlag, Heidelberg, 1995

- Weibel, R., M. Heller; 'Digital terrain modelling', *Geographical Information Systems (D.J. Maguire, M.F. Goodchild, D.W. Rhind)*, volume 1 (1991), p. 269-297

- Worboys, M.F.; *GIS a Computative Perspective*; Taylor & Francis Ltd., London, 1997

Appendix A:

Alfred Wegener Institute for Polar and Marine Research

The master research was a combined research of the Alfred Wegener Institute for Polar and Marine Research (AWI) and the Delft University of Technology (TU) Delft. During the period from December 2000 till April 2001 a practical work was carried out, and from May 2001 until December 2001 the work was concentrated on the Master Thesis.
This chapter is an introduction in the organization of the AWI, it gives an impression of the research and the work that is carried out.

The Alfred Wegener Institute

Polar and Marine research are central themes of Global system and Environmental Science. The AWI conducts research in the Arctic, the Antarctic and at temperate latitudes. It coordinates polar research in Germany and provides both the necessary equipment and the essential logistic backup for polar expeditions. Recent additional research themes include North Sea research, contributions to marine biological monitoring, marine pollution research, investigation of naturally occurring marine substances and technical marine developments.

The Institute was established as a public foundation in 1980. The Foundation Alfred Wegener Institute for Polar and Marine Research includes the AWI in Bremerhaven, the Potsdam Research Unit (1992), the Biologische Anstalt Helgoland, and the Wadden Sea Station Sylt. The Foundation Alfred Wegener Institute is a member of the Hermann von Helmholtz Association of German Research Centres.
The German Federal Ministry of Education and Research covers 90% of financing, the state of Bremen 8% and the states of Brandenburg and Schleswig-Holstein provide 1% each. The Foundation had 700 employees and a total budget of 165 million DM in 1999.

Mission

The Institute's research mission is to improve the understanding of ocean-ice-atmosphere interactions, the animal and plant kingdoms of the Arctic and Antarctic, and the evolution of the polar continents and seas. Given the major role played by these regions within the Earth's climate system, global change is a central focus of the research effort at the AWI.

International collaboration

AWI collaborates in numerous international research programmes and maintains close contacts with many universities and institutes in Europe and all over the world. It sends scientists to other institutes throughout the world, to other research ships and stations, and invites scientists from other nations to expeditions aboard Research Vessel (RV) 'Polarstern', as well as to the institutes in Bremerhaven and Potsdam. About a quarter of those participating in the expeditions on board RV 'Polarstern' are scientists from abroad.

Organization

The Alfred Wegener Institute Foundation for Polar and Marine Research consists of three parts. First there is the Directorate, then the scientific part, and finally there is the general part. The scientific part has four Departments: Climate System, Pelagic Ecosystems, Benthic Ecosystems and Geosystem. The scientific part is supported by the general part. In Figure A the organization is shown in a diagram.

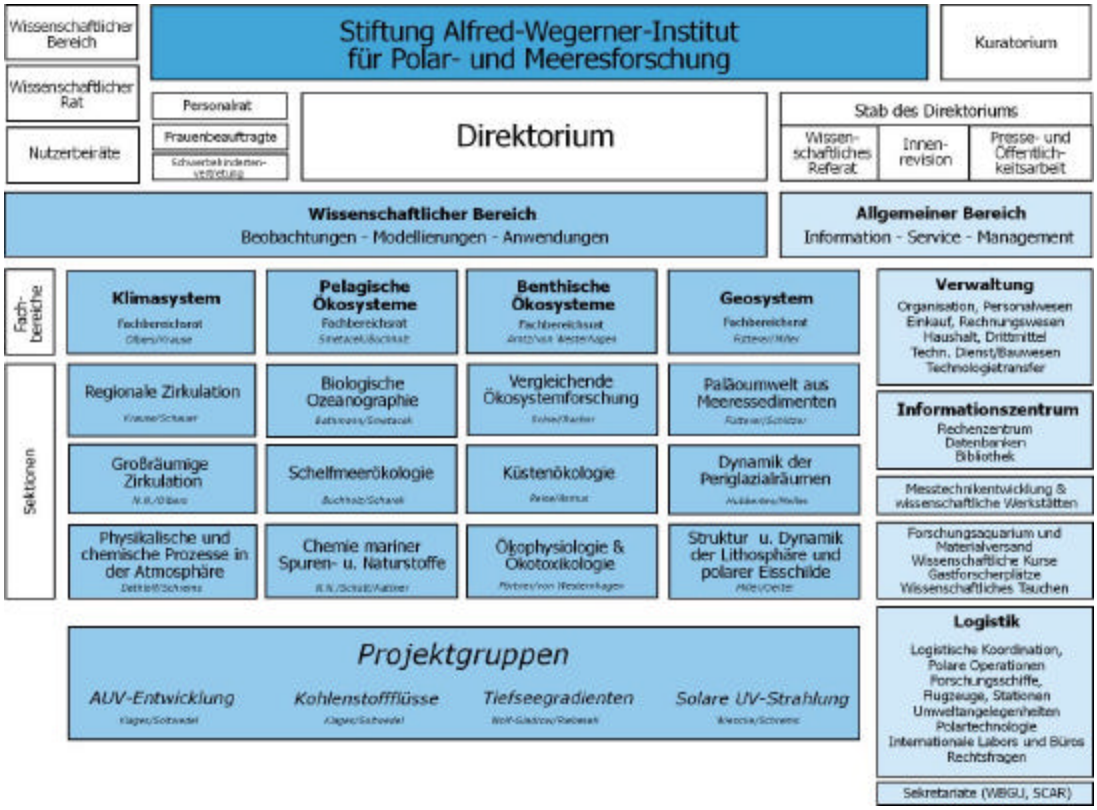

Figure A: The organization of the Alfred Wegener Institute

Climate System

The coupled ocean-ice-atmosphere system and its importance for world climate form the central focus of work in the Physics Section of the Alfred Wegener Institute. AWI researchers conduct surveys and model calculations relating to oceanic circulation, transport of substances and energy in the polar seas and the polar atmosphere, and to the influence exerted by these processes on the global climate system. Oceanographic studies are concentrated on the modification of water masses in the Weddell Sea and the North Polar Seas, and on the movement of modified deep and bottom water masses into the world ocean. Atmospheric studies examine variations in the concentrations of climate-forcing trace gases and aerosols, and their impacts on the Earth's radiation balance.

Pelagic System

This department deals with the interactions between the biology of pelagic organisms and the biogeochemical aspects of the oceans. There are many topics that form the main research lines, these are: carbon and silica global cycles, ecology and ecophysiology of krill, sea ice dynamics, vertical particle fluxes in the polar regions, phylogeny and evolution of plankton, genetic properties of toxic algae, ecology and biodiversity of shelf seas, marine bacteria and fungi, anthropogenic chemical tracers and biogenic elements research, and long-term speciation in the North Sea.

Benthic Ecosystem

This department deals with ecological, physiological and ecotoxicological topics. Shelf and coastal waters of the polar seas as well as coastal waters of the North Sea are the areas of major interest. Central themes are the reactions of cells, individuals, populations and communities towards external influences, and organisation and dynamics of populations, communities and ecosystems.

Geosystem

Geoscientists at the Alfred Wegener Institute are reconstructing the history of the polar continents and seas. They study sedimentation history, the processes of deposition and geological transformation in the oceans, marine biogeochemical cycles, and the paleoclimate of the polar regions. Glaciologists are working on the reconstruction of climate history from ice cores, researching the mass balance and the dynamics of the large ice masses in Greenland and the Antarctic, as well as their interactions with the global climate. Seismic measurements and the identification of anomalies in the Earth's gravitational and magnetic field provide the scientists with valuable information about the structure of the Arctic and Antarctic continental shelfs. Atmospheric chemists at AWI are unravelling the chemical processes in the troposphere and stratosphere that determine our environment. The bathymetry deals with seafloor mapping with the multibeam system Hydrosweep installed on RV 'Polarstern'.

Scientific Stations

'Georg von Neumayer' Station

Ekström Shelf Ice, Atka Bay, northeast Weddell Sea
Position: 70°39'S, 08°15'W

The first 'Georg von Neumayer' Station in the Antarctic was established in 1981 on the Ekström Shelf Ice as a research observatory for geophysical, meteorological and air chemistry measurements, as well as a logistics base for summer expeditions. Georg von Neumayer, whom the station is named after, was an important promoter of Germany's research activities in Antarctica. Ice movements and heavy snow deposits necessitated the construction of a new station building in the early 1990's. In March 1992, the new Neumayer station was completed only ten kilometers from the original site.

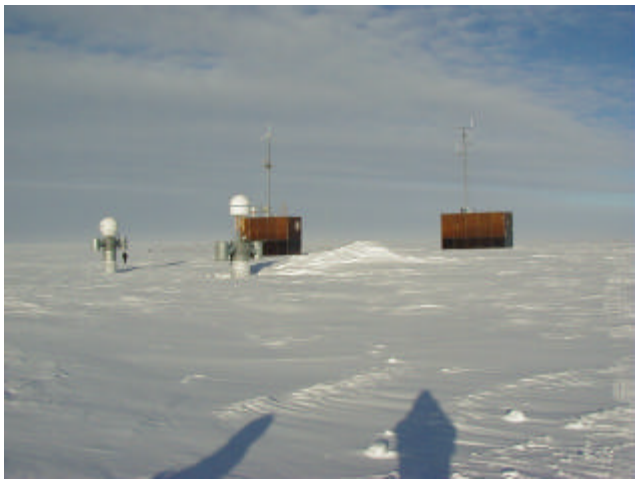

Figure B: The 'Georg von Neumayer' station.

The snow-covered Neumayer Station is located on shelf ice that is 200 meters thick and almost completely flat. All that can be seen from the distance are the towers of the station entrance, which project a couple of meters over the snow. The shelf ice margin, where supply ships moor, is ten kilometers away. The station consists of two parallel steel tubes, each eight meters in diameter and around 90 meters long, in which containers are inserted to accommodate living quarters, kitchen, mess, hospital, various laboratories, workshops, radio operator's room, sanitary facilities, two power supply stations and a snow melting plant. Another transverse tube of similar length contains storage, waste and tank containers, as well as space for vehicles. A tunnel links the main station with a special garage for all the vehicles used at the station, which range from motor sleds to a rotary snowplough. The station's power supply comes from diesel generators, the waste heat is used for the heating system and for melting snow. A 20 kW wind generator is an innovative and eco-friendly source of energy in Antarctica. When the station was being designed, the requirements laid down in the new Protocol on Environmental Protection

to the Antarctic Treaty were adhered to, for example through the use of environmentally neutral construction materials, catalytic converters for the diesel generators and oil collecting equipment for the oil tanks. Waste is routinely collected and shipped back to Germany once a year. Nine or at most ten people live and work at Neumayer Station during the Antarctic winter: a medical doctor who also acts as the head of the station, two meteorologists, two geophysicists, an engineer, an electrician, a radio operator/electronics engineer and a cook. Each team overwintering at the station stays there for 14 to 15 months, for nine months their only link to the outside world is by radio, and nowadays also by the internet.

'Dallmann' Labor

Antarctic Peninsula, South Shetland Islands
Position: 62°14'S, 58°40'W

In January 1994, AWI and the Instituto Antártico Argentino jointly opened the Dallmann Laboratory at Argentina's Jubany Station on King George Island. The laboratory is named after Eduard Dallmann, a polar explorer from Bremen. The laboratory is the first research facility in the Antarctic for which an international agreement was concluded for collaboration between scientists from Argentina, The Netherlands and Germany. The Dallmann Laboratory offers living and working space for twelve scientists, and is equipped with four laboratories, workshops, storage space, an aquarium container, diving equipment and some igloo huts. Although the Jubany Station is staffed throughout the year, the Dallmann Laboratory is only open during the summer months, from October to March. Supported by the logistics available at the Argentinean station, the laboratory offers biologists and earth scientists the facilities. The scientists need to work in ice-free areas and shallow waters close to the coast. This is possible only in the few Antarctic areas where the coastline is not covered by thick shelf ice. Research divers investigate the composition and stability of algal and faunal communities. Research findings on feeding relations and the physiology of species enable scientists to advance our knowledge about the development of polar communities under the impact of global environmental changes.

'Filchner' Station

Filchner-Ronne Shelf Ice, southern Weddell Sea

The Filchner Station, opened in 1982, was situated in the southern Weddell Sea on one of the largest ice shelves in the Antarctic (470,000 km2). It was named after Wilhelm Filchner, geographer and leader of Germany's second South Pole Expedition (1911/12).
The calving of a several thousand square kilometer large iceberg from the Ronne Shelf Ice, which took the Filchner Station with it, was observed via satellite on 13th October 1998. The Rescue Operation succeeded in February 1999; the station was unmanned and drifted in the Weddell Sea. Within ten days containers and laboratories were removed and 170 tons of equipment were loaded on the research vessel 'Polarstern'. The station was used during the Antarctic summer only. It served as a base for glaciological work in the international Filchner-Ronne Ice Shelf Programme (FRISP). Research focused on the flow properties of the ice shelf, substance loads to ice from the atmosphere and the

interactions between ice shelf and the ocean. AWI also operated an automatic weather station in the immediate vicinity of the station since 1990. From here, data on air pressure, temperature, and wind speed and wind direction were continuously fed into the global weather data network. The containers comprising the Filchner Station were on stilts, and provided accommodation for up to twelve researchers and technicians. Snowfall caused a steady increase in the height of snow on the ice, so the containers had been raised by about a meter every two to three years. The station's position was subject to constant alteration due to movement of the ice shelf. Its north-easterly drift was in the order of 1,000 meters per year.
After the rescue operation the station was rebuild as 'Kohnen' station on the Antarctic highlands.

'Koldewey' Station

Spitsbergen, Königsfjord, Ny-Ålesund
Position: 78.9°N, 11.9°O

Spitsbergen belongs to the most northerly group of islands in the Arctic. Ny-Ålesund on the west coast is now an international centre for research activities in the Arctic region.
Carl Koldewey, leader of the first German North Pole Expedition, cruised the waters off Spitsbergen as far back as 1868. Scientists from the Alfred Wegener Institute have been working in Ny-Ålesund since 1988. In August 1991, Germany opened its new Koldewey research station here. It offers research facilities for scientists in the disciplines of biology, chemistry, geophysics and atmosphere physics. The station comprises several buildings. The 'Blue House', for example, has rooms where up to eight scientists can live, work and sleep. One of the main foci of research at Koldewey Station is monitoring the stratosphere over the North Pole. In 1995, a new laboratory for this purpose entered service, featuring a special roof design that permits the installation of optical equipment. Using an infrared spectrometer, it is possible to determine the type and concentration of trace elements in the troposphere and stratosphere. A photometer that uses the sun and moon as a light source is used throughout the year to measure the spectral optical density of atmospheric aerosols. A 'laser-radar' device is used to determine the concentration of ozone and the amount of aerosols at high altitudes. In addition, balloon-borne radiosondes measure temperature, water vapour pressure and vertical distribution of ozone. Since 1992, the Koldewey Station has formed part of the global 'Network for Detection of Stratospheric Change'. AWI is conducting the stratospheric monitoring programme in conjunction with the University of Bremen and the Norwegian Institute for Air Research. The meteorological and aerological data measured at the station are sent on a regular basis to the World Meteorological Organisation, WMO.

Research Vessel 'Polarstern'

Arctic and Antarctic Ocean

The most important tool in Germany's polar research program is RV 'Polarstern', a research and supply vessel; see Figure B. Since she was first commissioned in 1982, RV 'Polarstern' has completed many expeditions to the Arctic and Antarctic, at the time of writing 17 in the Arctic, and the 19th expedition in the Antarctic started. She was specially

designed for working in the polar seas and is currently the most sophisticated polar research vessel in the world.

The RV ‘Polarstern’ spends almost 320 days a year at sea. Between November and March she usually sails to and around the waters of the Antarctic, while the northern summer months are spent in Arctic waters. The ship is equipped for biological, geological, geophysical, glaciological, chemical, oceanographic and meteorological research, and contains nine research laboratories. Additional laboratory containers may be stowed on and below deck. Refrigerated rooms and aquaria permit the transport of samples and living marine fauna. Research equipment and measuring instruments are positioned with the help of cranes and winches, sometimes at extreme depths. Special sounding devices with depth ranges up to 10,000 meters and which can penetrate up to 150 meters into the seafloor, are available for scientific investigations. The computer system on board continuously captures and stores meteorological, oceanographic and other data as required. The ship has a crew of at most 44, and offers work facilities for a further 50 scientists and technicians.

Figure C: RV ‘Polarstern’.

The RV ‘Polarstern’ is a double-hulled icebreaker operational at temperatures as low as minus 50 °C, which enables her to overwinter in the ice sheets of the polar seas. RV ‘Polarstern’ can break through ice 1.5 meters thick at a speed of approx. 5 knots. Ramming must break thicker ice.

Bathymetry & Geodesy

The group Bathymetry & Geodesy is a part of the section Paleoclimate and Marine Sediments and forms together with the sections Periglacial Dynamics and Lithosphere and Polar Ice Sheets the department Geosystem. The senior scientist is Hans-Werner Schenke, he coordinates the research in the group consisting of a research staff of four scientists and, at this moment, four students. The work tasks split up in two. The first task is the bathymetry, geodesy is the second task.

Bathymetry

Multibeam bathymetric survey techniques provide a rapid means of determining the morphology and nature of the seafloor. The Hydrosweep System onboard RV 'Polarstern' provides 59 individual soundings of the water depth and echo strength for each ping. Moreover side scan information and backscatter is retrieved. Automatic seafloor tracking programs determine depths and echo strengths for each beam element, correct for transducer motion, and calculate geographic coordinates for each individual sounding.

Hydrosweep multibeam bathymetry is a major reconnaissance mapping tool used by AWI geo-scientists for marine geology surveys. Multibeam bathymetry, backscatter intensity and side scan data are collected as the first stage of multiparameter geophysical surveys. The multibeam bathymetric data are used to create shaded relief images that depict seafloor morphology. These images are used to interpret features on the seafloor such as channels, areas of bedrock outcrop, small-scale bed forms, rocks and other small objects. Acoustic backscatter intensity measurements are used to determine physical properties, for example the distribution of coarse and fine sediments. The maps and images form the basis for the preliminary interpretation of geological processes and features, and are used to plan subsequent surveys using higher resolution side scan sonar and seismic reflection systems to better define features identified on the multibeam data.

Geodesy

The role of surveying and geodesy in classical polar research expeditions has mainly been restricted to determine positions and to provide geodetic reference frames for mapping. But the field of application has been expanding dramatically in the last decades. New satellite techniques with increasing accuracies, especially the Global Positioning System (GPS) and satellite altimetry, provide excellent weather independent and highly accurate tools for the operation under harsh conditions in polar regions.

Geodetic methods, such as GPS and tide gauge measurements, can be used to determine both relative and absolute rates of tectonic plate movements. A global network of IGS (International GPS service) sites provides a geodetic datum in the International Earth Reference System's (IERS) International Terrestrial Reference Frame (ITRF). These precisely known IGS stations are available as long term stable reference for local measurements.

Long-term observations of the sea surface with tide gauge measurements are used to detect variations in the mean sea level. By linking the tide gauge benchmarks to ITRF-referenced GPS markers, a vertical datum can be derived for the local site. This allows a separation of sea level changes from plate uplift, which might result either from geodynamic processes or possibly from climate changes, e.g. melting of polar ice masses. Thus geodetic techniques contribute not only to geophysics, but also to global climate research.

Gravity measurements on land, as well as at sea, are needed for the derivation of the gravity field, which provides a fundamental basis for the understanding of tectonic processes. Gravity anomalies, additionally computed from satellite altimetry, reveal plate boundaries, fracture zones and bathymetric structures. Together with tide gauge records gravity data provide information about the vertical datum. This also is important to reduce ellipsoid-based GPS data to orthometrical heights.

Appendix B:

Geological Stations ANTXII/4

Listed are the geological stations in the Eltanin Impact Area, made during expedition ANTXII/4.

Longitude	Latitude	Station Number
-89° 48. 780'	-55° 39. 180'	PS2667-6
-91° 14. 100'	-57° 16. 620'	PS2668-2
-90° 25. 260'	-57° 31. 140'	PS2669-1
-90° 28. 080'	-57° 29. 220'	PS2670-1
-90° 29. 580'	-57° 28. 920'	PS2671-1
-90° 21. 780'	-57° 31. 200'	PS2672-1
-91° 49. 980'	-57° 58. 740'	PS2674-1
-93° 30. 660'	-57° 52. 920'	PS2675-1
-90° 11. 700'	-57° 37. 960'	PS2702-1
-91° 10. 800'	-57° 36. 060'	PS2703-1
-90° 48. 420'	-57° 23. 370'	PS2704-1
-90° 29. 580'	-57° 28. 800'	PS2705-1
-91° 51. 540'	-57° 58. 020'	PS2706-1
-90° 39. 360'	-57° 55. 300'	PS2707-1
-90° 59. 880'	-57° 46. 760'	PS2708-1
-91° 13. 200'	-57° 35. 390'	PS2709-1
-90° 50. 940'	-57° 00. 930'	PS2710-1
-91° 37. 620'	-57° 15. 270'	PS2711-1
-91° 55. 440'	-57° 21. 640'	PS2712-1
-89° 17. 880'	-57° 23. 040'	PS2713-1
-89° 16. 080'	-57° 22. 680'	PS2714-2
-88° 00. 480'	-57° 02. 460'	PS2715-1

Appendix C:

Geological Stations ANTXVIII/5a

Listed are the geological stations in the Eltanin Impact Area, made during expedition ANTXVIII/5a.

Longitude	Latitude	Station Number
-93° 49. 800'	-57° 32. 700'	PS58280-1/2
-91° 57. 585'	-57° 24. 577'	PS58281-1
-91° 28. 679'	-57° 13. 047'	PS58282-1
-91° 28. 164'	-57° 12. 871'	PS58283-1
-90° 50. 100'	-57° 01. 000'	PS58284-1
-89° 34. 914'	-56° 43. 639'	PS58285-1
-89° 16. 415'	-57° 23. 347'	PS58286-1
-90° 29. 610'	-57° 28. 930'	PS58287-1
-91° 48. 850'	-57° 58. 813'	PS58288-1
-91° 10. 703'	-57° 34. 643'	PS58289-1
-91° 09. 300'	-57° 38. 800'	PS58290-1/2
-92° 22. 760'	-57° 02. 230'	PS58291-1
-93° 47. 710'	-56° 34. 090'	PS58292
-92° 18. 980'	-55° 46. 000'	PS58293
-92° 06. 950'	-55° 51. 030'	PS58294
-91° 26. 400'	-56° 50. 310'	PS58295
-91° 37. 800'	-56° 27. 000'	PS58296
-91° 13. 190'	-57° 35. 390'	PS58297
-91° 14. 560'	-57° 23. 790'	PS58298
-90° 24. 800'	-57° 23. 400'	PS58299
-91° 55. 450'	-57° 15. 230'	PS58300

Appendix D:

List of Planned Profiles

In this table the planned profiles are listed. This profiles were planned during expedition ANTXVIII/5a to make it possible to fill the data gaps that were still left after the surveying during expedition ANTXII/4.

Point number	Latitude Degrees/minutes		Longitude Degrees/minutes		Profile number	Distance in seamiles
1	57	29.2	92	11.5	1	
2	57	52.8	92	11.5	1	23.6
3	57	50.5	92	14	2	
4	57	50.5	91	35	2	20.52632
5	57	31.5	92	0	3	
6	57	45.8	92	0	3	14.3
7	57	31.5	91	50	4	
8	57	51	91	50	4	19.5
9	57	22.5	91	50	5	
10	57	28.5	91	50	5	6
11	57	17.5	91	48	6	
12	57	12.3	91	50	6	5.305472
13	57	5.5	91	25	6	14.81115
14	57	16.4	91	32.8	7	
15	57	12.8	91	13	7	11.02535
16	57	9.5	91	6	8	
17	57	7.2	91	1	8	3.495026
18	57	21.5	91	42	9	
19	57	29	91	32.5	9	9.013878
20	57	20.8	91	16	9	11.94385
21	57	24.4	91	9	10	
22	57	34	91	26	10	13.12309
23	57	15.2	90	44	11	
24	57	18	90	49	11	3.842552
25	57	31.5	91	38.5	12	
26	57	44.5	91	39.5	12	13.01065
27	57	44.5	91	22.5	12	8.947368
28	57	37.5	91	30	13	
29	57	41	91	23	13	5.081674
30	57	50.5	91	21.5	14	
31	57	44.5	91	6.5	14	9.915991

point number	Latitude Degrees/minutes		Longitude Degrees/minutes		Profile #	Distance in seamiles
32	57	54.5	91	15.5	15	
33	57	54.5	91	7	15	4.473684
34	57	48.8	91	0	15	6.787003
35	57	46	90	54	16	
36	57	34	90	34.5	16	15.79026
37	57	37	90	21.5	17	
38	57	48.2	90	40.5	17	15.01466
39	57	52	90	47.5	18	
40	57	55.5	90	53	18	4.541971
41	57	59.2	90	58	19	
42	58	2	91	3	19	3.842552
43	57	59	92	7.5	20	
44	58	9.5	92	7.5	20	10.5
45	58	9.5	91	58	20	5
46	58	1.5	91	58	20	8
47	57	23.8	90	21	21	
48	57	13	90	2	21	14.7187
49	57	14.4	90	10.5	22	
50	57	5	90	48	22	21.86099
51	57	18	90	17	22	20.86157
52	57	18.8	89	24.5	23	
53	57	28	90	8	23	24.67405
54	57	20.5	89	56	23	9.80506
55	57	16	89	36	23	11.44785
56	57	27.5	89	16	24	
57	57	33.5	89	23	24	7.040839
58	57	29	89	31	25	
59	57	35.8	89	52	25	12.97693
60	57	38.2	89	35.5	25	9.009745
61	57	40.5	89	14	26	
62	57	42.5	89	6	26	4.661387
63	57	28.5	88	53	26	15.5825
64	57	15	89	17	27	
65	57	9.5	89	37	27	11.87659
66	56	59	89	43	28	
67	57	2.5	89	35	28	5.475265
68	57	4	89	29	29	
69	57	11	89	9	29	12.64133
70	57	36	90	6	30	
71	57	44	89	51	30	11.23952

Appendix E:

Usefull ArcInfo Commands

Import xyz-files:

- xy-file: three columns seperated by a blank, and longitude and latitude in decimal degrees {Pointnr. Longitude Latitude}.
- z-file: two columns seperated by a blank, and z in meters {Pointnr. Depth}.

Generate <coverage name 1>
Input <xy-filename>
Points
Quit
Build <coverage name 1> point

Tables
Define <info name>
<item name 1> (same as point item in <coverage name 1>)
…
<item name 2> (for example depth)
…
Add from <z-filename>
Quit

Joinitem <coverage name 1>.pat tmp <coverage name 1>.pat <item name 1>

Create TIN:

Createtin <out tin> <weed-tolerance> <proximal-tolerance>
Cover <coverage name 1> point <item> # # # <weed-tolerance>
…
End

Tincontour <tin> <coverage name 2> <interval> 0 contour # <weed-tolerance>

Inverse Distance Weighting:

<grid name> = idw(<coverage>, <item>, <boundary coverage>, <power>, radius,
500, 5, <cellsize>, <xmin>, <ymin>, <xmax>, <ymax>)

<grid name> = idw(<coverage>, <item>, <boundary coverage>, <power>, sample,
100, 500, <cellsize>, <xmin>, <ymin>, <xmax>, <ymax>)

Empirical Standard Deviation:

Latticespot <lattice> <coverage> <spot item>

Arcedit
Editcoverage <coverage>
Editfeature points
Select for <spot item> EQ -9999
Delete
Save
Quit

Build <coverage> point

Additem <coverage>.pat <coverage>.pat <item name> 4 12 f 3
Tables
Select <coverage>.pat
Items
Calc <item name> = (<item> - <spot item>) * (<item> - <spot item>)
Quit

<grid name_pnt> = pointstats(<coverage>, <item name>, 100, npoints, rectangle, 100, 100)
<grid name_sum> = pointstats(<coverage>, <item name>, 100, sum, rectangle, 100, 100)
<grid name_std> = sqrt (<grid name_sum>/(<grid name_pnt> - 1))

<grid name_mean> = pointstats(<coverage>, <item name>, 100, mean, rectangle, 100, 100)
<grid name_percent> = (sqrt (<grid name_sum> / (<grid name_pnt> - 1)) /
<grid name_mean>) * 100

Slope-dependent Filtering:

<slope grid name> = slope(<input grid name>, percentrise)

<slopemax grid name> = focalmax(<slope grid name>, rectangle, 7, 7, data)

If (<slopemax grid name> >= 30) <output grid name> = <input grid name>
Else if (<slopemax grid name> < 30 & <slopemax grid name> >= 15)
<output grid name> = focalmean(<input grid name>, weight, 3x3bino.ker, nodata)
Else if (<slopemax grid name> < 15 & <slopemax grid name> >= 5)
<output grid name> = focalmean(<input grid name>, weight, 5x5bino.ker, nodata)
Else if (<slopemax grid name> < 5)
<output grid name> = focalmean(<input grid name>, weight, 7x7bino.ker, nodata)
End if

Grid Contouring:

<contour coverage name> = contour(<output grid name>, interval, 20, 0)

Replacing extrapolated areas with no-data value:

<output grid name> = con(isnull(<input grid name>),<input grid name>,
<original grid name>)

Export ArcInfo coverages:

Export coverage <coverage name> <export file name>.e00

Export grid <grid name> <export file name>.e00

Grid out of Pointdata:

<grid name> = pointgrid(<coverage name>, <item>, <lookup table>,<weight table>, 50, nodata)

Replacing zero for nodata:

<grid name_nodata> = setnull(<grid name> eq 0, <grid name>)

Unsupervised Classification:

makestack <stack name> list <grid name_1> … <grid name_x>

stackhistogram <stack name>

stackscattergram <stack name>

<signature name> = isocluster(<stack name>, 4, 50, <minimum class size>, 1)

drawsig <signature name> all

<classification grid name> = mlclassify(<stack name>, <signature name>, <reject fraction>, equal)

Classification Filtering and Enlargement:

<classification grid name_filter> = blockmajority(<classification grid name>, rectangle, 5, 5, data)

<classification grid name_eucal> = eucallocation(<classification grid name_filter>, #, #, 100)

Appendix F:

CD-Rom Data Structure

CD-ROM 1:

ANTXVIII5a_schiff:

surf_dux_schiff	Original surf- and dux-format data
hyd_schiff	Original hyd-format data
nak_schiff	Original nak-format data (navigation)
stations	Locations of the geological stations
10minuten_schiff	Trackinfo of ANTXVIII/5a for GMT and ArcInfo

ANTXII4_schiff:

dat_schiff	Original dux-format data
hyd_schiff	Original hyd-format data
nak_schiff	Original nak-format data (navigation)
stations	Locations of the geological stations
10minuten_schiff	Trackinfo of ANTXVIII/5a for GMT and ArcInfo

Preprocess:

Edited and cleaned dux-format data, after the editing and cleaning within HIPS.

CD-ROM 2:

Eltanin_HIPS_pc:

Fieldsheets.zip	Fieldsheets, grids, and tiles in HIPS
HDCS.zip	Cleaned and edited data in HIPS-format
Session.zip	Eltanin session in HIPS

Test_areas_arcinfo

Dtm_fn	ArcInfo export files of dtm-fn data within the testarea 1
Testarea_1	ArcInfo export files of test area 1
Testarea_2	ArcInfo export files of test area 2
Testarea_3	ArcInfo export files of test area 3

A description of the ArcInfo export files, Testarea_1:

POLYGOON_T1.e00	Polygon test area 1
ELTANIN_T1.e00	Data within test area 1
T1_GRID01CON.e00	Contour lines of grid 1
T1_GRID02CON.e00	Contour lines of grid 2
T1_GRID03CON.e00	Contour lines of grid 3
T1_GRID05CON.e00	Contour lines of grid 5
T1_GRID07CON.e00	Contour lines of grid 7
T1_GRID09CON.e00	Contour lines of grid 9
T1_GRID11CON.e00	Contour lines of grid 11
T1_GRID13CON.e00	Contour lines of grid 13
T1_GRID14CON.e00	Contour lines of grid 14
T1_TINCONTOUR.e00	Contour lines of the TIN
T1_DGM_OUTCON.e00	Contour lines of the DEM

T1_GRID01.e00	idw(eltanin_t1,depths,polygoon_t1,0.5,radius,500,5,100,-15000,-4206500,15000,-4178800)
T1_GRID02.e00	idw(eltanin_t1,depths,polygoon_t1,1.5,radius,500,5,100,-15000,-4206500,15000,-4178800)
T1_GRID03.e00	idw(eltanin_t1,depths,polygoon_t1,0.5,radius,750,5,100,-15000,-4206500,15000,-4178800)
T1_GRID04.e00	idw(eltanin_t1,depths,polygoon_t1,1.5,radius,750,5,100,-15000,-4206500,15000,-4178800)
T1_GRID05.e00	idw(eltanin_t1,depths,polygoon_t1,0.5,radius,250,5,100,-15000,-4206500,15000,-4178800)
T1_GRID06.e00	idw(eltanin_t1,depths,polygoon_t1,1.5,radius,250,5,100,-15000,-4206500,15000,-4178800)
T1_GRID07.e00	idw(eltanin_t1,depths,polygoon_t1,0.5,sample,50,500,100,-15000,-4206500,15000,-4178800)
T1_GRID08.e00	idw(eltanin_t1,depths,polygoon_t1,1.5,sample,50,500,100,-15000,-4206500,15000,-4178800)
T1_GRID09.e00	idw(eltanin_t1,depths,polygoon_t1,0.5,sample,75,500,100,-15000,-4206500,15000,-4178800)
T1_GRID10.e00	idw(eltanin_t1,depths,polygoon_t1,1.5,sample,75,500,100,-15000,-4206500,15000,-4178800)
T1_GRID11.e00	idw(eltanin_t1,depths,polygoon_t1,0.5,sample,75,750,100,-15000,-4206500,15000,-4178800)
T1_GRID12.e00	idw(eltanin_t1,depths,polygoon_t1,1.5,sample,75,750,100,-15000,-4206500,15000,-4178800)
T1_GRID13.e00	idw(eltanin_t1,depths,polygoon_t1,0.5,sample,100,500,100,-15000,-4206500,15000,-4178800)
T1_GRID14.e00	idw(eltanin_t1,depths,polygoon_t1,0.5,sample,100,250,100,-15000,-4206500,15000,-4178800)

T1_DGM_OUT.e00	Final DEM of test area 1
T1_DGM_SLO.e00	DEM without removing no-data areas
T1_SLOPE.e00	Slope grid
T1_SLOPE_INP.e00	Input grid for slope computation
T1_SLOPE_MAX.e00	Slope grid after computing the maximum within a neighbourhood

T1_DIFF0102.e00	Difference between grid 1 and 2
T1_DIFF0103.e00	Difference between grid 1 and 3
T1_DIFF0107.e00	Difference between grid 1 and 7
T1_DIFF0109.e00	Difference between grid 1 and 9
T1_DIFF0709.e00	Difference between grid 7 and 9
T1_DIFF0111.e00	Difference between grid 1 and 11
T1_DIFF0911.e00	Difference between grid 9 and 11
T1_DIFF0913.e00	Difference between grid 9 and 13
T1_DIFFDTM13.e00	Difference between DTM grid and grid 13
T1_DIFFDTM12.e00	Difference between DTM grid and grid 12
T1_DIFF11DTM.e00	Difference between grid 11 and DTM grid
T1_GRID01STD.e00	Standard deviation of grid 1
T1_GRID09STD.e00	Standard deviation of grid 9
T1_GRID11STD.e00	Standard deviation of grid 11
T1_GRID13STD.e00	Standard deviation of grid 13
T1_GRID01SUM.e00	Sum of the points within a grid cell of grid 1
T1_GRID09SUM.e00	Sum of the points within a grid cell of grid 9
T1_GRID11SUM.e00	Sum of the points within a grid cell of grid 111
T1_GRID13SUM.e00	Sum of the points within a grid cell of grid 13
T1_GRID01WAT.e00	Standard deviation in % of water depth of grid 1
T1_GRID09WAT.e00	Standard deviation in % of water depth of grid 9
T1_GRID11WAT.e00	Standard deviation in % of water depth of grid 11
T1_GRID13WAT.e00	Standard deviation in % of water depth of grid 13
T1_GRID01PNT.e00	Number of points within a grid cell of grid 1
T1_GRID09PNT.e00	Number of points within a grid cell of grid 9
T1_GRID11PNT.e00	Number of points within a grid cell of grid 11
T1_GRID13PNT.e00	Number of points within a grid cell of grid 13
T1_GRIDMEAN.e00	Mean water depth in a grid cell of test area 1

A description of the ArcInfo export files, Testarea_2:

POLYGOON_T2.e00	Polygon test area 2
ELTANIN_T2.e00	Data within test area 2
T2_GRID01CON.e00	Contour lines of grid 1
T2_GRID02CON.e00	Contour lines of grid 2
T2_GRID03CON.e00	Contour lines of grid 3
T2_GRID04CON.e00	Contour lines of grid 4
T2_GRID05CON.e00	Contour lines of grid 5
T2_GRID06CON.e00	Contour lines of grid 6
T2_DGM_OUTCON.e00	Contour lines of the DEM

T2_GRID01.e00	idw(eltanin_t2,depths,polygoon_t2,0.5,radius,500,5,100,-15000,-4253100,15000,-4225100)
T2_GRID02.e00	idw(eltanin_t2,depths,polygoon_t2,0.5,radius,750,5,100,-15000,-4253100,15000,-4225100)
T2_GRID03.e00	idw(eltanin_t2,depths,polygoon_t2,0.5,sample,50,500,100,-15000,-4253100,15000,-4225100)
T2_GRID04.e00	idw(eltanin_t2,depths,polygoon_t2,0.5,sample,75,500,100,-15000,-4253100,15000,-4225100)

T2_GRID05.e00	idw(eltanin_t2,depths,polygoon_t2,0.5,sample,100,500,100,-15000,-4253100,15000,-4225100)
T2_GRID06.e00	idw(eltanin_t2,depths,polygoon_t2,0.5,sample,150,500,100,-15000,-4253100,15000,-4225100)
T2_GRID07.e00	idw(eltanin_t2,depths,polygoon_t2,0.5,sample,100,250,100,-15000,-4253100,15000,-4225100)

T2_DGM_OUT.e00	Final DEM of test area 2
T2_DGM_SLO.e00	DEM without removing no-data areas
T2_SLOPE.e00	Slope grid
T2_SLOPE_INP.e00	Input grid for slope computation
T2_SLOPE_MAX.e00	Slope grid after computing the maximum within a neighbourhood
T2_DIFF0102.e00	Differences between grid 1 and grid 2
T2_DIFF0104.e00	Differences between grid 1 and grid 4
T2_DIFF0405.e00	Differences between grid 4 and grid 5
T2_GRID02STD.e00	Standard deviation of grid 2
T2_GRID04STD.e00	Standard deviation of grid 4
T2_GRID05STD.e00	Standard deviation of grid 5
T2_GRID02SUM.e00	Sum of the points within a grid cell of grid 2
T2_GRID04SUM.e00	Sum of the points within a grid cell of grid 4
T2_GRID05SUM.e00	Sum of the points within a grid cell of grid 5
T2_GRID02WAT.e00	Standard deviation in % of water depth of grid 2
T2_GRID04WAT.e00	Standard deviation in % of water depth of grid 4
T2_GRID05WAT.e00	Standard deviation in % of water depth of grid 4
T2_GRID02PNT.e00	Number of points within a grid cell of grid 2
T2_GRID04PNT.e00	Number of points within a grid cell of grid 4
T2_GRID05PNT.e00	Number of points within a grid cell of grid 5
T2_GRIDMEAN.e00	Mean water depth in a grid cell of test area 2

A description of the ArcInfo export files, Testarea_3:

POLYGOON_T3.e00	Polygon test area 3
ELTANIN_T3.e00	Data within test area 2
T3_GRID01CON.e00	Contour lines of grid 1
T3_GRID04CON.e00	Contour lines of grid 4
T3_GRID05CON.e00	Contour lines of grid 5
T3_DGM_OUTCON.e00	Contour lines of the DEM

T3_GRID01.e00	idw(eltanin_t3,depths,polygoon_t3,0.5,radius,500,5,100,35000,-4243700,65000,-4215700)
T3_GRID02.e00	idw(eltanin_t3,depths,polygoon_t3,0.5,radius,750,5,100,35000,-4243700,65000,-4215700)
T3_GRID03.e00	idw(eltanin_t3,depths,polygoon_t3,0.5,sample,50,500,100,35000,-4243700,65000,-4215700)
T3_GRID04.e00	idw(eltanin_t3,depths,polygoon_t3,0.5,sample,75,500,100,35000,-4243700,65000,-4215700)
T3_GRID05.e00	idw(eltanin_t3,depths,polygoon_t3,0.5,sample,100,500,100,35000,-4243700,65000,-4215700)

T3_GRID06.e00	idw(eltanin_t3,depths,polygoon_t3,0.5,sample,100,250,100,-15000,-4253100,15000,-4225100)
T3_DGM_OUT.e00	Final DEM of test area 3
T3_DGM_SLO.e00	DEM without removing no-data areas
T3_SLOPE.e00	Slope grid
T3_SLOPE_INP.e00	Input grid for slope computation
T3_SLOPE_MAX.e00	Slope grid after computing the maximum within a neighbourhood
T3_DIFF0104.e00	Differences between grid 1 and grid 4
T3_DIFF0105.e00	Differences between grid 1 and grid 5
T3_DIFF0405.e00	Differences between grid 4 and grid 5
T3_GRID01STD.e00	Standard deviation of grid 1
T3_GRID04STD.e00	Standard deviation of grid 4
T3_GRID05STD.e00	Standard deviation of grid 5
T3_GRID01SUM.e00	Sum of the points within a grid cell of grid 1
T3_GRID04SUM.e00	Sum of the points within a grid cell of grid 4
T3_GRID05SUM.e00	Sum of the points within a grid cell of grid 5
T3_GRID01WAT.e00	Standard deviation in % of water depth of grid 1
T3_GRID04WAT.e00	Standard deviation in % of water depth of grid 4
T3_GRID05WAT.e00	Standard deviation in % of water depth of grid 4
T3_GRID01PNT.e00	Number of points within a grid cell of grid 1
T3_GRID04PNT.e00	Number of points within a grid cell of grid 4
T3_GRID05PNT.e00	Number of points within a grid cell of grid 5
T3_GRIDMEAN.e00	Mean water depth in a grid cell of test area 2

A description of the ArcInfo export files, DTM-fn:

DTM_FN_T1M.e00	DTM-fn data in Mercator
DTMT1_GRID_C.e00	Contour lines of DTM-fn
DTM_T1_GRID.e00	DTM-fn grid
DTM_T1_PNT.e00	Number of points within a grid cell of the DTM-fn grid
DTM_T1_WAT.e00	Standard deviation in % of water depth of the DTM-fn grid
DTM_T1_SUM.e00	Sum of the points within a grid cell of the DTM-fn grid
DTM_T1_STD.e00	Standard deviation of the DTM-fn grid

CD-ROM 3:

Eltanin_dgm:

Arcinfo data of the DEM computation of the Eltanin Impact Area

Fledermaus:

The fledermaus input data

Eltanin_grid:

The Eltanin grid in xyz-format

A description of the ArcInfo export files, Eltanin_dgm:

ELTANIN.e00	Original data points in the Eltanin Impact Area
ELTANIN_CLEAN.e00	Cleaned data, with standard deviation < 2% of water depth
ELTANIN_ERROR.e00	Removed data with standard deviation >2% of water depth
ELT_SLOPE.e00	Input grid for slope computation
ELT_SLOPE_IN.e00	Eltanin Slope grid, input for slope-dependent filtering
ELT_SLOPE_MAX.e00	Slope grid after computing the maximum within a neighbourhood
ELTANIN_IDW.e00	DEM as input for the cleaning of data >2 % of the water depth
ELTANIN_IDW2.e00	DEM as input for removing extrapolated data
ELTANIN_IDWCL.e00	DEM after cleaning of the data and before removing extrapolated data
ELT_DGM_INP.e00	DEM before removing extrapolated data
ELT_DGM_OUT.e00	DEM after removing extrapolated data
E_MAP_DGM_CL.e00	Contour lines of the Eltanin Impact mapping Area
ELT_DGM_CON.e00	Contour lines in the whole gridded area
ELTANIN_GRID.e00	DEM of the Eltanin Impact mapping area
ELTANIN_SLOPE.e00	Slope grid of the Eltanin Impact mapping area
ELTANIN_ASPCT.e00	Aspect grid of the Eltanin Impact mapping area
ELT_GRID_PNT.e00	Number of points within a grid cell
ELT_GRID_SUM.e00	Sum of the points within a grid cell
ELT_GRIDMEAN.e00	Mean water depth in a grid cell
ELTANIN_STD.e00	Standard deviation
ELTANIN_WAT.e00	Standard deviation in % of water depth
ELTANIN_GT1.e00	Standard deviation in % of water depth, but >1%

CD-ROM 4:

ArcInfo:

Antxii4	AntXII/4 data in Arcinfo
Antxviii5a	AntXVIII/5a data in ArcInfo
Backscatter_ArcInfo	ArcInfo data of the backscatter segmentation
Contourlines	ArcInfo files of the contour lines for the Eltanin Impact mapping area
Filters	Used filters in ascii
Geographic-mercator	Projection files
Mappolygons	ArcInfo files of the four map sheets
Polygoon	ArcInfo files of the polygon for the DEM computation
Polygoon_eltanin	ArcInfo files of the polygon for the Eltanin Impact mapping area
Stations	ArcInfo files of the geological stations
Trackinfo	ArcInfo files of the track data

Backscatter_data/ backscatter:

The computed backscatter files, in dux-format

Alles_antxii4	Backscatter data in dux-format, and x-y and backscatter-angle format of expedition ANTXII/4
Alles_antxviii5a	Backscatter data in dux-format, and x-y and backscatter-angle format of expedition ANTXVIII/5a
Classification	GMT files of the backscatter areas for the classification
DEM_bscat	The DEM files as input for the backscatter computation
Scripts	Used scripts for the computation and analyses of the backscatter data
Test_90_120	Test files for the change of the fan aperture
Test_oud_nieuw	Test files for the changes between backscatter data of AntXII/4 and AntXVIII/5a
Test_pulselength	Test files for change of pulse length
Voor_classificatie	Data used as inputfor classification in ArcInfo

A description of the ArcInfo export files, Backscatter_arcinfo:

Ant124_ba_m	Backscatter data of expedition AntXII/4
Ant185a_ba_m	Backscatter data of expedition AntXVIII5a
Ant185a_class	The input for the grids
Bsct05grd –Bsct50grid	Grids as input for the stack, depending on incidence angle
Bsct05grdn –Bsct50grd	Grids as input for the stack, depending on incidence angle, without the zero data points
Bsct	Stack of the grids
Bsct_sig	Signature file of the classification
Bsct_ant185a	mlclassify(bsct,bsct_sig.gsg)
Bsct_ant185a2	mlclassify(bsct,bsct_sig.gsg,0.5)
Bsct_ant185a3	blockmajority(bsct_ant185a2,rectangle,5,5,data)
Bsct_ant185a4	eucallocation(bsct_ant185a3,#,#,100)
Green/Yellow/Red/Lila	Polygons of areas for testing the classification
Green_ba/Yellow_ba/Red_ba/Lila_ba	The backscatter data within the polygons
Class1-Class4	Grids showing the different classes

A description of the ArcInfo export files, Contourlines:

E_map_dgm_00	100 meter contour lines
E_map_dgm_20	20 meter contour lines
E_map_dgm_col	1000 meter polygons

CD-ROM 5:

DTM-fn:

Data in ascii format for ArcInfo of the whole Eltanin Impact Area and test area 1 and 2

Hyd-HDCS:

Data in different formats for ArcInfo or other programs:

HYD	Hyd-format, binary format
LLZ	Longitude, Latitude, Depth, ascii format
XY.GEO	Point number, Longitude, Latitude for example for ArcInfo
Z.GEO	Point number, Depth for example for ArcInfo

CD-ROM 6:

Eltanin_arcmap:

Ant124_ba	Backscatter and incidence angle data coverage of AntXII/4
Ant185a_ba	Backscatter and incidence angle data coverage of AntXIII/5a
Bsct_class	Backscatter segmentation grid
Eltanin_00	100 meter contour line coverage
Eltanin_20	20 meter contour line coverage
Eltanin_aspct	Aspect grid of the DEM
Eltanin_col	1000 meter polygon coverage
Eltanin_grid	DEM grid of the Eltanin Impact Area
Eltanin_pnt	Point density grid
Eltanin_slope	Slope grid of the DEM
Eltanin_wat	Empirical standard deviation grid
Mappolygons	Polygon coverage of the four map sheets
Polygoon_t1	Polygon coverage of test area 1
Polygoon_t2	Polygon coverage of test area 2
Polygoon_t3	Polygon coverage of test area 3
Station_12_4	Geological stations coverage of AntXII/4
Station_18_5a	Geological stations coverage of AntXVIII/5a
Track_xii4	Geological stations coverage of AntXII/4
Track_xviii5a	Geological stations coverage of AntXVIII/5a
Pdf-files	Figure files of some maps of the Eltanin Impact Area

LYR	Layer files of the different coverages and grids
EXP	Files defining an expression used for the contour line annotation

Eltanin_1a.mxd - Eltanin_4a.mxd	Eltanin maps 1:100 000
Eltanin_overview.mxd	Eltanin map 1:200 000
Eltanin_overview_a3_aspect.mxd	Eltanin aspect map 1:500 000
Eltanin_overview_a3_bathymetry.mxd	Eltanin map 1:500 000
Eltanin_overview_a3_backscatter.mxd	Eltanin backscatter map 1:500 000
Eltanin_overview_a3_DEMgrid.mxd	Eltanin DEM 1:500 000
Eltanin_overview_a3_incidence angle.mxd	Eltanin incidence angle map 1:500 000
Eltanin_overview_a3_segmentation.mxd	Eltanin segmentation map 1:500 000
Eltanin_overview_a3_slope.mxd	Eltanin slope map 1:500 000
Eltanin_overview_a3_Trackinfo.mxd	Eltanin track information map 1:500 000